Nonlocal Dynamical Correlations in in Strongly Interacting Fermion Systems

Nonlocal Dynamical Correlations in Strongly Interacting Fermion Systems

Dissertation

zur Erlangung des Doktorgrades
der Naturwissenschaften (Dr. rer. nat.)
der Naturwissenschaftlichen Fakultät II – Physik
der Universität Regensburg

vorgelegt von
Thomas Maier
aus Regensburg
2000

Contents

Introduction **1**

1 High-T_c superconductors **4**

1.1 Structural and electronic properties 4

1.2 Single-band models for the CuO_2-layers 12

2 The Dynamical Cluster Approximation **16**

2.1 Introduction 16

2.2 Dynamical Mean Field Approximation - Local approximation . . . 18

2.3 Dynamical Cluster Approximation - Spatial correlations 24

2.3.1 Microscopic derivation and formalism 25

2.3.2 Discussion of the DCA 29

2.4 Effective cluster model and methods 34

2.5 Resolvent technique for clusters 37

2.6 Generalizations for symmetry broken phases 41

2.6.1 Finite homogeneous magnetic field 42

2.6.2 Superconductivity 43

2.6.3 Antiferromagnetism 47

2.7 DCA for the tJ-model 52

2.8 Technical details 55

2.8.1 Cluster size and choice of cluster **K**-points 55

2.8.2 Interpolation of the cluster self-energy 57

3 Results **59**

3.1 Preliminary remarks 59

3.2 Half-filling - Antiferromagnetic correlations 66

3.2.1 Antiferromagnetic state 66

3.2.2 Normal state precursors 70

3.2.3 Finite values of t' 75

3.2.4 Dependence on cluster size N_c 76
3.2.5 Summary 78
3.3 Finite doping - From non-Fermi liquid to Fermi liquid behavior . . 78
3.3.1 Density of states 79
3.3.2 Pseudogap 81
3.3.3 Spin susceptibility 82
3.3.4 Nonlocal spectra 84
3.3.5 Fermi surface 86
3.3.6 Dependence on the magnitude of U 89
3.3.7 tJ-model 91
3.3.8 Summary 93
3.4 Optimal doping - Superconductivity 94
3.4.1 Order parameter 94
3.4.2 Density of states 97
3.4.3 Doping dependence 98
3.4.4 Finite values of t' 101
3.4.5 Dependence on the magnitude of U 106
3.4.6 Summary 107
3.5 The DCA phase-diagram 108

4 Summary and Outlook 111
4.1 Summary 111
4.2 Outlook 116

A Properties of the hybridization function $\Gamma(\mathbf{K}, z)$ 119
A.1 On the analyticity of $\Gamma(\mathbf{K}, z)$ 119
A.2 Proof of $\Gamma(\mathbf{K}) \sim \mathcal{O}(1/N_c)$ 122
A.3 $\Gamma(\mathbf{K}, z)$ from cavity construction 122

B Non Crossing Approximation 126

C Generalizations for symmetry broken states 131
C.1 Cluster-NCA in the superconducting state 131
C.2 Cluster-NCA in the antiferromagnetic state 137
C.3 DMFA in the antiferromagnetic state 140

Literature 142

Acknowledgements 153

Introduction

The quantum mechanics of interacting many-particle systems is one of the greatest challenges to condensed matter theory. Motivated by a wide variety of new and unexpected phenomena, the development of accurate methods to describe these systems is one of the most exciting and active fields in physics. Depending on the magnitude of the interactions between the constituting particles, different approaches may succeed in describing real materials. The nature of the atomic orbitals supplying the electrons can be used to classify the systems according to the importance of the Coulomb interaction between electrons.

The overlap of neighboring atomic orbitals in systems with s- or p-electrons is large. This results in strongly delocalized electronic states and hence the mean distance between two electrons is large. Therefore the Coulomb interaction is rendered unimportant compared to the kinetic energy. Applied to these systems, single-particle methods yield reasonable results. Here the complexity of the underlying problem is strongly reduced by mapping the correlated system onto an effective non-interacting one. The most established representative of those methods is the Local Density Approximation (LDA) in the context of the Density Functional Theory (DFT). This *ab-initio* method has been shown to capture the main physics and in particular ground-state properties of a vast variety of materials are in agreement with experiments within a few percent. DFT-LDA has been established as the standard method for s- and p-electron systems. The most appealing fact about this method is that DFT-LDA calculations are parameter-free, i.e. they are starting from first principles.

However DFT-LDA fails for systems, where d- or f-electrons play an important role. Compared to s- or p-electrons, these electrons are localized, originating in much smaller overlaps of neighboring d- or f-orbitals compared to s- and p-orbitals. This results in narrow bands and hence large effective masses. Many-particle effects are not negligible anymore and single-particle methods fail on a very basic level. In strongly correlated electron systems the Coulomb interaction between electrons plays a dominant role and hence strongly influences the electronic properties and the physics of the ground-state phase. The strong interest in developing suitable models and methods that account for the many particle effects is justified by various physical phenomena, including high-temperature superconductivity, heavy fermions, magnetism and the rich phenomenology occurring in quasi one-dimensional compounds. However, despite a multitude of attempts to describe such systems theoretically, a complete understanding of the observed rich physics in these systems has not yet been accomplished. The complexity of the underlying many particle problem usually inhibits the consideration of the full electronic structure and the restriction to low energy scales becomes indispensable. The considered models comprise relevant bands at or close to the Fermi energy only, while the influence of the neglected degrees of freedom is effectively taken into account by adjusting the parameters of the remaining terms of the model.

Despite this number of simplifications, the resulting models are not (or only in special cases) exactly solvable. Existing approximative methods are either based on perturbative expansions in the electron-electron interaction or lack the desired physical effects because the approximations are too crude. On the other hand there are numerically exact approaches like Quantum Monte Carlo or Exact Diagonalization which basically diagonalize the Hamiltonian of a given finite size system. An important limitation encountered in these methods is that the number of degrees of freedom grows rapidly with the system size. As a consequence, the calculations are restricted to small finite size systems and statements for the thermodynamic limit seem problematic. Another promising route to quantum simulations was developed in the last few years. The Dynamical Mean Field Approximation (DMFA) uses the limit of infinite dimensions, where correlation effects are purely local, to reduce the complexity of the problem. Despite the neglect of nonlocal renormalizations, the DMFA has been shown to capture many important aspects of strongly correlated electron systems. But due to its local nature the DMFA has some significant shortcomings. The lack of spatial correlations inhibits transitions to phases with nonlocal order parameters, like e.g. the d-wave superconducting phase in the high-T_c cuprates.

Despite important progresses in the last few years, the field of strongly correlated electron systems still lacks a standard method. One goal of this thesis is to present a novel non-perturbative technique, the Dynamical Cluster Approximation (DCA), a systematic extension of the DMFA by adding nonlocal dynamics. Furthermore, the DCA will be used to study the two-dimensional (2D) Hubbard and tJ-model, two models believed to describe the motion of Fermions in the CuO_2-planes of the high-T_c superconductors.

Chapter 1 reviews relevant experiments on the electronic properties of the high-T_c-cuprates. Their rich phenomenology including the observed unusual normal state behavior is discussed. Two generic models for strongly interacting Fermion systems, the 2D Hubbard model and tJ-model are introduced as models that describe the electronic low-energy physics of the CuO_2-planes common to these materials.

The need for a new approach to strongly correlated electron systems is motivated in the introduction to **Chapter 2** by stressing the shortcomings of existing approaches. A brief review of the DMFA, which is recovered by the DCA in a special limit, follows. A comprehensive introduction to the DCA-formalism along with its microscopic derivation and an extensive discussion of the nature and limitations of the approximation is presented. The DCA-formalism implies the mapping of the lattice system onto a self-consistent periodic cluster model. An extended resolvent technique to solve this cluster model is developed and modifications for symmetry broken phases will be described.

As one of the new perspectives, offered by the DCA, **Chapter 3** discusses results for the 2D Hubbard and tJ-model. It is particularly instructive to look at the effects of nonlocal fluctuations on static and dynamic properties by comparing DCA- to DMFA-results. After a brief summary of already established results on the 2D Hubbard model a systematic study of its single-particle properties in different doping and parameter regimes is presented. The DCA phase-diagram summarizes these results.

The thesis closes with a **Summary** and an **Outlook** with perspectives.

To enhance the readability, the value for the Planck constant $\hbar$, Boltzmann constant k_B and Bohr magneton μ_B is set to 1. Furthermore, the lattice constant in square lattices $a = 1$.

Parts of this work are published in [Mai00a, Mai00b].

Chapter 1

High-T_c superconductors

One of the most famous examples of strongly correlated electron systems are the high-T_c superconductors (HTSC). The goal of this chapter is to review the rich phenomenology occurring in these systems by providing a gross experimental overview of their unusual electronic properties (Sec.1.1). By discussing the electronic structure of the HTSC, the single-band Hubbard model and the tJ-model are motivated as microscopic models that are suitable for describing the physics of the CuO_2-planes in the HTSC (Sec.1.2).

1.1 Structural and electronic properties

The common characteristic feature of all HTSC is a strongly anisotropic layered perovskite-like crystal-structure with conducting CuO_2-planes separated by insulating layers comprised of other elements [Map98] (see Fig. 1.1). Therefore

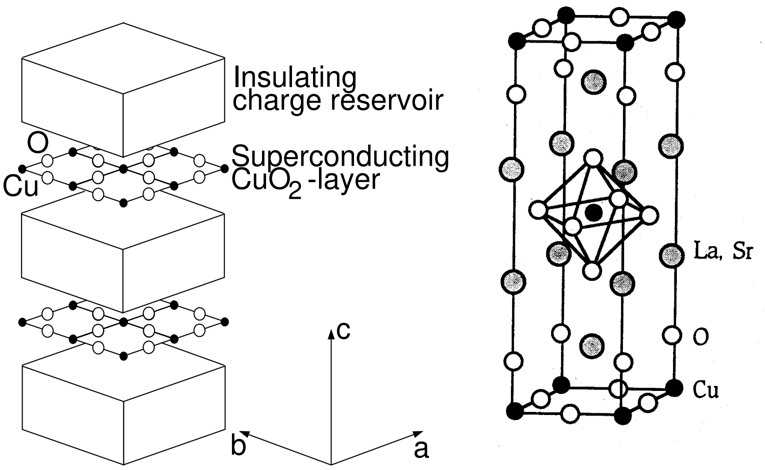

FIGURE 1.1: *Schematic structure of the HTSC (left) and unit cell of LSCO (right). Insulating barriers separate the superconducting* CuO_2*-layers.*

superconductivity is believed to take place within the CuO_2-layers with the insulating barriers only providing charge carriers, usually holes to the layers and thus controlling the doping of the CuO_2-planes. Investigations on the high-T_c compounds $La_{2-\delta}Sr_\delta CuO_4$ (LSCO), $YBa_2Cu_3O_{6+\delta}$ (YBCO) and other systems point to a common phenomenology. Hence a generic temperature T versus doping δ phase-diagram can be drawn, which is shown in Fig. 1.2. Neutron scattering ex-

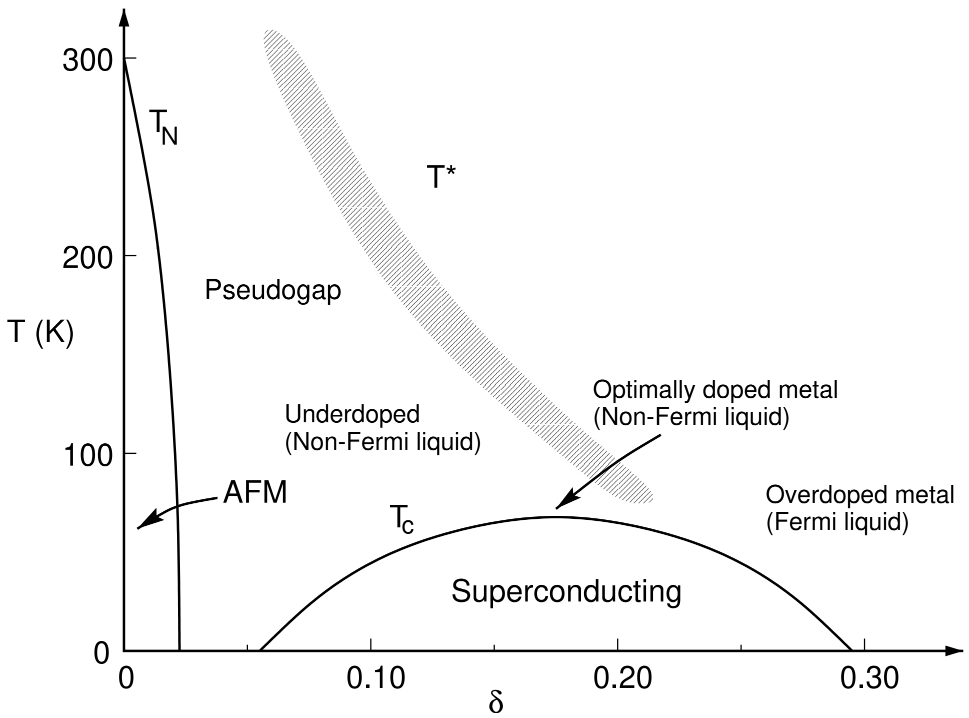

FIGURE 1.2: *Schematic generic temperature-doping phase-diagram for HTSC. The solid lines denoted T_N and T_c delimit the antiferromagnetic and superconducting regions, respectively. The hatched line labeled $T^\star$ delineates the crossover into the pseudogap regime.*

periments on undoped ($\delta = 0$) substances display 2D in-plane antiferromagnetic ordering[1] at low temperatures with the magnetic moments residing on the Cu-sites. Upon doping the antiferromagnetic insulating phase is destroyed and the material is rendered superconducting at low enough temperatures.

The transition temperature T_c as a function of the composition δ first increases with doping (underdoped regime), has a maximum at about 15-20% doping (optimally doped regime) and then drops again for further doping (overdoped regime). It has been established from various experiments that the electrons responsible for superconductivity are paired in singlet spin states. Angle resolved photoemission (ARPES) experiments besides other techniques has been used to

[1] The coupling to the third dimension along the c-axis renders the Mermin-Wagner theorem [Mer66] irrelevant, which inhibits finite-temperature phase transitions in less than 3 dimensions, if the broken symmetry is continuous.

determine the symmetry of the superconducting order parameter[2] $\Delta(\mathbf{k})$. Fig. 1.3 shows a plot of the magnitude $|\Delta(\mathbf{k})|$ of the superconducting gap as a function of the angle on the Fermi surface as shown in the inset. The gap is maximal

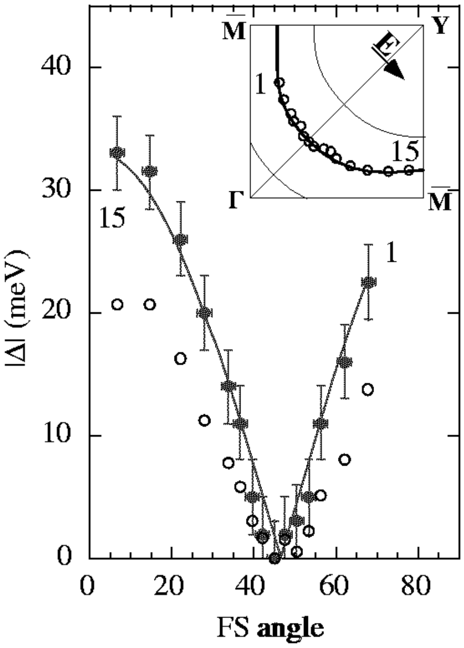

FIGURE 1.3: *The magnitude of the superconducting gap $|\Delta(\mathbf{k})|$ as a function of the angle on the Fermi surface (filled circles) as indicated in the inset. Here, the points in the first Brillouin-zone are denoted $\Gamma = (0,0)$, $\bar{M} = (\pi, 0)$ and $Y = (\pi, \pi)$. The solid line shows a $d_{x^2-y^2}$-wave fit to the filled symbols. Taken from [Ran97].*

along the direction $\bar{\mathrm{M}} = (\pi, 0) \to \mathrm{Y} = (\pi, \pi)$, i.e. at 15° and has a node along the diagonal $\Gamma = (0,0) \to \mathrm{Y} = (\pi, \pi)$, i.e. at 45°. This is consistent with a $d_{x^2-y^2}$-wave symmetry of the order parameter, where the gap can be written as $\Delta(\mathbf{k}) = \Delta_o(\cos k_x - \cos k_y)$. Evidence from various other experimental techniques supports the $d_{x^2-y^2}$-wave nature of the order parameter. A number of experiments, sensitive to the phase of the order parameter $\Delta(\mathbf{k})$ that involve the Josephson-effect are also consistent with a $d_{x^2-y^2}$-wave order parameter [Map98].

A great deal of effort has been devoted to investigate the *normal state* of the cuprate superconductors. It is widely believed that a comprehension of the nature of high-T_c-superconductivity requires achieving a better understanding of the normal state first, which displays very unusual behavior and appears to violate the Landau Fermi liquid picture. The crucial assumption in the Fermi liquid picture is an one-to-one correspondence between the elementary excitations of the strongly correlated electron system, called quasiparticles and those of an ideal Fermi gas. The scattering rate τ^{-1} of these quasiparticles due to interactions with other electrons then obeys the law (a and b are positive real constants)

$$\frac{1}{\tau} = a(\varepsilon - \varepsilon_F)^2 + bT^2 \tag{1.1}$$

[2]For further details and a number of relevant references please see [Map98].

at low temperatures T, if their energy ε is close to the Fermi energy ε_F. This implies that in Fermi liquids quasiparticles on the Fermi surface are well defined objects since their scattering rate vanishes at zero temperature. As a consequence the momentum distribution function $n(\mathbf{k})$ shows a discontinuity in the reciprocal ($\mathbf{k}$-) space separating the regions with occupied and unoccupied states. The Fermi surface defined by the set of $\mathbf{k}$-points where this discontinuity occurs hence is also a well defined object.

Furthermore, since the excitations in Fermi liquids can be bijectively mapped onto those of an ideal Fermi gas, physical quantities display the same behavior as those in an ideal Fermi gas. For example, in a normal Fermi liquid metal the resistivity is quadratic in temperature, $\rho \sim T^2$, and the Pauli spin susceptibility is expected to be temperature independent. The latter can be probed by nuclear magnetic resonance experiments. The Knight-shift ΔK is proportional to the real part of the spin susceptibility $\chi'(\mathbf{q}=0,\omega)$, measuring the polarization of electrons by the applied magnetic field. The spin lattice relaxation rate $1/(T_1T)$ on the other hand is related to the imaginary part of the spin susceptibility χ''. Hence the spin-lattice relaxation rate $1/(T_1T)$ and the Knight-shift ΔK are expected to be temperature independent in the context of a Fermi liquid. Furthermore the Hall-coefficient R_{H} is temperature independent in a normal metal since it only depends on the carrier concentration, which in a metal is temperature independent.

Fig. 1.4 displays a collection of these physical quantities as a function of temperature and various dopings in the high-T_c materials LSCO and YBCO. The following indications of non-Fermi liquid behavior are observed:

- In optimally doped samples the in-plane resistivity $\rho_{ab}(T)$ is a linear function of temperature for a wide range of temperatures from about 1000 K down to T_c.

- The Hall coefficient R_{H}, relaxation rate $1/(T_1T)$ and Knight shift ΔK depend on temperature in underdoped and optimally doped systems. As a function of decreasing temperature they first increase, go through a maximum, and then decrease again.

The evolution of the normal state properties as a function of doping is particularly interesting. In contrast to under- and optimally doped systems Fermi liquid behavior seems to be recovered in overdoped systems, signaled by the resistivity $\rho_{ab} \sim T^2$ (not shown) and temperature independent Hall coefficient R_{H}, relaxation rate $1/(T_1T)$ and Knight shift ΔK [Tim99].

One of the most remarkable aspects of the normal state in underdoped cuprates is the observation of a depression of spin and charge excitations, called the pseudogap (for a review see [Tim99]). The existence of this pseudogap in underdoped samples has been inferred from transport and magnetic experiments (see Fig. 1.4). In underdoped samples at a characteristic temperature $T^\star$ the in-plane resistivity $\rho_{ab}(T)$ deviates from its linear temperature dependence at higher

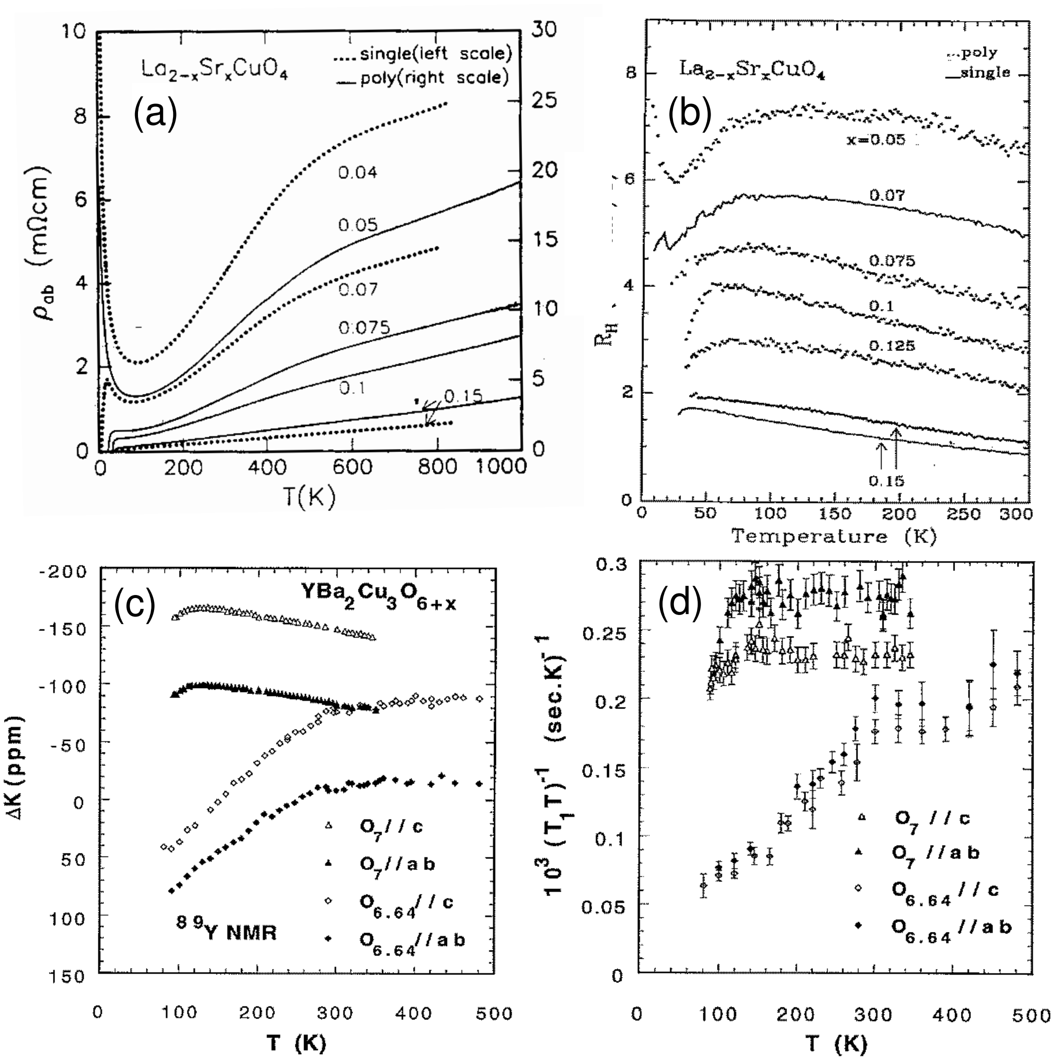

FIGURE 1.4: *Panel a: Temperature dependence of the in-plane resistivity ρ_{ab} for single-crystal films (dotted line) and polycrystalline materials (solid line) for under- to optimally doped ($x = 0.15$) LSCO [Tak92]. Panel b: Hall-coefficient R_{H} of under- to optimally doped LSCO for single-crystal films (solid lines) and polycrystalline samples (dotted line) [Hwa94]. The Knight-shift ΔK (panel c) and the NMR-relaxation rate $1/(T_1T)$ (panel d) of under- ($\mathrm{O}_{6.64}$) and overdoped (O_7) YBCO measured with magnetic fields parallel to the c- and ab-axis of the sample [All93]. All the measured quantities show unusual non-Fermi liquid behavior and indications of a pseudogap in the low energy excitation spectrum: The resistivity ρ_{ab} for optimal doping ($x = 0.15$) increases linearly with temperature, $\rho_{ab} \sim T$ instead of quadratic, as expected for a Fermi liquid. In underdoped samples the resistivity drops below a certain temperature due to reduced scattering and the linear behavior changes to a power law behavior. Instead of being temperature independent, the Hall-coefficient R_{H}, the Knight-shift ΔK and the relaxation rate $1/(T_1T)$ show a depression at low temperatures.*

temperatures and even changes to a semiconducting behavior ($d\rho/dT < 0$) upon further lowering the temperature (see Fig. 1.4, panel a). Concomitant to this anomaly in the charge-channel, spin excitations are suppressed as indicated by the downturn of the NMR data with decreasing temperature (see Fig. 1.4, panel c and d). With increasing doping the crossover temperature $T^\star$, below which the pseudogap is observed, decreases and merges into the superconducting phase boundary in the slightly overdoped regime (see Fig. 1.2).

The most direct and reliable measurements performed to study the existence and nature of the normal state pseudogap are ARPES experiments. Fig. 1.5 shows

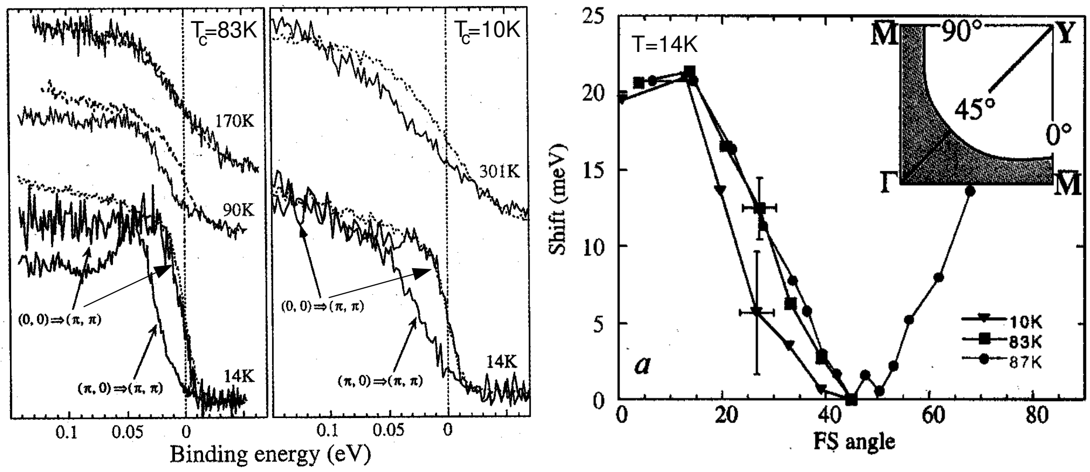

FIGURE 1.5: *Left panel: ARPES spectra [Din96] on weakly (T_c = 83K, left) and highly (T_c = 10K, right) underdoped BSCCO for various temperatures at two points on the Fermi surface, defined where the latter crosses the lines $\bar{M} = (\pi, 0) \to Y = (\pi, \pi)$ and $\Gamma = (0, 0) \to Y = (\pi, \pi)$ (see inset to right panel). The gap in the electronic spectrum observed in the superconducting state persists into the normal state with the same d-wave anisotropy. Right panel:* **k***-dependence of the gap in the* $87\,\mathrm{K}\,T_c$*,* $83\,\mathrm{K}\,T_c$ *and* $10\,\mathrm{K}\,T_c$ *samples, measured at* $T = 14\,\mathrm{K}$.

in the left panel the ARPES spectra [Din96] of weakly underdoped ($T_c = 83\,\mathrm{K}$, left) and highly underdoped ($T_c = 10\,\mathrm{K}$, right) $Bi_2Sr_2CaCu_2O_{8+\delta}$ (BSCCO) at two points on the Fermi surface (see inset to right panel), where the latter crosses the lines $\bar{\mathrm{M}} = (\pi, 0) \to \mathrm{Y} = (\pi, \pi)$ and $\Gamma = (0, 0) \to \mathrm{Y} = (\pi, \pi)$, respectively. In the superconducting state the characteristic $d_{x^2-y^2}$-wave anisotropy with a gap along the $(\pi, 0) \to (\pi, \pi)$ direction and a node along the diagonal $(0, 0) \to (\pi, \pi)$ can clearly be seen. Obviously the pseudogap persists into the normal state, eventually vanishing at $T^\star \approx 170\,\mathrm{K}$ for the $T_c = 83\,\mathrm{K}$ sample (left). The pseudogap in the highly underdoped $T_c = 10\,\mathrm{K}$ sample persists to even higher temperatures, consistent with the doping dependence of the crossover temperature T^* (see Fig. 1.2) as identified by the NMR and transport data. The right panel of

Fig. 1.5 shows the variation of the magnitude of the gap as a function of the angle on the Fermi surface measured at $T = 14\,\mathrm{K}$ for different dopings as indicated by the different T_c's. The $T_c = 10\,\mathrm{K}$ sample is in the normal state, the two other samples are in the superconducting state. Remarkably, the magnitude of the normal state pseudogap displays the same **k**-dependence as the magnitude of the superconducting gap. It has a node along the diagonal and maxima along the directions of k_x and k_y, consistent with $d_{x^2-y^2}$-wave anisotropy. In summary, it appears that the superconducting gap emerges from the normal state pseudogap in underdoped samples.

Three fundamental properties, common to all the cuprate-superconductors provide a constraint on viable microscopic theories of high-T_c-superconductivity (see Fig. 1.2):

- The presence of *antiferromagnetic ordering* in undoped samples in proximity to
- the *superconducting phase with a $d_{x^2-y^2}$-wave order parameter* and
- the *normal state pseudogap* dominating the physics in the underdoped samples.

A successful theory must at least describe all these fundamental features at the same time.

Several theories have been propagated to describe this anomalous behavior found in the HTSC. Scenarios based on the pronounced non-Fermi liquid behavior in the CuO_2-layers have been proposed. The most prominent example is P. W. Anderson's "Interlayer Tunneling Theory" which uses the concept of spin-charge separation known from one-dimensional systems [And97]. There is also a great variety of Fermi liquid based theories. Some of them try to combine the paring idea with the presence of strong antiferromagnetic correlations, e.g. the spin-bag theory [Sch89]. In this family is also the Nearly Antiferromagnetic Fermi Liquid (NAFL) Theory (for a review see [Pin97]) proposed by D. Pines and coworkers, a phenomenological approach, where the electron-electron interaction is mediated by the exchange of spin fluctuations. Since this theory is also relevant to the results presented in this thesis it will be briefly described in the following.

In the NAFL theory the bare dispersion of the quasiparticles is chosen to yield the same Fermi surface observed in the underdoped to optimally doped cuprates, i.e. the hole like Fermi surface closed around (π, π) depicted in Fig. 1.6. The magnetic interaction between these quasiparticles is then held responsible for the anomalous behavior observed in the normal state of the cuprates. Within this approach the electron-electron interaction is mediated by an empirically determined dynamical spin susceptibility [Mil90]. Since in the underdoped to optimally doped systems the latter is strongly peaked at the antiferromagnetic wave

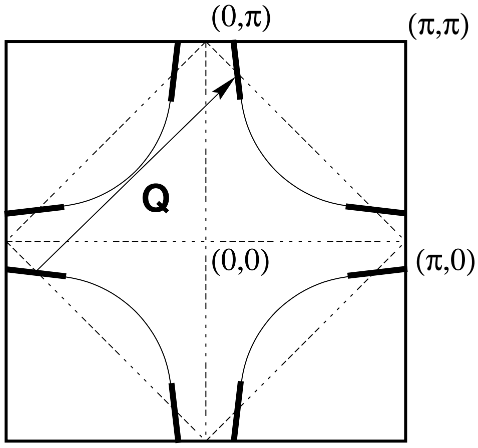

FIGURE 1.6: *The NAFL model for the Fermi surface (solid line) in the cuprates and the magnetic Brillouin zone boundary (dashed line). The intercept of the two lines marks regions on the Fermi surface which can be connected by the antiferromagnetic wave vector* **Q**. *States in these regions (hot spots) are strongly renormalized because they couple strongly to spin excitations.*

vector $\mathbf{Q} = (\pi, \pi)$, the Fermi surface contains two distinct groups of quasiparticles (see Fig. 1.6). "Hot quasiparticles" are located in the vicinity of the "hot spots" (near $(\pi, 0)$ and $(0, \pi)$), regions on the Fermi surface which can be connected by **Q**. Hence, in these regions the magnetic interaction is anomalously large. Cold quasiparticles are located in the remaining parts of the Fermi surface. As a consequence of the strongly anisotropic magnetic interaction, the spectrum near $(\pi, 0)$ becomes gapped for temperatures below $T^\star$ [Sch99], whereas well defined quasiparticles are found along the diagonal $(0, 0) \to (\pi, \pi)$, in agreement with experiments. The magnetic interaction is found to alter the Fermi surface only slightly compared to the non-interacting Fermi surface [Sch99].

Furthermore the transition to the superconducting state can also be understood within the NAFL scenario. It is well known that the exchange of antiferromagnetic spin fluctuations leads inexorably to a transition to a superconducting state with a $d_{x^2-y^2}$-wave order parameter [Mon91] (for a review on spin-fluctuation induced superconductivity see [Sca99]).

However, the field of high-T_c superconductivity still lacks a complete description on a microscopic level. The next section motivates models, believed to capture the gross features of the planar electrons moving in the CuO_2-planes.

1.2 Single-band models for the CuO_2-layers

First principle calculations for high-T_c-compounds provide evidence, that the band, which crosses the Fermi surface has mainly CuO_2-character [Ful91]. Therefore the CuO_2-states are relevant for charge-transport and hence superconductivity. Thus, to reduce the complexity of the problem, it seems reasonable to restrict the model to a 2D model with electrons moving in a single CuO_2-layer. Furthermore such a 2D model can be motivated by the strong in-plane Cu-O-bonds compared to the weak bonds in c-direction. The short c-axis coherence length ξ in the superconducting state, which is much smaller than the distance of neighboring CuO_2-layers further supports the restriction to two dimensions. Therefore the system can be thought of a quasi-2D superconductor.

The counting of electrons in the undoped planar CuO_2-problem, e.g in the parent compound La_2SrCuO_4, results in a $3d^9$-configuration of the copper-ions. As a further simplification, the lattice structure in the vicinity of the copper-ions

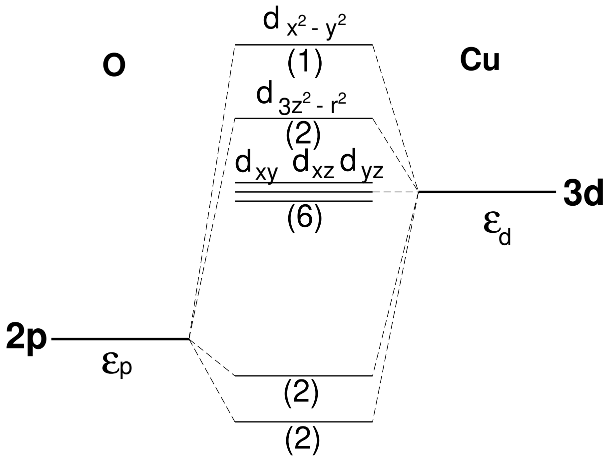

FIGURE 1.7: *Bonding between one* Cu^{2+} *and two* O^{2-} *ions. Only the d-orbitals of* Cu *and the* p_x*- and* p_y*-orbitals of* O *are considered. The energetically highest anti-bonding orbital has* $d_{x^2-y^2}$*-character and contains the hole of the unit cell. The numbers in parentheses indicate the occupation in the undoped compound. Taken from [Ful91].*

removes the degeneracy of the isolated ions. It can be shown [Ful91] that the missing electron (i.e. hole) resides in a hybridized Cu-O-orbital with mainly $d_{x^2-y^2}$-character (see Fig. 1.7). All the other orbitals are occupied and hence are not considered in the construction of the Hamiltonian. Consequently, in the absence of doping these materials contain one hole per unit cell and one would expect a metallic ground-state. The ground-state obtained by DFT-LDA calculations indeed has metallic character. However, experimentally the undoped substances are insulators with antiferromagnetic ordering (see Fig. 1.2). This shortcoming of the LDA emphasizes the importance of a proper treatment of the Coulomb repulsion on the copper-sites within a suitable many-particle approach. The spin dynamics of the undoped cuprates is fairly well described by an antiferromagnetic Heisenberg model, representing the mostly localized spin-1/2 states at the copper-sites.

Upon hole doping the additional hole goes on the oxygen-sites, since the Coulomb repulsion between two holes residing at the same copper-site makes double occupancy energetically unfavorable. This picture is in agreement with electron-energy-loss spectroscopy [Nüc87]. Based on these considerations one can construct a model containing the copper-$d_{x^2-y^2}$- and the oxygen-p_x- and p_y-orbitals, the hybridization between them and the on-site Coulomb-repulsions on copper- and oxygen sites [Eme87, Eme88].

This 3-band Hamiltonian is still somewhat complex to handle and a further reduction to a model containing only one band would be aspiring. Motivated by the strong Cu-O bonds in the plane, a model treating a whole Cu-O_2 plaquette as one site can be constructed.[3] The resulting model is the (single-band) Hubbard model

$$H = \sum_{ij,\sigma} t_{ij} c^\dagger_{i\sigma} c_{j\sigma} + U \sum_i n_{i\uparrow} n_{i\downarrow}\,, \tag{1.2}$$

describing the motion of electrons within a single CuO_2-plane.The Fermionic operator $c^\dagger_{i\sigma}$ ($c_{i\sigma}$) creates (destroys) an electron at site i with spin σ and $n_{i\sigma} = c^\dagger_{i\sigma} c_{i\sigma}$ is the corresponding number operator. The hopping term t_{ij} describes the hybridization between neighboring sites i and j and is usually taken to have the form

$$t_{ij} = \epsilon_o \delta_{ij} - t\delta_{\langle ij \rangle} - t'\delta_{\langle\langle ij \rangle\rangle}\,, \tag{1.3}$$

where ϵ_o is the on-site energy and t and t' are the hybridization magnitudes between nearest $\langle ij \rangle$ and next-nearest $\langle\langle ij \rangle\rangle$ neighbors i and j, respectively. The kinetic term of the Hamiltonian (1.2) is diagonal in the reciprocal space, $\sum_{\mathbf{k}} \epsilon_{\mathbf{k}} c^\dagger_{\mathbf{k}\sigma} c_{\mathbf{k}\sigma}$, with the Fourier transforms $c^\dagger_{\mathbf{k}\sigma}$ ($c_{\mathbf{k}\sigma}$) of the operators $c^\dagger_{i\sigma}$ ($c_{i\sigma}$). For the 2D model on a square lattice the dispersion $\epsilon_{\mathbf{k}}$ has the form

$$\epsilon_{\mathbf{k}} = \epsilon_o - 2t(\cos k_x + \cos k_y) - 4t' \cos k_x \cos k_y\,. \tag{1.4}$$

U represents the on-site Coulomb-repulsion, two electrons feel when residing on the same site. Due to screening the magnitudes of longer-ranged interactions are believed to be small compared to the on-site interaction.

If the oxygen degrees of freedom are explicitly added to the single-band Hamiltonian (1.2), the 3-band Hubbard model [Eme87, Eme88] is obtained. This consists of the copper $d_{x^2-y^2}$, the oxygen p_x, p_y orbitals and the on-site Coulomb repulsion on the copper and eventually oxygen sites.[4] With an effective value of the Coulomb-repulsion U and a finite next-nearest neighbor hopping amplitude t' the (single-band) Hubbard model (1.2) tries to mimic the low energy physics

[3] A more detailed discussion of the relevance of a one-band model towards the physics in the CuO_2-planes can be found in [And97] or in the enlightening discussion between Anderson and Schrieffer published in [And91].

[4] For a DMFA study of its magnetic properties see [Mai97, Mai99], for its optical properties [Zöl97, Zöl00].

of the 3-band Hubbard model [Dag94a, Zan85]. Exact diagonalization studies for finite size clusters of the single-band Hubbard model present convincing evidence that this reduction to an one-band model is indeed possible [Bac91, Hyb90]. Therein it is shown that the single-band Hubbard model can describe the low energy charge and spin excitations of the 3-band model by taking appropriate values for the parameters $U \gtrsim W$, where $W = 8t$ is the bare bandwidth, and a finite $t' < 0$.

The relevance of the Hubbard model for a description of the parent high-T_c compounds, which are dominated by antiferromagnetic correlations can be easily understood. In the strong coupling regime ($U \gg W$) the charge excitations involving doubly occupied sites can be integrated out (see e.g. [Ful91]) to obtain an effective Hamiltonian for the low energy excitations. The neglected degrees of freedom are then effectively reflected in a spin interaction acting between neighboring sites. The resulting model is known as the tJ-model, which for $t' = 0$ reads

$$H_{tJ} = \sum_{ij,\sigma} (\epsilon_o \delta_{ij} - t\delta_{\langle ij \rangle}) \tilde{c}^\dagger_{i\sigma} \tilde{c}_{j\sigma} + J \sum_{\langle ij \rangle} (\vec{S}_i \cdot \vec{S}_j - \frac{1}{4} \tilde{n}_i \tilde{n}_j) \,, \tag{1.5}$$

where the quasiparticle operators

$$\tilde{c}^\dagger_{i\sigma} = (1 - n_{i\bar{\sigma}}) c^\dagger_{i\sigma} \quad , \quad \tilde{c}_{i\sigma} = c_{i\sigma}(1 - n_{i\bar{\sigma}}) \tag{1.6}$$

act in the reduced Hilbert space with only empty and singly occupied sites. The second term stands for the spin interaction between neighboring sites i and j with the spin operators

$$\vec{S}_i = \frac{1}{2} \sum_{\alpha\beta} \tilde{c}^\dagger_{i\alpha} \vec{\sigma}_{\alpha\beta} \tilde{c}_{i\beta} \,, \tag{1.7}$$

where $\vec{\sigma}_{\alpha\beta}$ denote the components of the Pauli spin matrices (see App. C, Eq. (C.4)). The exchange interaction

$$J = \frac{4t^2}{U} \tag{1.8}$$

results from virtual hopping processes from site i to the neighboring site j and back involving a doubly occupied site. In the expansion in t/U an additional term $\sim \mathcal{O}(t^2/U)$ involving three sites occurs. The relevance of this term is still somewhat unclear. However, with decreasing doping δ, where δ denotes the deviation from half-filling, $\delta = 1 - n$, this term is expected to become less important. Since it simultaneously involves one singly occupied and one empty site, it diminishes like $\delta(1-\delta)$. At half filling ($n = 1$) charge fluctuations are frozen out and the tJ-model further reduces to the widely studied Heisenberg model

$$H_{\mathrm{H}} = J \sum_{\langle ij \rangle} \vec{S}_i \cdot \vec{S}_j \,, \tag{1.9}$$

which describes the interaction between spins on a given lattice. Since $J > 0$, this model favors antiferromagnetism and within numerous studies the Heisenberg model has been proven to describe the low energy spin excitations of the undoped cuprates (see e.g. [Bir99]).

The necessity for a relatively large magnitude of U in the Hubbard model puts a constraint on the parameter range, relevant for a proper description of the high-T_c cuprates. Results obtained by approaches based on perturbative expansions in the on-site interaction U are therefore rather questionable, and methods capable of handling strongly correlated electrons in the CuO_2-planes have to be applied.

Chapter 2

The Dynamical Cluster Approximation

After a brief overview about major progresses in the development of numerical approaches towards high-T_c systems (Sec. 2.1), this chapter provides a review of the Dynamical Mean Field Approximation (DMFA), which is reproduced by the Dynamical Cluster Approximation (DCA) for a single-site cluster (Sec. 2.2). Sec. 2.3 presents a comprehensive description of the DCA along with its microscopic derivation. An extensive description of the algorithm and the details of the formalism follow. The DCA reduces the complexity of the lattice problem by mapping it onto an effective periodic cluster (Sec. 2.4). In Sec. 2.5 an extended resolvent technique to solve the cluster problem is developed and the nature of this approximation in the framework of the DCA is discussed. At low temperatures the Hubbard model is expected to show instabilities towards ordered phases. This requires extensions of the DCA algorithm to symmetry broken phases (Sec. 2.6). The DCA equations are derived by means of the Hubbard model. Sec. 2.7 describes the application of the DCA to the tJ-model. Technical details about the actual DCA-NCA calculation follow.

2.1 Introduction

As discussed in Sec. 1.2 it is believed that the 2D Hubbard model (1.2) should capture the essential physics of the high-T_c cuprates. However, despite years of intensive studies, this model remains unsolved, except in one or infinite dimensions. Analytical methods, based on perturbative calculations in the Coulomb interaction U suffer from the strong interaction between the electrons that renders these calculations questionable. Thus many theorists turned to numerical approaches, which can be used to close the gap between the model defined by its Hamiltonian and its actual properties.

Well controlled numerically exact methods like Exact Diagonalization (ED) or Quantum Monte Carlo (QMC) have been developed. These methods basically diagonalize the Hamiltonian for a finite size system. Hence an important problem encountered in these methods is the fact that the number of degrees of freedom grows rapidly with the lattice size. Consequently these calculations are restricted to relatively small system sizes and statements for the thermodynamic limit seem problematic, since they depend on a particular scaling ansatz. Moreover, the limited system size inhibits the study of the low-energy physics of the Hubbard model because of the presence of finite size gaps in the low energy spectrum. Furthermore the infamous “fermion sign” problem limits finite size QMC calculations to high temperatures and small values of the interaction strength U compared to the bare bandwidth W. Hence the temperatures reached within finite size QMC are often too high to observe transitions to symmetry broken phases (see e.g. [Sca99]).

These limitations do not apply to approximate self-consistent many-particle methods like the Fluctuation Exchange Approximation (FLEX) [Bic89, Mor90], which is a conserving extension of the Hartree-Fock theory and Random Phase Approximation. The FLEX method as an approximation based on a perturbative expansion in U breaks down in the strong coupling regime $U > W$. On the other hand it is believed that a proper description of the high-T_c cuprates in terms of the one-band Hubbard model requires $U \gtrsim W$ as discussed in Sec.1.2.

Recently another route to non-perturbative quantum simulations has been proposed. The Dynamical Mean Field Approximation[1] (DMFA) [Bra89, Jan91, Jar92, Geo92] uses the limit of infinite dimensions [Met89, Mül89] to map the lattice problem onto a single-impurity embedded in a medium, which has to be determined self-consistently. The dynamics of the problem become purely local. Due to the availability of many well-controlled techniques to solve the single-impurity Anderson problem, the DMFA has become one of the most widely used methods applied to strongly correlated electron systems. Calculations within DMFA can be performed in the strong coupling regime and take place in the thermodynamic limit. However, in the context of finite dimensional systems, the DMFA assumes that only local dynamics are present. Despite the neglect of spatial fluctuations, the DMFA has been shown to capture several important features of e.g. the Hubbard model [Pru95a, Geo96]. Nevertheless, the local nature of the DMFA entails some significant shortcomings. It does not include nonlocal correlations like antiferromagnetic spin-fluctuations, believed to be essential in many strongly correlated electron systems. Furthermore the lack of spatial correlations inhibits a transition to a state with a nonlocal order parameter. However, both effects are essential for a theoretical description of the high-T_c-cuprates. Here the normal state spectrum exhibits a preformed pseudogap due to spin or superconducting fluctuations and the superconducting order parameter has $d_{x^2-y^2}$-wave symmetry

[1] For a review see [Pru95a, Geo96].

(see Sec.1.1).

Methods that include at least short-ranged correlations by mapping the lattice problem onto a cluster instead of a single site in the spirit of the DMFA have been the object of intensive research [Don94, Sch95, Obe97]. A successful extension of the DMFA that includes nonlocal fluctuations in a self-consistent way must meet certain requirements. It must become exact in the limit of large cluster sizes, recover the DMFA when the cluster size equals one and preserve the translational and point group symmetries of the lattice. Finally and most significantly, it must be fully causal so that the single-particle Green function and self-energy are analytic in the upper half of the complex plane, i.e.

$$\mathrm{Im}\,\Sigma(\mathbf{k},z) < 0 \quad \forall \mathbf{k}, z = \omega + i\delta\,. \tag{2.1}$$

Presently existing extensions of the DMFA do not satisfy all these requirements. A common problem to most of these approaches is that they experience causality problems ($\mathrm{Im}\,\Sigma(\mathbf{k},z) > 0$) for some $\mathbf{k}$ and z. These are caused by the inclusion of nonlocal Green functions, which do not have a negative semi-definite imaginary part [Don94]. Nevertheless, one should mention an extension of the DMFA for a bilayer system, i.e. two coupled planar tJ-models [Hei99, Hei00a, Hei00b]. By selecting two neighboring sites on different layers as "DMFA impurity" this approach was able to include nonlocal correlations between the sites without encountering causality problems. This work can be thought of preparatory work for the DCA.

Since the DCA is based on the DMFA and recovers the latter for a cluster size $N_c = 1$, this section starts with a discussion of the DMFA formalism.

2.2 Dynamical Mean Field Approximation - Local approximation

Mean field theories approximate lattice problems with many degrees of freedom by an effective single-site problem with less degrees of freedom. The dynamics at a given site i is controlled by the the coupling to an effective bath representing all the other sites in the lattice. The first illustration of the mean field idea was carried out by P. Weiss for lattice spin systems described by the Heisenberg Hamiltonian (Eq. (1.9) for $J > 0$) to investigate the ferromagnetic phase transition. The Weiss mean field theory views a given $\vec{S}_i$ spin at site i coupled to an effective field generated by the remaining spins in the lattice. To obtain the mean field equations, spin-fluctuations $\vec{S}_i - \langle \vec{S}_i \rangle$ are neglected. Then, by decoupling the spin interaction in the Heisenberg Hamiltonian (1.9)

$$\begin{aligned} \vec{S}_i \cdot \vec{S}_j &\approx \vec{S}_i \cdot \langle \vec{S}_j \rangle + \langle \vec{S}_i \rangle \cdot \vec{S}_j - \langle \vec{S}_i \rangle \cdot \langle \vec{S}_j \rangle \\ &= S_i^z \langle S_j^z \rangle + \langle S_i^z \rangle S_j^z - \langle S_i^z \rangle \langle S_j^z \rangle\,, \end{aligned} \tag{2.2}$$

neglecting the trivial last term and interchanging the summation indices in the second term one obtains an effective local problem

$$H_{\mathrm{H}}^{\mathrm{MF}} = 2J \sum_{\langle ij \rangle} S_i^z \langle S_j^z \rangle = J \sum_i S_i^z h_i^{\mathrm{MF}} , \tag{2.3}$$

where the spin at site i couples to the Weiss field

$$h_i^{\mathrm{MF}} = 2 \sum_{\langle j \rangle_i} \langle S_j^z \rangle . \tag{2.4}$$

Due to the translational invariance $\langle S_j^z \rangle = \langle S_i^z \rangle$, thus the effective field h_i^{MF} is related to the spin localized at site i. Hence the resulting mean field equations have to be solved self-consistently.

The mean field idea has been extended to quantum many body systems with itinerant degrees of freedom as described e.g. by the Hubbard model (Eq. (1.2)). The prescription of the classical Weiss mean field method can be directly transfered to the fermionic model. In the DMFA approach the dynamics of a given site i is determined by the coupling to an effective external bath created by the remaining sites. However, as described below, the relevant quantities here are dynamical Green functions, not static expectation values of operators as in the conventional case. The frequency dependence of the Green function takes care of local temporal quantum fluctuations.

Since mean field theories replace the many particle system with nonlocal interactions by an effective problem with only local correlations, intersite fluctuations are neglected. Therefore the quality of mean field theories increases with increasing coordination number. Due to its many neighbors each site sees only small fluctuations in its effective bath. Mean field theories even become exact in the limit of infinite coordination number or dimensions D [Itz89]. Hence the DMFA equations can be derived from the limit $D \to \infty$.

The limit of infinite dimensions

Metzner and Vollhardt [Met89] realized that lattice models with local interactions undergo significant simplifications in infinite dimensions $D \to \infty$, while remaining non-trivial. For models like the Hubbard model (1.2), the single-particle self-energy $\Sigma_{ij}(z)$ in direct space is defined via the single-particle Green function $G_{ij}(z) = \langle\langle c_{i\sigma}; c_{j\sigma}^{\dagger} \rangle\rangle_z$ by the Dyson equation

$$G_{ij}(z) = G_{ij}^o(z) + \sum_{kl} G_{ik}^o(z) \Sigma_{kl}(z) G_{lj}(z) , \tag{2.5}$$

where G^o is the Green function of the non-interacting system ($U = 0$) and $z = \omega + i\delta$.

By inspecting the diagrammatic expansion for the self-energy $\Sigma[G_{ij}, U]$, which is a functional of G_{ij} and the Coulomb interaction U, Metzner and Vollhard showed that in the limit $D \to \infty$ the skeleton expansion for Σ collapses onto local diagrams only [Met89]. As a result the single-particle self-energy in infinite dimensions is purely local in real space

$$\Sigma_{ij}(z) \equiv \Sigma(z)\delta_{ij}\,. \tag{2.6}$$

Müller-Hartmann rederived the same result in reciprocal space by inspecting the momentum dependence of vertices in the diagrammatic expansion for the self-energy as $D \to \infty$ [Mül89]. In momentum space the self-energy $\Sigma[G(\mathbf{k}), U]$

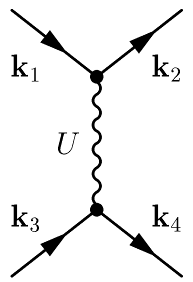

FIGURE 2.1: *Vertex for Hubbard-like models with local interaction U (wavy line). The solid arrows stand for the Green function $G(\mathbf{k})$. The legs labeled $\mathbf{k}_1$ and $\mathbf{k}_3$ ($\mathbf{k}_2$ and $\mathbf{k}_4$) denote momenta entering (leaving) the vertex.*

is a functional of the Green function $G(\mathbf{k}) = \langle\langle c_{\mathbf{k}\sigma}; c^\dagger_{\mathbf{k}\sigma}\rangle\rangle_z$ and the interaction U. Since the Coulomb repulsion U is local, the momentum dependence of each vertex (see Fig. 2.1) in a diagrammatic expansion for the self-energy is completely characterized by the Laue-function

$$\Delta(\mathbf{k}_1, \mathbf{k}_2, \mathbf{k}_3, \mathbf{k}_4) = \sum_{\mathbf{r}} \mathrm{e}^{i(\mathbf{k}_1 - \mathbf{k}_2 + \mathbf{k}_3 - \mathbf{k}_4)\cdot\mathbf{r}}\,, \tag{2.7}$$

where $\mathbf{k}_1$ and $\mathbf{k}_3$ ($\mathbf{k}_2$ and $\mathbf{k}_4$) are the momenta entering (leaving) the vertex. In a conventional diagrammatic approach, $\Delta(\mathbf{k}_1, \mathbf{k}_2, \mathbf{k}_3, \mathbf{k}_4) = N\delta(\mathbf{k}_1 - \mathbf{k}_2 + \mathbf{k}_3 - \mathbf{k}_4)$ for a lattice of N sites, which expresses momentum conservation on the vertex. However as $D \to \infty$ Müller-Hartmann showed that the Laue-function reduces to

$$\Delta_{D\to\infty} = 1 + \mathcal{O}(1/D)\,. \tag{2.8}$$

This means that momentum conservation at the internal vertices of irreducible diagrams can be disregarded in infinite dimensions. The DMFA assumes the same Laue-function even in the context of finite dimensions, and therefore neglects momentum conservation at the internal vertices. If this Laue-function (2.8) is applied to the vertices in self-energy diagrams, one can freely sum the momenta of the Green function legs $G(\mathbf{k})$ over the whole Brillouin-zone (BZ). Hence, in each internal leg $G(\mathbf{k})$ is replaced by the local Green function $G_{ii} = 1/N \sum_{\mathbf{k}} G(\mathbf{k})$. This collapse of the momentum dependent contributions,

$$\Sigma[\{G(\mathbf{k})\}] \rightarrow \Sigma[G_{ii}] \tag{2.9}$$

onto diagrams involving the local Green function G_{ii} only is illustrated in Fig. 2.2 for a second order diagram. Consequently the DMFA self-energy $\Sigma[G_{ii}(z)] \equiv \Sigma(z)$

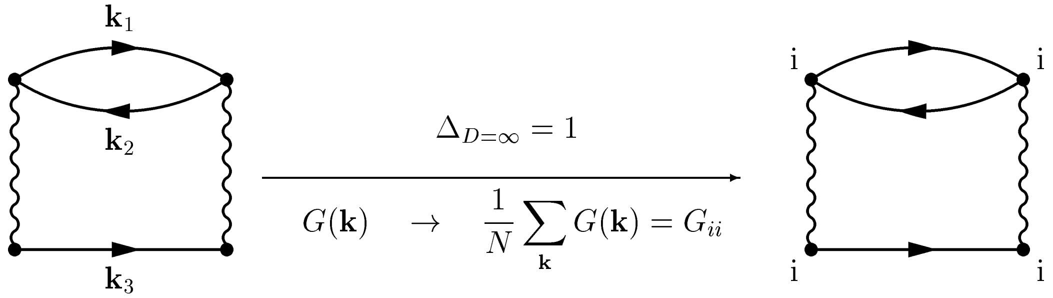

FIGURE 2.2: *The Laue-function (2.8) leads to a collapse of the momentum dependence of the self-energy in infinite dimensions $D = \infty$, illustrated for a second order diagram. Only local contributions remain in the DMFA self-energy.*

becomes a constant in momentum space. Thus the mean field idea applied to correlated fermions on a lattice corresponds to approximating the single-particle self-energy $\Sigma_{ij}(z)$ by a local self-energy $\Sigma(z)$. Thus the DMFA retains only local correlations and neglects nonlocal contributions. Analogously to the conventional mean field theory this finally leads to the mapping onto an effective local problem.

DMFA: Mapping onto single impurity model

The locality of the self-energy Σ (Eq. (2.6)) can now be used to reduce the complexity of the lattice system by mapping it onto an effective impurity model embedded in a host which has to be determined self-consistently. After replacing the self-energy Σ_{kl} by the local quantity Σ and going over to $\mathbf{k}$-space, Eq. (2.5) can be written as

$$G(\mathbf{k}, z) = \frac{1}{z - \epsilon_{\mathbf{k}} + \mu - \Sigma(z)}\,, \tag{2.10}$$

where $\epsilon_{\mathbf{k}}$ denotes the Fourier transform of t_{ij} (see Eq. (1.4)). The local Green function

$$G_{ii}(z) = \frac{1}{N}\sum_{\mathbf{k}} \frac{1}{z + \mu - \epsilon_{\mathbf{k}} - \Sigma(z)} \tag{2.11}$$

can then be written in the form

$$G_{ii}(z) = \frac{1}{z - \epsilon_o + \mu - \Sigma(z) - \Gamma(z)}\,, \tag{2.12}$$

since $\Sigma(z)$ does not depend on the integration variable $\mathbf{k}$ in Eq. (2.11). The on-site energy of site i, $\epsilon_o = 1/N \sum_{\mathbf{k}} \epsilon_{\mathbf{k}}$ and $\Gamma(z)$ describes hybridization effects with the remainder of the system. Thus, according to Eq. (2.12) the problem can now be viewed as an effective local problem where the "impurity site i" is coupled to a dynamic host represented by $\Gamma(z)$. As a consequence the self-energy due to the Coulomb repulsion U can be obtained by solving an effective Single-Impurity Anderson model (SIAM)

$$H_i = \sum_{\sigma}(\epsilon_o - \mu) f^{\dagger}_{i\sigma} f_{i\sigma} + U n_{fi\uparrow} n_{fi\downarrow} + \frac{1}{\sqrt{N}} \sum_{\mathbf{k}\sigma} (V_{\mathbf{k}} f^{\dagger}_{i\sigma} a_{\mathbf{k}\sigma} + \text{h.c.}) + \sum_{\mathbf{k}\sigma} \varepsilon_{\mathbf{k}} a^{\dagger}_{\mathbf{k}\sigma} a_{\mathbf{k}\sigma} \,. \tag{2.13}$$

The first two terms in (2.13) describe the creation and destruction of Fermions on the impurity site i in terms of the impurity operators $f_{i\sigma}$ ($f^{\dagger}_{i\sigma}$) and the corresponding number operators $n_{fi\sigma} = f^{\dagger}_{i\sigma} f_{i\sigma}$. The last term simulates the bath described by $\Gamma(z)$ as a conduction band with help of the introduced auxiliary operators $a_{\mathbf{k}\sigma}$ ($a^{\dagger}_{\mathbf{k}\sigma}$). The third term stands for the coupling between the orbital on site i and the bath. The energy levels $\varepsilon_{\mathbf{k}}$ of the auxiliary particles and coupling constants $V_{\mathbf{k}}$ are not known a priori. They are determined from the requirement that the impurity Green function $G_f = \langle\langle f_{i\sigma}; f^{\dagger}_{i\sigma} \rangle\rangle_z$ equals the local lattice Green function G_{ii} (Eq. (2.12)). Solving the equation of motion for the impurity Green function G_f is straightforward and yields

$$G_f = \frac{1}{z - \epsilon_o + \mu - \Sigma_U(z) - \Gamma_f(z)} \quad \text{with} \quad \Gamma_f(z) = \frac{1}{N} \sum_{\mathbf{k}} \frac{|V_{\mathbf{k}}|^2}{z - \varepsilon_{\mathbf{k}}} \,, \tag{2.14}$$

formally identical to the local lattice Green function G_{ii} (Eq. (2.12)). Provided that the diagrammatic expansion for the impurity self-energy Σ_U equals that for the lattice self-energy Σ one can then use the impurity model to calculate the lattice self-energy. The self-energy of the impurity model $\Sigma_U[U, G^o_f]$ is a functional of U and the bare impurity Green function, which in inverse notation is given by $[G^o_f]^{-1} = G^{-1}_f + \Sigma_U$. The corresponding quantity of the lattice system is given by the bare Green function corresponding to the local lattice Green function G_{ii} and is therefore obtained from the reverse Dyson equation for G_{ii} as

$$\mathcal{G}^{-1}(z) = G^{-1}_{ii}(z) + \Sigma(z) \,. \tag{2.15}$$

It can then be shown by comparing skeleton diagrams that the functional dependence of Σ_U on G^o_f is formally identical to that of Σ on $\mathcal{G}$ (see e.g. [Jar92]). Thus the condition that the impurity Green function G_f and self-energy Σ_U equal the local lattice Green function G_{ii} and self-energy Σ requires that the bare Green function of the impurity model is replaced by $\mathcal{G}$

$$G^o_f(z) = \mathcal{G}(z) \,. \tag{2.16}$$

Then the lattice self-energy $\Sigma = \Sigma_U[\mathcal{G}]$ is obtained by solving the impurity model where the bare propagator is fixed by $\mathcal{G}$. Eq. (2.16) is the self-consistent equation of the theory which determines the auxiliary quantities of the impurity model. It ensures that the solution of the impurity model is also the solution of the lattice system.

Since $\mathcal{G}$ determines the bath, which the impurity site i is embedded in, $\mathcal{G}$ is called the effective medium Green function. The addition of the self-energy Σ on the r.h.s. of Eq. (2.15) corresponds to a site-exclusion to prevent the over-counting of self-energy diagrams on site i, when the impurity model is used to calculate the lattice self-energy. In fact, it can be shown (see App. A.3), that the inverse of the bath function $\mathcal{G}$ can be written as

$$\mathcal{G}^{-1}(z) = z - \epsilon_o + \mu - \sum_{j,l\neq i} t_{ij}\tilde{G}_{jl}(z)t_{li}\,, \tag{2.17}$$

where $\tilde{G}(z)$ describes the propagation of Fermions in the Hubbard model with the impurity site i removed. Hence $\mathcal{G}$ contains self-energy effects on all the lattice sites except the impurity site.

The DMFA equations (2.11) and (2.15), supplemented by the self-consistency condition (2.16) for the effective impurity Hamiltonian (2.13) form a closed set of functional equations to determine the local Green function G_{ii} and the effective medium $\mathcal{G}$. The resulting DMFA algorithm consists of the following steps:

(0) Start with a guess for the self-energy $\Sigma(z)$, usually zero.

(1) Calculation of the local Green function $G_{ii}(z)$ with Eq. (2.11).

(2) Calculation of the effective medium $\mathcal{G}(z)$ using Eq. (2.15). $\mathcal{G}$ defines the undressed Green function of the generalized Anderson impurity model (Eq. (2.13)).

(3) Solve the associated impurity problem with a suitable technique, e.g the resolvent technique presented in App. B.

(4) Calculate the new estimate for the self-energy $\Sigma(z) = \mathcal{G}^{-1}(z) - [G_f(z)]^{-1}$, from the dressed impurity Green function G_f. $\Sigma(z)$ is then used in (1) to continue the procedure.

The iteration continues until the local lattice Green function $G_{ii}(z)$ is identical to the impurity Green function $G_f(z)$ within the desired accuracy. This procedure can be shown to stay fully causal throughout the iterations (see Sec. 2.3 for $N_c = 1$).

Due to its local nature the DMFA neglects spatial correlations, but takes full account of local temporal fluctuations. Therefore, in contrast to the conventional mean field theory, the impurity problem given by the Hamiltonian (2.13) remains a complicated many-body problem. But nevertheless there is a wide variety of methods, which can be applied to solve the impurity problem. Since the DMFA is recovered by the DCA for a cluster size of $N_c = 1$, a discussion of these methods is postponed to the next section.

2.3 Dynamical Cluster Approximation - Spatial correlations

The DCA [Het98, Het00, Mai00a, Mai00b, Hus99, Mou00, Jar00] extends the DMFA by adding short-ranged dynamical correlations to the purely local dynamics of the DMFA. Like the DMFA the DCA is an iterative self-consistency scheme. Intersite correlations are incorporated by replacing the 'DMFA impurity' by a cluster of size N_c.

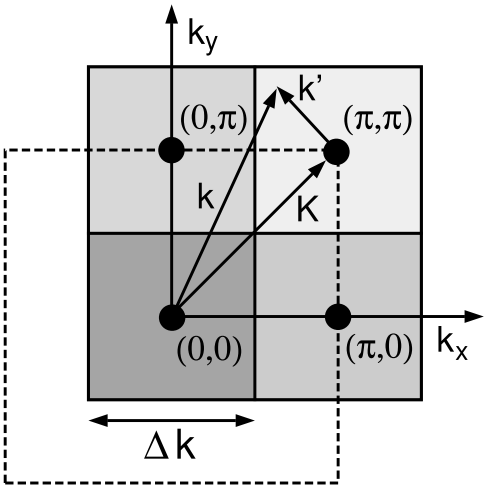

FIGURE 2.3: *The cluster momenta* $\mathbf{K}$ *(filled dots) and coarse graining cells (different fill patterns) for a* $N_c = 4$ *cluster in the BZ of a two dimensional lattice. The cells adjacent to the BZ boundary extend periodically to the opposite side.*

The DMFA lacks nonlocal fluctuations because it approximates the self-energy by a constant in momentum space: $\Sigma(\mathbf{k}, z) \to \Sigma(z)$. The basic idea of the DCA is to (partially) restore the $\mathbf{k}$-dependence by calculating the self-energy on a finite subset of the $\mathbf{k}$-points, on a coarse grid of N_c cluster $\mathbf{K}$-points (see Fig. 2.3): $\Sigma(\mathbf{k}, z) \to \Sigma(\mathbf{K}, z)$. As in the DMFA the crucial assumption of the DCA is that the self-energy of the real system is only weakly momentum dependent or equivalently that the dynamical intersite correlations have only short spatial range $b \lesssim L/2$, where $L = N_c^{1/D}$ is the linear dimension of the cluster. Then, according to Nyquist's sampling theorem [Ell82], to reproduce these correlations in the self-energy, the reciprocal space needs to be sampled at intervals of $\Delta k \approx 2\pi/L$ only, i.e. on a set of $N_c = L^D$ points in the first BZ. Thus the self-energy $\Sigma(\mathbf{K} + \mathbf{k}')$ can be approximated by the cluster self-energy $\Sigma(\mathbf{K})$

$$\Sigma(\mathbf{K} + \mathbf{k}', z) = \Sigma(\mathbf{K}, z) \tag{2.18}$$

for each $\mathbf{k}'$ within a cell of size $(2\pi/L)^D$ about the cluster momentum $\mathbf{K}$ (see Fig. 2.3). Thus the self-energy is approximated by a constant within a cell. Knowledge of the self-energy on a finer grid in momentum space is unnecessary and is discarded to reduce the complexity of the problem.

2.3.1 Microscopic derivation and formalism

The relationship of the DCA to the DMFA and the exact formulation of the DCA is illustrated by its microscopic diagrammatic definition. As mentioned in Sec. 2.2 the properties of the bare vertex (see Fig. 2.1) in a diagrammatic expansion for Hubbard-like models are completely characterized by the Laue-function Δ (2.7). In a conventional diagrammatic approach the Laue-function expresses momentum conservation at each vertex. In the DMFA the Laue-function $\Delta_{\mathrm{DMFA}} = 1$, disregarding momentum conservation.

The basic idea of the DCA is to partially restore momentum conservation relinquished by the DMFA. To this end the BZ is divided into $N_c = L^D$ cells of size $(2\pi/L)^D$ (see Fig. 2.3). Each cell is represented by a cluster momentum $\mathbf{K}$ (filled dots) in the center of the cell. A given momentum $\mathbf{k}$ may then be written as $\mathbf{k} = \mathbf{K} + \mathbf{k}'$ where $\mathbf{K}$ denotes the cluster momentum representing the cell containing $\mathbf{k}$ and $\mathbf{k}'$ is a momentum within the cell (see Fig. 2.3). With this definition the Laue-function (2.7) can be written in terms of the cluster momenta $\mathbf{K}$ as [Het00]

$$\begin{aligned}\Delta(\mathbf{k}_1,\mathbf{k}_2,\mathbf{k}_3,\mathbf{k}_4) &= \sum_{\mathbf{r}} \mathrm{e}^{i(\mathbf{k}'_1-\mathbf{k}'_2+\mathbf{k}'_3-\mathbf{k}'_4+\mathbf{K}_1-\mathbf{K}_2+\mathbf{K}_3-\mathbf{K}_4)\cdot\mathbf{r}} &(2.19)\\ &= N_c\sum_n \frac{1}{n!}[(\mathbf{k}'_1-\mathbf{k}'_2+\mathbf{k}'_3-\mathbf{k}'_4)\cdot\nabla_{\mathbf{K}_1}]^n\delta(\mathbf{K}_1-\mathbf{K}_2+\mathbf{K}_3-\mathbf{K}_4)\,.\end{aligned}$$

The DCA keeps only the first term ($n = 0$) in this expansion, so that the Laue-function, defining the DCA, is given by

$$\Delta_{\mathrm{DCA}} = N_c\delta(\mathbf{M}(\mathbf{k}_1)-\mathbf{M}(\mathbf{k}_2)+\mathbf{M}(\mathbf{k}_3)-\mathbf{M}(\mathbf{k}_4))\,, \tag{2.20}$$

where $\mathbf{M}(\mathbf{k})$ is a function that maps $\mathbf{k}$ onto the cluster momentum $\mathbf{K}$ of the cell containing $\mathbf{k}$ (see Fig. 2.3)[2]

$$\mathbf{M}(\mathbf{k}):\ \mathbf{k}\to\mathbf{K} \quad ; \quad \mathbf{K}\in\{\text{cell containing }\mathbf{k}\}\,. \tag{2.21}$$

Therefore, this form of the Laue-function partially restores momentum conservation, since it observes momentum transfers between different cells, i.e. larger than $\Delta k_x, \Delta k_y = 2\pi/L$, but neglects momentum transfers within the same cell, i.e. smaller than $\Delta k_x, \Delta k_y$. With this choice of the Laue-function Δ_{DCA}, the mo-

[2] For a cluster size $N_c = 1$ the DCA Laue-function Δ_{DCA} becomes 1 and equals the DMFA Laue function, since $\mathbf{M}$ maps all the momenta to the zone center.

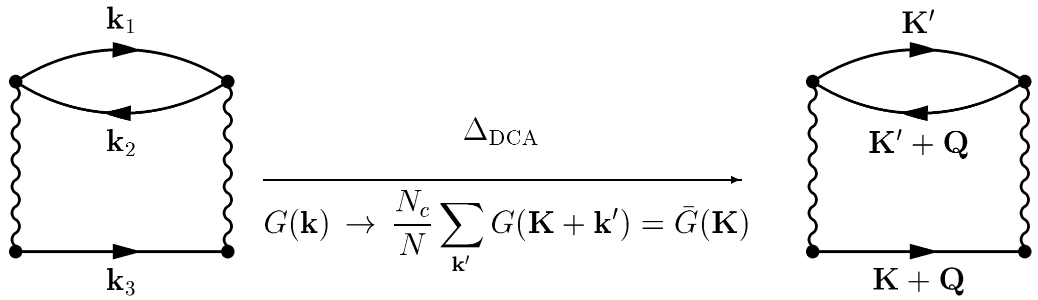

FIGURE 2.4: *The DCA choice of the Laue-function (2.20) leads to the replacement of the lattice propagators $G(\mathbf{k}_1)$, $G(\mathbf{k}_2)$ and $G(\mathbf{k}_3)$ by coarse grained propagators $\bar{G}(\mathbf{K}')$, $\bar{G}(\mathbf{K}'+\mathbf{Q})$ and $\bar{G}(\mathbf{K}+\mathbf{Q})$ (Eq. (2.22)) in the internal lines of the self-energy, illustrated for a second order diagram.*

menta in each internal leg of the self-energy may be freely summed over the cell. Thus, each leg $G(\mathbf{k}, z)$ is replaced by the "coarse grained average"

$$\bar{G}(\mathbf{K}, z) = \frac{N_c}{N}\sum_{\mathbf{k}'} G(\mathbf{K}+\mathbf{k}', z)\,, \tag{2.22}$$

where the summation runs over the N/N_c momenta $\mathbf{k}'$ within a cell so that $\mathbf{k} = \mathbf{K}+\mathbf{k}'$ lies in the cell containing the cluster momentum $\mathbf{K} = \mathbf{M}(\mathbf{K}+\mathbf{k}')$ (see Fig. 2.3). G is the full lattice propagator. Fig. 2.4 schematically illustrates this collapse of the self-energy

$$\Sigma[\{G(\mathbf{k})\}] \to \Sigma[\{\bar{G}(\mathbf{K})\}]\,, \tag{2.23}$$

onto diagrams involving the coarse grained averages (2.22) for a second order contribution. Furthermore, since the external momenta $\mathbf{k}$ enter the diagrams only through $\mathbf{M}(\mathbf{k})$, the self-energy $\Sigma[\bar{G}(\mathbf{K})] \equiv \Sigma(\mathbf{K})$ depends on the cluster momenta $\mathbf{K}$ only. As a result the lattice system may be mapped onto a system with less degrees of freedom, i.e. an effective periodic cluster model embedded in a self-consistently determined host.

DCA: Mapping onto periodic cluster model

The form (2.20) of the Laue-function Δ_{DCA} completely prescribes the DCA formalism. Then the coarse grained Green function (2.22) reads

$$\bar{G}(\mathbf{K}, z) = \frac{N_c}{N}\sum_{\mathbf{k}'} \frac{1}{z - \epsilon_{\mathbf{K}+\mathbf{k}'} + \mu - \Sigma(\mathbf{K}, z)}\,, \tag{2.24}$$

where the lattice self-energy $\Sigma(\mathbf{k})$ was already replaced by $\Sigma(\mathbf{K}) = \Sigma(\mathbf{M}(\mathbf{k})$. By making use of the independence of $\Sigma(\bar{\mathbf{K}})$ on the integration variable $\mathbf{k}'$, Eq. (2.24) can be written in the form

$$\bar{G}(\mathbf{K}, z) = \frac{1}{z - \bar{\epsilon}_{\mathbf{K}} + \mu - \Sigma(\mathbf{K}, z) - \Gamma(\mathbf{K}, z)}, \tag{2.25}$$

where the hybridization function Γ has a negative imaginary part, $\operatorname{Im}\Gamma(\mathbf{K}, z) < 0$ (see App. A.1) and the coarse grained energy average is given by

$$\bar{\epsilon}_{\mathbf{K}} = \frac{N_c}{N} \sum_{\mathbf{k}'} \epsilon_{\mathbf{K}+\mathbf{k}'} . \tag{2.26}$$

The expression (2.25) has exactly the form of the Green function of a periodic cluster model, where the cluster states for each $\mathbf{K}$ are coupled to a Fermionic bath described by the hybridization function $\Gamma(\mathbf{K}, z)$. Hence the self-energy $\Sigma(\mathbf{K})$ can be obtained by solving a generalized cluster model described in Sec. 2.4. In analogous fashion to the DMFA, the bare Green function of this cluster model, describing the effective medium for the embedding of the periodic cluster, is given by the bare part $\mathcal{G}(\mathbf{K})$ of the coarse grained Green function $\bar{G}(\mathbf{K})$ and reads in inverse notation

$$\mathcal{G}^{-1}(\mathbf{K}, z) = \bar{G}^{-1}(\mathbf{K}, z) + \Sigma(\mathbf{K}, z) . \tag{2.27}$$

As in the DMFA the addition of $\Sigma(\mathbf{K})$ on the r.h.s. of Eq. (2.27) corresponds to a cluster exclusion, to prevent over-counting of self-energy diagrams on the cluster. In fact it can be shown (see App. A.3) that $\mathcal{G}$ can also be obtained from a cavity construction, i.e. $\mathcal{G}$ can be written in terms of a Green function, which describes the propagation of Fermions through the lattice without touching the sites on the real space analogon of the cluster. Therefore $\mathcal{G}(\mathbf{K})$ contains self-energy effects on all the lattice sites except the sites defining the real space analogon of the cluster. In contrast to the DMFA, the DCA effective medium $\mathcal{G}$ dependends on $\mathbf{K}$ when $N_c > 1$ and hence takes account of temporal as well as spatial short-ranged quantum fluctuations.

DCA: Algorithm

The DCA equations (2.24) and (2.27) define a closed system of functional equations, which along with the solution of the corresponding effective periodic cluster model are used to determine the coarse grained Green function $\bar{G}(\mathbf{K}, z)$ and the effective medium Green function $\mathcal{G}(\mathbf{K}, z)$.

The DCA cluster problem may then be solved by iteration. Fig. 2.5 sketches the self-consistency loop for the DCA:

(0) It starts with a guess for the initial cluster self-energy $\Sigma(\mathbf{K})$, usually zero, which is then used to

(1) calculate the coarse grained Green function $\bar{G}(\mathbf{K})$ using Eq. (2.24).

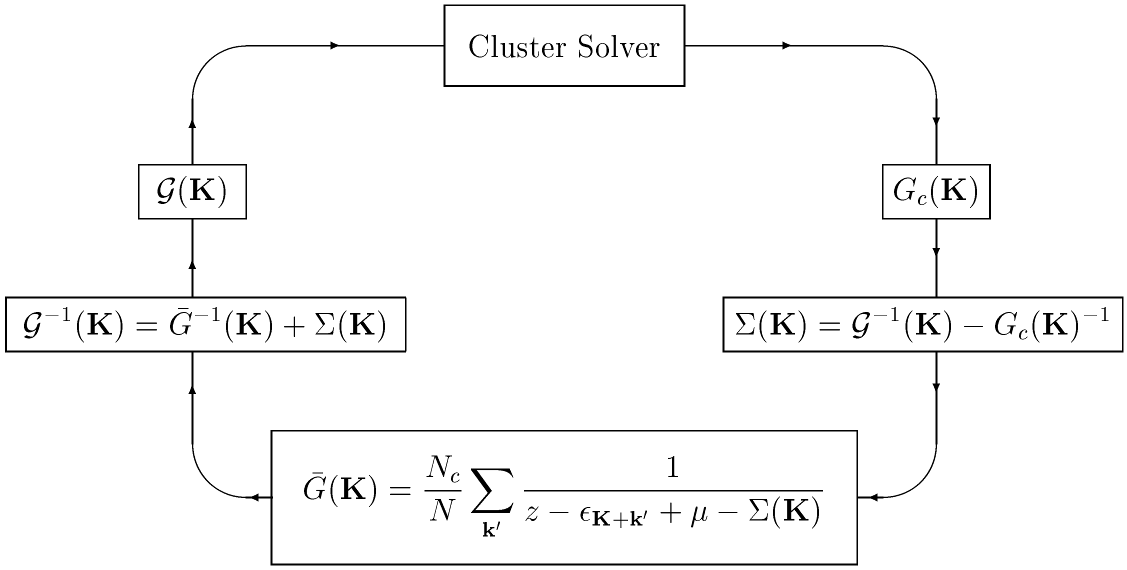

FIGURE 2.5: *Sketch of the DCA-algorithm.*

(2) The generalized cluster model is then defined by the interactions on the cluster sites and the bath function $\mathcal{G}(\mathbf{K})$, obtained via Eq. (2.27).

(3) Given the effective medium $\mathcal{G}$, the interacting Green function $G_c(\mathbf{K})$ of the effective periodic cluster model may then be computed using a suitable method. $G_c(\mathbf{K})$ is then used to

(4) calculate a new estimate for the cluster self-energy $\Sigma(\mathbf{K}) = \mathcal{G}^{-1}(\mathbf{K}) - G_c(\mathbf{K})^{-1}$. The iteration closes by calculating a new $\bar{G}(\mathbf{K})$ in step (1).

This procedure is repeated until the cluster Green function $G_c(\mathbf{K})$ equals the coarse grained Green function $\bar{G}(\mathbf{K})$ within the desired accuracy. It should be noted that the DCA equations (2.24) and (2.27) (step (1) and (2)) are formally identical to the DMFA equations (2.11) and (2.15). Thus at this point the DCA is equivalent to N_c independent DMFA's, one for each $\mathbf{K}$. Correlations between the different momentum cells and therefore nonlocal interactions are introduced by solving the effective periodic cluster problem in step (3).

It is important to stress that the coarse graining step (Eq. (2.24)) has two well defined limits with respect to the cluster size: For N_c=1 the $\mathbf{k}'$-sum runs over the full BZ, $\bar{G}$ is the local Green function G_{ii}, thus the DMFA algorithm is recovered. When $N_c = N = \infty$ the $\mathbf{k}'$-summation vanishes and the DCA becomes equivalent to the exact solution of the Hubbard model.

2.3.2 Discussion of the DCA

A comprehensive discussion of the DCA formalism was presented in [Het00]. The following section gives a short overview of fundamental properties of the DCA which are necessary to gain a more profound understanding of its nature and hence are useful for the interpretation of the results presented in Chapter 3. Furthermore important features like causality, one of the main advantages favoring the DCA approach over other extensions of the DMFA are discussed.

Range of spatial correlations

The DCA is completely formulated in **k**-space to avoid causality problems (see the discussion below). Nevertheless, to gain insight in the nature of the DCA approximation, it is helpful to examine the DCA equations, in particular the coarse graining step (Eq. (2.24)) in real space. The range of the incorporated spatial dynamical fluctuations is determined by the cluster size N_c. This can be seen by dividing the lattice into clusters of size L^D. To this end it is convenient to introduce the discrete real space vectors $\mathbf{R}+\mathbf{r} \equiv \mathbf{x}_i - \mathbf{x}_j$, where $\mathbf{R}$ denotes the centers of the clusters and $\mathbf{r}$ is a vector within a cluster. Then it is appropriate to change the notation for the Green function G_{ij} to $G(\mathbf{R}+\mathbf{r})$. With these definitions the coarse graining step (Eq. (2.24)) may be transformed to real space and can then be written as [Het00]

$$\bar{G}(\mathbf{r}) = \sum_{\mathbf{R}} \delta^c(\mathbf{R}+\mathbf{r}) G(\mathbf{R}+\mathbf{r})\,, \tag{2.28}$$

with the Fourier transform of the coarse grained (real) Green function $\bar{G}(\mathbf{r})$ ($G(\mathbf{R}+\mathbf{r})$) and a cluster δ-like function $\delta^c(\mathbf{R}+\mathbf{r})$ which is defined as

$$\delta^c(\mathbf{R}+\mathbf{r}) := \frac{N_c}{N} \sum_{\mathbf{k}'} \mathrm{e}^{i\mathbf{k}'(\mathbf{R}+\mathbf{r})}\,. \tag{2.29}$$

There is considerable freedom in the choice of cluster **K**-points and corresponding coarse graining cells within the first BZ, because no special assumption was made in the derivation of the DCA. However the most natural choice is given by the crystal momentum points of the corresponding real space cluster with periodic boundary conditions, $K_n^l = \pi(2n_l/L - 1)$, where n_l is an integer, $1 \leq n_l \leq L$, $L = N_c^{1/D}$ is the linear cluster size and l indicates the spatial direction. Then $\delta^c(\mathbf{R}+\mathbf{r})$ can be evaluated to give

$$\delta^c(\mathbf{R}+\mathbf{r}) = \prod_{l=1}^{D} \frac{\sin[(x_l + X_l)\pi/L]}{(x_l + X_l)\pi/L}\,, \tag{2.30}$$

where x_l (X_l) is the l^{th} component of the vector $\mathbf{r}$ ($\mathbf{R}$). Thus $\delta^c(\mathbf{R}+\mathbf{r})$ falls off like $|\mathbf{r}+\mathbf{R}|^{-D}$ at large distances $|\mathbf{r}+\mathbf{R}|$. The main contribution to the sum in Eq. (2.28) comes from $\mathbf{R}=0$. For short distances $r=|\mathbf{r}|$ it can be seen that

$$\delta^c(\mathbf{R}+\mathbf{r}) \approx 1 - \sum_{l=1}^{D} \frac{1}{6}((x_l + X_l)\pi/L)^2 \tag{2.31}$$

by expanding the sinusoidal enumerator in Eq. (2.30). Thus $\bar{G}(0)=G(0)$, since $\delta^c(\mathbf{R}+\mathbf{r}=0)=1$, and for $r \le L/2$

$$\begin{aligned} \bar{G}(r) &\approx G(r) + \mathcal{O}((r\Delta k)^2) \\ \bar{\Sigma}(r) &\approx \Sigma(r) + \mathcal{O}((r\Delta k)^2)\,, \end{aligned} \tag{2.32}$$

where $\bar{\Sigma}(r)$ and $\Sigma(r)$ denote the Fourier transform of the cluster self-energy $\Sigma(\mathbf{K})$ and real self-energy $\Sigma(\mathbf{k})$ to direct space, respectively and $\Delta k = 2\pi/L$ is the linear size of a coarse graining cell. The second relation follows from the first together with the fact that the cluster self-energy $\Sigma[\bar{G},U]$ is a functional of $\bar{G}$. Contributions from $G(\mathbf{R}+\mathbf{r})$ for finite values of $\mathbf{R}$ in the sum (2.28) are cut off by $\delta^c(\mathbf{R}+\mathbf{r}) \ll 1$ for $\mathbf{R} \neq 0$. Thus short-ranged correlations are accurately described by the cluster self-energy $\Sigma(\mathbf{K})$ and longer-ranged correlations are cut off by the finite cluster size. The relations (2.32) show that cluster quantities differ from those of the real lattice by terms of the order $(\Delta k)^2 = 4\pi^2/L^2 = 4\pi^2/N_c^{2/D}$. In particular for two dimensions this means that the DCA is exact with corrections of the order of $\mathcal{O}(1/N_c)$. Thus, the DCA is a systematic approximation in the inverse cluster size $1/N_c$, not in the inverse dimension $1/D$.

The same conclusion can be drawn by examining Eqs. (2.24) and (2.25) in detail. If the cluster size $N_c \to \infty$, the summation in Eq. (2.24) vanishes and hence the hybridization function $\Gamma(\mathbf{K}) \to 0$ in Eq. (2.25). As already stressed before, the DCA becomes exact in this limit. In fact, in App. A.2 it is shown that $\Gamma(\mathbf{K}) \sim \mathcal{O}(1/N_c)$ in two dimensions, yielding the same result as the consideration above, i.e. that the DCA is systematic in $1/N_c$ and in two dimensions exact with corrections of the order of $1/N_c$ represented by the bath function $\Gamma(\mathbf{K})$.

The DCA-Φ functional and corresponding free energy

The DCA approximates the lattice self-energy $\Sigma(\mathbf{k})$ by the cluster self-energy $\Sigma(\mathbf{K})$. However another approach could be defined by approximating the true lattice Green function G by the cluster Green function G_c. The purpose of this paragraph is to show that it is indeed the first choice, i.e. the approximation of the irreducible quantity Σ by the corresponding cluster quantity, which minimizes the free energy.

The free energy Ω can be expressed in terms of the "linked cluster expansion" [Bay62]

$$\Omega = -k_B T(\Phi[\mathbf{G}] - \mathrm{tr}[\mathbf{\Sigma}(\mathbf{k})\mathbf{G}(\mathbf{k})] - \mathrm{tr}\ln[-\mathbf{G}(\mathbf{k})]) \tag{2.33}$$

where $\mathbf{G}(\mathbf{k})$ is the dressed lattice Green function related to the self-energy $\mathbf{\Sigma}$ and the bare Green function $\mathbf{G}_o$ via the Dyson equation $\mathbf{G}^{-1} = \mathbf{G_o}^{-1} - \mathbf{\Sigma}$. $\mathbf{G}$ and $\mathbf{\Sigma}$ are conveniently written as matrices in frequency and spin and the trace indicates summation over these variables and momentum. The Baym-Kadanoff Φ functional [Bay62] is diagrammatically defined as

$$\Phi[\mathbf{G}(\mathbf{k})] = \sum_l \frac{1}{2l} \mathrm{tr}\left[\mathbf{\Sigma}^{(l)}(\mathbf{k})\mathbf{G}(\mathbf{k})\right] , \tag{2.34}$$

where $\Sigma^{(l)}(\mathbf{k})$ is the set of irreducible self-energy diagrams of l^{th} order in the interaction U. The factor $1/(2l)$ is a counting factor corresponding to the number of occurrences of $\mathbf{G}$ in Φ. With this definition it holds that $\mathbf{\Sigma} = \delta\Phi/\delta\mathbf{G}$, as required for a Φ-derivable theory [Bay62]. This assures that one-particle properties and thermodynamic properties, given by two-particle correlation functions as the second derivative of Φ with respect to the Green function, are calculated on the same level and therefore yield consistent results.

The explicit form of Φ determines the nature of the approximation. The DCA (and also the DMFA) is a Φ-derivable theory. The DCA can be microscopically defined by the explicit form of the Laue-function Δ_{DCA} (Eq. (2.20)). If Δ_{DCA} is applied to the vertices of the diagrams defining the functional Φ (Eq. (2.34)), the Green function legs $\mathbf{G}$ are replaced by their coarse grained averages $\bar{\mathbf{G}}$. Hence Δ_{DCA} replaces the self-energy $\mathbf{\Sigma}(\mathbf{k})$ by the cluster quantity $\mathbf{\Sigma}(\mathbf{K})$, $\mathbf{G}(\mathbf{k})$ by its coarse grained quantity $\bar{\mathbf{G}}(\mathbf{K})$ and consequently the DCA Φ-functional reads [Het00, Mai00a]

$$\Phi_{\text{DCA}}[\bar{\mathbf{G}}(\mathbf{K})] = \frac{N}{N_c} \sum_l \frac{1}{2l} \mathrm{tr}_c \left[\mathbf{\Sigma}^{(l)}(\mathbf{K})\bar{\mathbf{G}}(\mathbf{K})\right] . \tag{2.35}$$

tr_c indicates summation over the cluster degrees of freedom only so that a factor N/N_c must be added to account for the remaining degrees of freedom. Φ_{DCA} can then be used to calculate the DCA estimate for the free energy Ω_{DCA} of the lattice. If Φ in Eq. (2.33) is replaced by Φ_{DCA}, the DCA estimate for the lattice free energy reads

$$\Omega_{\text{DCA}} = -k_B T (\Phi_{\text{DCA}}[\bar{\mathbf{G}}(\mathbf{K})] - \mathrm{tr}[\mathbf{\Sigma}(\mathbf{k})\mathbf{G}(\mathbf{k})] - \mathrm{tr}\ln[-\mathbf{G}(\mathbf{k})]) . \tag{2.36}$$

Then the requirement of a Φ-derivable theory, i.e.

$$\Sigma(\mathbf{k}, z) = \frac{\delta\Phi_{\text{DCA}}}{\delta G(\mathbf{k}, z)} = \frac{\delta\Phi_{\text{DCA}}}{\delta\bar{G}(\mathbf{K}, z)} \frac{\delta\bar{G}(\mathbf{K}, z)}{\delta G(\mathbf{k}, z)} = \Sigma(\mathbf{M}(\mathbf{k}), z) \tag{2.37}$$

ultimately determines the way lattice quantities have to be constructed out of cluster quantities.[3] According to Eq. (2.37), the self-energy $\Sigma(\mathbf{k}, z)$ of the full

[3] The r.h.s. follows from $\delta\Phi_{DCA}/\delta\bar{G}(\mathbf{K}) = N/N_c\Sigma(\mathbf{K})$ and $\delta\bar{G}(\mathbf{K})/\delta G(\mathbf{k}) = N_c/N\delta_{\mathbf{K},\mathbf{M}(\mathbf{k})}$.

lattice Green function $G(\mathbf{k}, z)$ has to be replaced by the corresponding cluster quantity $\Sigma(\mathbf{M}(\mathbf{k}), z)$ and the explicit form (2.24) for $G(\mathbf{K}+\mathbf{k}, z)$ used in the coarse graining step (2.22) then follows naturally.

Furthermore it follows that the DCA free energy Ω_{DCA} is stationary with respect to the lattice Green function $G(\mathbf{k}, z)$

$$\frac{\delta\Omega_{\mathrm{DCA}}}{\delta G(\mathbf{k}, z)} = k_B T[-\Sigma(\mathbf{M}(\mathbf{k}), z) + \Sigma(\mathbf{k}, z)] = 0\,, \tag{2.38}$$

since $\Sigma(\mathbf{M}(\mathbf{k}), z)$ is taken as an approximation for the self-energy $\Sigma(\mathbf{k}, z)$ of the full lattice Green function $G(\mathbf{k}, z)$.

Therefore the DCA is an approximation for the irreducible quantity Σ. The lattice reducible quantity G is then deduced from the irreducible cluster quantity $\Sigma(\mathbf{K})$. This can also be motivated physically [Het00, Mou00]: Since the cluster irreducible self-energy $\Sigma[\bar{G}(\mathbf{K})]$ is constructed from coarse grained propagators $\bar{G}(r) \approx G(r) + \mathcal{O}((r\Delta k)^2)$, it accurately reflects short-ranged correlations, whereas longer-ranged fluctuations are cut off by the finite size of the cluster. On the other hand it is important that the propagation of particles through the system, described by the lattice Green function $G(\mathbf{k})$ remains accurate also at long length scales. So G should not be approximated by its corresponding cluster quantity but may be calculated using $G(\mathbf{k}) = (z - \epsilon_{\mathbf{k}} + \mu - \Sigma[\bar{G}(\mathbf{M}(\mathbf{k}))])^{-1}$.

Proof of Causality

As pointed out in the introduction, there have been attempts to extend the DMFA through so-called $1/D$-corrections by replacing the DMFA impurity by a cluster in real space. A common problem encountered in these approaches was the violation of causality, i.e. $\mathrm{Im}\,\Sigma(\mathbf{k}, z) > 0$ for some $\mathbf{k}$ and z.

The DCA instead can be shown to remain fully causal throughout the iteration procedure (Fig. 2.5), i.e. the imaginary part of the self-energy and local Green function remains negative definite.

The basic assumption of the following proof is that, given a causal effective medium $\mathcal{G}$, i.e. $\mathrm{Im}\,\mathcal{G} < 0$, the method used to solve the effective cluster problem is fully causal, i.e. provides a causal Green function $G_c(\mathbf{K})$ (step (3)) and a causal self-energy $\Sigma(\mathbf{K})$ (step (4)). Then, since the coarse grained Green function (Eq. (2.24)) (step (1)) is a sum over terms with negative definite imaginary parts, $\bar{G}(\mathbf{K})$ is also causal per construction. Hence, only the calculation of the bath function $\mathcal{G}(\mathbf{K})$ in step (2) remains, where causality violations could possibly occur.

There are two ways to show that this step is also causal: First, by using Eq. (2.25), the inverse bath function $\mathcal{G}^{-1}$ can be written as

$$\mathcal{G}^{-1}(\mathbf{K}, z) = z - \bar{\epsilon}_{\mathbf{K}} + \mu - \Gamma(\mathbf{K}, z)\,. \tag{2.39}$$

Thus $\mathrm{Im}\,\mathcal{G} < 0$, if the imaginary part of the r.h.s. is positive. Since $\mathrm{Im}(z) > 0$ it remains to be shown that $\mathrm{Im}\,\Gamma(\mathbf{K}, z) < 0$. A formal proof of the analycity of Γ using a continued fraction decomposition is presented in App. A.1.

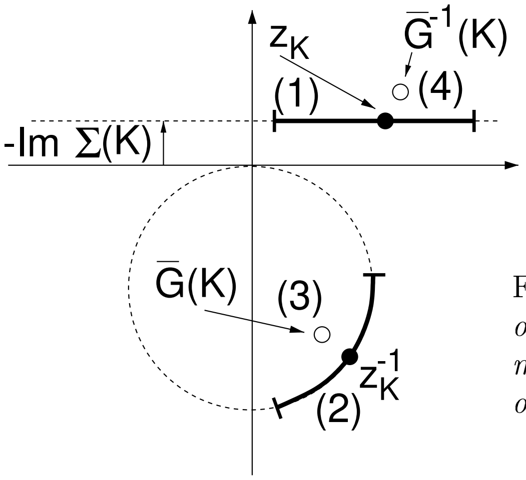

FIGURE 2.6: *Graphical illustration of the proof, that the DCA remains causal throughout the iteration steps. Taken from [Het00].*

The second proof is based on geometrical arguments presented in [Het00]. Fig. 2.6 illustrates a sketch of the following argument, which is based on the fact that the self-energy $\Sigma(\mathbf{K})$ is constant within a given DCA coarse graining cell. The inverse of the terms in the sum of the coarse graining step (Eq. (2.24)) reads

$$z_{\mathbf{K}+\mathbf{k}'} = z - \epsilon_{\mathbf{K}+\mathbf{k}'} - \Sigma(\mathbf{K})\,. \tag{2.40}$$

Then, for any given $\mathbf{K}$ and z, $z_{\mathbf{K}+\mathbf{k}'}$ lies on a segment of the dashed horizontal line in Fig. 2.6 in the upper half-plane (1). The distance from the real axis is given by $-\mathrm{Im}\,\Sigma(\mathbf{K}) > 0$. Taking the inverse of these points maps the line segment onto the segment of the dashed circle in the lower half-plane (2). $\bar{G}(\mathbf{K}, z) = N_c/N \sum_{\mathbf{k}'} (z_{\mathbf{K}+\mathbf{k}'})^{-1}$ is obtained by summing the points on the circle segment, therefore lies within the circle and is given by the empty dot (3). To calculate $\mathcal{G}^{-1}$, one has to take the inverse of $\bar{G}(\mathbf{K}, z)$, which maps the empty dot within the circle to the empty dot in the upper half-plane above the horizontal line (4). Thus, $\mathrm{Im}\,\bar{G}^{-1}(\mathbf{K}, z) \geq -\mathrm{Im}\,\Sigma(\mathbf{K}, z)$, yielding a $\mathcal{G}(\mathbf{K}) = [\bar{G}^{-1}(\mathbf{K}) + \Sigma(\mathbf{K})]^{-1}$ with a negative definite imaginary part.

It is important to note that interpolating the self-energy $\Sigma(\mathbf{K}) \rightarrow \Sigma(\mathbf{k})$ onto the full lattice BZ between the cluster $\mathbf{K}$-points within the iteration procedure (see e.g. [Lie99]) after step (4) violates the causality proof. Then the interpolated self-energy $\Sigma(\mathbf{k})$ is not a constant within a given cell and hence $z_{\mathbf{K}+\mathbf{k}'}$ does not lie on the horizontal line anymore. As a consequence, its inverse is not mapped onto the segment of the circle and the proof is violated. Therefore causality cannot be guaranteed if the self-energy is interpolated within the iteration procedure. However, after convergence of the algorithm, the self-energy may be interpolated onto the full lattice BZ by means of a suitable interpolation scheme, which preserves causality, i.e. bilinear interpolation.

2.4 Effective cluster model and methods

In the last sections it was shown that the DCA is a fully causal approach which systematically incorporates nonlocal corrections to the DMFA. By coarse graining, the DCA formalism reduces the complexity of the lattice problem by mapping the system with N degrees of freedom onto an effective cluster problem with N_c degrees of freedom, while remaining in the thermodynamic limit. For $N_c = 1$ the DCA is equivalent to the DMFA and by increasing the cluster size N_c the dynamic correlation length can be gradually increased. The DCA becomes exact in the limit of large cluster sizes. Thus, the accurate solution of the cluster problem is the vital part for the DCA scheme.

In analogous fashion to the DMFA (=DCA for the cluster $N_c = 1$), the effective cluster model is reversely defined by the form (2.25) of the coarse grained Green function $\bar{G}$. The corresponding cluster Hamiltonian

$$H_{\text{cluster}} = H_{\text{loc}} + H_{\text{hyb}} + H_{\text{med}} \tag{2.41}$$

is most conveniently constructed in momentum space. Its local part

$$H_{\text{loc}} = H_f + H_U \tag{2.42}$$

consists of the two contributions

$$H_f = \sum_{\mathbf{K}\sigma} (\bar{\epsilon}_{\mathbf{K}} - \mu) f^\dagger_{\mathbf{K}\sigma} f_{\mathbf{K}\sigma} \quad , \quad H_U = \frac{U}{N_c} \sum_{\substack{\mathbf{K},\mathbf{K}' \\ \mathbf{Q}}} f^\dagger_{\mathbf{K}+\mathbf{Q}\uparrow} f_{\mathbf{K}\uparrow} f^\dagger_{\mathbf{K}'-\mathbf{Q}\downarrow} f_{\mathbf{K}'\downarrow} , \tag{2.43}$$

where $f^\dagger_{\mathbf{K}\sigma}$ ($f_{\mathbf{K}\sigma}$) creates (destroys) an electron with momentum $\mathbf{K}$ and spin σ on the cluster. U is the local Coulomb repulsion for two electrons residing on the same site of the real space analogon of the cluster. Since this interaction is local, it is unchanged by the coarse-graining procedure. The effective dispersion $\bar{\epsilon}_{\mathbf{K}}$ of the cluster states is given by the average bare dispersion in the cell (Eq. (2.26)). The effective medium

$$H_{\text{med}} = \sum_{\mathbf{k}\sigma} \varepsilon_{\mathbf{k}} a^\dagger_{\mathbf{k}\sigma} a_{\mathbf{k}\sigma} \tag{2.44}$$

is simulated by the auxiliary Fermions $a^\dagger_{\mathbf{k}\sigma}$ ($a_{\mathbf{k}\sigma}$) in terms of non-interacting particles with a dispersion $\varepsilon_{\mathbf{k}}$. The coupling of the local cluster states to the effective medium is simulated by the hybridization term

$$H_{\text{hyb}} = \frac{1}{\sqrt{N}} \sum_{\mathbf{K},\mathbf{k}',\sigma} (V_{\mathbf{K},\mathbf{k}'} f^\dagger_{\mathbf{K}\sigma} a_{\mathbf{K}+\mathbf{k}'\sigma} + \text{h.c.}) . \tag{2.45}$$

The sum over $\mathbf{k}'$ is restricted to the N/N_c momenta within a cell so that $\mathbf{k} = \mathbf{K}+\mathbf{k}'$ lies in the cell containing $\mathbf{K}$. For $N_c = 1$ the sums over $\mathbf{K}$ vanish, sums over $\mathbf{k}'$ extend over the full BZ and the cluster Hamiltonian (2.41) reduces to the impurity Hamiltonian (2.13) of the DMFA. Since for $N_c > 1$ the local states represented by $f^\dagger_{\mathbf{K}\sigma}$ couple only to auxiliary Fermions with momenta $\mathbf{k} = \mathbf{K} + \mathbf{k}'$ in the cell containing the cluster momentum $\mathbf{K}$, the corresponding hybridization function

$$\Gamma_{\mathrm{c}}(\mathbf{K}, z) = \frac{1}{N} \sum_{\mathbf{k}'} \frac{|V_{\mathbf{K},\mathbf{k}'}|^2}{z - \varepsilon_{\mathbf{K}+\mathbf{k}'}} \tag{2.46}$$

becomes $\mathbf{K}$-dependent and the interacting cluster Green function

$$G_{\mathrm{c}}(\mathbf{K}, z) = \frac{1}{z - \bar{\epsilon}_{\mathbf{K}} + \mu - \Sigma(\mathbf{K}, z) - \Gamma_{\mathrm{c}}(\mathbf{K}, z)} \tag{2.47}$$

has the same form as the expression (2.25) for the coarse grained Green function $\bar{G}$. Finally the substitution

$$[z - \bar{\epsilon}_{\mathbf{K}} + \mu - \Gamma_{\mathrm{c}}(\mathbf{K}, z)]^{-1} \equiv G^o_c = \mathcal{G} \equiv [z - \bar{\epsilon}_{\mathbf{K}} + \mu - \Gamma(\mathbf{K}, z)]^{-1} \tag{2.48}$$

of the effective medium $\mathcal{G}$, which is the bare coarse grained Green function defined in Eq. (2.27), for the bare cluster Green function G^o_c ensures that the solution of the effective cluster model is also the solution of the lattice system. Therefore the remaining task is to solve the cluster model (2.41), with its bare Green function fixed by the effective medium $\mathcal{G}$.

Methods

A wide variety of methods has been applied to solve the single impurity model of the DMFA (N_c=1). A comprehensive summary can be found e.g. in the review article by [Geo96]. Numerical methods employ e.g. the QMC or Numerical Renormalization Group (NRG) method. The QMC method, or more specifically the Hirsch-Fye algorithm [Hir86] solves the single impurity Anderson model numerically exact at finite temperatures for a large parameter range on the imaginary time axis and hence provides data as a function of Matsubara frequencies. Therefore the QMC results have to be analytically continued to the real axis, which is a numerically ill conditioned problem due to the statistical nature of the QMC data. Furthermore, off half filling the minus-sign problem forms another obstacle for the QMC method at low temperatures and large values for the Coulomb repulsion U. Except for these problems QMC supplies reliable and well controlled results for the impurity model of the DMFA.

As another numerically exact method, Wilson's NRG approach [Wil75] has been applied to the DMFA [Sak94, Bul97] (for a review see [Bul00]). The discrete NRG spectrum is thereby broadened artificially to get continuous functions of frequency. The parameter range accessible by this T=0 method is vast and even broader than for the QMC method. Recently the NRG was even extended to obtain results at finite temperatures [Bul00]. As a Renormalization group based method, the NRG is precise at low frequencies but inaccurate on large energy scales.

The Exact Diagonalization approach [Caf94] for the DMFA maps the impurity problem approximately onto a finite linear chain, which then is solved exactly. Since the linear chain has a finite length, this approach lacks the thermodynamic limit, one of the main advantages of the DMFA method. In addition, studies of the low energy physics are limited by the finite length of the chain because of the presence of finite size gaps in the low energy spectrum.

Analytical methods like e.g. weak coupling perturbation theory form another access to the impurity problem. The main advantage of the Iterated Perturbation Theory (IPT) [Geo92], another synonym for second order perturbation theory in U, is that it is easy to apply and numerically not expensive. However the interesting parameter regime of the Hubbard model is $U \geq W$, and results obtained by perturbation theory in U are therefore rather questionable.

Another analytical approach, used in this work, makes use of the opposite limit, the strong coupling limit $U \gg W$. The idea of the Non Crossing Approximation (NCA), an application of the resolvent technique [Kei71, Bic87, Pru89], is to view the small term $H_{\rm hyb}$ (2.45) as perturbation to the impurity (cluster) term $H_{\rm loc}$ (2.42). It then performs a particular resummation of the perturbative expansion in powers of the hybridization V (or Γ in the DMFA (DCA) context). For the SIAM it was shown by classifying the skeleton diagrams in terms of the bandwidth, that the graphs contained in the NCA are sufficient to describe the correct exponential dependence on model parameters [Mül84]. Correlation functions and thermodynamic properties are accessible for a wide range of parameters and temperatures and numerical results for the single impurity model show an outstanding agreement with results obtained by exact methods like the Bethe-ansatz or NRG [Bic87]. However the NCA applied to the SIAM encounters problems at very low temperatures. Due to the neglect of a class of diagrams, i.e. crossing diagrams, pathologies occur for temperatures $T/T_{\rm K} \lesssim 0.1$, where the Kondo temperature $T_{\rm K}$ indicates the relevant low temperature scale below which all physical quantities scale with $T_{\rm K}$ and hence show universal behavior. However, since the DMFA (DCA) involves a self-consistent mapping of the lattice to the impurity (cluster) model, it is a priori not clear which parameter and temperature regime the NCA in the context of the DMFA (DCA) can handle. Nevertheless, a large number of DMFA-NCA calculations show that the NCA supplies reliable results for $U/(-\mathrm{Im}\,\Gamma(\omega = 0+)) > 1$ and for doping levels $\delta \lesssim 0.20$.

In principal extensions of all these methods can also be applied to solve the effective cluster problem (2.41) of the DCA. So far QMC has been applied in Mark Jarrell's group [Het98, Het00, Hus99, Mou00, Jar00] to obtain well-controlled and reliable results for the weak to intermediate coupling regime $U \lesssim W$ of the Hubbard model. Therefore, it would be desirable to also cover the strong coupling regime $U > W$ by extending the NCA approach to the cluster model (Eq. (2.41)). The goal of the next section is to develop an extended NCA formalism for clusters[4] and discuss the advantages and limitations of this approach in the context of the DCA.

2.5 Resolvent technique for clusters

This section describes how to solve the effective cluster model with an extended version of the resolvent technique [Kei71] and its application, the NCA. For a derivation and details of the NCA-method for the single impurity Anderson model the reader is referred to [Kei71]. App. B presents a brief summary of the concepts of the resolvent technique, so that this section can be focused on the essential extensions only, necessary to apply the NCA to the cluster model.

The effective cluster model is defined by the Hamiltonian (2.41) with the bare cluster Green function fixed by the effective medium $\mathcal{G}$ (see Eq. (2.48)). The resolvent technique is a perturbational expansion around the molecular limit, i.e. it starts with the eigenstates of the local part H_{loc} (Eq. (2.42)) of the cluster Hamiltonian (Eq. (2.41)). The expansion is performed with respect to the coupling H_{hyb} (Eq. (2.45)) to the effective medium simulated by H_{med} (Eq. (2.44)), where the properties of the quasi-free auxiliary Fermions $a^\dagger_{\mathbf{k}\sigma}$ are determined by the host function $\Gamma(\mathbf{K})$ (see Eq. (2.48)). To apply the resolvent technique, the Fermionic operators defined on the cluster are expanded in terms of the Hubbard-operators $X_{mn} = |m\rangle\langle n|$

$$f_{\mathbf{K}\sigma} = \sum_{m,n} F^{\mathbf{K}\sigma}_{mn} X_{mn} \quad , \quad f^\dagger_{\mathbf{K}\sigma} = \sum_{m,n} (F^{\mathbf{K}\sigma}_{mn})^\star X_{nm} \tag{2.49}$$

where $\{|m\rangle\}$ are the eigenstates of the local Hamiltonian

$$H_{\text{loc}} = \sum_m E_m X_{mm} \tag{2.50}$$

with eigenenergies E_m and

$$F^{\mathbf{K}\sigma}_{mn} = \langle m | f_{\mathbf{k}\sigma} | n \rangle \, . \tag{2.51}$$

Then the hybridization term (2.45) becomes

$$H_{\text{hyb}} = \frac{1}{\sqrt{N}} \sum_{\mathbf{K},\mathbf{k}',\sigma} \sum_{m,n} \left[V_{\mathbf{K},\mathbf{k}'} (F^{\mathbf{K}\sigma}_{mn})^\star X_{nm} a_{\mathbf{K}+\mathbf{k}'\sigma} + V^\star_{\mathbf{K},\mathbf{k}'} F^{\mathbf{K}\sigma}_{mn} a^\dagger_{\mathbf{K}+\mathbf{k}'\sigma} X_{mn} \right] \, . \tag{2.52}$$

[4]Parts of the formalism were already published in [Mai00a].

Since the Hubbard-operators X_{mn} do not obey standard Fermionic or Bosonic commutation relations, the conventional Feynman diagram technique cannot be used for a perturbation expansion, and the concept of resolvents must be introduced instead (see App. B). The matrix elements of these resolvents in the space of the local eigenstates have the form (see App. B, Eq. (B.24))

$$[\bar{R}^{-1}]_{mn}(z) = (z - E_m)\delta_{mn} - \Sigma^R_{mn}(z)\,. \tag{2.53}$$

Depending on the expression for the coupling term (2.52) non-diagonal elements $\bar{R}_{mn}$ with $m \neq n$ may or may not exist. In the paramagnetic phase they vanish, and Eq. (2.53) reduces to the diagonal parts only. However, in the next section it will be demonstrated that the non-diagonal elements are essential in symmetry broken phases, where a generalized coupling term H_{hyb} breaks some symmetries of the local part H_{loc}. Σ^R describes self-energy effects due to the coupling H_{hyb} to the effective medium H_{med}. It is important to emphasize that the matrix elements of Σ^R collect the renormalizations of the individual local states $\{|m\rangle\}$ and must not be confused with the proper one-particle self-energy of the cluster, $\Sigma(\mathbf{K}, z)$. The vertices in the NCA self-energy diagrams are defined by the coupling term H_{hyb}. The expression (2.52) for the coupling term leads to the two vertices

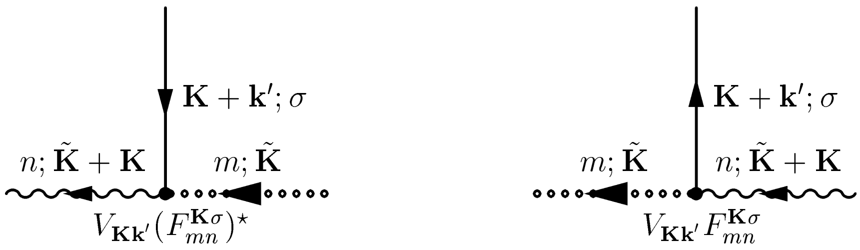

.

The diagram on the left corresponds to the first term in H_{hyb} (Eq. (2.52)) and describes hopping of a conduction electron (solid line) with momentum $\mathbf{K} + \mathbf{k}'$ and spin σ onto the cluster. Thus the cluster, which originally was in state m (dotted line) with momentum $\tilde{\mathbf{K}}$, performs a transition to a state n with one particle more (wavy line) and momentum $\tilde{\mathbf{K}} + \mathbf{K}$. The amplitude for this process is given by the product $V_{\mathbf{K},\mathbf{k}'}(F^{\mathbf{K}\sigma}_{mn})^\star$. The graph on the right hand side stands for the reverse process.

In contrast to the single impurity case (see App. B) additional labels $\mathbf{K}$ are added to the lines and the momentum of the conduction electron line $\mathbf{k} = \mathbf{K} + \mathbf{k}'$ is restricted to the DCA coarse graining cell containing $\mathbf{K}$. Thus momentum conservation is partially observed on the vertices.

In the spirit of the NCA (see App. B) the self-energy matrix Σ^R is then obtained by calculating the two diagrams illustrated in Fig. 2.7 in matrix notation. The energy is conserved on the vertices and the matrix elements $F^{\mathbf{K}\sigma}_{mn}$ ($(F^{\mathbf{K}\sigma}_{mn})^\star$), which have to be applied on the vertices take care of momentum and spin conservation. After adding products of $V_{\mathbf{K},\mathbf{k}'}F^{\mathbf{K}\sigma}_{mn}$ to the vertices, observing

$$\Sigma^R \quad = \quad$$ 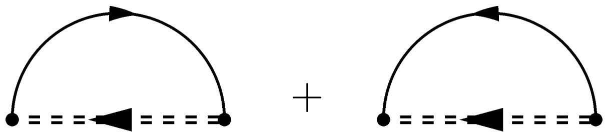

FIGURE 2.7: *The NCA self-energy matrix of the reduced resolvent $\bar{R}$ due to the coupling term H_{hyb}. The solid curved lines from left to right and right to left stand for the Fermi functions $f(\varepsilon_{\mathbf{K}+\mathbf{k}'})$ and $1-f(\varepsilon_{\mathbf{K}+\mathbf{k}'}) = f(-\varepsilon_{\mathbf{K}+\mathbf{k}'})$, respectively. The double dashed line represents the reduced resolvent $\bar{R}$.*

energy conservation and summing over degrees of freedom of the internal lines, the analytical expression for the matrix element mn of these two diagrams reads

$$\begin{aligned}\Sigma^R_{mn}(z) &= \frac{1}{N}\sum_{\mathbf{K},\mathbf{k}',\sigma}|V_{\mathbf{K},\mathbf{k}'}|^2\sum_{l,l'}\left[f(\varepsilon_{\mathbf{K}+\mathbf{k}'})F^{\mathbf{K}\sigma}_{ml}\bar{R}_{ll'}(z+\varepsilon_{\mathbf{K}+\mathbf{k}'})(F^{\mathbf{K}\sigma}_{nl'})^\star\right.\\ &\quad \left.+\, f(-\varepsilon_{\mathbf{K}+\mathbf{k}'})(F^{\mathbf{K}\sigma}_{lm})^\star\bar{R}_{ll'}(z-\varepsilon_{\mathbf{K}+\mathbf{k}'})F^{\mathbf{K}\sigma}_{l'n}\right] . \qquad (2.54)\end{aligned}$$

In contrast to the NCA for a single impurity (see App. B) there is an additional sum over the cluster momentum points $\mathbf{K}$, and the sum over $\mathbf{k}'$ extends only over the N/N_c momenta within a cell.

Expression (2.54) still contains the energy levels $\varepsilon_{\mathbf{k}}$ of the auxiliary particles of the term H_{med}, simulating the effective medium. The substitution (2.48) of the corresponding lattice quantity Γ can now be taken care of by making use of the identity $\frac{1}{\omega+i\delta} = P\frac{1}{\omega} - i\pi\delta(\omega)$ such that

$$\frac{1}{N}\sum_{\mathbf{k}'}|V_{\mathbf{K},\mathbf{k}'}|^2\delta(\omega-\epsilon_{\mathbf{K}+\mathbf{k}'}) = -\frac{1}{\pi}\mathrm{Im}\,\frac{1}{N}\sum_{\mathbf{k}'}\frac{|V_{\mathbf{K},\mathbf{k}'}|^2}{\omega+i\delta-\epsilon_{\mathbf{K}+\mathbf{k}'}} = -\frac{1}{\pi}\mathrm{Im}\,\Gamma_{\mathrm{c}}(\mathbf{K},\omega)\,. \qquad (2.55)$$

Γ_{c} is the hybridization function defined in Eq. (2.46), which is now replaced, $\Gamma_{\mathrm{c}} \leftarrow \Gamma$, by the corresponding lattice quantity Γ defined by the coarse grained Green function (see Eq. (2.25)). The resolvent self-energy in NCA approximation then finally reads

$$\begin{aligned}\Sigma^R_{mn}(z) &= -\frac{1}{\pi}\sum_{\mathbf{K},\sigma}\sum_{l,l'}\left[\int_{-\infty}^{+\infty}\mathrm{d}\varepsilon\, f(\varepsilon)\mathrm{Im}\,\Gamma(\mathbf{K},\varepsilon)F^{\mathbf{K}\sigma}_{ml}\bar{R}_{ll'}(z+\varepsilon)(F^{\mathbf{K}\sigma}_{nl'})^\star\right.\\ &\quad \left.+\int_{-\infty}^{+\infty}d\varepsilon\, f(-\varepsilon)\mathrm{Im}\,\Gamma(\mathbf{K},\varepsilon)(F^{\mathbf{K}\sigma}_{lm})^\star\bar{R}_{ll'}(z-\varepsilon)F^{\mathbf{K}\sigma}_{l'n}\right] . \qquad (2.56)\end{aligned}$$

The coupled equations (2.53) and (2.56) then have to be solved self-consistently to compute the matrix elements of the resolvent $\bar{R}$.

Finally, by using the expansion (2.49), the cluster Green function for the f-electrons $G_c = \langle\langle f_{\mathbf{K}\sigma}; f^\dagger_{\mathbf{K}\sigma}\rangle\rangle$ can be written in terms of the Hubbard-operators X_{mn} as

$$G_c(\mathbf{K}, z) = \sum_{\substack{m,m' \\ n,n'}} F^{\mathbf{K}\sigma}_{mm'} (F^{\mathbf{K}\sigma}_{nn'})^\star \langle\langle X_{mm'}; X_{n'n}\rangle\rangle_z \,. \tag{2.57}$$

Within the NCA, the correlation function on the right hand side of Eq. (2.57) can then be written in terms of the reduced resolvents $\bar{R}$ (Eq. (2.53)) as (see App. B Eq. (B.27))

$$\langle\langle X_{mm'}; X_{n'n}\rangle\rangle_z = \frac{1}{Z_f} \int_{-\infty}^{+\infty} \mathrm{d}\varepsilon\, \mathrm{e}^{-\beta\varepsilon} [\rho_{nm}(\varepsilon) \bar{R}_{m'n'}(\varepsilon+\omega) - \rho_{m'n'}(\varepsilon) \bar{R}^\star_{nm}(\varepsilon-\omega)] \,. \tag{2.58}$$

Here ρ_{nm} is the spectral density of the resolvents, $\rho_{nm}(\omega) = -\frac{1}{\pi}\mathrm{Im}\,\bar{R}_{nm}(z)$. $Z_f = \sum_n \int_{-\infty}^{+\infty} \mathrm{d}\varepsilon\, \mathrm{e}^{-\beta\varepsilon} \rho_{nn}(\varepsilon)$ is the cluster partition function, where the sum runs over the cluster eigenstates $\{|n\rangle\}$ and $\beta = 1/T$ is the inverse temperature.

Discussion of the cluster-NCA approximation

As mentioned in Sec. 2.3 the DCA becomes exact as $N_c \to \infty$. This means further that the NCA approach to the resulting cluster model (2.41) has to become exact in this limit. That this is indeed the case can be seen by performing the limit $N_c \to N$ for a fixed finite number N of sites in the original lattice before setting $N = \infty$. Then for $N_c = N$ the summation over $\mathbf{k}'$ in the coarse graining step (Eq. (2.24)) vanishes since the cluster $\mathbf{K}$-points represent the full system ($\{\mathbf{K}\} = \{\mathbf{k}\}$). Hence the hybridization function $\Gamma(\mathbf{K}, z)$ in Eq. (2.25) vanishes for $N_c = N$. As a consequence the NCA resolvent self-energy Σ^R (Eq. (2.56)) becomes zero because $\Gamma(\mathbf{K}, z) = 0$ for $N_c = N$ and the sum over $\mathbf{K}$ is finite, of the order of N. The cluster problem is then solved exactly by the eigenstates $\{|m\rangle\}$. Thus the NCA approach to the cluster problem is exact in the limit $N_c = N = \infty$.

The only approximation for finite N_c in the above presented resolvent algorithm is the restriction to non-crossing diagrams in the evaluation of the resolvent self-energy Σ^R (see Fig. 2.7). In the form (2.56) the NCA equations contain all diagrams of second order in the coupling V, i.e. first order in $\Gamma \sim \mathcal{O}(1/N_c)$ (see App. A.2). Higher order corrections to these equations come in the form of crossing diagrams which can be incorporated as vertex corrections [Pru89]. Fig. 2.8 shows a leading order correction to the NCA self-energy. The diagram itself is second order in Γ, i.e. of the order of $1/N_c^2$. However the two sums over $\mathbf{K}$ and $\mathbf{K}'$ are of the order of N_c^2. Taken together, the diagram and the sums, the contribution of neglected crossing diagrams is of the order of one, i.e. the same order in $1/N_c$ as the included diagrams. Therefore no $1/N_c$ estimation of the quality of the NCA approach in the context of the DCA can be made.

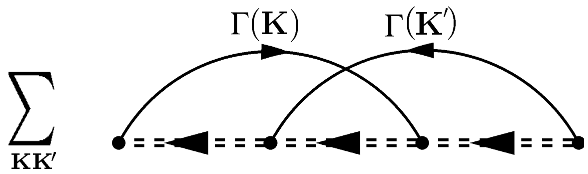

FIGURE 2.8: *Leading order crossing diagram neglected in the NCA approximation.*

However, if the resolvent technique is applied to the orbitally non-degenerate SIAM (Eq. (2.13)) with finite Coulomb repulsion U, it is well known that to obtain the correct low energy scale one has to sum all diagrams up to fourth order in the coupling V [Pru89]. Applied to the cluster model (Eq. (2.41)) this requirement would mean that vertex corrections, i.e. crossing diagrams must be included if U is finite for all cluster sizes including $N_c = 1$ and if $U = \infty$ for $N_c > 1$. In the case of the single impurity model ($N_c = 1$) former experiences with vertex corrections show that renormalizations of low-energy scales must be expected. However, as the most important fact, the qualitative behavior of spectra or physical quantities in general is unchanged by the inclusion of leading order crossing diagrams [Pru89, Hei00b].

A priori it is not clear how and if these arguments can be transferred to the cluster ($N_c > 1$) case. The question rather is, if there is any low-energy scale present in the system or if it is suppressed by nonlocal correlations on the cluster. Furthermore, in contrast to the single impurity case, there are N_c different conduction electron channels represented by the N_c $\mathbf{K}$-points. A priori, the effect of this multi-channel conduction electron system on the quality of the NCA is not clear. Nevertheless it can be expected that at least qualitative aspects of the results obtained with this technique are unaffected by crossing diagrams. Since on the other hand an inclusion of vertex corrections is associated with a tremendous numerical effort, they are not taken into account in this work.

2.6 Generalizations for symmetry broken phases

In the preceding sections the DCA equations and the cluster-NCA formalism have been derived for the paramagnetic phase. However, at low enough temperatures instabilities of the Hubbard model towards symmetry broken phases have to be expected and the algorithm needs to be generalized to implicitly account for the possibility of transitions to symmetry broken phases. This section presents generalizations of the DCA-algorithm to symmetry broken phases along with the mapping onto corresponding cluster models and develops a generalized cluster-NCA to handle the symmetry broken state.

2.6.1 Finite homogeneous magnetic field

A finite external magnetic field h acts on the spin of the Fermions according to the Zeeman term

$$-h\sum_{i\sigma}\sigma c_{i\sigma}^{\dagger}c_{i\sigma} \quad , \quad \sigma\in\{1,-1\} \quad , \quad \bar{\sigma}:=-\sigma\,. \tag{2.59}$$

The effect of h on the motion of the electrons, i.e. the diamagnetic contribution can in principle be taken into account too but shall be neglected here since it is not relevant for the studies presented in this manuscript. In the presence of a finite homogeneous magnetic field h or a uniform magnetization the Green functions for up- and down-electrons are not equivalent. To account for this symmetry breaking, the spin index of the Green function G_σ, self-energy Σ_σ and effective medium $\mathcal{G}_\sigma$ (and hence Γ_σ) in the derivation of the DCA-equations in Sec. 2.3.1 has to be retained. For a finite uniform magnetic field h the DCA lattice Green function then reads

$$G_\sigma(\mathbf{k},z)=\frac{1}{z-\epsilon_{\mathbf{K}+\mathbf{k}'}+\mu+h\sigma-\Sigma_\sigma(\mathbf{K},z)}\,. \tag{2.60}$$

The coarse grained Green function

$$\bar{G}_\sigma(\mathbf{K},z)=\frac{N_c}{N}\sum_{\mathbf{k}'}G_\sigma(\mathbf{K}+\mathbf{k}',z) \tag{2.61}$$

depends on the spin and can again be written as

$$\bar{G}_\sigma(\mathbf{K},z)=\frac{1}{z-\bar{\epsilon}_{\mathbf{K}}+\mu+h\sigma-\Sigma_\sigma(\mathbf{K},z)-\Gamma_\sigma(\mathbf{K},z)}\,, \tag{2.62}$$

due to the independence of $\Sigma_\sigma(\mathbf{K})$ on the integration variable $\mathbf{k}'$. The additional term $h\sigma$ in the denominator of the coarse grained Green function requires an additional magnetic field term

$$H_{\mathrm{MF}}=-h\sum_{\mathbf{K}\sigma}\sigma f_{\mathbf{K}\sigma}^{\dagger}f_{\mathbf{K}\sigma}\,, \tag{2.63}$$

which has to be added to the local part H_{loc} (Eq. (2.42)) of the effective cluster Hamiltonian. The resulting cluster Hamiltonian $H_{\mathrm{cluster}}+H_{\mathrm{MF}}$ with H_{cluster} defined in Eq. (2.41) then describes cluster states in a uniform magnetic field h coupled to a spin dependent effective medium, which in inverse notation is given by

$$\mathcal{G}_\sigma^{-1}(\mathbf{K},z)=\bar{G}_\sigma^{-1}(\mathbf{K},z)+\Sigma_\sigma(\mathbf{K},z)\,. \tag{2.64}$$

The coarse grained Green function (2.61) may then be used to calculate the magnetization $m := n_\uparrow - n_\downarrow$ with $n_\sigma := \langle n_{i\sigma} \rangle$ according to

$$m = -\frac{1}{\pi}\frac{1}{N_c}\sum_{\mathbf{K}\sigma}\int_{-\infty}^{+\infty} \mathrm{d}\varepsilon\, \sigma \mathrm{Im}\, \bar{G}_\sigma(\mathbf{K}, \varepsilon)\,. \tag{2.65}$$

2.6.2 Superconductivity

In this and the next section the DCA-NCA formalism will be generalized to perform calculations in the superconducting and antiferromagnetic phase, respectively. Although the combined treatment of superconductivity and antiferromagnetism at the same time is formally possible, the two phases will be treated separately to reduce the complexity of the problem. This is partly motivated by the generic phase diagram of the cuprates where no region of coexistence of the two phases is found. Furthermore it will be justified a posteriori by the results for the 2D Hubbard model presented in Sec. 3 where also no region of coexistence is found.

Transitions to superconducting phases where the electrons are paired in spin singlet states are signalled by a finite order parameter

$$\Delta_\mathbf{k} := \langle c_{\mathbf{k}\uparrow} c_{-\mathbf{k}\downarrow} \rangle \neq 0 \quad \text{for some}\, \mathbf{k}\,. \tag{2.66}$$

Thus, in addition to the normal Green function

$$G(\mathbf{k}, z) = \langle\langle c_{\mathbf{k}\uparrow}\,;\, c^\dagger_{\mathbf{k}\uparrow} \rangle\rangle_z \tag{2.67}$$

the anomalous Green function

$$F_{\uparrow\downarrow}(\mathbf{k}, z) = \langle\langle c_{\mathbf{k}\uparrow}\,;\, c_{-\mathbf{k}\downarrow} \rangle\rangle_z \tag{2.68}$$

has to be introduced. A finite anomalous Green function $F_{\uparrow\downarrow}(\mathbf{k}, z)$ then signals the existence of off-diagonal long-range order and the spatial and temporal symmetry of the pairing state is given by the $\mathbf{k}$- and time dependence of $F_{\uparrow\downarrow}$. By utilizing the concept of Nambu-spinors [Sch61]

$$\Psi^\dagger_\mathbf{k} := \left(c^\dagger_{\mathbf{k}\uparrow}\,,\, c_{-\mathbf{k}\downarrow}\right) \quad , \quad \Psi_\mathbf{k} := \begin{pmatrix} c_{\mathbf{k}\uparrow} \\ c^\dagger_{-\mathbf{k}\downarrow} \end{pmatrix}\,, \tag{2.69}$$

the following equations can be conveniently written in a more compact form, since the Green function matrix in Nambu space

$$\mathbf{G}(\mathbf{k}, z) = \langle\langle \Psi_\mathbf{k}\,;\, \Psi^\dagger_\mathbf{k} \rangle\rangle_z = \begin{pmatrix} G(\mathbf{k}, z) & F_{\uparrow\downarrow}(\mathbf{k}, z) \\ F^\star_{\uparrow\downarrow}(\mathbf{k}, z^\star) & -G^\star(\mathbf{k}, -z^\star) \end{pmatrix} \tag{2.70}$$

contains information about both the normal and anomalous Green function.[5]

With the Pauli-spin matrices σ_i defined in App. C.1, Eq. (C.4) the full lattice Green function of the Hubbard model then reads in the DCA context

$$\mathbf{G}(\mathbf{k},z) = [z\sigma_o - (\epsilon_{\mathbf{k}} - \mu)\sigma_3 - \mathbf{\Sigma}(\mathbf{K},z)]^{-1}\,, \tag{2.71}$$

where $\mathbf{K}$ is the cluster momentum representing the cell containing $\mathbf{k}$. The diagonal parts Σ of the cluster self-energy matrix

$$\mathbf{\Sigma}(\mathbf{K},z) = \begin{pmatrix} \Sigma(\mathbf{K},z) & S_{\uparrow\downarrow}(\mathbf{K},z) \\ S^{\star}_{\uparrow\downarrow}(\mathbf{K},z^{\star}) & -\Sigma^{\star}(\mathbf{K},-z^{\star}) \end{pmatrix}\,. \tag{2.72}$$

describe quasiparticle renormalizations, whereas the off-diagonal parts $S_{\uparrow\downarrow}$ are nonzero in the superconducting state only and contain information about the $\mathbf{K}$- and frequency dependence of the pairing state. Then, in analogous fashion to the paramagnetic case (see Sec. 2.3.1), the coarse grained Green function

$$\bar{\mathbf{G}}(\mathbf{K},z) = \frac{N_c}{N}\sum_{\mathbf{k}'}\mathbf{G}(\mathbf{K}+\mathbf{k}',z) = \begin{pmatrix} \bar{G}(\mathbf{K},z) & \bar{F}_{\uparrow\downarrow}(\mathbf{K},z) \\ \bar{F}^{\star}_{\uparrow\downarrow}(\mathbf{K},z^{\star}) & -\bar{G}^{\star}(\mathbf{K},-z^{\star}) \end{pmatrix} \tag{2.73}$$

is used to calculate the effective medium $\mathcal{G}$, which reads in inverse notation

$$\mathcal{G}^{-1}(\mathbf{K},z) = \bar{\mathbf{G}}^{-1}(\mathbf{K},z) + \mathbf{\Sigma}(\mathbf{K},z) = [z\sigma_o - (\bar{\epsilon}_{\mathbf{K}} - \mu)\sigma_3 - \mathbf{\Gamma}(\mathbf{K},z)]\,, \tag{2.74}$$

where the second identity follows again from the fact that $\mathbf{\Sigma}(\mathbf{K})$ does not depend on the integration variable $\mathbf{k}'$. In contrast to the paramagnetic phase, the hybridization function

$$\mathbf{\Gamma}(\mathbf{K},z) = \begin{pmatrix} \Gamma(\mathbf{K},z) & \Omega_{\uparrow\downarrow}(\mathbf{K},z) \\ \Omega^{\star}_{\uparrow\downarrow}(\mathbf{K},z^{\star}) & -\Gamma^{\star}(\mathbf{K},-z^{\star}) \end{pmatrix} \tag{2.75}$$

is a matrix in Nambu-space and has non-zero off-diagonal elements $\Omega_{\uparrow\downarrow}$ in the superconducting state, which describe pairing correlations in the host. The normal (quasiparticle) part of the host is represented by the diagonal elements Γ.

Within the DCA the resolution in $\mathbf{k}$-space is restricted to the cluster $\mathbf{K}$ points and the order parameter (Eq. (2.66)) is coarse grained, i.e. averaged over the cells about the cluster momenta $\mathbf{K}$

$$\bar{\Delta}_{\mathbf{K}} = \frac{N_c}{N}\sum_{\mathbf{k}'}\langle c_{\mathbf{K}+\mathbf{k}'\uparrow}c_{-(\mathbf{K}+\mathbf{k}')\downarrow}\rangle \equiv \bar{F}_{\uparrow\downarrow}(\mathbf{K},\tau=0)\,, \tag{2.76}$$

[5] $\mathbf{G}$ contains only the two independent matrix elements G and F. The second row can be related to the first one, using general symmetry relations for Green functions (see e.g. [Mah90]).

and given by the anomalous part of the coarse grained equal time Green function $\bar{F}_{\uparrow\downarrow}(\mathbf{K}, \tau = 0)$. The sum runs over the N/N_c momenta $\mathbf{k}'$ within the cell about the cluster momentum $\mathbf{K}$. By using Matsubara frequencies $\omega_n = (2n+1)\pi/\beta$ and applying Poison's summation formula (see e.g. [Mah90]) one arrives at

$$\bar{F}_{\uparrow\downarrow}(\mathbf{K}, \tau = 0) = \frac{1}{\beta} \sum_{\omega_n} \bar{F}_{\uparrow\downarrow}(\mathbf{K}, i\omega_n) = \frac{1}{\pi} \int_0^\infty \mathrm{d}\omega \, \tanh\left(\frac{\beta\omega}{2}\right) \mathrm{Im}\, \bar{F}_{\uparrow\downarrow}(\mathbf{K}, \omega) \, . \quad (2.77)$$

It should be pointed out that the coarse graining step (Eq. (2.76)) inhibits the detection of some possible symmetries for the order parameter $\Delta_{\mathbf{k}}$. For instance, for the cluster size $N_c = 1$ the sum over $\mathbf{k}'$ extends over the full BZ and the only detectable order parameters are the ones with local contributions, i.e. the s-wave order parameter, where $\Delta^s_{\mathbf{k}} = \text{const.}$ or the extended s-wave order parameter with $\Delta^{xs}_{\mathbf{k}} \propto \cos k_x + \cos k_y$. Nonlocal order parameters like e.g. p-wave or d-wave cannot be described with a cluster size of $N_c = 1$. This is a result of the neglect of nonlocal correlations in the DMFA, so that it cannot describe order parameters with a symmetry lower than the lattice symmetry [Jar92, Jar93] (see also [Ste98]).

Generalized cluster-NCA in the superconducting phase

The generalization necessary to apply the NCA to a single-impurity coupled to the quasiparticles of a superconducting host can be found in [Ste98]. A detailed description and derivation of the generalized cluster-NCA algorithm modified to treat the effective cluster model in the superconducting state is presented in App. C.1. The essential results are presented in the following.

To account for the anomalous components $\Omega_{\uparrow\downarrow}$ of the host-function $\mathbf{\Gamma}$, the effective medium term H_{med} of the cluster model has to be replaced by a superconducting effective medium term. The existence of paired states in the effective medium breaks the particle number symmetry of the cluster states and hence additional diagrams in the self-energy Σ^R of the reduced resolvent for the cluster eigenstates have to be considered. Skeleton diagrams, e.g.

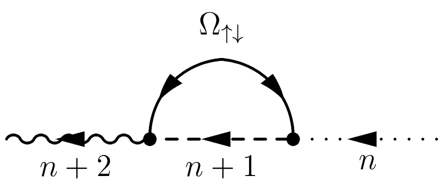

describe a process, where a Cooper pair (indicated by the doubly arrowed line) hops onto the cluster, involving a transition from an arbitrary n particle state to a state with $n + 2$ particles. To account for this symmetry breaking, Nambu spinors

$$\Psi^\dagger_{f\mathbf{K}} := (f^\dagger_{\mathbf{K}\uparrow}, f_{-\mathbf{K}\downarrow}) \quad , \quad \Psi_{f\mathbf{K}} := \begin{pmatrix} f_{\mathbf{K}\uparrow} \\ f^\dagger_{-\mathbf{K}\downarrow} \end{pmatrix} \quad (2.78)$$

for the cluster operators $f_{\mathbf{K}\sigma}$ are introduced to conveniently formulate the equations in Nambu space.

After substituting the hybridization function $\mathbf{\Gamma}$ (see App. C.1) for the auxiliary quantities, the resolvent self-energy in the superconducting state is obtained by calculating the diagrams illustrated in Fig. 2.9. The diagrams for Σ^R are formally

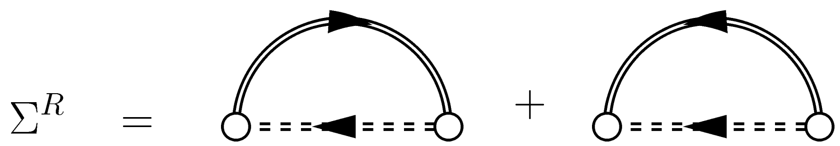

FIGURE 2.9: *The NCA self-energy Σ^R in the superconducting state. Formally the diagrams are identical to the ones in the paramagnetic state, but the curved Fermion line now represents the matrix $\mathbf{\Gamma}$ in Nambu space (indicated by the double solid line) and therefore contains anomalous propagators $\Omega_{\uparrow\downarrow}$. The dashed double line represents the reduced resolvent $\bar{R}$.*

identical to the corresponding diagrams in the paramagnetic state (see Fig. 2.7). However, the vertices are now replaced by $\sigma_3 \mathbf{F}^{\mathbf{K}}_{mn}$ and $(\mathbf{F}^{\mathbf{K}}_{mn})^\dagger \sigma_3$, respectively (represented by the circle), with the vectors

$$(\mathbf{F}^{\mathbf{K}}_{mn})^\dagger := \langle n|\Psi^\dagger_{f\mathbf{K}}|m\rangle \quad , \quad \mathbf{F}^{\mathbf{K}}_{mn} := \langle m|\Psi_{f\mathbf{K}}|n\rangle \,. \tag{2.79}$$

Furthermore, the curved Fermion lines are now matrices in Nambu space, i.e. they represent the matrix $\mathbf{\Gamma}$ and hence also contain diagrams involving the anomalous propagator $\Omega_{\uparrow\downarrow}$. The dashed double line again represents the reduced resolvent $\bar{R}$. In second order in the coupling to the anomalous medium, i.e. first order in $\Omega_{\uparrow\downarrow}$ these anomalous diagrams yield off-diagonal elements between states with a particle number difference of two. In higher orders, also off-diagonal elements between states with a particle number difference of two, four, six, ..., in general an integer multiple of two are generated. The dressed resolvent $\bar{R}$ is connected to the self-energy Σ^R via the Dyson equation (see App. B, Eqs. B.24)

$$[\bar{R}^{-1}]_{mn}(z) = (z - E_m)\delta_{mn} - \Sigma^R_{mn}(z) \,. \tag{2.80}$$

Since the matrix Eq. (2.80) has to be inverted to obtain the matrix elements of the reduced resolvent $\bar{R}$, the "anomalous" diagrams in Σ^R also affect the diagonal parts of $\bar{R}$. Therefore the cluster eigenstates and hence the character of the quasiparticles are renormalized in a self-consistent, non-BCS like manner, and feedback effects of the presence of superconductivity onto the nature of quasiparticles are implicitly taken into account.

The corresponding analytical expression (see App. C.1, Eq. (C.28)) for the resolvent self-energy then reads

$$
\begin{aligned}
\Sigma^R_{mn}(z) \;=\; & -\frac{1}{\pi}\sum_{\mathbf{K}}\sum_{l,l'}\Bigg\{ \qquad (2.81)\\
& \int_{-\infty}^{+\infty} \mathrm{d}\varepsilon\, [\mathbf{F}^{\mathbf{K}}_{ml}]^T \sigma_3 f(\varepsilon)\sigma_o \mathrm{Im}\,\mathbf{\Gamma}(\mathbf{K},\varepsilon)\sigma_o \bar{R}_{ll'}(z+\varepsilon)\sigma_3[(\mathbf{F}^{\mathbf{K}}_{nl'})^\dagger]^T \\
& + \int_{-\infty}^{+\infty} \mathrm{d}\varepsilon\, (\mathbf{F}^{\mathbf{K}}_{lm})^\dagger \sigma_3 f(-\varepsilon)\sigma_o \mathrm{Im}\,\mathbf{\Gamma}(\mathbf{K},\varepsilon)\sigma_o \bar{R}_{ll'}(z-\varepsilon)\sigma_3 \mathbf{F}^{\mathbf{K}}_{l'n}\Bigg\} .
\end{aligned}
$$

$[\ldots]^T$ denotes the corresponding transposed vector of the vector in brackets. In analogous fashion to the paramagnetic case, Eq. (2.80) and Eq. (2.81) form a set of coupled equations which is solved self-consistently to compute the matrix-elements of the reduced resolvent $\bar{R}$. The latter are then used to calculate the cluster Green function

$$\mathbf{G}_{\mathrm{c}}(\mathbf{K},z) = \langle\langle \Psi_{f\mathbf{K}}; \Psi^\dagger_{f\mathbf{K}}\rangle\rangle_z \,. \qquad (2.82)$$

By expanding the Nambu spinors $\Psi_{f\mathbf{K}}$ ($\Psi^\dagger_{f\mathbf{K}}$) in terms of the Hubbard-operators X_{mn} (see App. C.1, Eq. (C.19)), $\mathbf{G}_{\mathrm{c}}$ can be written as

$$\mathbf{G}_{\mathrm{c}}(\mathbf{K},z) = \sum_{\substack{m,m'\\ n,n'}} \mathbf{F}^{\mathbf{K}}_{mm'}(\mathbf{F}^{\mathbf{K}}_{nn'})^\dagger \langle\langle X_{mm'}; X_{n'n}\rangle\rangle_z \qquad (2.83)$$

with the correlation function $\langle\langle X_{mm'}; X_{n'n}\rangle\rangle_z$ given by Eq. (2.58). Finite off-diagonal propagators are essential for a non-vanishing anomalous part of the cluster Green function

$$
\begin{aligned}
F_c(\mathbf{K},z) \;=\; & \sum_{\substack{m,m'\\ n,n'}} F^{\mathbf{K}\uparrow}_{mm'} F^{-\mathbf{K}\downarrow}_{n'n} \times \qquad (2.84)\\
& \frac{1}{Z_f}\int_{-\infty}^{+\infty} \mathrm{d}\varepsilon\, \mathrm{e}^{-\beta\varepsilon}[\rho_{nm}(\varepsilon)\bar{R}_{m'n'}(\varepsilon+\omega) - \rho_{m'n'}(\varepsilon)\bar{R}^\star_{nm}(\varepsilon-\omega)] ,
\end{aligned}
$$

since it involves at least one off-diagonal propagator $\bar{R}_{mn}$.

2.6.3 Antiferromagnetism

The antiferromagnetically ordered state may be characterized by a variation of the magnetization according to

$$\mathbf{m}(\mathbf{x}_i) = \mathbf{m}(0)\mathrm{e}^{i\mathbf{Q}\mathbf{x}_i} \,, \qquad (2.85)$$

where $\mathbf{x}_i$ are the sites of the lattice and $\mathbf{Q}$ is the antiferromagnetic wave-vector $\mathbf{Q} = (\pi, \pi)$. Hence bipartite lattices can be divided into two sub-lattices A and B according to

$$e^{i\mathbf{Q}\mathbf{x}_i} = \begin{cases} 1 & : \quad \mathbf{x}_i \in \mathrm{A} - \text{sub-lattice} \\ -1 & : \quad \mathbf{x}_i \in \mathrm{B} - \text{sub-lattice} \end{cases} . \tag{2.86}$$

Fig. 2.10 illustrates this schematically. The magnetic ordering reduces the trans-

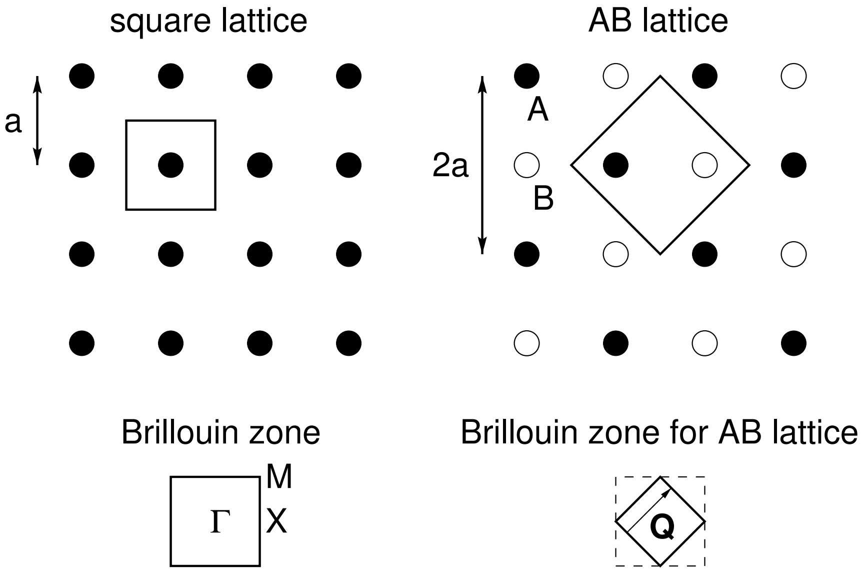

FIGURE 2.10: *Sketch of the square lattice and the AB-lattice with lattice constants a and $2a$ and its respective unit cells. The volume of the magnetic BZ (bottom, right) is reduced to one-half of the volume of the BZ in the paramagnetic state (bottom, left) and $\mathbf{Q} = (\pi, \pi)$ becomes a reciprocal lattice vector.*

lational symmetry of the original lattice. Hence the volume of the magnetic unit cell (right hand side) is doubled as compared to the structural unit cell (left hand side). The volume of the first BZ in the antiferromagnetic state is consequently reduced to half the original volume and $\mathbf{Q} = (\pi, \pi)$ becomes a reciprocal lattice vector. Hence, in neutron scattering experiments Bragg peaks are found at the wave-vector $\mathbf{Q}$ corresponding to a period of two lattice spacings. As a consequence the correlation function

$$F_\sigma^{\mathbf{Q}}(\mathbf{k}, z) = \langle\langle c_{\mathbf{k}\sigma}\, ;\, c^\dagger_{\mathbf{k}+\mathbf{Q}\sigma} \rangle\rangle_z \tag{2.87}$$

is finite in the antiferromagnetic state. It is important to stress that $F_\sigma^{\mathbf{Q}}(\mathbf{k}, z)$ is off-diagonal in $\mathbf{k}$ indicated by the index $\mathbf{Q}$. The second argument $\mathbf{k} + \mathbf{Q}$ was dropped for convenience. The strategy to deal with finite values for this correlation function can be easily adopted from the formalism in the superconducting state: Spinors are introduced

$$\Psi^\dagger_{\mathbf{k}\sigma} := \left(c^\dagger_{\mathbf{k}\sigma}\,,\, c^\dagger_{\mathbf{k}+\mathbf{Q}\sigma}\right) \quad , \quad \Psi_{\mathbf{k}\sigma} := \begin{pmatrix} c_{\mathbf{k}\sigma} \\ c_{\mathbf{k}+\mathbf{Q}\sigma} \end{pmatrix}, \tag{2.88}$$

along with the corresponding Green function matrix

$$\mathbf{G}_\sigma(\mathbf{k}, z) = \langle\langle \Psi_{\mathbf{k}\sigma}\,;\, \Psi^\dagger_{\mathbf{k}\sigma}\rangle\rangle_z = \begin{pmatrix} G_\sigma(\mathbf{k}, z) & F^{\mathbf{Q}}_\sigma(\mathbf{k}, z) \\ F^{\mathbf{Q}}_\sigma(\mathbf{k}+\mathbf{Q}, z) & G_\sigma(\mathbf{k}+\mathbf{Q}, z) \end{pmatrix} \tag{2.89}$$

to account for the symmetry breaking. Within the DCA spirit the self-energy matrix

$$\mathbf{\Sigma}_\sigma(\mathbf{K}, z) = \begin{pmatrix} \Sigma_\sigma(\mathbf{K}, z) & S^{\mathbf{Q}}_\sigma(\mathbf{K}, z) \\ S^{\mathbf{Q}}_\sigma(\mathbf{K}+\mathbf{Q}, z) & \Sigma_\sigma(\mathbf{K}+\mathbf{Q}, z) \end{pmatrix} \tag{2.90}$$

is a function of the cluster $\mathbf{K}$-points only. Σ_σ represents the part of the self-energy diagonal in $\mathbf{K}$ and $S^{\mathbf{Q}}_\sigma$ the off-diagonal part with a non-vanishing contribution for momenta $\mathbf{K}$ and $\mathbf{K}+\mathbf{Q}$. The second argument $\mathbf{K}+\mathbf{Q}$ in $S^{\mathbf{Q}}_\sigma$ was again omitted for convenience. The matrix-elements of $\mathbf{G}_\sigma$ (Eq. (2.89)) then read

$$G_\sigma(\mathbf{k}, z) \;=\; z - (\epsilon_{\mathbf{k}} - \mu) - \Sigma_\sigma(\mathbf{K}, z) \tag{2.91}$$

$$F^{\mathbf{Q}}_\sigma(\mathbf{k}, z) \;=\; -S^{\mathbf{Q}}_\sigma(\mathbf{K}, z)\,, \tag{2.92}$$

where $\mathbf{K}$ is the cluster momentum representing the cell containing $\mathbf{k}$. After coarse graining the Green function over the cells

$$\bar{\mathbf{G}}_\sigma(\mathbf{K}, z) = \frac{N_c}{N}\sum_{\mathbf{k}'} \mathbf{G}(\mathbf{K}+\mathbf{k}', z) = \begin{pmatrix} \bar{G}_\sigma(\mathbf{K}, z) & \bar{F}^{\mathbf{Q}}_\sigma(\mathbf{K}, z) \\ \bar{F}^{\mathbf{Q}}_\sigma(\mathbf{K}+\mathbf{Q}, z) & \bar{G}_\sigma(\mathbf{K}+\mathbf{Q}, z) \end{pmatrix} \tag{2.93}$$

the effective medium Green function $\mathcal{G}_\sigma$ is obtained by solving the inverse Dyson equation

$$\mathcal{G}^{-1}(\mathbf{K}, z) \;=\; \bar{\mathbf{G}}^{-1}_\sigma(\mathbf{K}, z) + \mathbf{\Sigma}_\sigma(\mathbf{K}, z) \tag{2.94}$$

$$= \begin{pmatrix} z - (\bar{\epsilon}_{\mathbf{K}} - \mu) & 0 \\ 0 & z - (\bar{\epsilon}_{\mathbf{K}+\mathbf{Q}} - \mu) \end{pmatrix} - \mathbf{\Gamma}_\sigma(\mathbf{K}, z)\,,$$

where the host function matrix $\mathbf{\Gamma}_\sigma$

$$\mathbf{\Gamma}_\sigma(\mathbf{K}, z) = \begin{pmatrix} \Gamma_\sigma(\mathbf{K}, z) & \Omega^{\mathbf{Q}}_\sigma(\mathbf{K}, z) \\ \Omega^{\mathbf{Q}}_\sigma(\mathbf{K}+\mathbf{Q}, z) & \Gamma_\sigma(\mathbf{K}+\mathbf{Q}, z) \end{pmatrix}. \tag{2.95}$$

is a matrix in Nambu space. As a consequence of the reduced translational symmetry in the antiferromagnetic state, the host-function $\mathbf{\Gamma}_\sigma$ contains processes connecting the momenta $\mathbf{K}$ and $\mathbf{K}+\mathbf{Q}$ represented by the off-diagonal part $\Omega_\sigma^{\mathbf{Q}}$ in addition to the $\mathbf{K}$-diagonal processes described by the diagonal part Γ_σ. The existence of $\mathbf{K}$-non-diagonal elements in the correlation functions between momenta $\mathbf{K}$ and $\mathbf{K}+\mathbf{Q}$ puts a constraint on possible choices for the selection of the cluster $\mathbf{K}$ points within the first BZ. For a chosen momentum point $\mathbf{K}$ the cluster point $\mathbf{K}+\mathbf{Q}$ has to be part of the selected set, too. This is always established by taking the canonical set of $\mathbf{K}$-points, i.e. the crystal momenta of the corresponding periodic cluster in real space: $K_n^l = \pi(2n_l/L-1)$, where n_l is an integer, $1 \le n_l \le L$, and l indicates the spatial direction. Another consequence is that the presence of incommensurate ordering described by wave-vectors $\mathbf{q} \neq \mathbf{Q}$ but close to $\mathbf{Q}$ cannot be distinguished by this algorithm, since the resolution of the dynamical quantities in $\mathbf{k}$-space is limited to the resolution set by the cluster $\mathbf{K}$-points.

This algorithm requires the calculation of the self-energy at least at two $\mathbf{k}$-points in the first BZ, $\mathbf{K}$ and $\mathbf{K}+\mathbf{Q}$. Hence, since the self-energy $\Sigma(z)$ in the DMFA ($N_c = 1$) is purely local, i.e. does not have any $\mathbf{k}$-dependence, the cluster size $N_c = 1$ cannot be treated within this scheme. The treatment of antiferromagnetism within the DMFA requires modifications of the DMFA equations in real space using the AB-lattice structure in the AF phase. App. C.3 presents this extension.

The order parameter m which signals the presence of antiferromagnetic ordering is given by the sub-lattice magnetization on e.g. the A-sub-lattice

$$m := |m_A| = |n_{A\uparrow} - n_{A\downarrow}| \,, \tag{2.96}$$

where $n_{A\sigma} = \langle n_{i\sigma}\rangle$ for $\mathbf{x}_i \in$ A-sub-lattice. To calculate the latter, Green functions have to be defined which act on a given sub-lattice A or B only. To this end, the operators

$$c^\dagger_{A/B\mathbf{k}\sigma} = \frac{1}{\sqrt{2}}(c^\dagger_{\mathbf{k}\sigma} \pm c^\dagger_{\mathbf{k}+\mathbf{Q}}) \quad , \quad c_{A/B\mathbf{k}\sigma} = \frac{1}{\sqrt{2}}(c_{\mathbf{k}\sigma} \pm c_{\mathbf{k}+\mathbf{Q}}) \tag{2.97}$$

are introduced for momenta $\mathbf{k}$ within the reduced BZ. By taking the Fourier-transform it can easily be shown that $c^\dagger_{A/B\mathbf{k}\sigma}$ ($c_{A/B\mathbf{k}\sigma}$) act on a given (A or B) sub-lattice only. The corresponding Green functions

$$\begin{aligned} G^A_\sigma(\mathbf{k},z) &= \langle\langle c_{A\mathbf{k}\sigma}\,;\, c^\dagger_{A\mathbf{k}\sigma}\rangle\rangle_z = & (2.98)\\ &= \frac{1}{2}\left[G_\sigma(\mathbf{k},z) + G_\sigma(\mathbf{k}+\mathbf{Q},z) + F^{\mathbf{Q}}_\sigma(\mathbf{k},z) + F^{\mathbf{Q}}_\sigma(\mathbf{k}+\mathbf{Q},z)\right] \\ G^B_\sigma(\mathbf{k},z) &= \langle\langle c_{B\mathbf{k}\sigma}\,;\, c^\dagger_{B\mathbf{k}\sigma}\rangle\rangle_z = & (2.99)\\ &= \frac{1}{2}\left[G_\sigma(\mathbf{k},z) + G_\sigma(\mathbf{k}+\mathbf{Q},z) - F^{\mathbf{Q}}_\sigma(\mathbf{k},z) - F^{\mathbf{Q}}_\sigma(\mathbf{k}+\mathbf{Q},z)\right] \end{aligned}$$

with G_σ and $F_\sigma^{\mathbf{Q}}$ defined in Eqs. (2.91) and (2.92) act on a given sub-lattice only. The order parameter m (Eq. (2.96)) is then obtained from

$$m = -\frac{1}{\pi}\frac{1}{N_c}\sum_{\mathbf{K}\sigma}\int\limits_{-\infty}^{+\infty} \mathrm{d}\varepsilon\,\sigma \mathrm{Im}\,\bar{G}_\sigma^A(\mathbf{K},\varepsilon)\,, \tag{2.100}$$

with the coarse grained average $\bar{G}_\sigma^A(\mathbf{K}) = N_c/N\sum_{\mathbf{k}'} G_\sigma^A(\mathbf{K}+\mathbf{k}')$. Due to the additional symmetry relation in the antiferromagnetic state

$$G_\sigma^A = G_{\bar{\sigma}}^B \tag{2.101}$$

the magnetization on the B-sub-lattice $m_B = -m_A$. Since $G_\sigma(\mathbf{k},z)$ is defined on the full lattice, it is an averaged function with respect to the spin index and therefore does not depend on the spin σ in the antiferromagnetic state. With the symmetry relation (2.101) and Eqs. (2.98) and (2.99) it then follows that

$$F_\sigma^{\mathbf{Q}} = -F_{\bar{\sigma}}^{\mathbf{Q}} \tag{2.102}$$

and hence the spin index can be dropped in the actual calculation. However, by imposing the symmetry (2.101) one allows for antiferromagnetic ordering only, described by the wave-vector $\mathbf{Q}$ and the possibility for incommensurate ordering is eliminated.

Generalized cluster-NCA in the antiferromagnetic phase

App. C.2 presents a detailed discussion of the cluster-NCA algorithm in the antiferromagnetically ordered phase. The strategy can be easily adopted from the treatment of superconductivity. Again non-diagonal elements in the resolvent are essential for handling the symmetry breaking. Here the off-diagonal parts $\Omega_\sigma^{\mathbf{Q}}$ of the host function matrix $\mathbf{\Gamma}_\sigma$ in the antiferromagnetic state connect states on the cluster with momenta $\mathbf{K}$ and $\mathbf{K}+\mathbf{Q}$ and diagrams of the type

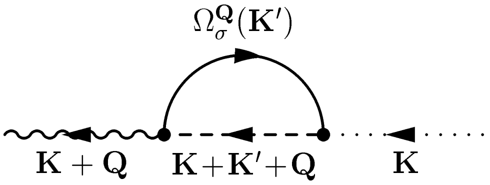

have to be included. In close analogy to the treatment of superconductivity, spinors

$$\Psi_{f\mathbf{K}\sigma}^\dagger = (f_{\mathbf{K}\sigma}^\dagger, f_{\mathbf{K}+\mathbf{Q}\sigma}^\dagger) \quad , \quad \Psi_{f\mathbf{K}\sigma} := \begin{pmatrix} f_{\mathbf{K}\sigma} \\ f_{\mathbf{K}+\mathbf{Q}\sigma} \end{pmatrix} \tag{2.103}$$

are introduced for the cluster operators $f_{\mathbf{K}\sigma}$ to conveniently handle the symmetry breaking. The diagrammatic form for the resolvent self-energy Σ^R is then formally identical to the one in the superconducting phase (see Fig. 2.9). However the curved Fermion lines now represent the host function matrix $\mathbf{\Gamma}_\sigma$ for the antiferromagnetic state defined in Eq. (2.95) and adequate matrices $\sigma_o \mathbf{F}^{\mathbf{K}\sigma}_{mn}$ and $(\mathbf{F}^{\mathbf{K}\sigma}_{mn})^\dagger \sigma_o$ for the antiferromagnetic state have to be applied to the vertices. Here the vectors

$$(\mathbf{F}^{\mathbf{K}\sigma}_{mn})^\dagger = \langle n|\Psi^\dagger_{f\mathbf{K}\sigma}|m\rangle \quad , \quad \mathbf{F}^{\mathbf{K}\sigma}_{mn} = \langle m|\Psi_{f\mathbf{K}\sigma}|n\rangle \, , \tag{2.104}$$

account for $\mathbf{K}$-diagonal and non-diagonal processes. The analytical expression is then found to read (see App. C.2, Eq. (C.49))

$$\begin{aligned}\Sigma^R_{mn}(z) \;=\; & -\frac{1}{\pi}\sum_{\mathbf{K}\sigma}\sum_{l,l'}\Bigg\{ \qquad (2.105)\\ & \int\limits_{-\infty}^{+\infty} \mathrm{d}\varepsilon\,[\mathbf{F}^{\mathbf{K}\sigma}_{ml}]^T \sigma_o f(\varepsilon)\sigma_o \mathrm{Im}\,\mathbf{\Gamma}(\mathbf{K},\varepsilon)\sigma_o \bar{R}_{ll'}(z+\varepsilon)\sigma_o[(\mathbf{F}^{\mathbf{K}\sigma}_{nl'})^\dagger]^T \\ & + \int\limits_{-\infty}^{+\infty} \mathrm{d}\varepsilon\,(\mathbf{F}^{\mathbf{K}\sigma}_{lm})^\dagger \sigma_o f(-\varepsilon)\sigma_o \mathrm{Im}\,\mathbf{\Gamma}(\mathbf{K},\varepsilon)\sigma_o \bar{R}_{ll'}(z-\varepsilon)\sigma_o \mathbf{F}^{\mathbf{K}\sigma}_{l'n}\Bigg\} \, .\end{aligned}$$

The matrix-elements of the resolvent $\bar{R}$ (see B.24) are then used to calculate the cluster Green function in the antiferromagnetic state

$$\mathbf{G}_\mathrm{c}(\mathbf{K},z) = \langle\langle \Psi_{f\mathbf{K}\sigma};\Psi^\dagger_{f\mathbf{K}\sigma}\rangle\rangle_z \, . \tag{2.106}$$

By expanding the Nambu spinors $\Psi_{f\mathbf{k}\sigma}$ $(\Psi^\dagger_{f\mathbf{K}\sigma})$ in terms of the Hubbard-operators X_{mn} (see App. C.3, Eq. (C.47)), $\mathbf{G}_\mathrm{c}$ can be written as

$$\mathbf{G}_\mathrm{c}(\mathbf{K},z) = \sum_{\substack{m,m'\\ n,n'}} \mathbf{F}^{\mathbf{K}\sigma}_{mm'}(\mathbf{F}^{\mathbf{K}\sigma}_{nn'})^\dagger \langle\langle X_{mm'};X_{n'n}\rangle\rangle_z \, , \tag{2.107}$$

where the correlation function $\langle\langle X_{mm'};X_{n'n}\rangle\rangle_z$ is given by Eq. (2.58). As in the superconducting state, the non-diagonal elements of the resolvent are needed for a non-vanishing cluster $\mathbf{K}$-off-diagonal part of $\mathbf{G}_c$.

2.7 DCA for the tJ-model

Since the projected operators $\tilde{c}_{i\sigma}$ (1.6) used in the tJ-model (Eq. (1.5)) do not obey standard Fermionic commutation relations, the conventional Feynman diagram technique cannot be used for a perturbative expansion and the diagrammatic motivation for the DCA presented in Sec. 2.3.1 cannot be applied to the tJ-model. However the spirit of the DCA, i.e. the approximation of the full lattice self-energy $\Sigma(\mathbf{k},z)$ by a cluster self-energy $\Sigma(\mathbf{K},z)$ can also be applied to the tJ-model. To this end, the Green function for the Fermions in the tJ-model $G(\mathbf{k}, z) = \langle\langle \tilde{c}_{\mathbf{k}\sigma}; \tilde{c}^{\dagger}_{\mathbf{k}\sigma} \rangle\rangle_z$, with the projected operators $\tilde{c}^{\dagger}_{\mathbf{k}\sigma}$ and $\tilde{c}_{\mathbf{k}\sigma}$ being Fourier transforms of the operators $\tilde{c}^{\dagger}_{i\sigma}$ and $\tilde{c}_{i\sigma}$ defined in Eq. (1.6), is written as

$$G(\mathbf{k}, z) = \frac{1}{z - \epsilon_{\mathbf{k}} + \mu - \Sigma(\mathbf{K}, z)}\,, \tag{2.108}$$

where the full lattice self-energy $\Sigma(\mathbf{k}, z)$ was already replaced by the cluster self-energy $\Sigma(\mathbf{K}, z)$ where $\mathbf{K}$ represents the cell containing $\mathbf{k}$. It should be remarked that one has some ambiguity in defining the self-energy. The fact that the projected operators (1.6) act on a reduced Hilbert space, with only empty and singly occupied sites, leads to a modified sum rule (usually normalized to unity) for the spectral function

$$-\frac{1}{\pi}\frac{1}{N}\sum_{\mathbf{k}}\int_{-\infty}^{+\infty} \mathrm{d}\omega\, \mathrm{Im}\, G(\mathbf{k}, \omega) = \alpha < 1\,. \tag{2.109}$$

Therefore an alternative definition of Σ would be to replace the nominator in Eq. (2.108) by α. However, to retain the usual definition of quasiparticle parameters, the form (2.108) is used here. Nevertheless it is important to stress that in the tJ-model Σ describes both the effects of the prohibition of double occupancy and the renormalizations due to the nonlocal spin interaction J. Then, in analogous fashion to the Hubbard model, $G(\mathbf{k}, z)$ is coarse grained over the DCA cells by using Eq. (2.24) and the coarse grained Green function is finally written in the form (2.25), which defines the parameters of the corresponding cluster Hamiltonian for the tJ-model.

So far the strategy is entirely equivalent to the treatment of the Hubbard model. The major difference to the latter lies in the presence of the intersite interaction J. Within the DMFA ($N_c = 1$) it can be shown [Mül89] that nonlocal interactions reduce to a mean field term, e.g. in the case of the tJ-model to $J\sum_i S^z_i h^{\mathrm{MF}}_i$ (see Eq. (2.3)). Thus, in the paramagnetic phase, the effect of the nonlocal interaction J is zero since the mean field $h^{\mathrm{MF}}_i \propto \langle S^z_i \rangle$ vanishes. For cluster sizes $N_c > 1$ however, nonlocal interactions should be accurately represented on the cluster and may be reduced to the mean field term between sites on the cluster and sites in the effective medium. In order to setup the corresponding cluster model, it is necessary to transform the tJ-Hamiltonian (Eq. (1.5)) to the reciprocal space where the DCA is defined on. Using the Fourier transform of the spin operators $\vec{S}_i$ (Eq. (1.7)),

$$\vec{S}(\mathbf{k}) = \frac{1}{2}\sum_{\mathbf{q}}\sum_{\alpha\beta} \tilde{c}^{\dagger}_{\mathbf{q}\alpha}\vec{\sigma}_{\alpha\beta}\tilde{c}_{\mathbf{q}+\mathbf{k}\beta}\,, \tag{2.110}$$

and the Fourier transform of the interaction J, $J(\mathbf{k}) = 2J(\cos k_x + \cos k_y)$, the tJ-Hamiltonian in $\mathbf{k}$-space reads

$$H_{tJ} = \sum_{\mathbf{k}\sigma} \epsilon_{\mathbf{k}} \tilde{c}^{\dagger}_{\mathbf{k}\sigma} \tilde{c}_{\mathbf{k}\sigma} + \sum_{\mathbf{k}} J(\mathbf{k}) \left[\vec{S}(-\mathbf{k}) \vec{S}(\mathbf{k}) - \frac{1}{4} \tilde{\rho}(-\mathbf{k}) \tilde{\rho}(\mathbf{k}) \right] . \tag{2.111}$$

The corresponding density operators in $\mathbf{k}$-space $\tilde{\rho}(\mathbf{k}) = \sum_{\mathbf{q}\sigma} \tilde{c}^{\dagger}_{\mathbf{q}\sigma} \tilde{c}_{\mathbf{q}+\mathbf{k}\sigma}$.

In analogous fashion to the Hubbard model (see Sec. 2.4), the cluster Hamiltonian for the tJ-model is then defined by reducing the set of $\mathbf{k}$-points onto the cluster $\mathbf{K}$-points and accounting for the remaining degrees of freedom by adding a coupling to an auxiliary medium term. The total cluster Hamiltonian then reads

$$H^{tJ}_{\text{cluster}} = H^{tJ}_{\text{loc}} + H^{tJ}_{\text{hyb}} + H_{\text{med}} , \tag{2.112}$$

where the auxiliary medium term H_{med} is the same as for the Hubbard model and given by Eq. (2.44) for the paramagnetic state or by the extensions (Eq. (C.1)) for the superconducting state and (Eq. (C.33)) for the antiferromagnetic phase, respectively. The local part is given by

$$H^{tJ}_{\text{loc}} = \sum_{\mathbf{K}\sigma} (\bar{\epsilon}_{\mathbf{K}} - \mu) \tilde{f}^{\dagger}_{\mathbf{K}\sigma} \tilde{f}_{\mathbf{K}\sigma} + \sum_{\mathbf{K}} \bar{J}(\mathbf{K}) (\vec{S}_f(-\mathbf{K}) \vec{S}_f(\mathbf{K}) - \frac{1}{4} \tilde{\rho}_f(-\mathbf{K}) \tilde{\rho}_f(\mathbf{K})) , \tag{2.113}$$

where the projected operators $\tilde{f}^{\dagger}_{\mathbf{K}\sigma}$ ($\tilde{f}_{\mathbf{K}\sigma}$) create (destroy) Fermions on the cluster with momentum $\mathbf{K}$ and spin σ, without producing double occupancy and the corresponding spin operators $\vec{S}_f(\mathbf{K})$ are given by Eq. (2.110) with the c-operators replaced by f-operators. Since the interaction J is nonlocal it is coarse grained

$$\bar{J}(\mathbf{K}) = \frac{N_c}{N} \sum_{\mathbf{k}'} J(\mathbf{K} + \mathbf{k}') , \tag{2.114}$$

where the sum runs over the N/N_c momenta within the cell about the cluster momentum $\mathbf{K}$. The coupling to the medium is described by the hybridization term

$$H^{tJ}_{\text{hyb}} = \frac{1}{\sqrt{N}} \sum_{\mathbf{K},\mathbf{k}',\sigma} (V_{\mathbf{K},\mathbf{k}'} \tilde{f}^{\dagger}_{\mathbf{K}\sigma} a_{\mathbf{K}+\mathbf{k}'\sigma} + \text{h.c.}) , \tag{2.115}$$

with the auxiliary operators $a_{\mathbf{k}\sigma}$ simulating the effective medium. Eq. (2.115) yields the same form (2.46) for the hybridization function $\Gamma_c(\mathbf{K})$. The first term in Eq. (2.113) is equivalent to the corresponding local part of the cluster Hamiltonian for the Hubbard model (Eq. (2.42)) for $U = \infty$. The second term introduces an additional nonlocal interaction J on the cluster, which has no equivalent term in the Hubbard model. However, since the local part is diagonalized within the NCA approach to the cluster problem, the effects of this term are implicitly contained in the cluster eigenstates and eigenenergies and this term needs no further attention. After diagonalizing the local part (2.113), the actual NCA algorithm to solve the cluster problem is identical to the scheme developed for the Hubbard model (see Sec. 2.5 for the paramagnetic state and Sec. 2.6 for symmetry broken phases). However, the transition matrix elements $F_{mn}^{\mathbf{K}\sigma}$ between eigenstates $\langle m|$ and $|n\rangle$ (see Eq. (2.51)) have to be replaced by $F_{mn}^{\mathbf{K}\sigma} = \langle m|\tilde{f}_{\mathbf{K}\sigma}|n\rangle$.

It should be noted that in order to diagonalize the Hamiltonian (2.113), it is useful to perform a Fourier transformation to its real space analogon first. There, the prohibition of double occupancy can be handled easier by just omitting states with doubly occupied sites. The transition matrix elements $F_{mn}^{\mathbf{K}\sigma}$ in $\mathbf{K}$-space are then easily obtained by taking the Fourier transform of the corresponding matrix elements in real space.

2.8 Technical details

2.8.1 Cluster size and choice of cluster K-points

The cluster size N_c, which can be handled by the presented DCA-NCA algorithm presented in Chapter 2 is limited by the NCA procedure to solve the effective cluster problem. The total number of cluster eigenstates (see Sec. 2.5) scales with the cluster size N_c like 4^{N_c}. The large number of eigenstates (256 for the 2x2 cluster ($N_c = 4$)) results in an expensive numerical calculation. The complexity of the problem can be reduced by imposing the symmetries of the cluster Hamiltonian (2.41). In the paramagnetic phase the spin index can be dropped due to the spin-rotational symmetry of the cluster Hamiltonian (2.41). A further reduction in complexity can be achieved by using the point-group symmetries of the cluster. However, this depends strongly on the choice of the cluster momenta $\mathbf{K}$ within the first Brillouin zone. A priori, there is no restriction in the choice of the cluster momenta $\mathbf{K}$ within the first Brillouin-zone, since in the derivation of the DCA algorithm no special assertion about the cluster $\mathbf{K}$-points was made. One e.g. could choose all $\mathbf{K}$-momenta to lie on the Fermi surface. However, to identify eigenstates which are degenerate due to the geometric symmetry, one has to classify the eigenstates according to the cluster momenta $\mathbf{K}$. Since the cluster Hamiltonian (2.41) conserves the cluster momentum, its many-particle eigenstates can be classified according to their total momentum, which is just the sum of the momenta of the participating one particle states. This approach restricts the freedom in choosing the cluster momenta $\mathbf{K}$ to exactly one possibility. The only set of cluster momenta $\mathbf{K}$ which form a group under addition is $K_n^l = \pi(2n_l/L - 1)$, where n_l is an integer, $1 \leq n_l \leq L$ and l indicates the spatial direction. In particular for two dimensions and $N_c = 4$ the cluster momentum points are given by the set

$$\{(0,0);(\pi,0);(0,\pi);(\pi,\pi)\}\,, \tag{2.116}$$

which is illustrated in Fig. 2.3. This set corresponds to periodic boundary conditions for the real space analogon of the cluster. With this choice of the cluster momenta the eigenstates can be classified according to their total particle number n_c, total momentum $\mathbf{K}$, total spin S and z-component of the spin S^z. The degeneracy in the cluster momentum points $(0,\pi)$ and $(\pi,0)$ and the spin-symmetry finally lead to an effective number of 123 non-degenerate eigenstates which have to be considered in the paramagnetic phase. Then, effectively only resolvents for eigenstates with different energies occur in the actual calculations.

The question of which symmetries can still be imposed in symmetry broken phases is related to the symmetry of the order parameter describing these phases. The spin-symmetry can still be imposed in the superconducting phase but not in the antiferromagnetic state since the off-diagonal parts $\Omega_\sigma^{\mathbf{Q}}(\mathbf{K})$ of the effective medium become spin dependent (see Sec. 2.6.3). The situation is more involved in case of the geometric symmetry between $\mathbf{K} = (\pi,0)$ and $(0,\pi)$. In the antiferromagnetic state the cluster states with momenta $(\pi,0)$ and $(0,\pi)$ are still degenerate. But due to the off-diagonal parts of the host function $\mathbf{\Gamma}$ that couple states with a momentum difference of $\mathbf{Q} = (\pi,\pi)$, states with the momenta $(\pi,0)$ and $(0,\pi)$ need to be separately taken into account for the calculation of the resolvent self-energy (see Eq. (2.105)). The superconducting phase on the other hand is described by the order parameter $\Delta_{\mathbf{k}}$ (Eq. (2.66)). If the symmetry of $\Delta_{\mathbf{k}}$ is lower than the lattice symmetry, it may lift the degeneracy between $(\pi,0)$ and $(0,\pi)$ and the symmetry must not be imposed. Since in the DCA calculation no assumption is made a priori about the symmetry of the order parameter the geometric symmetry is not imposed in the actual calculation in the superconducting phase.

At this point it is instructive to inspect the spectrum of the bare cluster Hamiltonian H_{loc} (Eq.(2.42)) defined by the set of $\mathbf{K}$ points (Eq. (2.116)), the averaged dispersion (Eq. (2.26)) and the magnitude of the Coulomb repulsion U. The corresponding cluster density of states $N_c(\omega)$ is defined as

$$N_c(\omega) = \frac{1}{\Xi}\sum_{\mathbf{K}}\sum_{mn} |\langle m|f_{\mathbf{K}\sigma}|n\rangle|^2 \mathrm{e}^{-\beta E_n}(e^{\beta\omega}+1)\delta(\omega-(E_n-E_m))\,, \qquad (2.117)$$

where $\Xi = \mathrm{Tr}\,\mathrm{e}^{-\beta(H-\mu N)}$ is the grand canonical partition function and $|n\rangle$ are the eigenstates of the local part H_{loc} of the cluster Hamiltonian (2.41) with eigenenergies $\{E_n\}$. The spectrum consists of δ-functions located at frequencies given by the energy difference of the cluster eigenstates. Fig. 2.11 illustrates this quantity for the temperature $T = 0.4t$ and $t' = 0$ for two values of the Coulomb repulsion, $U = 4t$ (top), well below the bandwidth of the non-interacting system $W = 8t$, and $U = 12t$, larger than W. The δ-functions of Eq. (2.117) were replaced by Lorentzians with a finite width $\tau = 0.1t$. One notices two separated bands at $\omega = \pm U/2$ for large U (bottom), which merge into one broad band when U is less than the bandwidth (top).

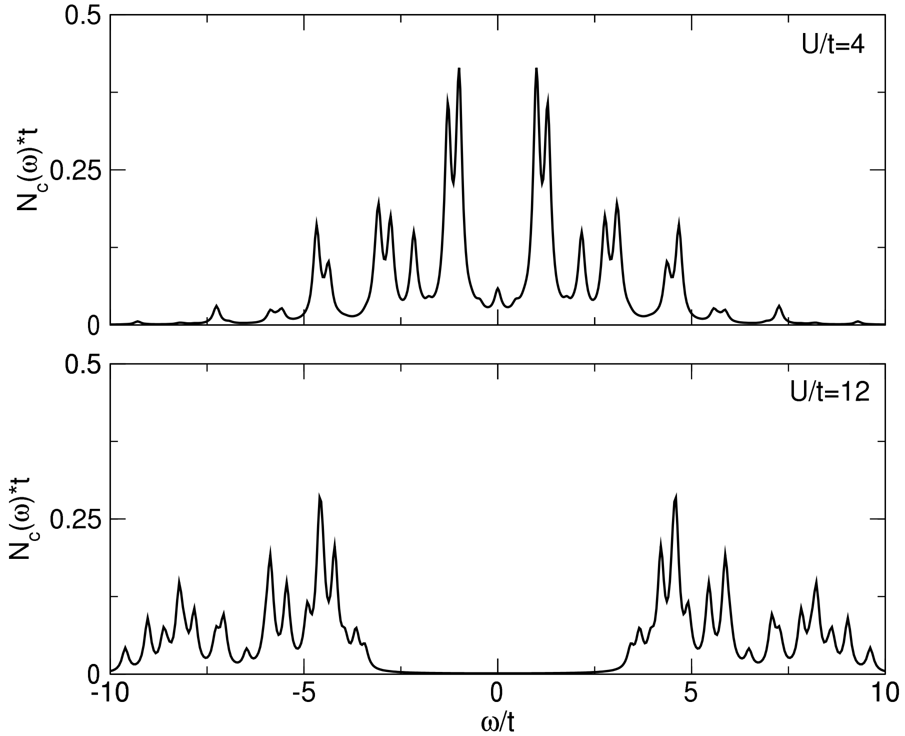

FIGURE 2.11: *The density of states of the bare periodic cluster for the set of* $\mathbf{K}$*-points (Eq. (2.116)) when* $U = 4t$ *(top) and* $U = 12t$ *(bottom) at half filling.*

As a first approximation, this result contains already the gross features that are expected for the spectrum of the Hubbard model. It will be particularly interesting, how the coupling to the self-consistently determined host Γ will affect these spectra.

The remaining numerical task of calculating the coupled equations (2.53) and (2.56) or the corresponding equations in symmetry broken phases self-consistently becomes formidable as the cluster size increases. Although the study of larger cluster sizes is in principle possible, presently this restricts the DCA-NCA calculations to a cluster size of $N_c = 4$. Also the evaluation of two-particle correlation functions is formally possible, but for cluster sizes $N_c > 1$ still beyond present numerical possibilities. Hence the calculations presented are limited to the evaluation of one-particle properties.

2.8.2 Interpolation of the cluster self-energy

The following sections present results for local single-particle spectra as well as for the band-structure in form of $\mathbf{k}$-resolved spectra. Since within the DCA the self-energy $\Sigma(\mathbf{K})$ is calculated at selected cluster-momenta $\mathbf{K}$ only, $\Sigma(\mathbf{K})$ is a step function in $\mathbf{k}$-space, i.e. a constant within the coarse graining cell containing

$\mathbf{K}$. In order to obtain smooth nonlocal spectra, the cluster result needs to be interpolated onto the full lattice BZ. As discussed in the causality paragraph in Sec. 2.3.2, performing the interpolation within the iteration procedure may violate causality. Therefore, the converged result is taken to be interpolated by a suitable scheme, which preserves the causality of the DCA result for the cluster self-energy $\Sigma(\mathbf{K})$. Bilinear interpolation[6] produces a causal result independently of the choice of the cluster $\mathbf{K}$-points, but leads to kinks at the cluster $\mathbf{K}$-points. A smoother way of interpolating the cluster result is obtained by using trigonometric functions[7]

$$\begin{aligned}\Sigma(k_x, k_y) = \; & \tfrac{1}{4}(\bar{\Sigma}(0,0) - \bar{\Sigma}(\pi,\pi))(\cos k_x + \cos k_y) \\ & + \tfrac{1}{4}(\bar{\Sigma}(0,0) - \bar{\Sigma}(\pi,0) - \bar{\Sigma}(0,\pi) + \bar{\Sigma}(\pi,\pi)) \cos k_x \cos k_y \\ & + \tfrac{1}{4}(\bar{\Sigma}(0,\pi) - \bar{\Sigma}(\pi,0))(\cos k_x - \cos k_y) \\ & + \tfrac{1}{4}(\bar{\Sigma}(0,0) + \bar{\Sigma}(\pi,0) + \bar{\Sigma}(0,\pi) + \bar{\Sigma}(\pi,\pi)) \,.\end{aligned} \tag{2.118}$$

This interpolation scheme is not generally applicable, since it violates causality for a set of cluster $\mathbf{K}$-points which do not coincide with the maxima of the cosines. However it can be used for the choice (2.116). The first two terms and the last term in Eq. (2.118) have the (s-wave) symmetry of the lattice, with the prefactors given by the corresponding Fourier transforms to real space.[8] The third term with d-wave symmetry vanishes in the paramagnetic phase since the $\mathbf{K}$-points $(\pi, 0)$ and $(0, \pi)$ are degenerate and therefore the prefactor vanishes. However it may be finite in phases where the symmetry of the order parameter is lower than the symmetry of the lattice, e.g. in the d-wave superconducting state. After performing this interpolation angle resolved spectral functions and also Fermi surfaces may be calculated.

[6]Linear in two dimensions.

[7]The frequency argument in Σ is dropped for convenience.

[8]The prefactor of the sum of cosines in the first line is just the self-energy contribution between nearest neighbors, whereas the prefactor of the product of cosines in the second line is the self-energy contribution between next-nearest neighbors. The last constant term represents the local self-energy.

Chapter 3

Results

This section presents results for the two-dimensional (2D) Hubbard model obtained with the DCA. Additional results for the 2D tJ-model are used as a supplement wherever they can help to gain a deeper understanding. The following sections are organized as follows: A brief summary of already established results on the properties of the 2D Hubbard model is presented in Sec. 3.1. A detailed study of the DCA-NCA results for single-particle spectra in different parameter regions is presented in the following sections 3.2-3.4. Systematics on the evolution of nonlocal correlations, present in the $N_c = 4$ result but neglected when $N_c = 1$, are presented. The DCA phase-diagram in Sec. 3.5 summarizes these results.

3.1 Preliminary remarks

In this Chapter results for the Hubbard model (1.2) on a square lattice in two dimensions will be presented. The Hubbard model is characterized by the Coulomb repulsion U and the bare dispersion (1.4)

$$\epsilon_{\mathbf{k}} = \epsilon_o - 2t(\cos k_x + \cos k_y) - 4t' \cos k_x \cos k_y\,, \tag{3.1}$$

which includes the on-site energy ϵ_o, nearest neighbor hopping t and next-nearest neighbor hopping t'. Since this model has attracted much interest and therefore has already been widely studied, it is instructive to first discuss already established results to gain a deeper understanding of its actual properties.

For a comprehensive discussion of numerical work on the 2D Hubbard and tJ-model the reader is referred to [Dag94a]. The physics of the half-filled Hubbard model ($n := 1/N \sum_{i\sigma}\langle n_{i\sigma}\rangle = 1$) on a square lattice with only nearest neighbor hopping t is well understood. In the strong coupling regime where the Coulomb repulsion U is large compared to the bare bandwidth W ($U \gg W$) charge excitations involving doubly occupied sites can be integrated out and the resulting Hamiltonian corresponds to the tJ-model (see Sec. 1.2). In the half-filled case, the latter reduces to the 2D Heisenberg model (1.9) with antiferromagnetic spin interaction J, which has been extensively studied using several different analytical and numerical methods.[1] The results of these calculations indicate that the ground state of the 2D Heisenberg model has antiferromagnetic long-range order at zero temperature. The Mermin-Wagner theorem prevents the existence of long-range order in one- and two-dimensional models at finite temperatures if the spontaneously broken symmetry is continuous [Mer66, Hoh67].

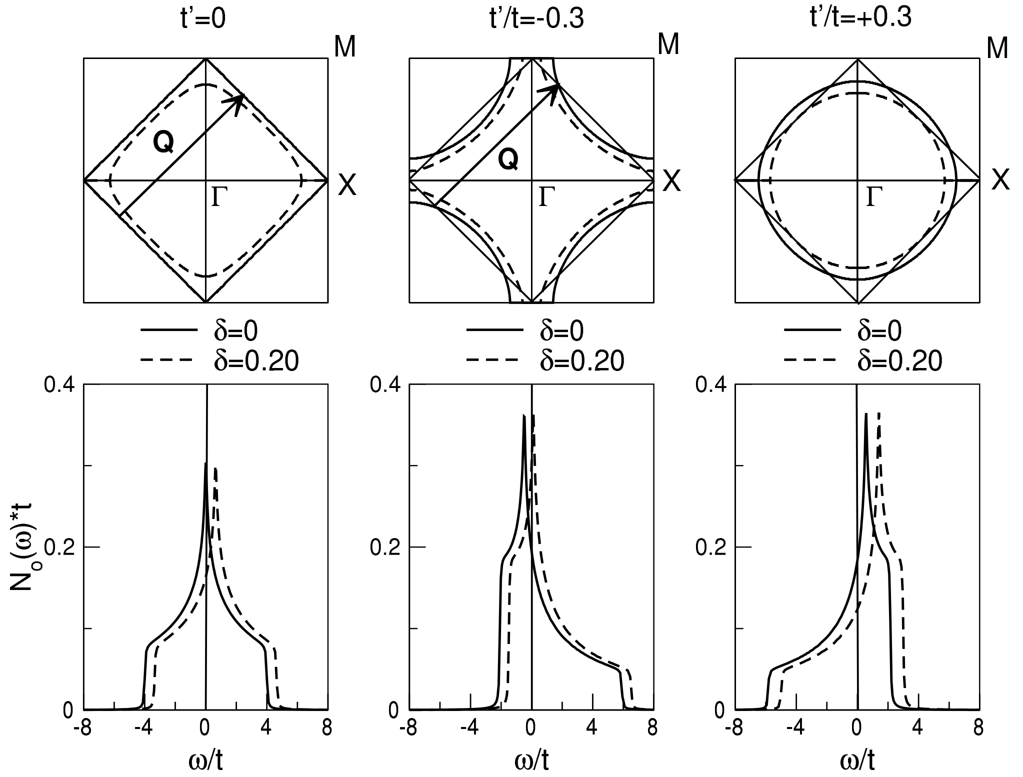

FIGURE 3.1: *The Fermi surface and density of states (DOS) $N_o(\omega)$ of the Hubbard model on a square lattice when $U = 0$ for different values of the next-nearest neighbor hopping t' when the doping $\delta = 0$ (solid line) and $\delta = 0.20$ (dashed line). For $t' = 0$ the Fermi surface is nested (all the points on the Fermi surface can be connected to other points on the Fermi surface by the antiferromagnetic wave-vector $\mathbf{Q} = (\pi, \pi)$). Finite values for t' as well as finite doping abolish the nesting condition by bending the Fermi surface and hence suppress antiferromagnetic correlations (The magnetic BZ boundary is depicted by the diagonal solid lines). Upon doping, the van-Hove singularity in the DOS moves away from the the Fermi surface, except when $t' < 0$.*

For small to intermediate couplings $U \lesssim W$, where double occupancy is al-

[1]For a compilation of references please see [Dag94a].

lowed, the half-filled Hubbard model on a square lattice still shows evidence of antiferromagnetic spin order at zero temperature. The tendency to antiferromagnetic order can be understood from a weak coupling point of view. For only nearest neighbor hybridization t on a square lattice the dispersion (3.1) fulfills the relation $\epsilon_{\mathbf{k}+\mathbf{Q}} = -\epsilon_{\mathbf{k}}$, where $\mathbf{Q}$ is the antiferromagnetic wave-vector $\mathbf{Q} = (\pi, \pi)$ which corresponds to a period of two lattice spacings (see Sec. 2.6.3). Thus, if $\mathbf{k}$ lies on the Fermi surface, $\mathbf{k} + \mathbf{Q}$ does too. This "perfect nesting" for $t' = 0$ is illustrated in Fig. 3.1, where the top row shows the Fermi surface of the non-interacting system ($U = 0$). Different regions on the Fermi surface can be connected by the antiferromagnetic wave-vector $\mathbf{Q}$. This Fermi surface is identical to the boundary of the magnetic BZ in the antiferromagnetically ordered state (see Fig. 2.10 in Sec. 2.6.3), where $\mathbf{Q}$ is a reciprocal lattice vector. There the M-point is identical to the Γ-point and states outside the reduced BZ but inside the full first BZ are shifted by $\mathbf{Q}$ into the reduced BZ. Fig. 3.2 illustrates this shifted bandstructure

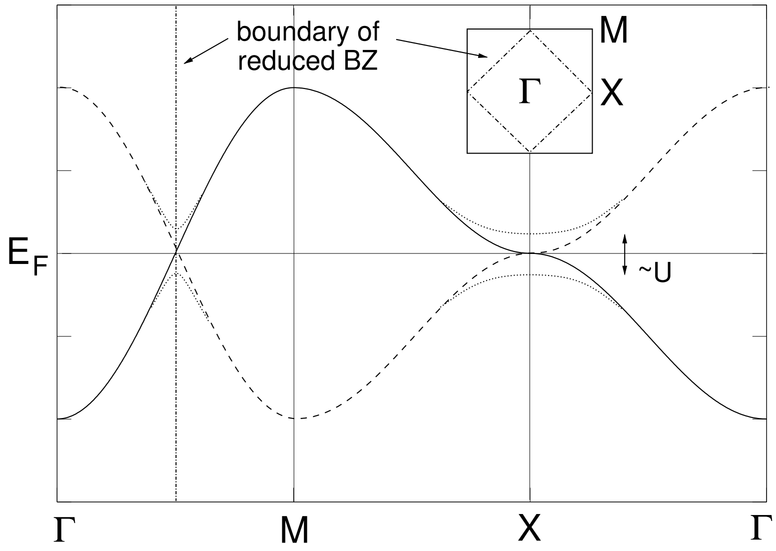

FIGURE 3.2: *Sketch of the back-folding of the bandstructure along the boundary of the reduced BZ (dashed dotted line). The band delineated by the dashed line originates in states of the full BZ shifted by* $\mathbf{Q}$*. The finite value of* U *distorts the bands near the Fermi energy* E_F *at the boundary of the reduced BZ and a gap* $\sim U$ *(indicated by the dotted line) opens at the Fermi surface.*

(dashed line), which due to the symmetries of the real lattice is obtained by back-folding the original bandstructure (solid line) along the boundary of the reduced BZ (indicated by the dash-dotted line). The occupied states completely fill up the BZ of the system with reduced translational symmetry since the Fermi surface is identical to magnetic BZ, i.e. it is nested. Every finite value of U will then lift the degeneracy of the states at the zone boundary of the reduced BZ (indicated by the dash-dotted line in Fig. 3.2) and hence lead to a stabilization of the state with reduced translational symmetry. As a consequence a gap (dotted line) of the order of U opens at the Fermi surface and the result is an antiferromagnetically ordered insulator.

There is evidence for an antiferromagnetic ground state of the 2D Hubbard model on the square lattice in various numerical studies [Hir85, Whi89a, Dag94a] as well as on the basis of a simple self-consistent mean field approach [Sch89]. It is therefore widely believed that the half-filled 2D Hubbard model has an antiferromagnetically ordered ground state at every finite coupling strength U. The actual state is referred to as spin density wave (SDW) state, since due to the finite coupling U the magnitude of the local moment is reduced from $1/2$.

Finite values for the next-nearest neighbor hopping integral t' deform the Fermi surface as illustrated in Fig. 3.1. As a consequence the antiferromagnetic correlations get suppressed, since the Fermi surface is not perfectly nested anymore. In real space this is equivalent to the fact that a finite t' frustrates the lattice by inducing virtual hopping processes between next-nearest neighbors in addition to the processes between nearest neighbors. Thus the resulting spin interaction $\propto {t'}^2/U$ between next-nearest neighbor sites frustrates the lattice and thus suppresses antiferromagnetism.

Another widely studied transition in the half-filled 2D Hubbard model, independent of the type of the underlying lattice, is the Mott-Hubbard transition, where the system undergoes a metal-insulator transition with increasing interaction strength U. Since this type of transition is not within the scope of this thesis, the interested reader is referred to the very detailed and comprehensive article by Imada et al. [Ima98].

For finite doping $\delta = 1 - n > 0$ numerical results agree on a strong suppression of antiferromagnetism with doping δ with incommensurate ordering in a finite interval of small doping levels. Sec. 3.2 will discuss the issue of antiferromagnetism in the framework of the DCA.

Motivated by the high-T_c cuprates strong numerical effort has also been devoted to the search of superconductivity in the doped 2D Hubbard model. The symmetry of the pairing state is characterized by the order parameter

$$\Delta_{\mathbf{k}} = \langle c_{\mathbf{k}\uparrow} c_{-\mathbf{k}\downarrow} \rangle \,. \tag{3.2}$$

Possible symmetries for the 2D system are illustrated in Table 3.1. Local pairing, corresponding to a s-wave order parameter is expected to be suppressed by the local Coulomb repulsion U. Relevant symmetries correspond to nonlocal order parameters with e.g. extended s-wave, $d_{x^2-y^2}$-wave, d_{xy}-wave or p-wave symmtry. Except for the p-wave symmetry, the corresponding pairing states are spin singlets since the corresponding order parameters have even spatial parity, i.e. $\Delta_{-\mathbf{k}} = \Delta_{\mathbf{k}}$. The p-wave symmetry of the order parameter is relevant for systems where the electrons are paired in spin-triplet states like e.g. in superfluid He-3.

Symmetries of $\Delta_\mathbf{k}$	
Symmetry	Order parameter $\Delta_\mathbf{k} \propto$
s-wave	const.
extended s-wave	$\cos k_x + \cos k_y$
$d_{x^2-y^2}$-wave	$\cos k_x - \cos k_y$
d_{xy}-wave	$\sin k_x \cdot \sin k_y$
p-wave	$a \sin k_x + b \sin k_y$

TABLE 3.1: *Possible symmetries for the superconducting order parameter $\Delta_\mathbf{k}$ in two dimensions.*

Perturbative self-consistent approximations for the 2D Hubbard model based on Feynman diagrams that describe the exchange of antiferromagnetic spin-fluctuations (FLEX) [Bic89, Mon94] are able to describe a transition to a superconducting state with $d_{x^2-y^2}$-wave symmetry of the order parameter (for a review on spin fluctuation induced pairing see [Sca99]). However studies that take into account all possible particle-particle and particle-hole Feynman diagrams are still beyond present numerical possibilities for large systems and low temperatures.

Nevertheless recent numerical renormalization group studies [Hal00] show strong evidence that the ground-state of the weak coupling 2D Hubbard model is superconducting with a $d_{x^2-y^2}$-wave order parameter in a finite doping regime $\delta > 0$. A finite temperature phase transition to a superconducting phase with long-range order of the conventional type is again inhibited by the Mermin-Wagner theorem. However, for 2D systems there exists another type of phase transition, the Kosterlitz-Thouless (KT) phase transition [Kos73], which describes the transition to a phase with topological order where the correlations display an algebraic fall-off with distance. Mainly QMC simulations on finite-size systems in the weak coupling regime were employed to search for such a transition [Whi89b, Mor92, Bul94, Hus96, Zha97, Fet99, Sca99]. These studies indicate an enhancement of the pairing susceptibility in the $d_{x^2-y^2}$-channel with decreasing temperature. But the Fermion sign-problem limits these studies to temperatures too high to observe the actual KT transition. Therefore, results based on finite size QMC have been inconclusive towards the issue of finite temperature superconductivity in the 2D Hubbard model. Furthermore, these studies were limited to the weak coupling regime ($U < W$). So far there have not been any calculations for the strong coupling regime $U > W$, which actually is the relevant regime for a description of the cuprate superconductors (see Sec. 1.2).

Another interesting issue concerns the effect of a finite next nearest neighbor hopping amplitude t' on superconductivity. As illustrated in Fig. 3.1, finite values of t' shift the frequency of the van-Hove singularity in the bare density of states (DOS) so that it occurs at the Fermi energy in finite doped systems. Finite values for t' may thus enhance or suppress pairing. Sec. 3.4 focuses on this and the question of superconductivity in the 2D Hubbard model in general by presenting results obtained within the DCA for the weak and strong coupling regime.

In addition to these collective effects, single particle spectra are of major importance for a complete understanding of the low temperature properties of the Hubbard model. Angle resolved spectra are represented by the **k**-dependent spectral function

$$A(\mathbf{k},\omega) = -\frac{1}{\pi}\mathrm{Im}\,G(\mathbf{k},\omega) \tag{3.3}$$

and the DOS $N(\omega)$ is equal to the integrated spectral function

$$N(\omega) = \frac{1}{N}\sum_{\mathbf{k}} A(\mathbf{k},\omega)\,. \tag{3.4}$$

Multiplied with the Fermi function $f(\omega)$ or $1-f(\omega)$, respectively, these quantities can be compared to (angle resolved) photoemission spectra ((AR)PES) or inverse (AR)PES, respectively. Besides QMC simulations and Exact Diagonalization studies on finite size systems, the DMFA was extensively used to investigate the spectrum of the 2D Hubbard model in the thermodynamic limit. For a review of finite size calculations consult [Dag94a], whereas for DMFA studies see [Geo96, Pru95a]. On large energy scales the DOS for $U \gg W$ is expected to show two separated Hubbard sub-bands centered at the atomic levels ϵ_o and ϵ_o+U with a width of the order of the hybridization t (see lower part of Fig. 2.11). The half-filled system has an insulating ground state then. For small interaction strength $U \ll W$ the two sub-bands should merge into a single gap-less band, similar to the DOS for $U=0$ illustrated in Fig. 3.1 (see also upper part of Fig. 2.11).

The nature of the quasiparticles on the other hand is determined by the excitations at low energy scales. Important issues contain the question of whether the 2D Hubbard model shows Fermi liquid or non-Fermi liquid behavior (see discussion of the normal state properties of the cuprates in Chapter 1) at low temperatures in some doping range. At half-filling e.g., it is still controversial if the 2D Hubbard model shows precursor effects at finite temperatures of the antiferromagnetic phase transition at $T=0$ in form of a pseudogap, i.e. a depression of the DOS at the Fermi energy. Sec. 3.2 sheds light on this issue and Sec. 3.3 discusses the character of the low energy excitations in doped systems.

Motivation and choice of parameters

The use of the DCA for a cluster size of $N_c = 4$ towards a description of the physics in HTSC can be motivated as follows: The basic idea of the DCA is to calculate the self-energy at selected **K**-points in the BZ and consider the self-energy at these points to represent the self-energy in the surrounding of these points $\mathbf{K}+\mathbf{k}'$: $\Sigma(\mathbf{K}+\mathbf{k}') = \Sigma(\mathbf{K})$. Therefore the use of the DCA as an approximation can be justified as long as the momentum dependence of the self-energy is weak, or in other words, as long as the dynamics is dominated by local and short-ranged nonlocal fluctuations. In particular, for the cluster size $N_c = 4$ corresponding to the set of cluster $\mathbf{K}$-points (2.116), the DCA includes dynamical correlations between nearest- and next-nearest neighbors in addition to local correlations. This neglect of longer-ranged dynamical fluctuations can be motivated by the observation that the physics in underdoped to optimally doped cuprates is dominated by short-ranged spin-fluctuations [Zha96]. Therefore the DCA as a microscopic theory which accounts for short-ranged dynamical correlations in addition to the local correlations of the DMFA is relevant and might succeed in describing the physics of the cuprates.

A second goal of the following sections will be to use the DCA to investigate the effects of the initial corrections to the DMFA results. Systematics on how the influence of the nonlocal corrections depends on system parameters will be presented. Calculations were performed for a 1x1 cluster ($N_c = 1$), which is equivalent to a DMFA calculation, and for a 2x2 cluster ($N_c = 4$) using the set of cluster $\mathbf{K}$-points (2.116). A comparison of the results for both cluster sizes is used to study the effect of nonlocal correlations present in the $N_c = 4$, but neglected in the $N_c = 1$ calculation.

The 2D Hubbard model is characterized by the dispersion $\epsilon_{\mathbf{k}}$ (Eq. (3.1)) and the local Coulomb repulsion U. The nearest neighbor hopping integral t is used as energy scale. In all calculations the next-nearest neighbor hopping integral $t' \in [-t/2; t/2]$, thus the bare bandwidth W corresponding to the dispersion $\epsilon_{\mathbf{k}}$ in Eq. (3.1) is given by $W = 8t$. To compare the results to experiments on cuprate superconductors t is set to $t = 0.25\,\mathrm{eV}$, which is widely used in the literature for a description of the cuprates. Furthermore the interaction strength is chosen to $U = 12t > W$, greater than the bare bandwidth so that a gap is present in the DOS and the half-filled model is insulating (see lower part of Fig. 2.11). This value of U is believed to be appropriate to simulate the physics in the CuO_2-planes in the high-T_c cuprates as discussed in Sec. 1.2.

To investigate the question of a possible pseudogap due to nonlocal correlations in the half-filled model as a precursor effect to the antiferromagnetic phase transition, U is set to $U = 4t$, half the bare bandwidth. This value of U is well below the critical value $U_c \sim W$ necessary to open up a Mott-Hubbard gap in the DOS, so that the system is metallic, even in the half-filled case. The chemical potential $\mu = 0$ and doping is controlled by changing the on-site energy ϵ_o.

The result section is organized as follows. In Sec. 3.2 the special case of half-filling is discussed. Sec. 3.3 presents a systematic study of the evolution of the single-particle spectra and the Fermi surface in the doped system. The question of a possible superconducting instability of the doped 2D Hubbard model at low temperatures is investigated in Sec. 3.4 and the DCA phase diagram for the 2D

Hubbard model in Sec. 3.5 summarizes the results.

3.2 Half-filling - Antiferromagnetic correlations

As explained in the introduction, the half-filled Hubbard model is expected to have an antiferromagnetically ordered ground state for every finite value of the Coulomb repulsion U. DMFA simulations for the half-filled Hubbard model in fact yield a finite temperature phase transition to the antiferromagnetic state (see e.g. [Jar92]). However, due to the neglect of nonlocal fluctuations the results do not show any precursor effects of the antiferromagnetic phase transition and the magnetic susceptibility $\chi \propto (T - T_{\mathrm{N}})^{-\gamma}$ as a function of temperature diverges at the Neél temperature T_{N} with mean field exponent $\gamma = 1$ [Jar92].

P. R. Weiss extended his conventional mean field theory for spin systems through the inclusion of nonlocal fluctuations by mapping the lattice system onto a cluster consisting of a site i and a closed shell of spins around it. Thus, this method extends the conventional mean field theory by the inclusion of spin-fluctuations. In the literature this method is referred to as the Bethe-Peierls-Weiss method (BPW) [Wei48, Bro55]. The result of these calculations is a suppression of ferromagnetism and antiferromagnetism, respectively, i.e. a reduction of the corresponding transition temperatures as compared to the conventional mean field result.

The relation of the DCA to the DMFA is similar to the relation of the BPW-method to the conventional mean field method. The inclusion of nonlocal fluctuations by the DCA for $N_c > 1$ is therefore expected to suppress antiferromagnetism in the 2D Hubbard model as compared to the DMFA result.

3.2.1 Antiferromagnetic state

To obtain solutions with a finite spontaneous sub-lattice magnetization, a staggered symmetry breaking magnetic field h is applied in the first DCA iteration[2] and then turned off again. The presence of antiferromagnetic ordering is then signalled by a finite sub-lattice magnetization $m = |n_{A\uparrow} - n_{A\downarrow}|$ calculated via Eq. (2.100). According to Eqs. (2.98), (2.99) and the symmetry relation (2.101 a finite order parameter m is a consequence of a finite **k**-off-diagonal Green function $F(\mathbf{k}, \omega) = \langle\langle c_{\mathbf{k}\sigma} ; c^{\dagger}_{\mathbf{k}+\mathbf{Q}\sigma}\rangle\rangle_z$ due to the reduced translational symmetry in the antiferromagnetic state. Fig. 3.3 shows this quantity coarse grained over the cell centered at the DCA cluster momentum $\mathbf{K} = (\pi, 0)$ in the inset when $U = 4t$, $t' = 0$ and $T = 0.172t$ at half-filling. The fact that $\bar{F}$ is finite signals the presence of a broken translational symmetry. The system is in the antiferromagnetic state!

[2] See Sec. 2.6.3 for a derivation of the DCA equations in the antiferromagnetic phase.

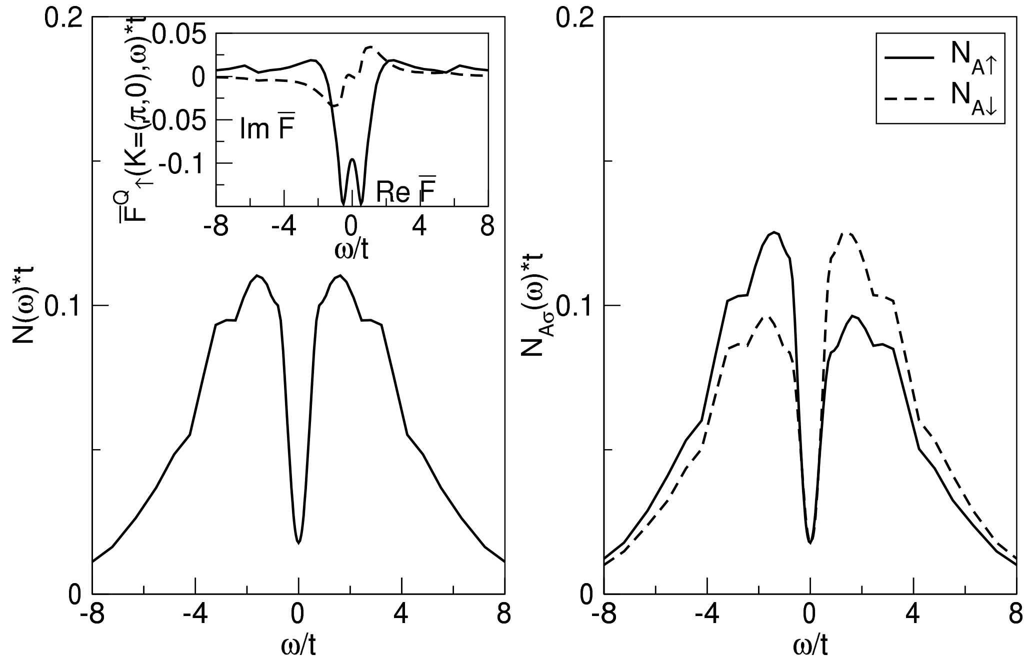

FIGURE 3.3: *The DOS $N(\omega)$ in the antiferromagnetic state when $N_c = 4$, $U = 4t$, $t' = 0$ and $T = 0.172t$ at half filling (left panel). The inset shows the finite coarse grained* **K***-off-diagonal Green function $\bar{F}(\mathbf{K}, \omega)$ at the DCA cluster* **K***-point $(\pi, 0)$. The local DOS $N_{A\sigma}(\omega)$ defined on the A-sub-lattice for majority and minority spin is shown on the right panel.*

$\bar{F}(\mathbf{K}, \omega)$ at the other cluster **K**-points (not shown) is also finite and shows similar structures as $\bar{F}(\mathbf{K}, \omega)$ at $(\pi, 0)$. The left panel illustrates the total DOS $N(\omega)$ averaged over the sites of the full lattice. Hence this quantity does not depend on the spin σ. The DOS displays the expected behavior in the antiferromagnetic state (see Sec. 3.1) including a gap-like depression of the DOS at the Fermi energy ($\omega = 0$) due to the doubling of the unit cell in the antiferromagnetic state. However, at finite temperatures the states close to the Fermi surface have a finite lifetime and therefore fill in the gap so that no full gap is present in the DOS at this temperature.

On the other hand the spectrum $N_{A\sigma}(\omega)$ on a given sub-lattice, e.g. the A-sub-lattice is obtained from the Green function $G^A_\sigma(\omega)$ (Eq. (2.98)). For both spins σ the corresponding DOS $N_{A\sigma}(\omega)$ is plotted on the right panel. Since this quantity is defined on the A-sub-lattice only it splits up for majority (spin-up) and minority (spin-down) spin. As a result the order parameter $m = |n_{A\uparrow} - n_{A\downarrow}|$ defined as the occupation difference in majority and minority spin is finite.

With increasing temperature the splitting in the spectral function $N_{A\sigma}(\omega)$ for majority and minority spin diminishes and consequently the magnitude of the order parameter m decreases. The temperature where the order parameter vanishes defines the Neél temperature $T_{\rm N}$. In Fig. 3.4 the magnitude of the sub-lattice magnetization m at half-filling for cluster sizes $N_c = 4$ and 1 is plotted against temperature T renormalized by the corresponding Neél temperatures $T_{\rm N}$. The

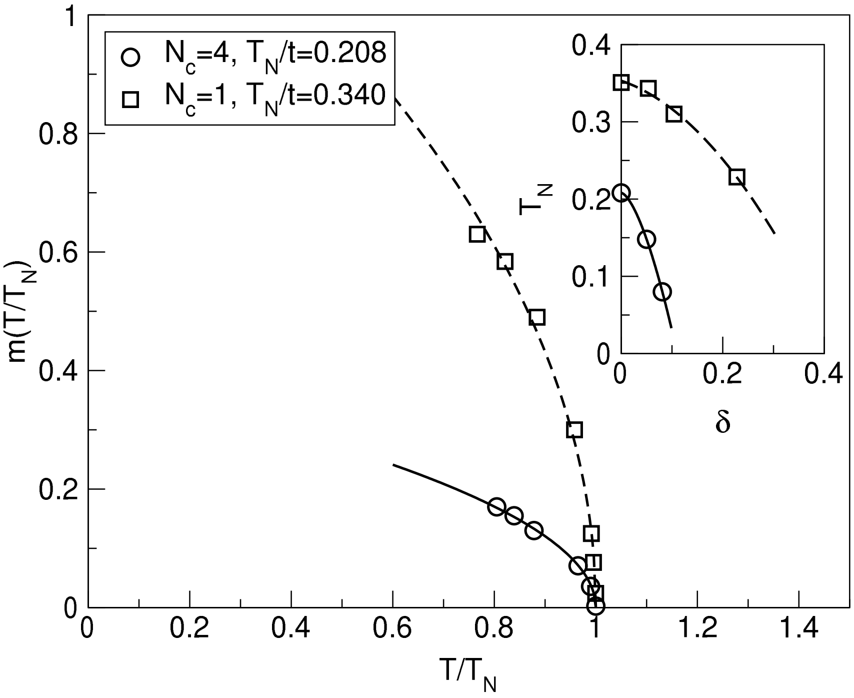

FIGURE 3.4: *The sub-lattice magnetization m as a function of temperature for $U = 4t$ and $N_c = 4$ and 1. The lines are fits to the function $m(T) = A(T_{\rm N} - T)^{\beta}$. Both curves can be fit by $\beta = 0.5$, the mean field result, for temperatures close to T_N. The constant A defined by the extrapolation to $T = 0$ is much smaller for $N_c = 4$. Fluctuations beyond mean field strongly suppress the sub-lattice magnetization m. Inset: Neél temperature T_N versus doping when $N_c = 4$ and 1 (the lines are guides to the eye only): Spin-fluctuations strongly suppress antiferromagnetism.*

transition temperature for $N_c = 1$, $T_{\rm N} = 0.340t \triangleq 992$K (for $t = 0.25\,$eV) is reduced to $T_{\rm N} = 0.208t \triangleq 604$K in the $N_c = 4$ result. As expected, the inclusion of nonlocal fluctuations strongly suppresses antiferromagnetism. This is also true inside the antiferromagnetic phase. The magnetization m is strongly reduced for $N_c = 4$ compared to the DMFA result $N_c = 1$. The solid and dashed line, respectively represent fits to the function $m(T) = A(T_{\rm N} - T)^{\beta}$. Both curves can be fit by $\beta = 0.5$, the mean field value, for temperatures $T \lesssim T_{\rm N}$. This originates in the fact that very close to the transition the properties of the system are dominated by long-ranged correlations which are neglected in the DCA result. However the extrapolation to $T = 0$ yields a much smaller magnetization for $N_c = 4$ compared to $N_c = 1$. Nonlocal fluctuations incorporated in the $N_c = 4$ result but neglected[3] when $N_c = 1$ suppress the magnetization inside the antiferromagnetic phase.

The inset to Fig. 3.4 presents the variation of T_N with doping. In the DMFA ($N_c = 1$) antiferromagnetism persists to relatively high temperatures and dopings, whereas when $N_c = 4$ the region where antiferromagnetism can exist is strongly reduced by the inclusion of nonlocal dynamical fluctuations. Since the NCA algorithm breaks down at very low temperatures, reliable values for the critical doping $\delta_c(T_\mathrm{N} = 0)$, beyond which antiferromagnetism vanishes cannot be predicted.

As discussed earlier in the introductory section 3.1 the Mermin-Wagner theorem [Mer66, Hoh67] prevents finite temperature phase transitions to phases with a broken continuous symmetry in the 2D model. Thus, the question arises if the results presented here are in contradiction to the rigorous result of the Mermin-Wagner theorem. For the following reasons they are not:

As pointed out in Sec. 2 the DCA includes short-ranged interactions (of the order of the cluster size) accurately, whereas longer-ranged interactions are treated on a mean field level. Hence fluctuations on short length scales are built in the DCA, but long length scale fluctuations are neglected which are essential to proof the Mermin-Wagner theorem. It is therefore well known that methods with mean field-like character, i.e. theories which neglect long-ranged correlations like the DCA yield finite transition temperatures even for 2D systems. The mean field-like character of the DCA can be viewed as imitating a finite coupling of the 2D model to the third dimension and therefore the Mermin-Wagner theorem is irrelevant in the context of the calculation presented here. However as the cluster size N_c increases the mean field-like nature of the DCA gradually decreases. Unfortunately $N_c = 4$ is the largest cluster size that can be treated within the DCA-NCA algorithm (see Sec. 2.8.1). Thus scaling calculations cannot be performed and no statements about the limit of large N_c can be made.

However, by using the QMC approach[4] to solve the DCA cluster problem, simulations on larger cluster sizes can be performed. Consistent with the Mermin-Wagner theorem, these calculations indicate that T_N continues to fall for larger values of N_c [Jar99]. Furthermore, within the QMC simulations two-particle correlation functions can be easily obtained. Calculations for the magnetic susceptibility in the paramagnetic phase are complementary to the calculations in the antiferromagnetic state. In agreement with the results presented here, these calculations indicate that nonlocal fluctuations beyond the $N_c = 1$ mean field result are responsible for suppressing antiferromagnetism.

---

[3] It should be stressed that even though the DMFA for the antiferromagnetic state is formulated on an AB-lattice and two independent self-energies Σ_A and Σ_B are calculated, Σ is still a purely local quantity and hence does not account for nonlocal fluctuations.

[4] The actual algorithm is based on the Hirsch-Fye impurity algorithm [Hir86] and is modified to simulate an embedded cluster [Mou00].

3.2.2 Normal state precursors

The interesting question arises of whether the same nonlocal fluctuations which are responsible for suppressing antiferromagnetism result in precursor effects preceding the phase transition. As possible precursor effects of the antiferromagnetic phase transition, one may expect two features in the paramagnetic state: First, the "back-folded" states of the antiferromagnetic phase resulting from the doubling of the unit cell as explained in Sec. 3.1 (see dashed line in Fig. 3.2) might show up as so-called shadow-bands in the normal state already as a consequence of short-range antiferromagnetic order. Second, since the two bands in the antiferromagnetic state are separated by a gap (see Fig. 3.2), a pseudogap[5] may open in the DOS as a precursor of the gap in the antiferromagnetic state. These two effects would signal the onset of antiferromagnetic ordering on short time and length scales.

The existence of these precursor features was predicted by Kampf and Schrieffer [Kam90] using a phenomenological ansatz for the weak coupling Hubbard model based on the presence of strong antiferromagnetic spin-fluctuations. On a microscopic level this question has been addressed by finite size lattice QMC for the 2D Hubbard model [Vek93, Cre95] and approximate many-body techniques [Dei96, Mou99]. But the results have been inconclusive and contradictory as to the existence of a pseudogap at low temperatures, due to the limitations of these techniques.

Fig. 3.5 presents the DCA results for the DOS $N(\omega)$ for $N_c = 4$ (left panel) and $N_c = 1$ (right panel) when $U = 4t$ and $t' = 0$ for the half-filled 2D Hubbard model for two temperatures T above the corresponding Neél temperatures $T_{\rm N}$ (dashed and solid lines) and one temperature below $T_{\rm N}$ (dash-dotted lines). When $N_c = 1$ no pseudogap is seen at the Fermi energy. The lack of nonlocal correlations prevents the system from showing possible precursor effects. Instead, a quasiparticle peak is found in the paramagnetic state at zero frequency which builds as the temperature is lowered. More detailed studies (see e.g. [Pru95b]) show that this feature indicates the formation of a Fermi liquid and is accompanied by a reduction of the effective local magnetic moment due to dynamical screening effects. This Kondo-like physics known from the single impurity Anderson model is closely related to the fact that the DMFA maps the lattice system onto an effective impurity model. It is still unclear if this feature is an intrinsic feature of the Hubbard model in two or three dimensions or if it is an artifact of the DMFA approach. After entering the ordered state a gap in $N(\omega)$ (see dash-dotted line) starts to emerge at the Fermi energy due to the doubling of the unit cell.

On the other hand, when $N_c = 4$ no quasiparticle peak is seen in the DOS.

[5] A pseudogap denotes the depression of the DOS without the opening of a full gap. However, the DOS can vanish at a singular frequency.

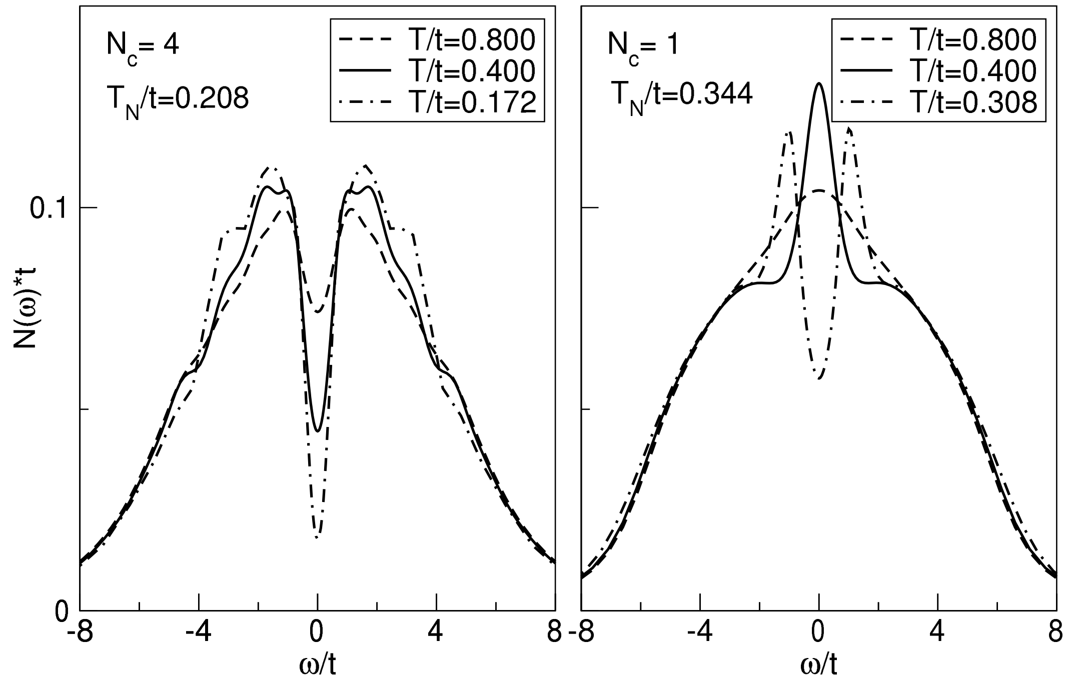

FIGURE 3.5: *The single particle DOS $N(\omega)$ at half-filling when $U = 4t$ and $N_c = 4$ (left panel) and $N_c = 1$ (right panel) for various temperatures T. The Neél temperatures are $T_{\rm N} = 0.208t$ for $N_c = 4$ and $T_{\rm N} = 0.340t$ for $N_c = 1$, respectively. The DMFA result ($N_c = 1$) shows a peak at the Fermi energy before entering the ordered state. The $N_c = 4$ result displays a pseudogap at zero frequency as a precursor of the antiferromagnetic phase transition.*

Instead, a pseudogap develops in the DOS already for temperatures above the Neél temperature $T_{\rm N}$. As the temperature is further decreased the pseudogap deepens upon entering the antiferromagnetic state. Obviously, the Kondo-like physics seen in the $N_c = 1$ result is completely suppressed by the inclusion of nonlocal correlations when $N_c = 4$. Thus, it must be concluded that at least in two dimensions the Kondo-like quasiparticle peak seen in DMFA simulations for the half-filled model is an artifact of the neglect of nonlocal correlations in the DMFA approach. In fact the $N_c = 4$ result clearly shows that the inclusion of nonlocal corrections results in the formation of a pseudogap that may be viewed as a precursor preceding the antiferromagnetic transition of the 2D Hubbard model at lower temperatures.

It is instructive to compare these results for $N(\omega)$ to the corresponding spectra $N_c(\omega)$ of the bare cluster depicted in the upper part of Fig. 2.11. $N_c(\omega)$ already captures the gross features of the full lattice DOS $N(\omega)$ when $N_c = 4$. The reduced number of states at zero frequency in the cluster spectrum is obviously still reflected in the thermodynamic limit as pseudogap. On the other hand, when

$N_c = 1$ the bare impurity spectrum (not shown) consists of two δ-peaks located at $\pm U/2$ and the features of the full lattice DOS $N(\omega)$ including the Kondo-like peak is almost completely generated by the coupling to the effective medium $\mathcal{G}$.

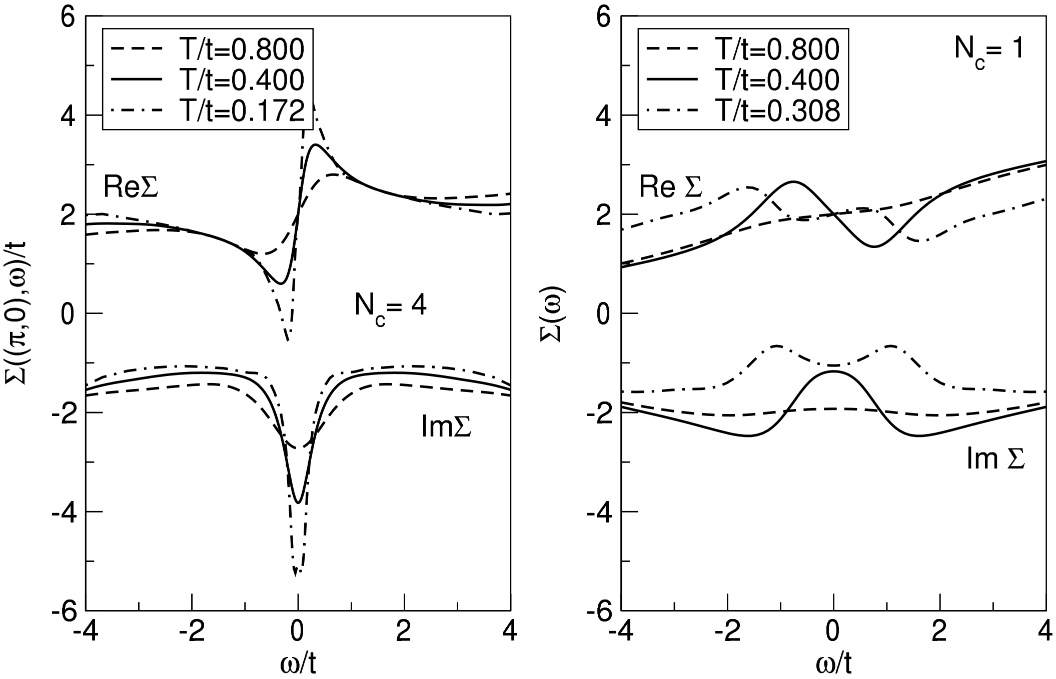

FIGURE 3.6: *Real and imaginary parts of the coarse grained self-energy* $\Sigma(\mathbf{K})$ *when* $N_c = 4$ *at the cluster* $\mathbf{K}$*-point* $(\pi, 0)$ *(left panel) and the local DMFA (*$N_c = 1$*) self-energy (right panel) for frequencies close to the Fermi energy for the same temperatures as in Fig. 3.5. The* $N_c = 4$ *result displays pronounced non-Fermi liquid behavior, whereas the* $N_c = 1$ *result shows Fermi liquid behavior in the paramagnetic phase.*

The DCA self-energy $\Sigma(\mathbf{K})$ in Fig. 3.6 with the same parameters as in Fig. 3.5 supports the results for the spectrum. For a Fermi liquid the self-energy

$$\Sigma(\mathbf{k}_F, \omega) \sim (1 - 1/Z)\omega - ia\omega^2 \tag{3.5}$$

for frequencies ω near the Fermi energy and momenta $\mathbf{k}_F$ on the Fermi surface. The quasiparticle weight $Z = (1 - \partial \mathrm{Re}\,\Sigma(\mathbf{k}, \omega)/\partial\omega)^{-1} < 1$ so that in Fermi liquids the real part of Σ crosses the Fermi surface with a negative slope. The constant $a > 0$ so that the imaginary part of Σ has a parabolic maximum at zero frequency. When $N_c = 1$ the self-energy is $\mathbf{k}$-independent and therefore is a constant over the full BZ. Thus, $\Sigma(\mathbf{k}_F, \omega) = \Sigma(\omega)$. When $N_c = 4$ however, $\Sigma(\mathbf{K})$ is calculated on a selected set of $\mathbf{K}$-points and is assumed to be constant in the surrounding of these points. Hence $\Sigma(\mathbf{k}_F, \omega)$ is determined by the self-energy at the closest cluster $\mathbf{K}$-point and therefore $\Sigma(\mathbf{k}_F,\omega)=\Sigma(\mathbf{M}(\mathbf{k}_F),\omega)$, where $\mathbf{M}(\mathbf{k})$ is the function defined in Sec. 2.3, Eq. (2.21) which maps $\mathbf{k}$ to the closest cluster momentum $\mathbf{K}$. The Fermi surface of the half-filled system for $t'=0$ however is identical to the magnetic BZ (see Fig. 3.1). Hence the cluster point $\mathbf{K}=(\pi,0)$ is the only momentum of the selected set of $\mathbf{K}$-points (2.116) which lies on the Fermi surface. Therefore the self-energy $\Sigma(\mathbf{K},\omega)$ at $\mathbf{K}=(\pi,0)=\mathbf{k}_F$ is considered in the following when $N_c=4$.

For $N_c=1$ (right panel) the imaginary part of the local self-energy $\Sigma(\omega)$ develops a parabolic maximum at $\omega=0$ in the normal state (solid line). As the temperature decreases to $T=0.4t$ the real part of $\Sigma(\omega)$ crosses the Fermi surface with a negative slope. According to Eq. (3.5) this behavior is indicative of the formation of a Fermi liquid. $\mathrm{Im}\,\Sigma(\omega)$ shows a minimum at the Fermi energy not until the antiferromagnetic state (dash-dotted line) is entered.

The $N_c=4$ result on the other hand displays non-Fermi liquid behavior. The left panel of Fig. 3.6 shows the $N_c=4$ DCA self-energy $\Sigma(\mathbf{K},\omega)$ at the cluster $\mathbf{K}$-point $(\pi,0)$ on the Fermi surface. With decreasing temperature a minimum develops in the imaginary part even in the paramagnetic phase, an indication of the breakdown of Fermi liquid behavior according to Eq. (3.5). The scattering rate increases at the Fermi energy upon approaching the transition as the temperature is lowered. The slope of the real part $\mathrm{Re}\,\Sigma((\pi,0),\omega)$ is positive when the pseudogap opens in the density of states, so that the quasiparticle weight Z is negative.

To search for the second precursor effect, the evolution of shadow states in the spectrum, Fig. 3.7 shows the $\mathbf{k}$-dependence of the spectral density $A(\mathbf{k},\omega)$ when $U=4t$, $t'=0$ at half-filling in the paramagnetic phase ($T=0.4t>T_{\mathrm{N}}(N_c=4)$) along the main symmetry directions $\Gamma=(0,0)\to M=(\pi,\pi)\to X=(\pi,0)\to\Gamma$ as indicated on the right. The spectra were obtained by interpolating the cluster self-energy $\Sigma(\mathbf{K})$ to the full BZ by means of the interpolation scheme discussed in Sec. 3.1. The spectra $A(\mathbf{k},\omega)$ for different values of $\mathbf{k}$ are shifted along the y-axis. To see the effects of the interaction U on the spectrum, it is instructive to compare it to the bare spectrum ($U=0$), illustrated on the right panel of Fig. 3.7. The bare spectrum $A_o(\mathbf{k},\omega)=\delta(\omega-\epsilon_{\mathbf{k}})$ displays the dispersion $\epsilon_{\mathbf{k}}$ (Eq. (3.1)) for $t'=0$ as a set of delta-peaks.

The interaction U has various effects on the spectrum. The δ-peaks of the non-interacting system get strongly damped and spread over a finite energy region. The most remarkable difference to $U=0$ however is the opening of the pseudogap at the Fermi energy. The pseudogap is most pronounced at the X-point $(\pi,0)$. The opening of the pseudogap is a consequence of the behavior of the self-energy, shown in Fig. 3.6. The positive slope of the real part signals the appearance of two new solutions in the quasiparticle equation $\mathrm{Re}(\omega-\epsilon_{\mathbf{k}}-\Sigma(\mathbf{K},\omega))=0$ on the positive and negative side of $\omega=0$ in addition to the strongly damped solution at $\omega=0$ which is also present in the non-interacting system. As a consequence, the

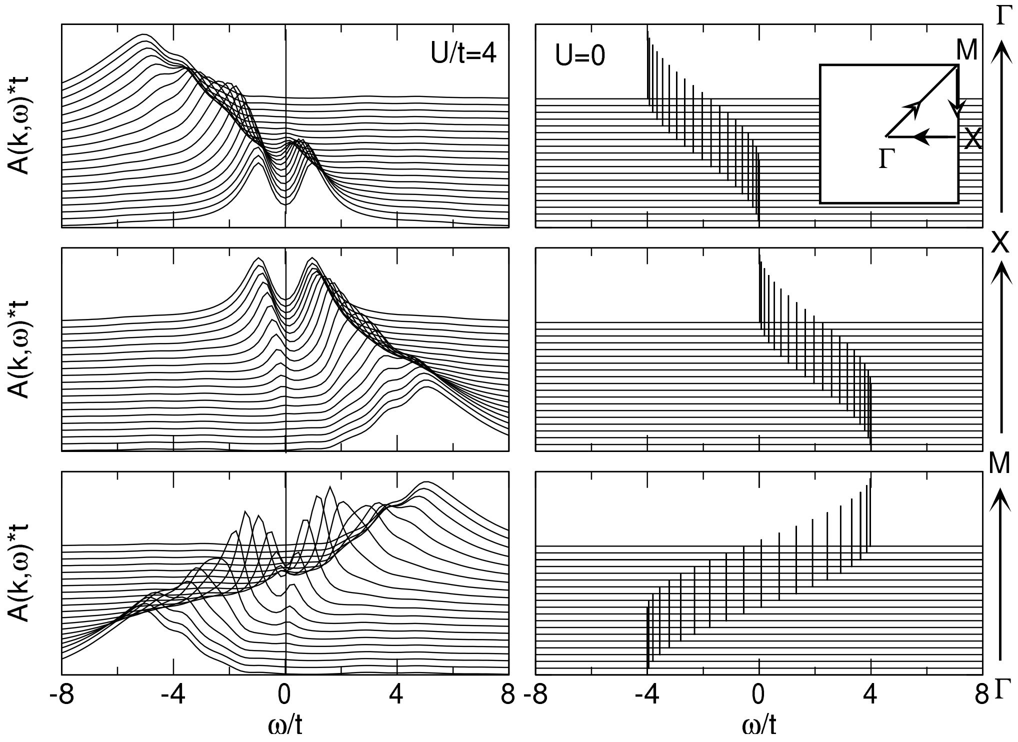

FIGURE 3.7: *The spectral density $A(\mathbf{k},\omega)$ for $N_c = 4$ along the main symmetry directions in the BZ as indicated on the right when $U = 4t$ and $T = 0.4t$ at half-filling. Spectra for different* $\mathbf{k}$ *are shifted along the y-axis. The pseudogap is most pronounced at the X-point. The right panel shows the corresponding bare ($U = 0$) spectral density.*

pseudogap opens at the Fermi energy and two bands, most pronounced near the X-point develop. The band-structure defined by the maxima of $A(\mathbf{k},\omega)$ is very similar to the band-structure in the antiferromagnetic state shown in Fig. 3.2 where the additional band develops due to the doubling of the unit cell. In the paramagnetic state they indicate precursor effects of the onset of antiferromagnetic order on short time and length scales. They are referred to as shadow states and are caused by antiferromagnetic spin fluctuations in the paramagnetic state [Kam90]. According to Fig. 3.2 these shadow states should also become visible at the Γ- and M- point, respectively. In order to better resolve these features, the spectral density at the Γ- and M-point is plotted versus frequency in Fig. 3.8. In addition to the main structure at $\omega < 0$ at the Γ-point ($\omega > 0$ at M) satellite structures at $\omega > 0$ at Γ ($\omega < 0$ at M) with small spectral weight develop. These new states are absent in the non-interacting system as well as in the DMFA result (not shown) and can be thought of precursor effects preceding the antiferromagnetic phase transition.

Fig. 3.7 and 3.8 show that even in the paramagnetic phase the short-ranged

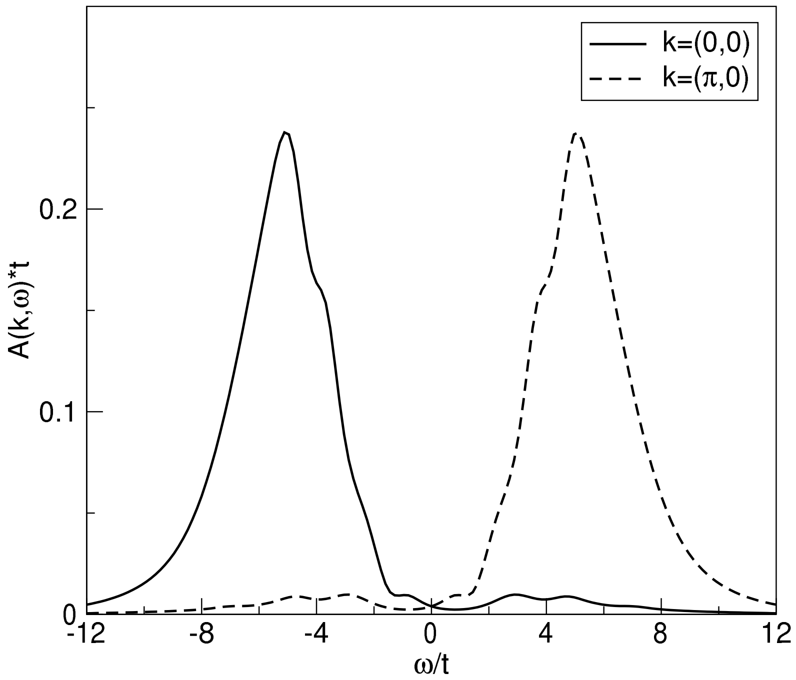

FIGURE 3.8: *The spectral density $A(\mathbf{k}, \omega)$ at the points $\Gamma = (0,0)$ and $M = (\pi, \pi)$. Shadow structures develop with small spectral weight in addition to the main structures.*

antiferromagnetic spin-fluctuations are sufficient to produce these indications of the ordered phase. Such precursor effects of the antiferromagnetic long-range order can for example be seen in the cuprates [Aeb94] in Fermi surface measurements. The observation of these spin-fluctuation induced shadow states accompanied by the opening of the pseudogap supports the scenario that the non-Fermi liquid behavior seen in the $N_c = 4$ result is driven by antiferromagnetic spin-correlations.

3.2.3 Finite values of t'

To gain more insight in the nature of the pseudogap and elucidate the physics of the observed non-Fermi liquid behavior for $N_c = 4$, calculations were performed with a finite next-nearest neighbor hopping integral $t' \neq 0$. Then the Fermi surface is no longer nested and the lattice is frustrated (see Sec. 3.1). Thus, the antiferromagnetic spin-correlations can be gradually suppressed by increasing the magnitude of t'.

Fig. 3.9 illustrates the behavior of the DOS $N(\omega)$ at $T = 0.5t$ as the next-nearest neighbor hopping t' and therefore the lattice frustration increases. The DOS is no longer particle-hole symmetric for $t' \neq 0$, because the bare DOS is not

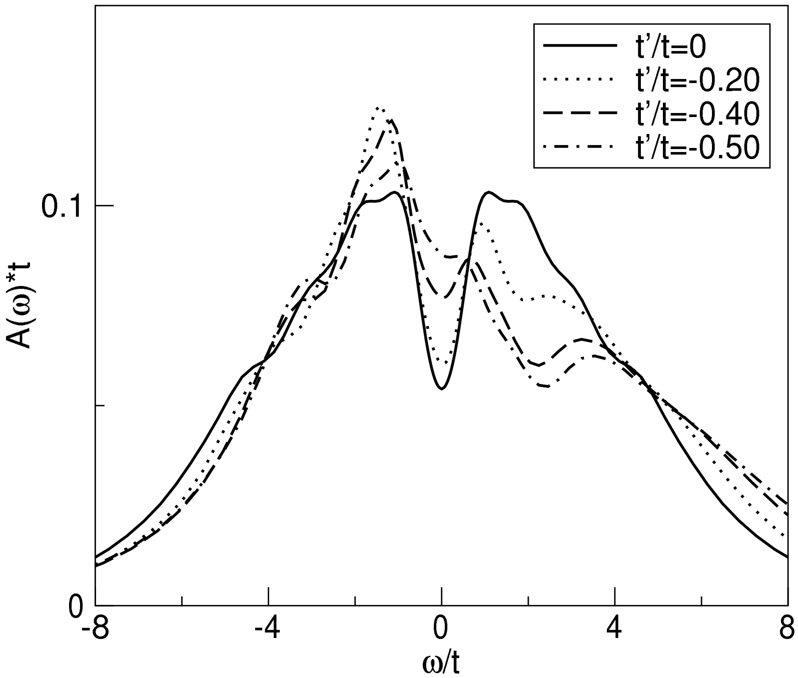

FIGURE 3.9: *The DOS $N(\omega)$ for $N_c = 4$ at fixed temperature $T = 0.5t$, $U = 4t$ and half-filling for various values of the next-nearest neighbor hopping integral t'. As t' increases the lattice is frustrated, antiferromagnetic correlations are suppressed and the pseudogap disappears.*

particle-hole symmetric when t' is finite (see Fig. 3.1). The DOS gets enhanced at negative frequencies, i.e below the Fermi energy ($\omega = 0$), since the negative t' moves the van-Hove singularity to negative frequencies (see Fig. 3.1). Obviously, as the magnitude of t' increases, the pronounced pseudogap seen when $t' = 0$ gets gradually reduced. However, even for the maximum value $t' = -0.5t$ a small dip at zero frequency can be seen, which possibly can be attributed to the fact that extreme short-ranged fluctuations are still present, which are however strongly reduced in magnitude as compared to the nested situation. Thus, it is concluded that indeed the short-ranged antiferromagnetic spin-correlations are responsible for the development of the pseudogap at the Fermi energy in the DOS of the half-filled 2D Hubbard model with $t' = 0$, which in fact must be viewed as a precursor of the antiferromagnetically ordered state at lower temperatures.

3.2.4 Dependence on cluster size N_c

Again, the question about the effect of the cluster size N_c on the observed pseudogap and non-Fermi liquid behavior arises. As already discussed, the NCA cannot be used to address this issue. However by applying the QMC to the DCA cluster problem, calculations can be carried through on larger cluster sizes for the half-filled model to investigate the evolution of the pseudogap as a function of N_c.

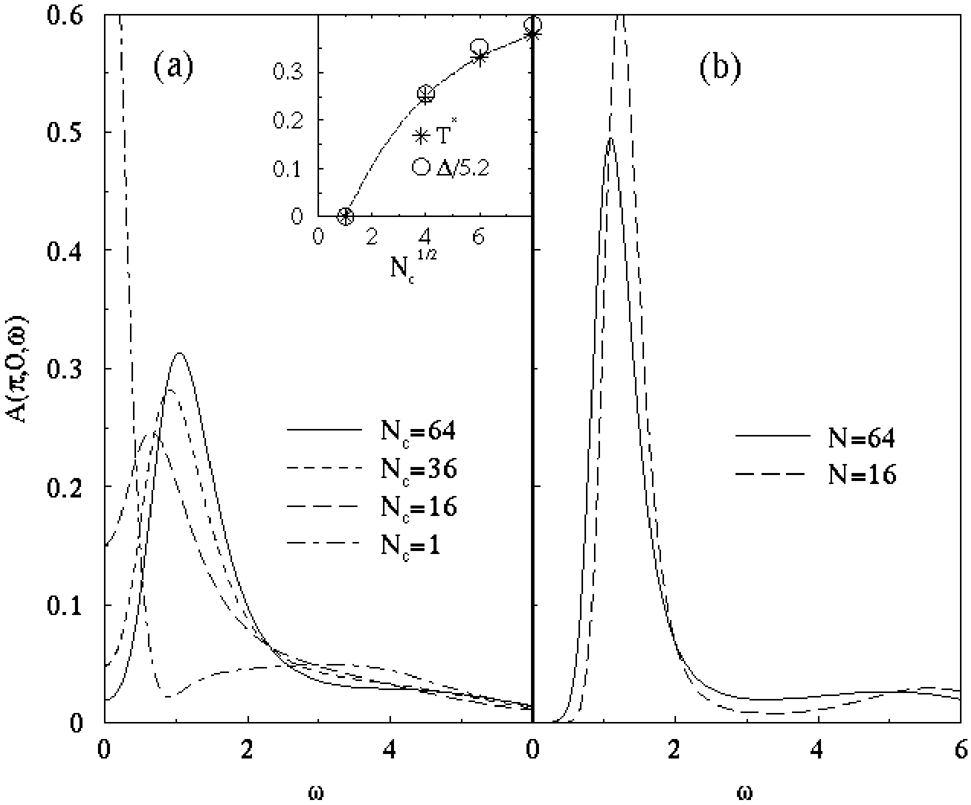

FIGURE 3.10: *The spectral density $A(\mathbf{k},\omega)$ at $\mathbf{k} = (\pi, 0)$ for the half-filled 2D Hubbard model via (a) DCA-QMC and (b) finite-size QMC for $U = 5.2t$ and $T = 0.2t$ on various cluster sizes N_c. The inset shows the N_c-dependence of the temperature $T^\star$, at which the pseudogap first becomes apparent in the DOS, and the full pseudogap width Δ measured from peak to peak. Taken from [Hus99].*

Fig. 3.10 summarizes the results of these DCA-QMC calculations published in [Hus99]. For various cluster sizes N_c the spectral density $A(\mathbf{k},\omega)$ at $\mathbf{k} = (\pi, 0)$ calculated via the DCA at $T = 0.2t$ is plotted versus positive frequencies in panel (a) for $U = 5.2t$. Panel (b) illustrates the result of a QMC simulation for a finite size lattice for the 2D Hubbard model using the same parameters as for the DCA calculation. The spectra are obtained by analytically continuing both the DCA-QMC and finite size QMC data. In spite of the difference of the two methods, the information they provide is complimentary.[6] In the finite size results, (b),

[6]For a detailed comparison of the DCA-QMC and finite size QMC methods see [Mou00].

the pseudogap is also seen. However, as the length of the antiferromagnetic correlations reaches the longest length on the finite size lattice, the system freezes into the antiferromagnetically ordered state and consequently a full gap develops. Therefore, with increasing system size N the pseudogap in the finite size QMC calculation becomes weaker and hence the question if the pseudogap is also present in the thermodynamic limit cannot be answered by these simulations. The DCA on the other hand is able to resolve this question. In the DCA result, (a), the pseudogap emerges as soon as $N_c > 1$. The temperature T^* at which the pseudogap becomes apparent in the spectra, as well as the full pseudogap width Δ measured from peak to peak is plotted in the inset. Both $T^\star$ and Δ increase with N_c. Since the DCA calculation remains in the thermodynamic limit, a full gap due to antiferromagnetic correlations alone cannot open until the correlation length diverges. However since these correlations are restricted to the size of the cluster, the DCA systematically underestimates the size of the gap. Thus it must be concluded that if a pseudogap exists in the DCA for finite N_c, it should persist in the limit of large N_c.

3.2.5 Summary

To summarize, the inclusion of nonlocal dynamical corrections to the DMFA result suppresses antiferromagnetism dramatically. The Neél temperature are strongly reduced as compared to the DMFA result as well as the sub-lattice magnetization in the ordered phase. In the paramagnetic state the low temperature character of the 2D half filled Hubbard model is changed significantly by nonlocal correlations. Whereas the $N_c = 1$ result displays Fermi liquid behavior, short-ranged antiferromagnetic spin-correlations incorporated in the $N_c = 4$ result induce pronounced non-Fermi liquid behavior. As a result, shadow bands emerge and a pseudogap opens in the DOS as precursors of the antiferromagnetic ordering at lower temperatures.

3.3 Finite doping - From non-Fermi liquid to Fermi liquid behavior

This section provides a detailed study of the evolution of the spectra, self-energy and Fermi surface with doping and temperature in the paramagnetic phase of the doped 2D Hubbard model. An important question to be addressed is whether the non-Fermi liquid behavior and the pseudogap seen at half-filling persist to finite doping levels. To compare the results with experiments on the HTSC the Coulomb repulsion is now set to $U = 12t$, larger than the bare bandwidth $W = 8t$.

3.3.1 Density of states

It seems instructive to look at the general features of the spectra first before focusing on low energy scales. As discussed in Sec. 3.1 the gross features of the DOS $N(\omega)$ for $U > W$ are expected to consist of two Hubbard sub-bands centered at the energies ϵ_o and ϵ_o+U. Fig. 3.11 presents a typical DCA result for the DOS

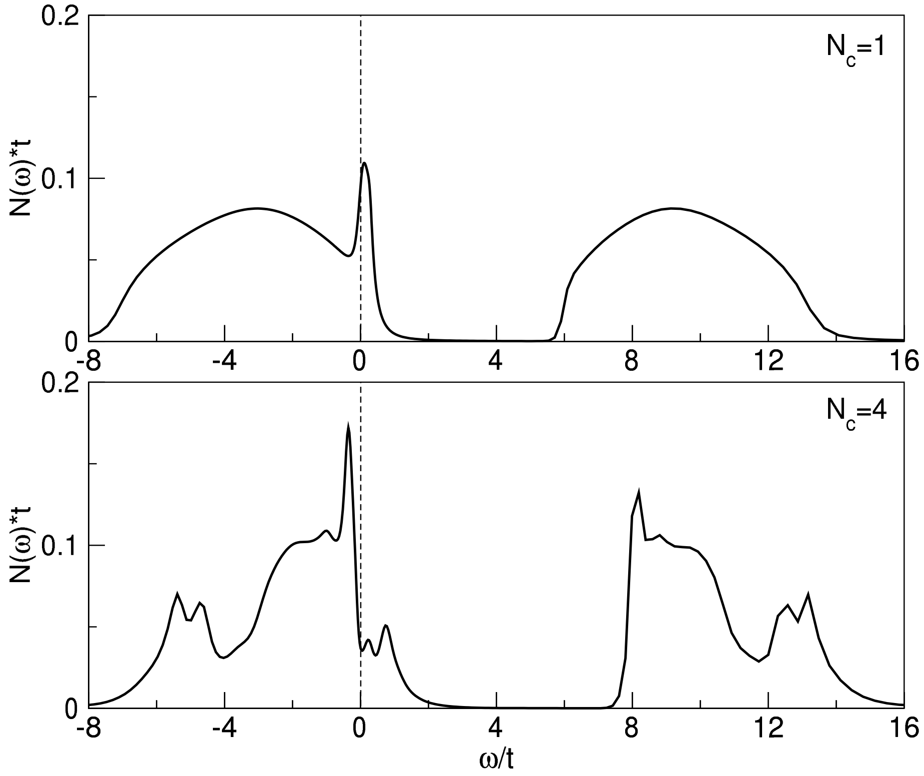

FIGURE 3.11: *The DOS $N(\omega)$ for $N_c = 4$ (bottom) and 1 (top) when $U = 12t$, $t' = 0$, doping $\delta = 0.05$ and temperature $T = 0.1t$ in the paramagnetic phase. For $N_c = 4$ a four-peak structure is found on large energy scales (two peaks per Hubbard sub-band), a narrow peak slightly below the Fermi energy and a depression of the DOS (pseudogap) at the Fermi energy.*

$N(\omega)$ of the doped system ($\delta = 0.05$) for $N_c = 1$ (top) and 4 (bottom) when $U = 12t$, $t' = 0$ and $T = 0.1t$ in the paramagnetic state. In addition to the two Hubbard sub-bands the $N_c = 1$ result displays a narrow quasiparticle peak located at the Fermi energy. As for the half-filled system (see preceding section), it was shown in the literature (see e.g. [Pru95b]) that this feature is connected to Kondo-like behavior, i.e. a reduction of the effective local magnetic moment with decreasing temperature accompanied by the formation of a Fermi liquid. The $N_c = 4$ result instead shows several features synthesizing the structure of the two sub-bands, however no sign of a Kondo-like peak at the Fermi energy. Two general features are observed: A narrow peak slightly below the Fermi energy as well as at the lower band edge of the upper Hubbard band and an incoherent broad background at larger energy scales. It is important to note that the spectrum of the bare cluster depicted in the lower part of Fig. 2.11 already captures these structures.

Similar features were also observed in finite size QMC simulations for an 8×8 sized lattice [Pre95]. Therein the narrow low energy feature, which was also seen at half-filling, was attributed to magnetic correlations. Such a narrow band has also been found in studies for the situation of one hole doped into an antiferromagnetic background in the tJ-model [Dag94b, Poi93] as well as for finite dopings in exact diagonalization studies for the 2D Hubbard model [Dag92, Leu92]. The underlying mechanism is schematically illustrated in Fig. 3.12 for the situation of one hole doped into the antiferromagnetically ordered background. Along its path the hole destroys antiferromagnetic bonds to nearest neighbors. As a consequence the total energy of the system increases with the number of steps of the hole. Effectively this acts on the hole as a confining potential linear in $J = 4t^2/U$, which tends to localize it. The result is a quasiparticle band of width $\sim J$ (for a detailed discussion see [Dag94a]).

In the paramagnetic state no long-range antiferromagnetic order is present. However even for short-range antiferromagnetic order this picture should still hold to some extent. Since the observed narrow peak in the DOS indeed has a width $\sim J = 4t^2/U \approx 0.3t$, it seems reasonable to conclude that it is closely related to the presence of short range antiferromagnetic order in the paramagnetic state.

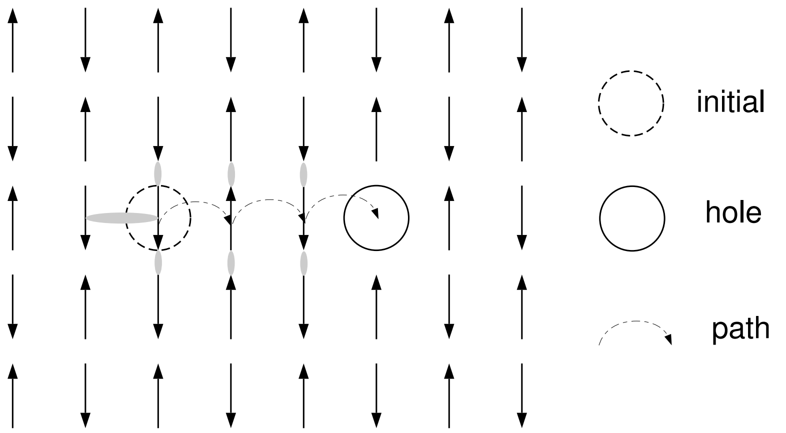

FIGURE 3.12: *Sketch of the motion of a hole in the antiferromagnetically ordered background. The hatched grey symbols indicate destroyed bonds.*

It is important to emphasize the difference in the origin of the narrow peaks in the $N_c = 1$ and 4 result, respectively. In the $N_c = 1$ result the narrow peak is located right at the Fermi energy, $\omega = 0$. It was shown that it is due to local

Kondo-like physics, where the local effective magnetic moment is screened due to the formation of a local singlet state [Pru95b]. The result is a Fermi liquid. In contrast, in the $N_c = 4$ result the narrow structure sits slightly below the Fermi energy ($\omega \lesssim 0$), in contrast to a Kondo-peak which is expected to be located at the the Fermi energy $w = 0$. When $N_c = 4$ the narrow peak rather originates in nonlocal antiferromagnetic correlations as explained by Fig. 3.12. As in the half-filled system Kondo-like physics is found to be completely suppressed in the $N_c = 4$ result at finite doping.

3.3.2 Pseudogap

This result is further substantiated by inspecting the low energy region of the spectrum, where a loss of spectral weight is detected right at $\omega = 0$ when $N_c = 4$. To better resolve this feature, Fig. 3.13 shows the DOS $N(\omega)$ in a narrow energy

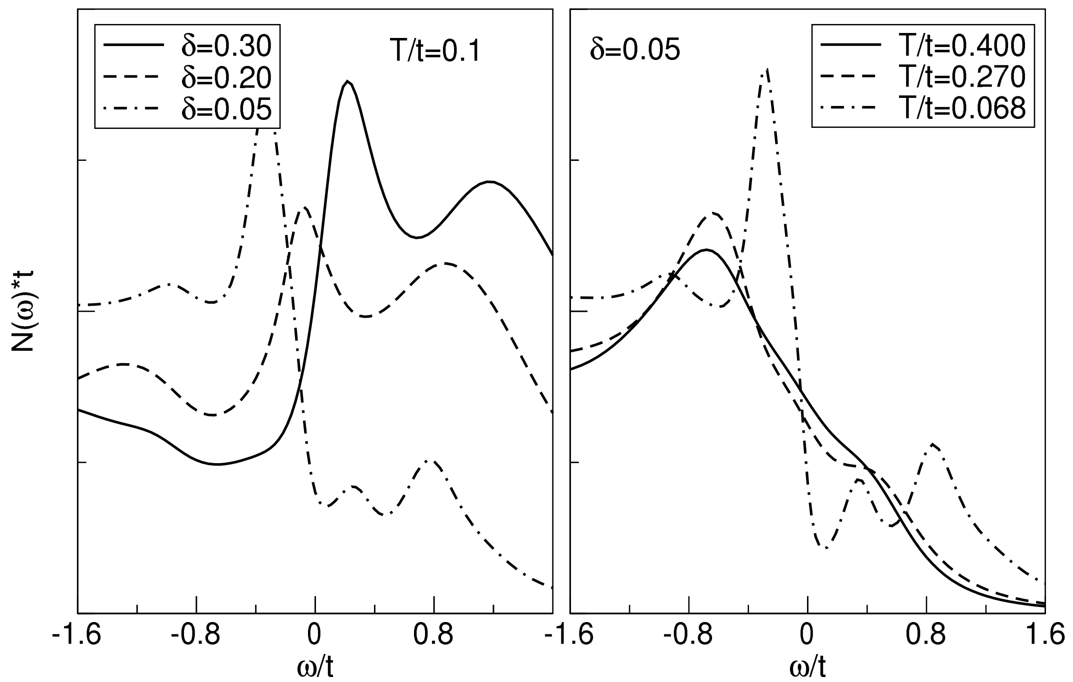

FIGURE 3.13: *The doping dependence at fixed temperature $T = 0.1t$ (left panel) and temperature dependence at fixed doping $\delta = 0.05$ (right panel) of the DOS when $N_c = 4$, $U = 12t$ and $t' = 0$ for energies near the Fermi level. With decreasing doping and temperature a pseudogap develops at the Fermi energy.*

region around the Fermi energy for three dopings δ at fixed temperature $T = 0.1t$ (left panel) and three temperatures T at fixed doping $\delta = 0.05$ (right panel) when $N_c = 4$, $U = 12t$ and $t' = 0$. At high doping, $\delta = 0.30$ and/or high temperature $T > 0.3t$ no pseudogap at $\omega = 0$ is seen. As the doping is reduced from $\delta = 0.20$

(left panel) the peak at the Fermi energy moves to negative frequencies and the pseudogap develops at the Fermi energy for low enough temperatures. And as the temperature is lowered at fixed doping $\delta = 0.05$ (right panel) the DOS distorts at the Fermi level and the pseudogap emerges for temperatures $T < 0.3t$. It is important to point out that the temperature $T \approx 0.3t$ where the pseudogap starts to develop in the weakly doped system ($\delta = 0.05$) is seen to be of the order of the magnetic exchange interaction $J = 4t^2/U \approx 0.3t$. This strongly suggests that the development of the pseudogap at finite doping has a magnetic origin as in the half-filled system. This would also explain the pronounced doping dependence of the pseudogap. As the doping level increases the antiferromagnetic correlations are weakened and hence the pseudogap diminishes. Also, a similar pseudogap behavior was found in self-consistent perturbative calculations (FLEX) for the weak coupling regime based on the exchange of spin-fluctuations [Lan95]. However, so far it was not clear if the pseudogap also survives in the strong coupling regime. The results presented in Fig. 3.13 clearly demonstrate that even in the strong coupling regime the low energy physics of the weakly doped 2D Hubbard model is dominated by the evolution of the pseudogap at the Fermi energy.

Another remarkable feature observed in Fig. 3.13 is the temperature dependence of the narrow peak below the Fermi surface. As the temperature is increased the peak broadens and simultaneously diminishes. Since the antiferromagnetic correlations are also suppressed with increasing doping and temperature, this is further evidence for the conjecture that the narrow quasiparticle structure below the Fermi surface results from the short-ranged antiferromagnetic ordering.

The evolution of a pseudogap in the DOS is also observed in ARPES experiments on under- and optimally doped cuprates (see Fig. 1.5 in Sec. 1.1). However, in experiments the pseudogap was first observed in the spin-channel, as probed e.g. by NMR-experiments (see Fig. 1.4 in Sec. 1.1).

3.3.3 Spin susceptibility

To investigate the spin channel within the DCA approach to the 2D Hubbard model, the uniform spin susceptibility $\chi(\mathbf{q} = 0)$ was calculated. In experiments this quantity is probed e.g. by Knight-shift measurements (see Sec. 1.1). To evaluate $\chi(\mathbf{q} = 0)$, a finite uniform magnetic field h is applied (see Sec. 2.6.1) and the magnetization $m(h) = |n_\uparrow - n_\downarrow|$ (Eq. (2.65)) is calculated for various magnitudes of the external magnetic field h. The uniform spin susceptibility at a given temperature T is then obtained from the relation

$$\chi(\mathbf{q} = 0, T) = \left.\frac{\partial m(h)}{\partial h}\right|_{h=0} . \tag{3.6}$$

For very small values of h the magnetization shows linear behavior in h so that the extrapolation to $h = 0$ can be easily performed. In Fermi liquid metals this quantity is expected to be temperature independent at low temperatures. Fig. 3.14

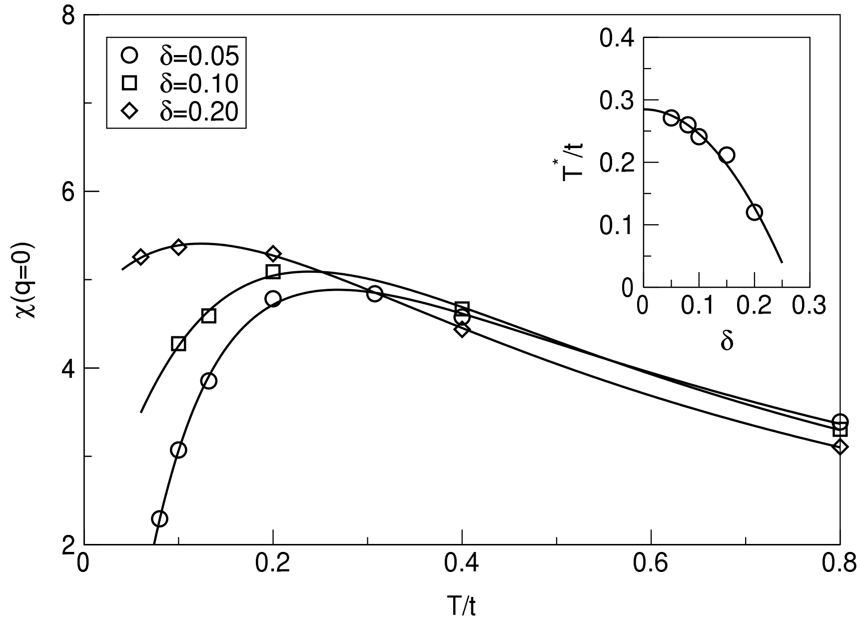

FIGURE 3.14: *The uniform spin susceptibility $\chi(\mathbf{q}=0)$ when $N_c = 4$, $U = 12t$ and $t' = 0$ plotted versus temperature for three dopings δ. The inset shows the doping dependence of the temperature $T^\star$ defined as the temperature where $\chi(\mathbf{q}=0)$ is maximal. The solid lines are guides to the eye only.*

shows the DCA result for the uniform spin susceptibility $\chi(\mathbf{q}=0)$ when $N_c = 4$, $U = 12t$ and $t' = 0$ as a function of temperature T for three dopings δ. As a function of decreasing temperature the susceptibility first increases, reaches a maximum and then drops again as the temperature further decreases. With increasing doping δ the temperature where this anomaly occurs moves to lower temperatures. For $\delta > 0.3$ (not shown) no sign of a maximum in $\chi(\mathbf{q}=0,T)$ can be seen anymore. This suppression of the spin susceptibility at low temperatures in the weakly doped system is similarly seen in Knight shift data on underdoped cuprates (see Fig.1.4 panel (c) in Sec. 1).

A temperature $T^\star$ can be defined as the temperature where the maximum in $\chi(\mathbf{q}=0,T)$ as a function of T occurs. The inset to Fig. 3.14 shows $T^\star$ as a function of doping. $T^\star$ is maximal near half-filling, $T^\star \approx 0.3t$, and decreases rapidly with increasing doping δ. The maximal $T^\star$ roughly equals $J = 4t^2/U \approx 0.3t$ and hence is quite close to the temperature where the pseudogap starts to emerge in the DOS of the weakly doped system. Furthermore both $T^\star$ and the temperature where the pseudogap becomes apparent in the DOS decrease with doping. Thus both effects, the pseudogap in the DOS and the anomaly in the susceptibility seem to be closely related. The fact that the relevant energy scale for these features is set by the exchange interaction J strongly suggests that antiferromagnetic correlations induce this behavior. Obviously even in the paramagnetic phase their effect is still significant for $\delta \lesssim 0.2$.

It is important to stress that for $N_c = 1$ the anomaly in the susceptibity and the pseudogap in the DOS are absent due to the lack of nonlocal fluctuations. In contrast to the $N_c = 4$ result the DMFA result shows Fermi liquid behavior indicated by a Kondo-like peak for the whole range of finite doping levels [Pru95b].

3.3.4 Nonlocal spectra

To gain more insight in the character and $\mathbf{k}$-dependence of the low energy excitations, it is useful to investigate the single-particle self-energy $\Sigma(\mathbf{k}, \omega)$ first, for frequencies ω and $\mathbf{k}$-vectors near the Fermi surface. Since within the DCA

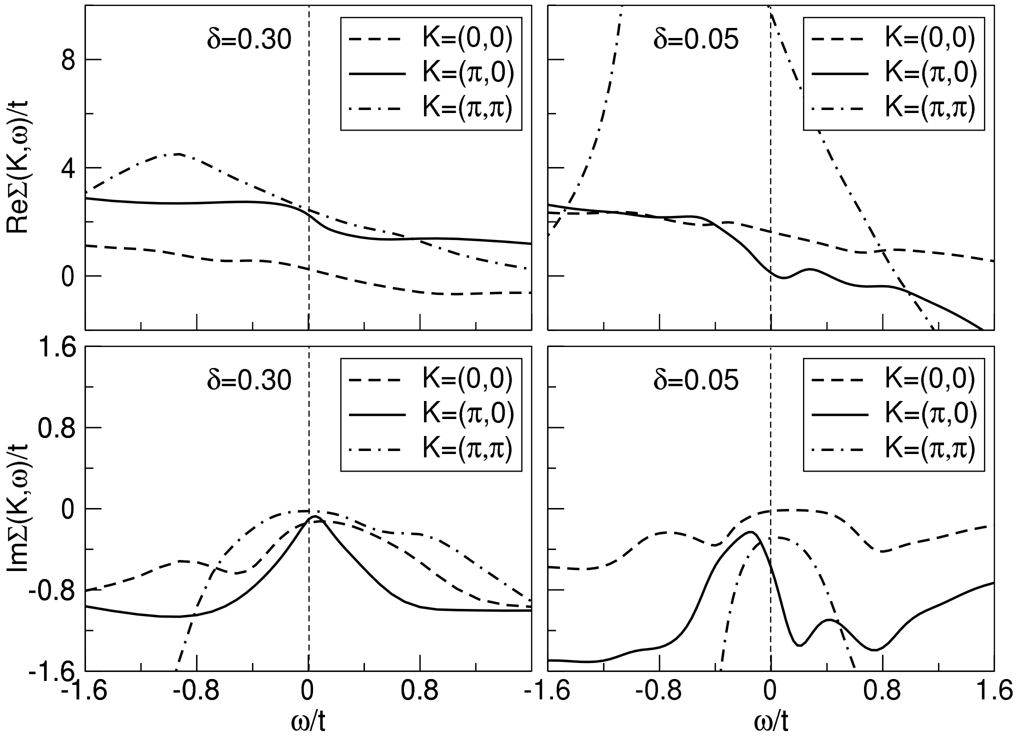

FIGURE 3.15: *The real and imaginary parts of the self-energy $\Sigma(\mathbf{K}, \omega)$ at the DCA cluster $\mathbf{K}$-points, plotted versus frequency near the Fermi energy for $N_c = 4$, $U = 12t$, $t' = 0$ and $T = 0.1t$. In the highly doped system ($\delta = 0.30$, left panel) the self-energy is Fermi liquid-like, whereas when $\delta = 0.05$ (right panel) it displays non-Fermi liquid behavior in the cell centered at the cluster $\mathbf{K}$-point $(\pi, 0)$.*

the self-energy $\Sigma(\mathbf{k}) = \Sigma(\mathbf{K} = \mathbf{M}(\mathbf{k}))$ is constant[7] within the cell about the cluster momentum $\mathbf{K}$, the lattice self-energy $\Sigma(\mathbf{k})$ at any $\mathbf{k}$ is given by the cluster self-energy $\Sigma(\mathbf{K})$ at the nearest $\mathbf{K}$. Fig. 3.15 presents the self-energy $\Sigma(\mathbf{K}, \omega)$ at

[7] $\mathbf{M}(\mathbf{k})$ is the function which maps $\mathbf{k}$ onto the nearest cluster $\mathbf{K}$-point (see Sec. 2.3.1).

the DCA cluster **K**-points for frequencies near the Fermi energy when $N_c = 4$, $U = 12t$, $t' = 0$ and $T = 0.1t$ in the highly doped ($\delta = 0.30$, left panel) and weakly doped ($\delta = 0.05$, right panel) system.

In Fermi liquids the self-energy fulfills the relation (3.5). When $\delta = 0.30$ (left panel) the imaginary part of $\Sigma(\mathbf{K}, \omega)$ shows a parabolic maximum at zero frequency at all **K**-points accompanied by a negative slope in the real part, clearly indicating Fermi liquid behavior with reduced quasiparticle weight Z according to Eq. (3.5). Near half-filling (right panel) the situation changes. When $\delta = 0.05$ non-Fermi liquid behavior is found. At $\mathbf{K} = (\pi, 0)$, and therefore in the DCA-cell centered at $(\pi, 0)$ the imaginary part of the self-energy crosses the Fermi surface almost linearly. On the other hand, for momenta near the zone center and $\mathbf{K} = (\pi, \pi)$ the self-energy is still Fermi liquid-like.

The observed doping dependence and the anisotropy of the character of the low energy excitations in the weakly doped system is also confirmed by an inspection of the **k**-dependent spectral function $A(\mathbf{k}, \omega)$. To obtain a smooth spectrum, the cluster self-energy $\Sigma(\mathbf{K}, \omega)$ is interpolated to the full lattice BZ using the interpolation scheme (2.118). It should be pointed out that e.g. bilinear interpolation yields almost identical results for the spectra. Thus, the qualitative behavior of the spectra is not expected to show any dependence on the choice of a particular interpolation scheme.

Fig. 3.16 depicts the spectral density $A(\mathbf{k}, \omega)$ for frequencies near the Fermi energy when $N_c = 4$, $U = 12t$, $t' = 0$ and $T = 0.1t$ along high symmetry directions for three different dopings $\delta = 0.30$ (left panel), $\delta = 0.20$ (center panel) and $\delta = 0.05$ (right panel). The overall dispersion of the band crossing the Fermi surface follows that of the non-interacting system, given by $\epsilon_{\mathbf{k}}$ (see right panel of Fig. 3.7). Independent of doping, the dispersion is very flat in the region near $X = (\pi, 0)$ with an extended saddle point, but strongly **k**-dependent between $\Gamma = (0, 0)$ and $M = (\pi, \pi)$, i.e. near $(\pi/2, \pi/2)$. As the life-time of a state is a function of its energy, the peak narrows and grows in height when it approaches the Fermi energy. In the highly doped system ($\delta = 0.30$) no signs of a pseudogap are found. The spectrum displays well defined quasiparticles at the Fermi surface near $(\pi/2, \pi/2)$ as well as near $X = (\pi, 0)$, indicating a weakly renormalized Fermi liquid. Upon reducing doping the quasiparticle life-time increases indicated by the reduced spectral density at the Fermi energy for $\delta = 0.20$. At this doping level the flat part of the dispersion is found very close to the Fermi energy, a feature that was also pointed out in ARPES experiments on near optimally doped BSCCO [Des93] as the most striking aspect of the spectrum. In the weakly doped system, $\delta = 0.05$, a depression of the spectral function $A(\mathbf{k}, \omega)$ at the Fermi energy $\omega = 0$ is found at the points near $X = (\pi, 0)$. Along the diagonal, i.e. near the point $(\pi/2, \pi/2)$, the spectrum is still peaked where the band crosses the Fermi surface. Thus, the observed anisotropy of the normal state pseudogap in the weakly doped 2D Hubbard model agrees with ARPES experiments on underdoped cuprates

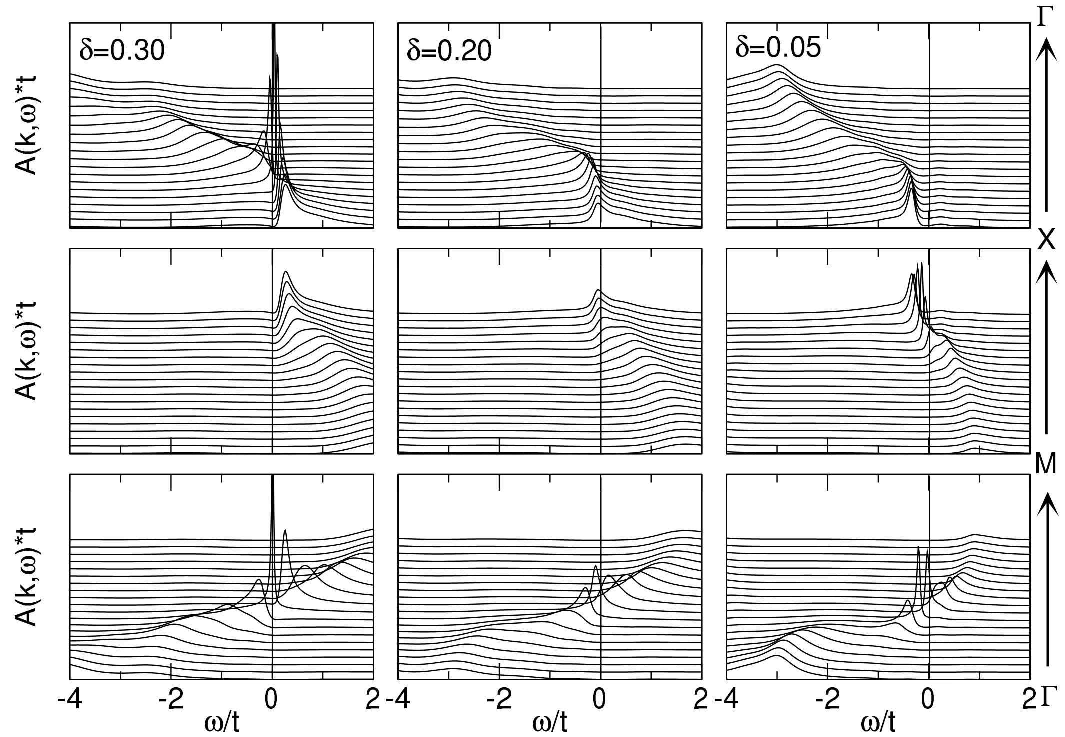

FIGURE 3.16: *The angle resolved spectral function $A(\mathbf{k},\omega)$ along the main symmetry directions in the BZ when $N_c = 4$, $U = 12t$, $t' = 0$ and $T = 0.1t < T^\star$ for $\delta = 0.30$ (left panel), $\delta = 0.20$ (center panel) and $\delta = 0.05$ (right panel). The low energy excitations change their character from Fermi liquid-like in the highly doped system to non-Fermi liquid-like in the weakly doped system.*

summarized in Fig. 1.5. The pseudogap has a node along the diagonal and opens along the direction of k_x, i.e. near $(\pi, 0)$.

Another noteworthy feature is the doping dependence of the energy of the states near $X = (\pi, 0)$. In the highly doped system they form a saddle point region above the Fermi surface. Upon decreasing doping, the energy of these states decreases until the flat part of the spectrum moves below the Fermi surface in the for $\delta = 0.05$.

3.3.5 Fermi surface

There is more than one way to define the Fermi surface of an interacting Fermionic system. It can be defined as the surface in **k**-space separating regions in the BZ where the momentum distribution function

$$n(\mathbf{k}) = \int_{-\infty}^{+\infty} \mathrm{d}\varepsilon\, f(\varepsilon) A(\mathbf{k}, \varepsilon) \tag{3.7}$$

is larger then 0.5 (occupied states) and smaller than 0.5 (unoccupied state), respectively. An alternative way is to define the Fermi surface as the set of $\mathbf{k}$-points, where $A(\mathbf{k}, \omega)$ is maximal for $\omega = 0$, which (in Fermi liquids) is equivalent to the solution of the equation $\omega - \epsilon_{\mathbf{k}} + \mu - \mathrm{Re}\,\Sigma(\mathbf{k}, \omega)$ for $\mathbf{k}$ and $\omega = 0$.

The method used in this work is based on the inspection of the $\mathbf{k}$-dependence of $n(\mathbf{k})$. As pointed out in Sec. 1.1, $n(\mathbf{k})$ shows a discontinuity as a function of $|\mathbf{k}|$ in Fermi liquids at zero temperature which then defines the Fermi surface. Thus the Fermi surface at finite temperatures may be defined by the maximum value of $|\nabla_{\mathbf{k}} n(\mathbf{k})|$. This way of defining the Fermi surface should be equivalent to the one before, since $n(\mathbf{k})$ is expected to show a significant drop at those $\mathbf{k}$-points where a maximum of the spectral function $A(\mathbf{k}, \omega)$ crosses the Fermi surface. The shape of $|\nabla_{\mathbf{k}} n(\mathbf{k})|$ at finite temperatures also contains information about the character of low energy excitations. The sharper $|\nabla_{\mathbf{k}} n(\mathbf{k})|$ is, the smaller is the scattering rate on the Fermi surface. Thus a broad shape of $|\nabla_{\mathbf{k}} n(\mathbf{k})|$ at low temperatures indicates non-Fermi liquid behavior.

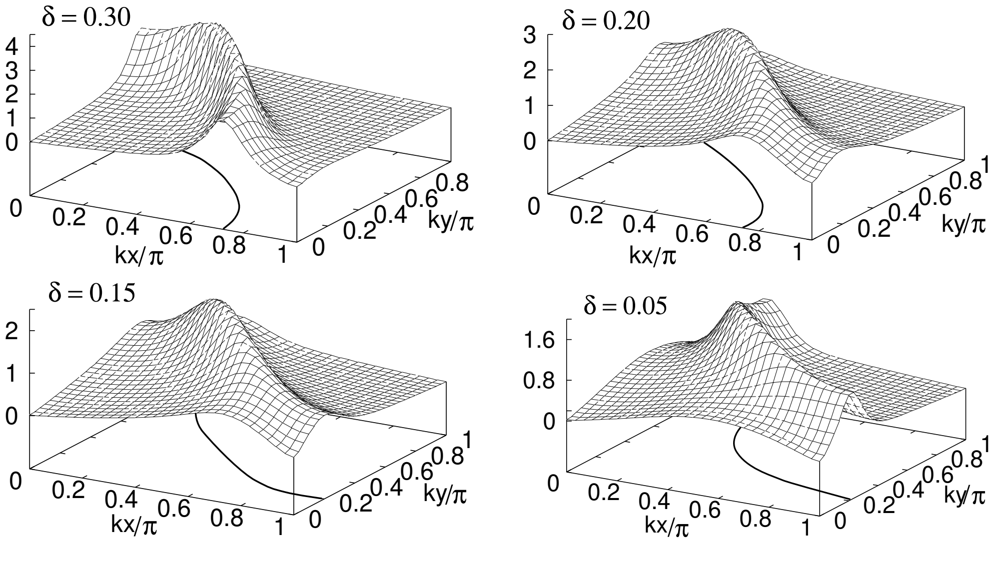

FIGURE 3.17: *The doping dependence of the absolute gradient of the occupation* $|\nabla_{\mathbf{k}} n(\mathbf{k})|$ *when* $N_c = 4$, $U = 12t$, $t' = 0$ *and* $T = 0.1t$. *The solid line on the bottom planes indicates the maximum of* $|\nabla_{\mathbf{k}} n(\mathbf{k})|$. *With decreasing doping the Fermi surface is smeared out and closes around the* M*-point.*

For $U = 0$ the Fermi surface of the half-filled system is depicted in Fig. 3.1. For every $\delta > 0$ the Fermi surface of the non-interacting system centers around $(0, 0)$ when $t' = 0$, since less states are occupied. Fig. 3.17 illustrates the effect of the correlations on the shape of the Fermi surface by plotting the gradient of the occupation in $\mathbf{k}$-space $|\nabla_{\mathbf{k}} n(\mathbf{k})|$ for $N_c = 4$, $U = 12t$, $t' = 0$ and $T = 0.1t$ for various dopings from the highly to the weakly doped regime in the first quadrant of the BZ.

In the highly doped system ($0.20 \leq \delta \leq 0.30$) the Fermi surface indeed shows the expected form, centered at $(0,0)$. This and its sharp structure resulting from the well defined quasiparticles found in $A(\mathbf{k},\omega)$ (see Fig. 3.16) indicate Fermi liquid behavior. With decreasing doping two remarkable effects set in. First, the Fermi surface begins to get blurry, especially in the region near $(\pi,0)$. The maximal value of $|\nabla_{\mathbf{k}} n(\mathbf{k})|$ decreases from 4.5 at $\delta = 0.30$ to about 2 at $\delta = 0.05$. Second, it starts to close around the M-point, i.e. (π,π). At $\delta = 0.05$ $|\nabla_{\mathbf{k}} n(\mathbf{k})|$ shows a blurry barrel shaped form, i.e. it is strongly reduced near the zone corners $(\pi,0)$ and $(0,\pi)$. This shape results from the anisotropy of the spectrum in the weakly doped system (see Fig. 3.16), which displays well defined quasiparticles near $(\pi/2,\pi/2)$ but a pseudogap near the zone corner $(\pi,0)$. Especially in the region near $(\pi,0)$ and $(0,\pi)$ the Fermi surface cannot be defined anymore.

This destruction of the Fermi surface at low temperatures is similarly observed in experiments on underdoped BSCCO [Nor97]. The authors find a Fermi surface closed around the M-point, which breaks up into disconnected arcs located near $(\pi/2,\pi/2)$ below a temperature $T^\star$. They determine the Fermi surface from ARPES measurements and find that the spectrum near $(0,\pi)$ becomes gapped first, consistent with the results presented here. The remarkable change in the topology of the Fermi surface, from an electron-like shape centered at Γ in the overdoped system to a hole-like Fermi surface centered at M in the underdoped case, is also found in experiments on LSCO samples [Ino98] (see Fig. 3.18). They find that this occurs through a decrease of the energy of the states near $(\pi,0)$ as the doping level is reduced. In the $(\delta =)x = 0.3$ sample these states are above the Fermi surface, whereas in the underdoped sample they form an extended saddle point about 100 meV below the Fermi surface. As a remarkable fact, the ARPES spectra obtained via the DCA for the 2D Hubbard model illustrated in Fig. 3.16 display exactly the same behavior.

It is important to stress that the results presented here are basically consistent with the predictions of the Nearly Antiferromagnetic Fermi Liquid Theory (NAFL) proposed by D. Pines and coworkers (see discussion in Sec. 1.1, for a review see [Pin97]). In this theory the magnetic interaction between the quasiparticles is held responsible for the anomalous normal state behavior found in the under- to optimally doped cuprates. As a result of the strong anisotropic antiferromagnetic correlations (see Sec. 1.1), the spectrum becomes gapped near $(\pi,0)$ but well defined quasiparticles are found along the diagonal, consistent with the results presented here.

However, it is important to point out a major difference. In the NAFL approach, the spectrum of the non-interacting quasiparticles is chosen so that it resembles the Fermi surface of the cuprates by taking a finite next-nearest neighbor hopping t' (see Fig. 1.6). The magnetic interaction is then found to alter the Fermi surface only slightly [Sch99]. In contrast to this, the DCA results presented

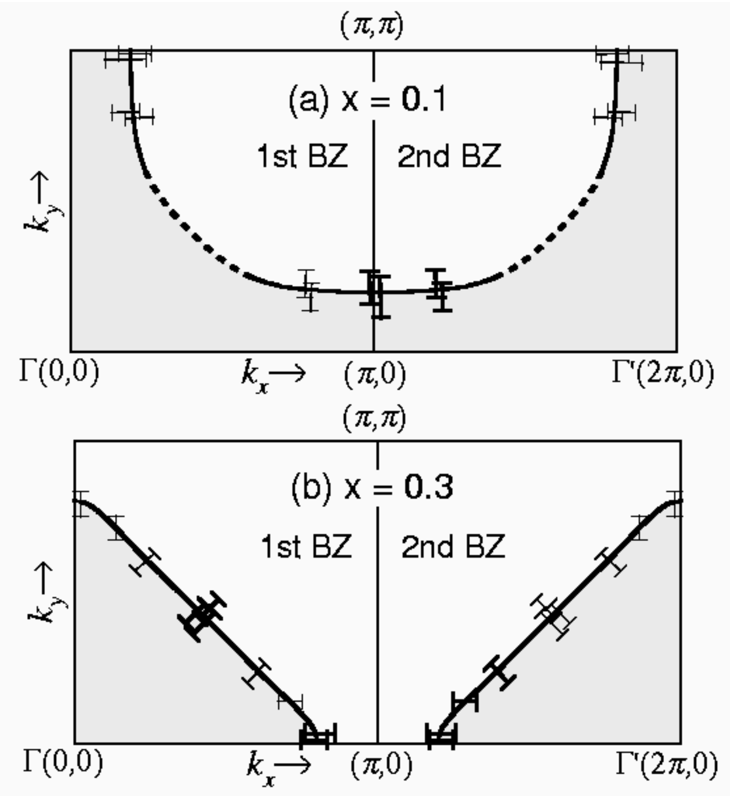

FIGURE 3.18: *Experimental Fermi surface in LSCO (solid line). The shaded region marks the occupied states. The Fermi surface in the highly doped system ($(\delta =)x = 0.3$, bottom) is electron-like since the states near $(\pi, 0)$ lie above the Fermi surface. With reduced doping ($(\delta =)x = 0.1$, top) the states at $(\pi, 0)$ drop below the Fermi level and a hole-like Fermi surface results. Taken from [Ino98].*

here are based on the dispersion with zero t'. Thus the $U = 0$ Fermi surface is closed around Γ and does not contain any hot spots (see Sec. 1.1). What is found here, is that in the underdoped system it is the nonlocal correlations that change the shape of the Fermi surface significantly to the Fermi surface closed around the M-point. No additional finite value of t' is needed to obtain the Fermi surface found in the high-T_c superconductors. Nevertheless, even though the weak coupling arguments of the NAFL theory do not apply to the calculations presented here, both methods yield consistent results.

3.3.6 Dependence on the magnitude of U

To substantiate the conjecture that antiferromagnetic spin fluctuations are responsible for the emergence of the pseudogap, it is instructive to inspect the spectrum near $(\pi, 0)$ as a function of the interaction strength U. To this end,

Fig. 3.19 displays the coarse grained spectrum $\bar{A}(\mathbf{K},\omega) = N_c/N \sum_{\mathbf{k}'} A(\mathbf{K}+\mathbf{k}',\omega)$ in the weakly doped system ($\delta = 0.05$) when $N_c = 4$ at $\mathbf{K} = (\pi, 0)$ and $T = 0.1t$ for frequencies near the Fermi energy and different values of U in the strong coupling regime ($U > W$). $\bar{A}((\pi,0),\omega)$ collects the spectrum in the cell centered at $(\pi, 0)$ and hence is the relevant object to resolve the pseudogap. The reduced DOS near the Fermi energy is clearly visible for all values of U. As U increases from $U = 8t$, the pseudogap first decreases in its width ($U = 12t$) and then diminishes for larger values of U. This result is obviously compatible with spin-fluctuation induced renormalizations of the quasiparticles. As U increases, the antiferromagnetic spin-correlations $\sim J \propto t^2/U$ are weakened and hence the pseudogap diminishes.

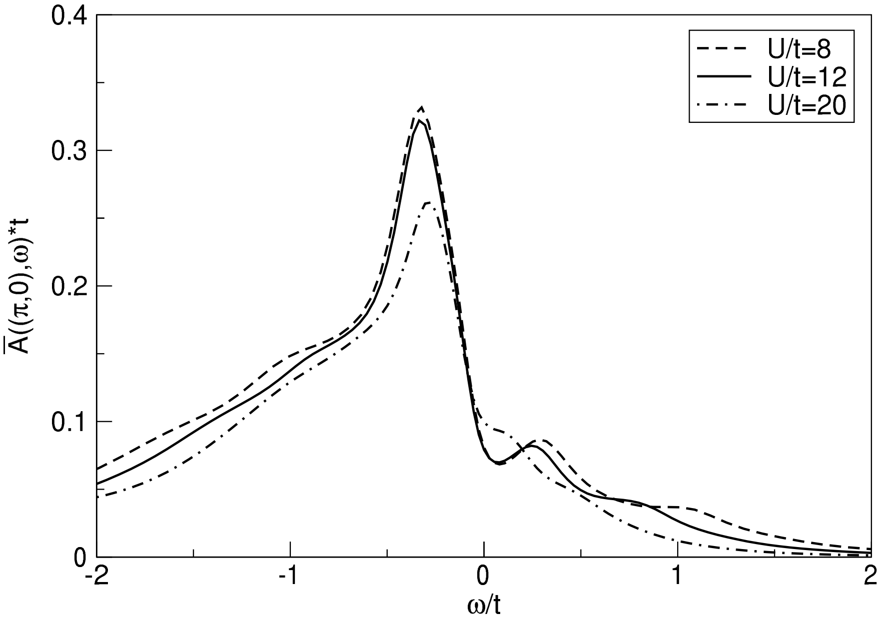

FIGURE 3.19: *The coarse grained spectrum $\bar{A}(\mathbf{K},\omega)$ for $\delta = 0.05$ when $N_c = 4$ at $\mathbf{K} = (\pi, 0)$ and $T = 0.1t$ for frequencies near the Fermi energy and different magnitudes of the interaction strength U. The pseudogap diminishes as U increases.*

The observed behavior of the pseudogap upon increasing U strongly suggests that the relevant energy scale in the weakly doped Hubbard model is determined by spin-correlations $\sim J \propto t^2/U$. Furthermore since the temperature scale, where the pseudogap vanishes, $T^\star \approx J$ it seems reasonable to expect that the weakly doped tJ-model exhibits similar pseudogap physics.

3.3.7 tJ-model

Motivated by the results for the Hubbard model, additional calculations for the tJ-model were performed. In the strong coupling regime ($U \gg W$) the tJ-model is believed to capture the physics of the Hubbard model. As an advantage, the strength of the antiferromagnetic correlations in the tJ-model can be directly controlled by the exchange parameter J, which when positive favors antiferromagnetic correlations. Recent ED studies for the tJ-model on finite size systems [Jak99] showed that indeed the weakly doped model exhibits a pseudogap in the DOS for temperatures $T < J$.

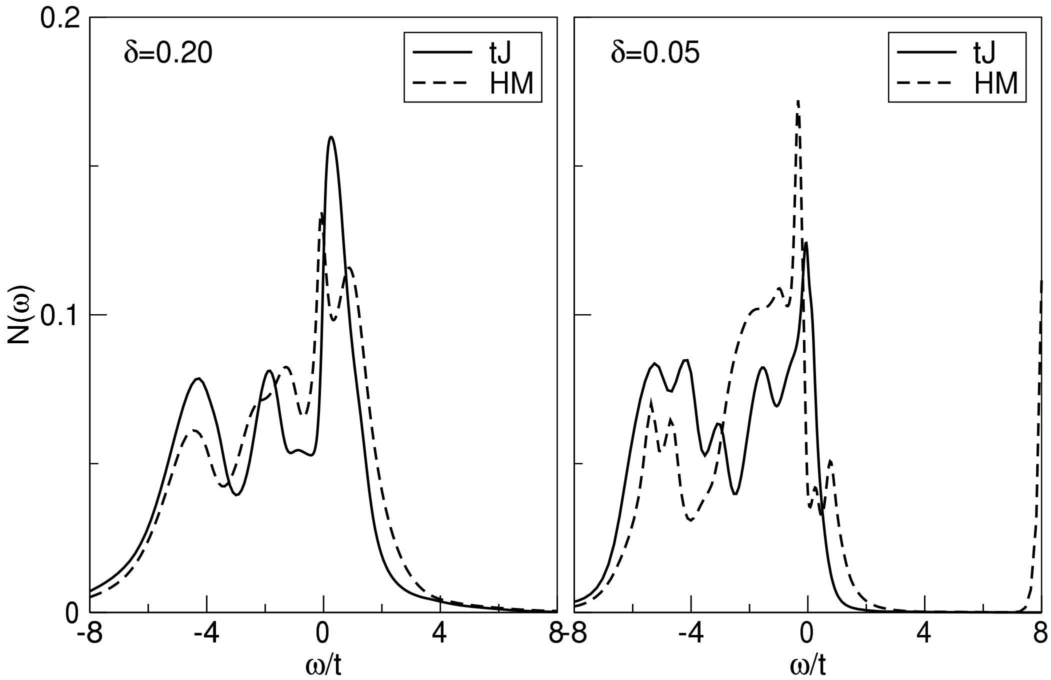

FIGURE 3.20: *The DOS $N(\omega)$ of the tJ-model (solid line) when $J = 0.3t$ compared to the DOS (lower Hubbard band) of the Hubbard model (dashed line) when $U = 12t$. The cluster size $N_c = 4$, temperature $T = 0.1t$ and doping $\delta = 0.20$ (left) and $\delta = 0.05$ (right). Whereas the overall spectrum is captured by the tJ-model, no pseudogap is seen in the DOS of the tJ-model for this magnitude of J.*

Fig. 3.20 depicts the DCA-NCA result for the DOS $N(\omega)$ of the tJ-model (solid line) when $\delta = 0.20$ (left panel) and $\delta = 0.05$ (right panel), $N_c = 4$ and $T = 0.1t$ compared to the low energy part of the DOS of the Hubbard model (dashed line) at the same doping level. For the tJ-model the exchange interaction $J = 0.3t \approx 4t^2/U$, where $U = 12t$ is the value of the Coulomb interaction of the corresponding results for the Hubbard model.[8]

[8]The full spectrum of the Hubbard model (see Fig. 3.11) displays a second band at hig-

On large energy scales the DOS of the tJ-model captures the spectrum of the lower sub-band of the Hubbard model fairly well, including the quasiparticle peak slightly below the Fermi energy in the weakly doped system ($\delta = 0.05$). The broadening of this peak with increasing doping is also well described by the tJ-model. However, the dominant feature of the Hubbard model, i.e. the pseudogap at zero frequency, is not reflected in the spectrum of the tJ-model, at least not for this magnitude of $J = 0.3t$.

Since this result seems to be in contrast to the corresponding result for the Hubbard model, further calculations with larger values for J were performed. The hope is that similarly to the Hubbard model where the pseudogap becomes more pronounced as U decreases (see Fig. 3.19), the tJ-model might show pseudogap behavior as the magnitude of $J \propto 1/U$ increases. Fig. 3.21 depicts the

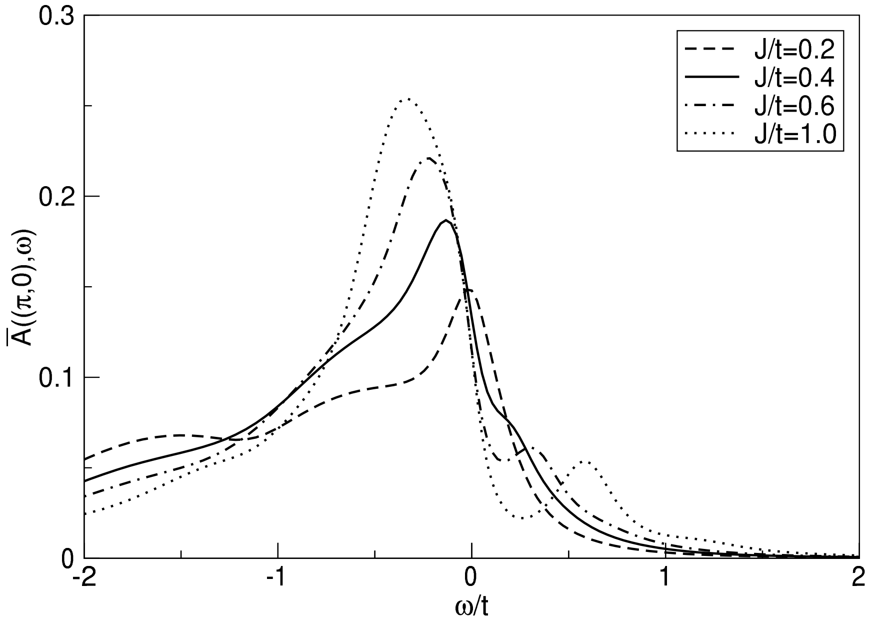

FIGURE 3.21: *The coarse grained spectrum $\bar{A}(\mathbf{K},\omega)$ of the tJ-model when $N_c = 4$ at $\mathbf{K} = (\pi, 0)$ and $T = 0.1t$ for frequencies near the Fermi energy, doping $\delta = 0.05$ and different magnitudes of the exchange interaction J. As J increases the pseudogap starts to emerge and widens proportional to J.*

coarse grained spectrum $\bar{A}(\mathbf{K},\omega)$ of the tJ-model when $N_c = 4$ and $T = 0.1t$ at $\mathbf{K} = (\pi, 0)$ for frequencies near the Fermi energy and different magnitudes of the exchange interaction J. When $J = 0.2t$ no sign of a pseudogap is observed. However, upon increasing magnitude of J, a pseudogap starts to develop near

her frequencies (upper Hubbard band) representing the high energy excitations which are not included in the tJ-model.

zero frequency ($J = 0.4t$). Obviously, as J is further raised, the pseudogap width measured from peak to peak increases. In fact, the width of the pseudogap $\sim J$.

However, the pseudogap in the DOS does not open until $J = 0.4t$, significantly larger than the temperature $T = 0.1t$. This is in contrast to the results presented for the Hubbard model where the pseudogap was found to emerge at $T^\star \approx J$. One possible explanation for this discrepancy could be the fact that for this value of U the tJ-model does not fully capture the low-energy physics of the Hubbard model. However, since the ED results for the spectrum of the weakly doped tJ-model presented in [Jak99] provide evidence that the pseudogap scale in the tJ-model is also given by J, the difference must be attributed to the fact that the DCA-NCA approach presented in Sec. 2.7 underestimates the effects of the exchange interaction J on the spectrum of the tJ-model.

For the following reason this indeed seems rather plausible: As pointed out in Sec. 2.7, the DCA-NCA approach to the tJ-model accurately describes the effect of J on the cluster, but reduces the interaction in J to a mean field like coupling between cluster and effective medium. Thus, in the paramagnetic state this mean field like coupling vanishes and J is accurately represented on the cluster only. In contrast, the Hubbard model implicitly contains the effects of the nonlocal antiferromagnetic coupling $\sim t^2/U$ between sites on the cluster and the effective medium by combining the kinetic energy term $\sim t$ with the local interaction U. The different pseudogap scales observed for the tJ-model and the Hubbard model follow as a natural consequence of the neglect of these effects in the tJ-model. An extended DCA approach to the tJ-model, or more generally to models with extended range interaction may be formulated by introducing a self-consistent Bosonic bath in addition to the Fermionic effective medium described by $\mathcal{G}$ (see App. D in [Het00]). These additional Bosonic baths reflect the influence on the two-particle level of the rest of the lattice on the DCA cluster and thus additionally renormalize the spectrum. However, an inclusion of such an additional Bosonic field in the presented NCA approach to the cluster model requires the evaluation of two particle correlations functions (the spin susceptibility in the case of the tJ-model). Though formally possible, due to the associated enormous numerical effort this is not feasible for the time being. Nevertheless, it was clearly shown that the weakly doped tJ-model exhibits qualitatively the same low energy behavior as the Hubbard model in that it forms a pseudogap with a width that scales with the exchange interaction J.

3.3.8 Summary

In summary, short-ranged antiferromagnetic correlations drive the weakly to moderately doped 2D Hubbard model to show non-Fermi liquid behavior. Below $T^\star$, the crossover temperature determined from the anomaly in the uniform spin susceptibility, a pseudogap opens in the DOS at the Fermi level. The study of the

$\mathbf{k}$-dependent spectrum reveals a strong anisotropy of the gap. The spectrum near $(\pi, 0)$ is gapped, whereas well defined quasiparticles are found near $(\pi/2, \pi/2)$, consistent with experiments on underdoped cuprate superconductors. Furthermore, the energy of the states at $(\pi, 0)$ is strongly renormalized so that they lie below the Fermi energy in the weakly doped system. As a consequence, the Fermi surface in the underdoped system closes around the M-point, topologically different from the corresponding non-interacting Fermi surface. As the doping level increases the magnetic correlations become less pronounced and hence Fermi liquid behavior is recovered. In the highly doped system the spectrum shows well defined quasiparticle peaks at all points in the BZ. The Fermi surface shows the expected shape closed around Γ and simultaneously becomes sharper, resulting from the weakly renormalized quasiparticles observed in the spectrum. The fact that $T^\star$, the temperature where the pseudogap first becomes apparent in the spectrum is of the order of the exchange interaction $J = 4t^2/U$ and the observed dependence of the pseudogap scale on the on-site repulsion U provide strong evidence that the non-Fermi liquid behavior in the weakly doped system originates in short-ranged antiferromagnetic spin-fluctuations.

3.4 Optimal doping - Superconductivity

In the last section the DCA for $N_c > 1$ was shown to accurately capture the effects of antiferromagnetic spin-correlations in the normal phase. Since from a weak coupling point of view the latter are known to induce $d_{x^2-y^2}$-superconductivity (see discussion of NAFL theory in Sec. 1.1) it seems reasonable to devote some effort to the search of superconductivity within the DCA approach.

3.4.1 Order parameter

In the DCA approximation the resolution in $\mathbf{k}$-space is restricted to the cluster $\mathbf{K}$-points and according to Eq. (2.76) superconducting order parameters

$$\bar{\Delta}_{\mathbf{K}} = \frac{N_c}{N} \sum_{\mathbf{k}'} \langle c_{\mathbf{K}+\mathbf{k}'\uparrow} c_{-(\mathbf{K}+\mathbf{k}')\downarrow} \rangle \tag{3.8}$$

are coarse grained or averaged over the cells centered at $\mathbf{K}$. The sum over $\mathbf{k}'$ in Eq. (3.8) runs over the N/N_c momenta within the DCA coarse graining cell centered at $\mathbf{K}$ (see Fig. 2.3). This means in particular for the cluster size $N_c = 1$ (DMFA) that phases with purely nonlocal order parameters $\Delta_{\mathbf{k}}$ cannot be described, since the average over the full BZ, $\sum_{\mathbf{k}} \Delta_{\mathbf{k}}$ then vanishes. When $N_c = 1$ only phases with the s-wave or extended s-wave order parameter (see Table 3.1), i.e. order parameters with local contributions can be described (see also [Jar92, Jar93, Ste98]). However, as stressed in the introduction, the local

Coulomb repulsion U inhibits states with local pairing. Calculations for $N_c = 1$ therefore do not show any instabilities towards the superconducting state.

When $N_c > 1$ nonlocal correlations are incorporated in the DCA and hence phases with nonlocal order parameter can be described. Table 3.2 illustrates the effect of the coarse graining process (Eq. (3.8)) on the different symmetries (see Tab. 3.1) of the order parameter $\Delta_{\mathbf{k}}$. For the different cluster momenta $\mathbf{K}$ the

Sign of $\bar{\Delta}_{\mathbf{K}}$				
symmetry/$\mathbf{K}$ =	$(0,0)$	$(\pi,0)$	$(0,\pi)$	(π,π)
s	$+$	$+$	$+$	$+$
xs	$+$	0	0	$-$
$d_{x^2-y^2}$	0	$-$	$+$	0
d_{xy}	0	0	0	0
p	0	0	0	0

TABLE 3.2: *Sign of the coarse grained order parameter $\bar{\Delta}_{\mathbf{K}}$ in the different DCA coarse graining cells for different pairing symmetries. "0" indicates that the average of $\Delta_{\mathbf{k}}$ over the cell vanishes. d_{xy}- and p-wave order parameters cannot be detected using this choice of the cluster $\mathbf{K}$-points.*

respective sign of the coarse grained order parameters $\bar{\Delta}_{\mathbf{K}}$ in the cell centered at $\mathbf{K}$ is illustrated for the different symmetries as indicated on the left. Due to symmetry reasons, $\bar{\Delta}_{\mathbf{K}}$ vanishes in all the cells for d_{xy}- and p- wave symmetries as indicated by the "0". Hence pairing states with these symmetries cannot be detected using this choice of the cluster $\mathbf{K}$-points for $N_c = 4$. To describe states with these order parameters, either a different set of $\mathbf{K}$ vectors has to be selected or calculations for larger cluster size N_c have to be performed. On the other hand, pairing states with s-wave, extended s- (xs) wave and $d_{x^2-y^2}$-wave symmetry can be described and, most importantly, also be distinguished by the selected set of $\mathbf{K}$-points. A coarse grained order parameter $\bar{\Delta}_{\mathbf{K}}$ consistent with e.g. $d_{x^2-y^2}$-wave symmetry vanishes in the cells around $(0,0)$ and (π,π), but is finite with opposite signs in the cells centered at $(\pi,0)$ and $(0,\pi)$. An order parameter with xs-symmetry on the other hand vanishes at $(\pi,0)$ and $(0,\pi)$ but is finite at $(0,0)$ and (π,π). $N_c = 4$ in fact is the smallest cluster size which allows for a $d_{x^2-y^2}$-wave transition and maintains the translational and point group symmetries of the lattice.

To allow for a possible symmetry breaking the DCA iteration procedure is initialized with finite anomalous parts $S_{\uparrow\downarrow}(\mathbf{K},\omega)$ of the self-energy matrix (Eq. (2.72)). A finite order parameter $\Delta_{\mathbf{k}}$ is then signalled by a finite anomalous part $F_{\uparrow\downarrow}(\mathbf{k},z) = \langle\langle c_{\mathbf{k}\uparrow}; c_{-\mathbf{k}\downarrow}\rangle\rangle_z$ of the converged Green function. Fig. 3.22 shows a typical result for the coarse grained anomalous Green function $\bar{F}_{\uparrow\downarrow}(\mathbf{K},\omega)$ defined in Eq. (2.73) at the four cluster $\mathbf{K}$-points for $U = 12t$, $t' = 0$, temperature $T = 0.048t \triangleq 137$K (for $t = 0.25\,$eV) and doping $\delta = 0.20$. $\bar{F}_{\uparrow\downarrow}(\mathbf{K},\omega)$

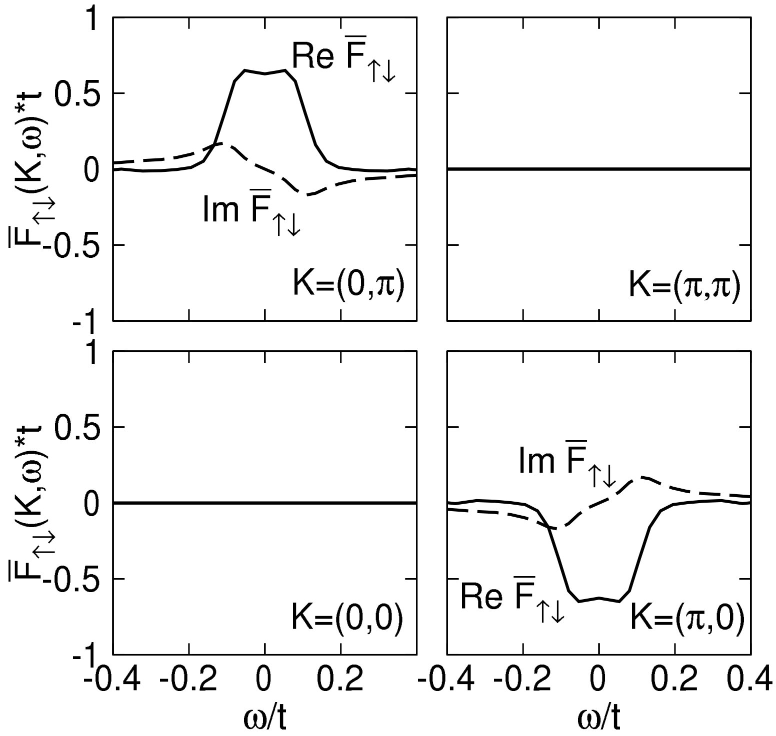

FIGURE 3.22: *The coarse grained anomalous Green function $\bar{F}_{\uparrow\downarrow}(\mathbf{K},\omega)$ when $U = 12t$, $t' = 0$, $T = 0.048t$ and $N_c = 4$ at the cluster $\mathbf{K}$-points. It is finite in the cells around $\mathbf{K} = (0,\pi)$ and $(\pi,0)$ and vanishes at $(0,0)$ and (π,π). This and the corresponding signs are consistent with a $d_{x^2-y^2}$-wave order parameter (see Tab. 3.2).*

vanishes at the cluster points $(0,0)$ and (π,π) but is finite at the points $(\pi,0)$ and $(0,\pi)$ with opposite signs. The system is in the superconducting state! Since the $\mathbf{K}$-dependence of the coarse grained order parameter $\bar{\Delta}_{\mathbf{K}} = \bar{F}_{\uparrow\downarrow}(\mathbf{K},\tau = 0)$ (see Eq. (2.76)) is given by the $\mathbf{K}$-dependence of $\bar{F}_{\uparrow\downarrow}(\mathbf{K})$, this result is consistent with a $d_{x^2-y^2}$-wave order parameter according to Table 3.2. It is important to stress that this result is independent of the particular initialization of the self-energy. Symmetries other than $d_{x^2-y^2}$-wave cannot be stabilized. Even if the anomalous parts of the self-energy are initialized corresponding to a s-wave symmetry, the order parameter changes its $\mathbf{K}$-dependence in the course of the iterations to the $d_{x^2-y^2}$-symmetry. This illustrates the stability of the $d_{x^2-y^2}$-wave symmetry of the order parameter.

The interesting question arises if the finite temperature superconducting instability in the 2D system survives as N_c increases, where the mean field character of the DCA is gradually reduced. This issue cannot be resolved by the NCA approach to the DCA cluster problem, since $N_c = 4$ is the largest cluster size that can be treated within the NCA. The QMC approach can in principle be applied to larger clusters $N_c > 4$. However the minus-sign problem limits calculations for the superconducting phase transition to small cluster sizes, so that no definite statements can be made towards the N_c-dependence of T_c for the time being.

3.4.2 Density of states

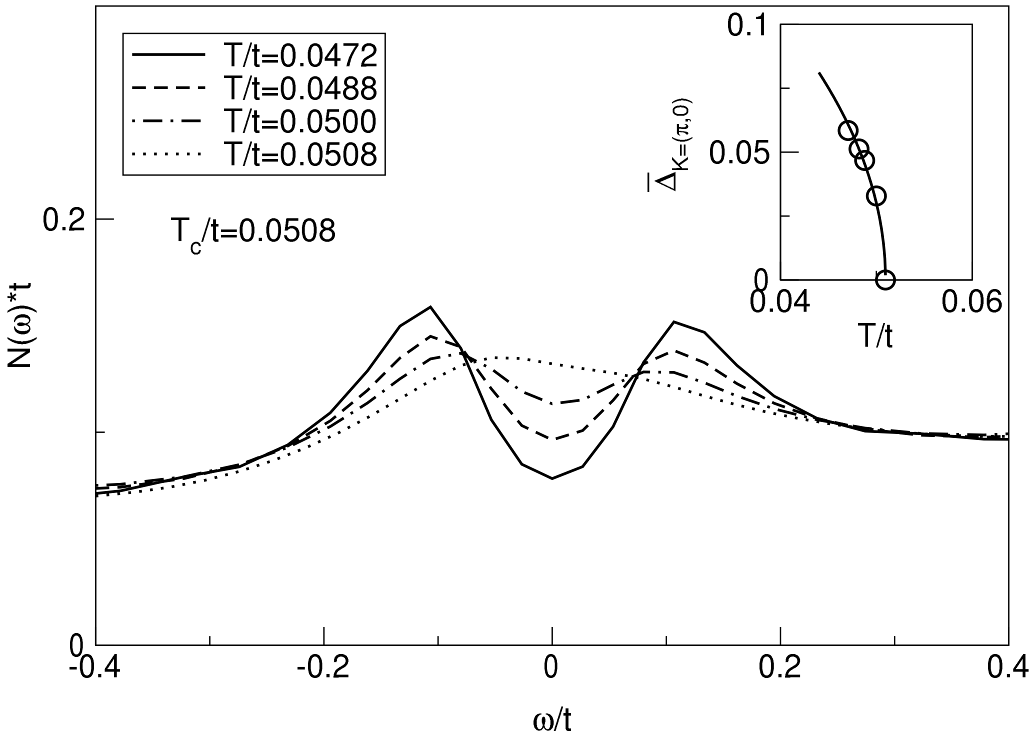

FIGURE 3.23: *The DOS $N(\omega)$ for energies near the Fermi energy when $N_c = 4$, $U = 12t$, $t' = 0$ at optimal doping $\delta = 0.20$ for various temperatures in the superconducting state. The critical temperature $T_c = 0.0508t$. The inset shows the magnitude of the coarse grained order parameter $\bar{\Delta}_{\mathbf{K}}$ at the cluster point* $\mathbf{K} = (\pi, 0)$ *as a function of temperature.*

The finite anomalous parts of the coarse grained Green function, depicted in Fig. 3.22 affect also the normal parts of the Green function, G (see Sec. 2.6.2), and hence the DOS. The BCS theory predicts a pseudogap[9] at the Fermi energy if the order parameter has $d_{x^2-y^2}$-symmetry.

Fig. 3.23 illustrates the DCA ($N_c = 4$) result for the DOS $N(\omega)$ calculated from the normal part of the Green function for $\delta = 0.20$ when $U = 12t$ and $t' = 0$

[9]In contrast to a s-wave order parameter, where a full gap opens in the DOS, the nodes of the d-wave order parameter result in the formation of a pseudogap, where the DOS vanishes at the singular point $\omega = 0$ only.

for various temperatures T in the superconducting state. At $T = 0.0472t$ the superconducting pseudogap at the Fermi energy is clearly observed with symmetrically placed peaks at $\omega/t \approx \pm 0.2$. In contrast to the BCS-case, the spectral density at zero frequency does not vanish. Electron-electron scattering processes, present at finite temperatures result in finite quasiparticle life times and hence fill in the gap. This is very similar to a BCS superconductor with magnetic impurities where scattering processes have the same effect. The temperature dependence of the coarse grained order parameter $\bar{\Delta}_{\mathbf{K}}$ at the cluster $\mathbf{K}$-point $(\pi, 0)$ is plotted in the inset. With increasing temperature the anomalous component $\bar{F}_{\uparrow\downarrow}(\mathbf{K}, \omega)$ of the Green function becomes smaller. Hence $\bar{\Delta}_{\mathbf{K}=(\pi,0)}$ decreases and the superconducting pseudogap in the DOS diminishes. Unlike for a BCS gap, this occurs only partially through a decrease of the frequency separation of the peaks. The gap rather fills in as the temperature is raised. The temperature where $\bar{\Delta}_{\mathbf{K}}$ vanishes for all $\mathbf{K}$ defines the critical temperature T_c. For this parameter set $T_c = 0.0508t \approx 150\,\mathrm{K}$ (for $t = 0.25\,\mathrm{eV}$). The solid line in the inset to Fig. 3.23 represents a fit to the function $\bar{\Delta}_{\mathbf{K}} = A(T_c - T)^{\beta}$ with $\beta = 0.45$ close to the BCS (mean field) result $\beta = 0.5$. As for the antiferromagnetic phase transition this indicates again that close to the transition the system is dominated by long-ranged correlations which are neglected by the DCA approach.

3.4.3 Doping dependence

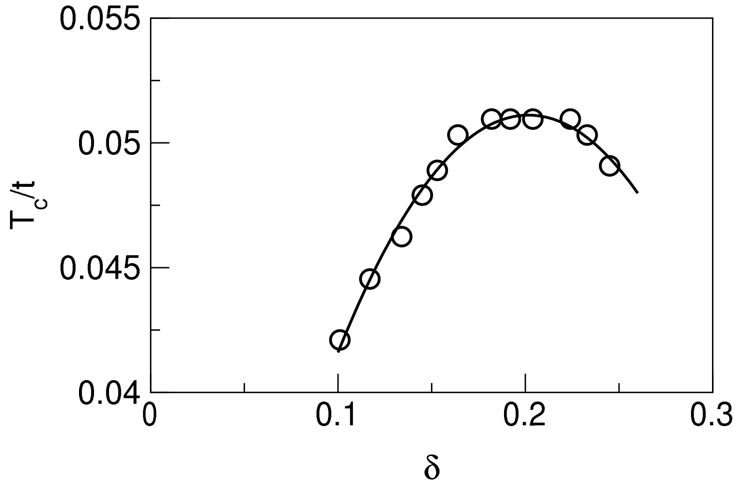

FIGURE 3.24: *The superconducting transition temperature T_c versus doping δ via DCA when $N_c = 4$, $U = 12t$, $t' = 0$. Optimal doping occurs at $\delta = 0.20$. The solid line is a guide to the eye only.*

The critical temperature T_c, where $\bar{\Delta}_{\mathbf{K}}$ vanishes $\forall\,\mathbf{K}$ depends on the system parameters. The doping dependence of T_c is shown in Fig. 3.24. As a function

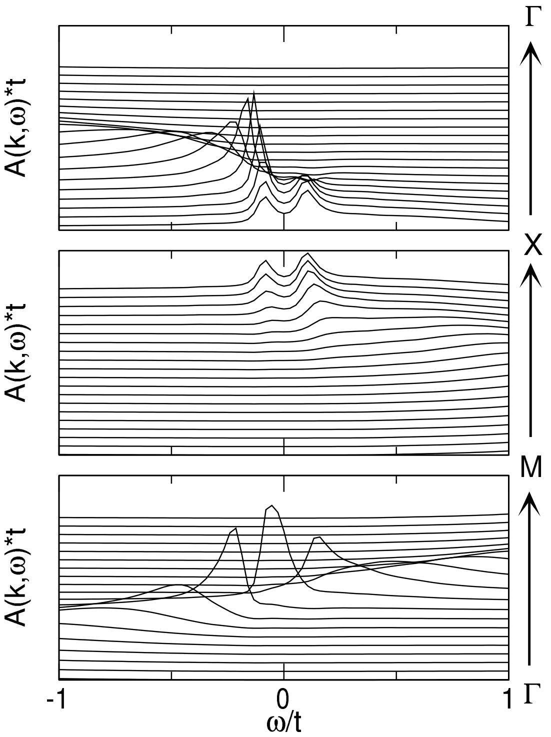

FIGURE 3.25: *The angle resolved spectral function* $A(\mathbf{k},\omega)$ *along the main symmetry directions in the BZ for energies near the Fermi surface when* $N_c = 4$, $U = 12t$, $t' = 0$ *and* $T = 0.0468t < T_c$ *at* $\delta = 0.20$ *in the superconducting state. The anisotropy of the superconducting gap reflects the* $d_{x^2-y^2}$*-symmetry of the order parameter.*

of doping $T_c(\delta)$ has a maximum $T_c^{\max} \approx 0.05t \approx 150\,\mathrm{K}$ (for $t = 0.25\,\mathrm{eV}$) at $\delta \approx 0.20$ (optimal doping) and strongly decreases with increasing (overdoping) or decreasing (underdoping) δ. As a remarkable fact, the doping dependence of T_c agrees fairly well with the experimental phase-diagram (see Fig. 1.2 in Sec. 1.1), including the doping level ($\delta \approx 0.20$) yielding the highest T_c, i.e. optimal doping. Unfortunately, due to the breakdown of the NCA at very low temperatures the phase-diagram cannot be extended beyond the region shown in Fig. 3.24. In particular this means that reliable values for the critical doping $\delta_c(T_c = 0)$, beyond which superconductivity vanishes, cannot be predicted.

Before exploring the dependence of T_c on other system parameters as U or t' it is instructive to further investigate the spectrum in the superconducting state. As an illustration of the anisotropy of the superconducting gap, Fig. 3.25 presents the **k**-resolved spectral density $A(\mathbf{k},\omega)$ for frequencies near the Fermi level along high symmetry directions in the BZ when $U = 12t$, $t' = 0$ and $T = 0.0472t$ in the superconducting state at $\delta = 0.20$. The $d_{x^2-y^2}$-wave anisotropy of the order parameter (see Fig. 3.22), i.e. finite in the cells centered at $\mathbf{K} = (\pi, 0)$ and $(0, \pi)$ and zero in the cells around $\mathbf{K} = (0, 0)$ and (π, π) is also visible in the excitation spectrum. Resulting from the $d_{x^2-y^2}$-wave order parameter, the gap in the spectrum opens near $X = (\pi, 0)$ and has a node along the diagonal between Γ and M, i.e. near $(\pi/2, \pi/2)$. The same anisotropy of the superconducting gap is observed in ARPES measurements on the cuprates (see Fig. 1.5 and also Fig. 1.3

in Sec. 1).

As another noteworthy feature, for this parameter set, i.e. at optimal doping, the saddle point region of the spectrum, near $(\pi, 0)$ and $(0, \pi)$, where the dispersion is flat and the number of states is large crosses the Fermi energy, consistent with experiments on cuprates [Des93]. This indicates that a large DOS at the Fermi energy caused by this saddle point region supports superconductivity. Optimal doping also coincides with the doping level where the Fermi surface in the normal state (see Fig. 3.17, $\delta = 0.20$) changes its shape from electron-like to hole-like. This corresponds to the doping level where the flat part of the spectrum near $(\pi, 0)$ coincides with the Fermi energy. Upon lowering the temperature, the superconducting gap emerges in this saddle point region.

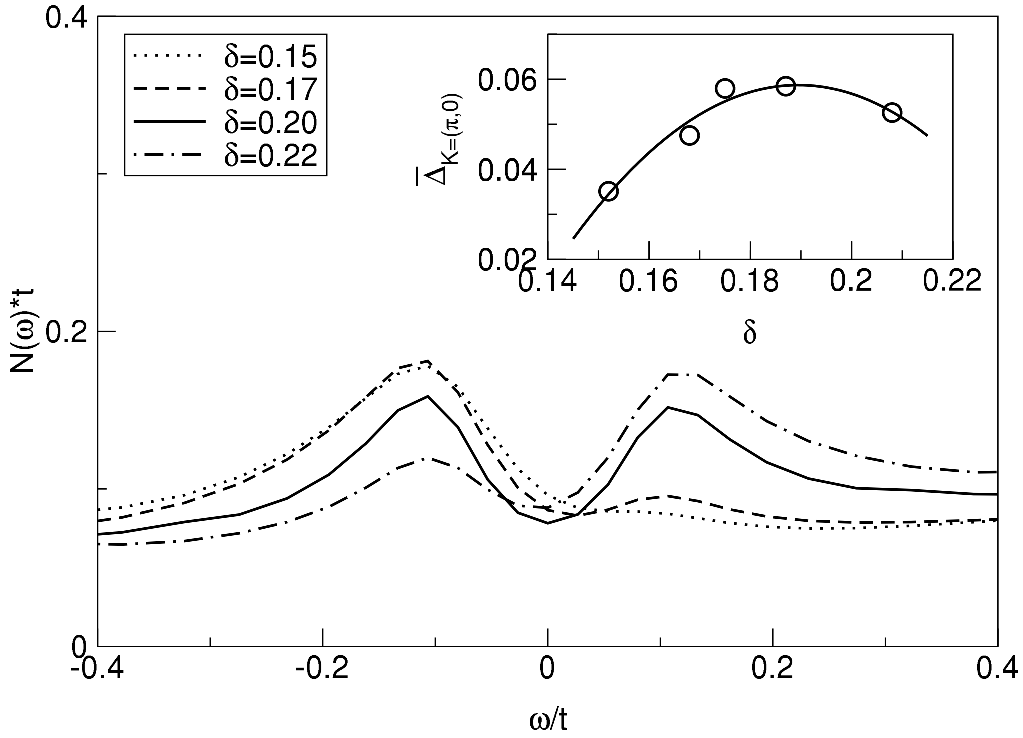

FIGURE 3.26: *The DOS $N(\omega)$ for energies near the Fermi energy when $N_c = 4$, $U = 12t$, $t' = 0$ and $T = 0.0472t < T_c$ for various doping levels in the superconducting state. The inset shows the doping dependence of the coarse grained order parameter $\bar{\Delta}_{\mathbf{K}}$ at the cluster point $\mathbf{K} = (\pi, 0)$ (the solid line is guide to the eye only).*

The doping dependence of the DOS when $T = 0.0472t$ in the superconducting state is depicted in Fig. 3.26 for the same parameters as in Fig. 3.23 but different doping levels. Obviously the size of the superconducting pseudogap, as measured from peak to peak, as well as the DOS at the Fermi energy do not depend strongly upon doping. This is contrary to the prediction of the BCS theory, where the ratio of the gap size to the transition temperature is a constant and the gap would grow in proportion to T_c. Hence, according to the doping dependence of T_c depicted in Fig. 3.24, one would expect a strong doping dependence of the gap size.

On the other hand the drop in the DOS measured from the gap edge to the $\omega = 0$ value first increases, reaches a maximum at about $\delta = 0.20$ and then falls again. This behavior originates in the doping dependence of the anomalous Green function or the coarse grained order parameter $\bar{\Delta}_{\mathbf{K}}$ at $\mathbf{K} = (\pi, 0)$ as illustrated in the inset. This quantity shows exactly the same behavior as a function of doping as the DOS and also as $T_c(\delta)$. Furthermore the particle-hole symmetry of the peaks near the Fermi surface is observed only at optimal doping $\delta = 0.20$. This again strongly suggests that for temperatures slightly above T_c the Fermi energy moves through a maximum in the DOS as a function of doping. In fact, a look at the doping dependence of the DOS in the paramagnetic phase illustrated in Fig. 3.13 brings clarity. As the doping is reduced from over- to underdoping the Fermi level $\omega = 0$ moves through the maximum in the DOS exactly at optimal doping $\delta = 0.20$, the doping level yielding the highest T_c.

Thus, within these DCA calculations, it must be concluded that a large DOS in the interacting system at the Fermi energy acts supportive to superconductivity. This is also consistent with the reduction of T_c in the underdoped system. The opening of the pseudogap results in a loss of density of states at the Fermi energy. If charge excitations are gapped, pairing is suppressed.

3.4.4 Finite values of t'

To further elucidate the question of how the magnitude of T_c is related to the DOS at the Fermi level, it is instructive to study the effects of finite values for the next-nearest neighbor hopping t'. As illustrated in Fig. 3.1 for the non-interacting system, a finite magnitude of t' affects the DOS at the Fermi energy by shifting the van-Hove singularity away from half-filling, so that the singularity might occur near the Fermi level in a doped system. On the other hand another possibly relevant effect might set in: As illustrated in Fig. 3.1, a negative value for t' bends the Fermi surface of the non-interacting system so that it closes around the M-point. Thus the points on the Fermi surface near $(\pi, 0)$ and $(0, \pi)$ fulfill the nesting condition, i.e. can be connected by the antiferromagnetic wave vector $\mathbf{Q} = (\pi, \pi)$ to equivalent $\mathbf{k}$-points in the opposite quadrant of the BZ. Thus the quasiparticles at these hot spots couple strongly to spin fluctuations and hence are expected to get strongly renormalized. Since these hot spots correspond to the region of the spectrum where the van-Hove singularity comes from, the large number of relevant states leads to a strong coupling to the spin-fluctuations. Hence one might expect this to yield pronounced non-Fermi liquid effects and a breakdown of the quasiparticle picture, which might act to suppress pairing. A priori it is not clear how relevant these weak coupling considerations are in the context of the strong coupling studies presented here.

In Fig. 3.27 the DCA result for the dependence of the superconducting transition temperature T_c on the value of t' is shown for $N_c = 4$ and $U = 12t$ at $\delta = 0.20$. As compared to $t' = 0$ T_c strongly decreases with growing negative t'

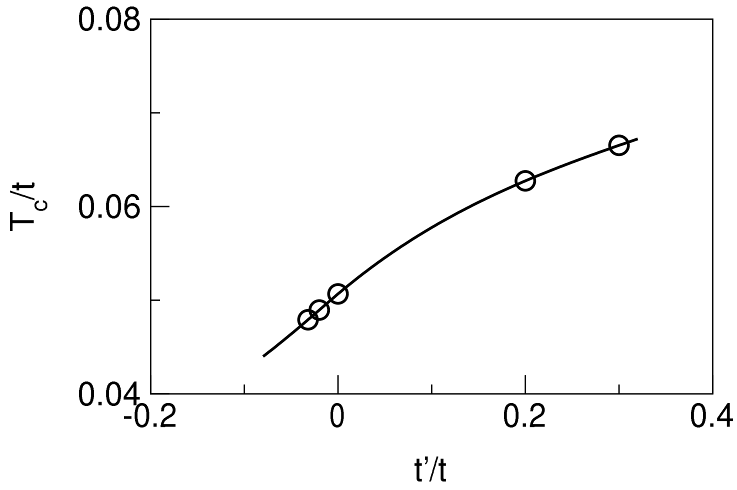

FIGURE 3.27: *The superconducting transition temperature T_c plotted versus the value of the next-nearest hopping integral t' when $N_c = 4$, $U = 12t$ at fixed doping $\delta = 0.20$ (the solid line is a guide to the eye). Negative values of t' suppress superconductivity, whereas positive values enhance pairing.*

but increases for $t' > 0$. From a weak coupling point of view this result seems counterintuitive, as according to Fig. 3.1 a negative value for t' tends to increase the DOS in the doped system at the Fermi energy and consequently should increase T_c. On the other hand the correlations might deform the DOS so that this argument is irrelevant for strong coupling.

In fact the strong coupling DCA calculations presented in Fig. 3.28 invalidate this argument. The coarse grained spectrum $\bar{A}(\mathbf{K}, \omega)$ at the relevant DCA cluster momentum $\mathbf{K} = (\pi, 0)$ for frequencies near the Fermi energy in the paramagnetic state is illustrated for positive and negative t' compared to $t' = 0$ when $U = 12t$ and $T = 0.1t > T_c$ at $\delta = 0.20$ (left panel) and $\delta = 0.05$ (right panel). This quantity as compared to the total DOS measures the number of states in a given DCA cell. Since the paired states evolve in the DCA cell centered at $\mathbf{K} = (\pi, 0)$, it seems reasonable to consider the spectrum in this cell only.

In the underdoped system ($\delta = 0.05$, right panel) the spectra for different signs of t' are qualitatively similar to the $t' = 0$ spectrum. However, the pseudogap is slightly deeper for $t' < 0$ and the peak below the Fermi energy slightly higher for $t' > 0$. At $\delta = 0.20$ the differences are more distinct. The spectra for $t' = 0$

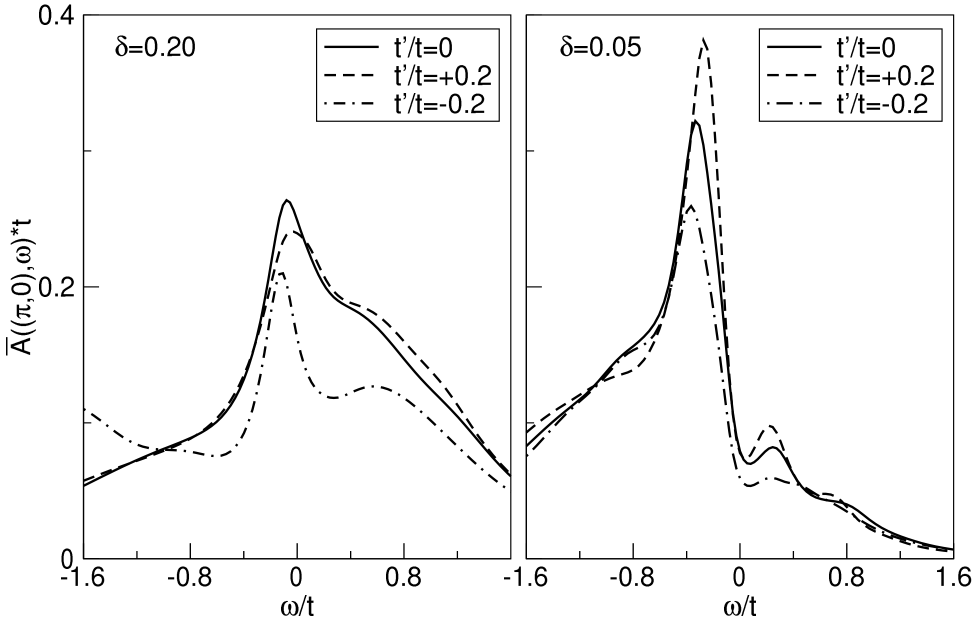

FIGURE 3.28: *The coarse grained spectrum* $\bar{A}(\mathbf{K},\omega)$ *at the DCA cluster momentum* $\mathbf{K} = (\pi, 0)$ *for frequencies near the Fermi energy when* $N_c = 4$, $U = 12t$ *and* $T = 0.1t > T_c$ *in the paramagnetic state for various values of* t'. *For negative* t' *the spectral density at the Fermi surface is reduced for* $\delta = 0.20$ *(left panel) as well as for* $\delta = 0.05$ *(right panel).*

and positive t' are still almost identical with a peak at the Fermi energy. The spectrum for $t' < 0$ however is qualitatively different. The spectral density at the Fermi level is strongly reduced and the pseudogap is already visible in the spectrum. It appears that for negative t' the doping range where non-Fermi liquid character of the low energy excitations is found in form of the pseudogap extends to much higher doping levels as compared to the $t' \geq 0$ case.

Further evidence to this observation is obtained by investigating the doping dependence of the magnitude of the gradient of the momentum distribution function in $\mathbf{k}$-space $|\nabla_{\mathbf{k}} n(\mathbf{k})|$ for different signs of t'. To this end, Fig. 3.29 displays $|\nabla_{\mathbf{k}} n(\mathbf{k})|$ obtained via DCA ($N_c = 4$) for different dopings from $\delta = 0.20$ (top) to $\delta = 0.05$ (bottom) for positive (left) and negative (right) t' when $U = 12t$ and $T = 0.1t$.

The results for this quantity support the spectral evidence. The Fermi surface for $t' > 0$ is very similar to the $t' = 0$ case depicted in Fig. 3.17, including the change from an electron-like shape closed around Γ in the overdoped system to a hole-like topology closed around M in the underdoped system as well as the blurry barrel like structure at $\delta = 0.05$. The latter again indicates the anisotropy in the spectrum, with well defined quasiparticles near $(\pi/2, \pi/2)$ and non-Fermi

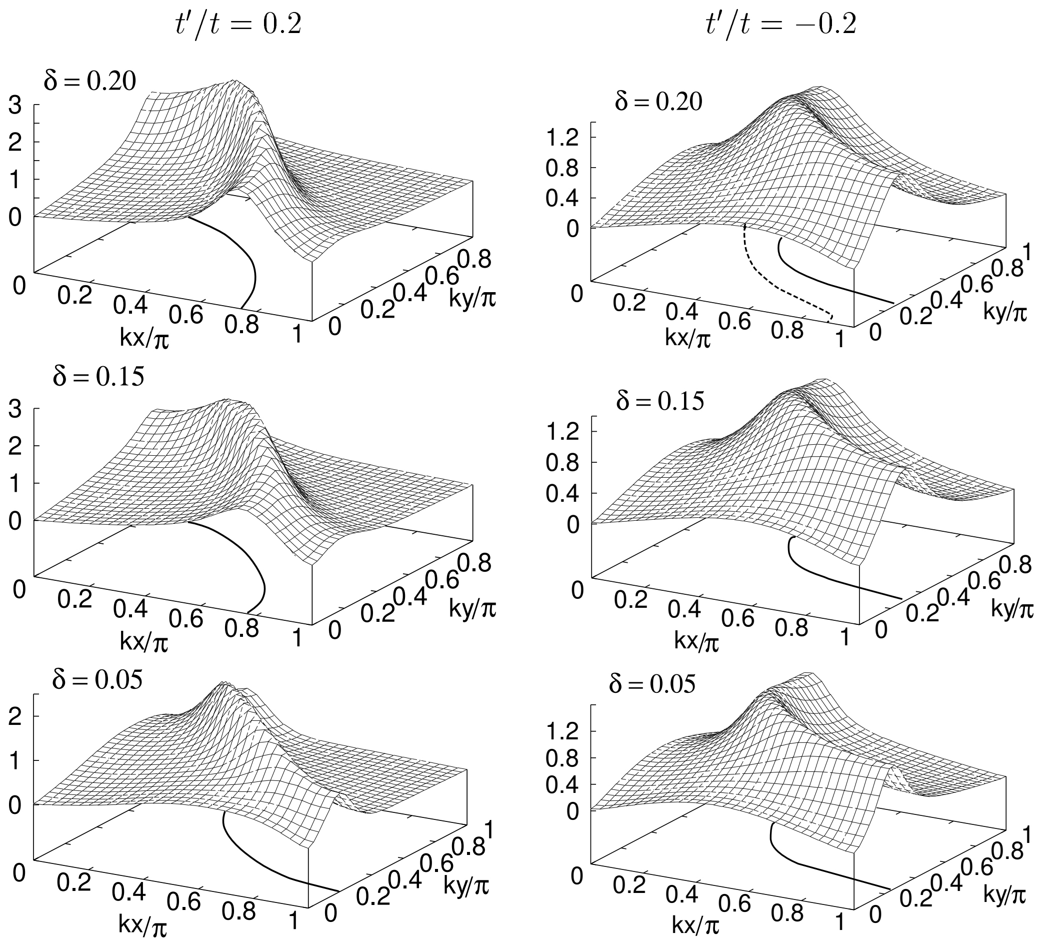

FIGURE 3.29: *The magnitude of* $|\nabla_{\mathbf{k}} n(\mathbf{k})|$ *when* $N_c = 4$, $U = 12t$ *and* $T = 0.1t > T_c$ *for different doping levels. When* $t' = -0.2t$ *(right) pronounced non-Fermi liquid behavior is found. The line on the bottom plane depicts the maximum of* $|\nabla_{\mathbf{k}} n(\mathbf{k})|$. *The dashed line on the bottom plane in the top right part delineates the corresponding Fermi surface of the non-interacting system. Luttingers theorem is violated.*

liquid behavior at the zone boundary near $(\pi, 0)$. However, at $\delta = 0.20$, a positive t' seems to even sharpen the Fermi surface compared to $t' = 0$. This indicates a reduction of the scattering rate of the quasiparticles near the Fermi surface. As a consequence pairing is enhanced by a positive t' and the transition temperatures are higher compared to $t' = 0$.

For negative t' however, compared to $t' \geq 0$, a significant change of the shape of $|\nabla_{\mathbf{k}} n(\mathbf{k})|$ is observed, especially at $\delta = 0.20$. Obviously, the overall shape, i.e. hole like closed around the M point does not depend at all on doping. Especially at $\delta = 0.20$ one notices that the corresponding Fermi surface of the non-interacting system depicted by the dashed line on the bottom plane encloses a considerably less volume. Luttinger's theorem [Lut60] states that in Fermi liquids due to the one-to-one correspondence of excitations in the interacting system and those of the non-interacting system, the volume enclosed by the Fermi surface is conserved when the interaction is turned on. Thus, Luttinger's theorem appears to be violated due to the lack of Fermi liquid formation. Another indication of pronounced Non Fermi liquid character over the full doping regime is the blurry shape of $|\nabla_{\mathbf{k}} n(\mathbf{k})|$. The maximum value of $|\nabla_{\mathbf{k}} n(\mathbf{k})|$ is strongly reduced to about 1.6 compared to $t' \geq 0$. No sign of a possible Fermi surface formation can be seen. As a natural consequence of the pronounced Non Fermi liquid behavior observed for $t' < 0$ over a wide doping range, pairing is suppressed and T_c is reduced.

Thus, provided that spin-fluctuations are the major source of renormalizations, the following conclusion is reached: When $t' < 0$, the coupling between quasiparticles and spin-fluctuations is so strong that the weak coupling NAFL picture breaks down and the low energy excitations cannot be described in the context of a Fermi liquid anymore. Hence, in contrast to the NAFL scenario, a negative t' strongly suppresses pairing and hence decreases T_c.

So far no statements about the pairing mechanism relevant to the numerical calculations presented here have been made. However, several features of the DCA results are consistent with spin-fluctuation induced pairing. The presence of strong antiferromagnetic spin-correlations even at finite doping is signalled by the anomaly in the uniform susceptibility and the opening of the pseudogap at the Fermi energy in the normal state. And it is well known that antiferromagnetic spin-fluctuations lead inexorably to a transition to a superconducting state with $d_{x^2-y^2}$ pairing [Mon91], consistent with the results of the DCA-NCA calculations. The observed doping dependence of the superconducting transition temperature $T_c(\delta)$ can also be understood in terms of the NAFL picture. Overdoping weakens the magnetic correlations and therefore, as expected for a scenario where spin-fluctuations induce pairing, brings out the reduction of T_c. On the other hand, within the same picture one would expect T_c to rise monotonically with decreasing doping due to an enhancement of the spin-fluctuations. However, the downturn of T_c with underdoping can be related to the evolution of the pseudogap with decreasing doping. The loss of density of states near the Fermi surface substantially weakens the overall NAFL pairing potential and thus suppresses pairing.

However it is important to stress that according to the DCA results, pairing is also destroyed by a negative value of t', which is the parameter choice, the NAFL approach is based on to setup the hot and cold spot scenario (see Sec. 1.1). The DCA studies presented here clearly show that negative values of t' strongly enhance the coupling to spin-fluctuations resulting in a breakdown of Fermi liquid behavior and therefore in a dramatic suppression of pairing. Positive values for t' on the other hand lead to a reduction of the scattering rate at the Fermi surface and thus promote pairing. Furthermore, irrespective of the shape of the non-interacting Fermi surface, i.e. even for $t' \geq 0$, the strong nonlocal correlations in underdoped systems change the shape of the Fermi surface to a hole-like topology closed around the M-point. Therefore it must be concluded that this hole-like shape of the Fermi surface in underdoped systems is not a band-structure effect simulated by a finite negative t', but rather an intrinsic feature of the dynamics in the Hubbard model caused by nonlocal spin-correlations.

3.4.5 Dependence on the magnitude of U

To substantiate the conjecture of the spin-fluctuation induced pairing mechanism, T_c at optimal doping ($\delta = 0.20$) was calculated for different values of the Coulomb repulsion U when $N_c = 4$ and $t' = 0$. The result is depicted in Fig. 3.30 along with

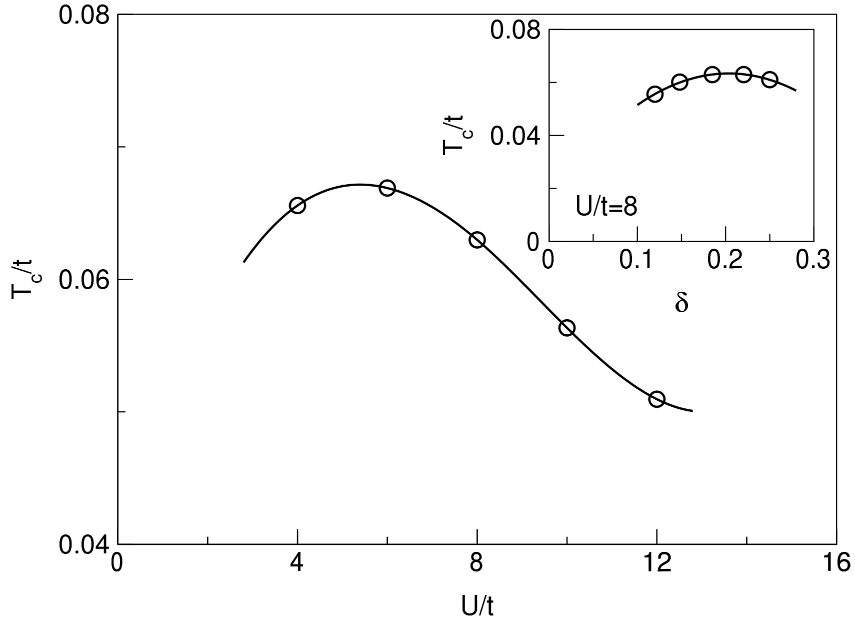

FIGURE 3.30: *The transition temperatures at optimal doping $\delta = 0.20$ plotted versus U when $N_c = 4$ and $t' = 0$. The inset depicts the doping dependence of T_c when $U = 8t$. Optimal doping also occurs at $\delta \approx 0.20$. The solid lines are guides to the eye.*

the doping dependence of T_c when $U = 8t$ plotted in the inset. As for $U = 12t$ the maximal T_c occurs at about $\delta = 0.20$ and T_c falls in the under- and overdoped system. Thus, at least in the strong coupling regime ($U \geq W$) the doping level corresponding to optimal doping does not change with U.

The U dependence of T_c is clearly compatible with the NAFL scenario where pairing occurs through the exchange of spin-fluctuations. At small values of U T_c

is reduced since the antiferromagnetic spin-correlations are suppressed.[10] At large values of U (U>W) T_c monotonically falls with increasing U since the antiferromagnetic exchange $\sim t^2/U$ decreases with increasing U. Thus, a peak develops in $T_c(U)$ for some intermediate value of $U \approx 6t$ slightly below the bandwidth W=8t. Moreover it should be pointed out that $T_c(U)$ reflects exactly the U dependence of the transition temperature to the antiferromagnetic phase in the half-filled Hubbard model (see e.g. [Don91, Jar92]).

In contrast to the Hubbard model, the tJ-model in the relevant parameter regime for J, $J \leq t$ did not show any superconducting instabilities within the DCA-NCA approach presented in Sec. 2.7. Although this result agrees with the findings in the literature (see e.g. [Dag94a]), it is in contrast to the presented results for the Hubbard model. However, based on the observations previously made for the difference in the pseudogap scales of the weakly doped Hubbard and tJ-model in the paramagnetic state (see Sec. 3.3), this discrepancy seems not surprising. There it was shown that due to the neglect of an additional Bosonic bath representing the effects of the interaction J in the effective medium on the cluster states, the energy scale associated with the pseudogap is reduced in the tJ-model as compared to the Hubbard model. Provided that the spin-fluctuations induce paring in these models, it is reasonable to assume that pairing in the tJ-model occurs at larger values of J as compared to the Hubbard model. However, when $J > t$ it turns out that the NCA approach to the DCA cluster problem fails at low temperatures inhibiting the observation of a possible transition in this parameter regime.

3.4.6 Summary

In this section it was shown that even in the strong-coupling regime the moderately doped 2D Hubbard model has an instability towards a superconducting state with $d_{x^2-y^2}$-wave order parameter. Furthermore it was demonstrated that the DCA-NCA results for the superconducting instability of the strong coupling Hubbard model are consistent with the scenario where the exchange of spin-fluctuation mediates pairing. However the results are not compatible with a simple BCS-like picture. In contrast to the strongly doping dependent transition temperature T_c, the superconducting gap width was found to remain constant over a wide range of dopings. Furthermore the dependence of T_c on the next-nearest neighbor hopping amplitude t' cannot be understood from a weak coupling point of view. Negative values of t' were shown to strongly suppress superconductivity, although they shift the van-Hove singularity in the bare DOS to finite dopings. This suppression of pairing occurs through pronounced non-Fermi liquid behavior in the interacting system induced by the strong coupling to spin excitations for

[10] In the half-filled Hubbard model the transition temperature to the antiferromagnetic state is exponentially small for small values of U (see e.g. [Don91, Jar92]).

negative values of t'. On the other hand, positive values of t' promote pairing as well as a large DOS at the Fermi energy in the interacting system. The dependence of T_c on the magnitude of the interaction strength U reflects exactly the behavior of the strength of the spin-fluctuations with varying U. This result provides strong evidence for the scenario with a magnetic pairing mechanism.

3.5 The DCA phase-diagram

Based on the results presented in the preceding sections, a temperature-doping (T-δ) phase-diagram for the 2D Hubbard model can be drawn. The phase boundaries are determined by the vanishing of the corresponding order parameters. To compare with the generic phase-diagram of the cuprates the Coulomb repulsion is set to $U = 12t$, so that the half filled system is gapped and therefore insulating.

Calculations in the relevant region for antiferromagnetism (near half-filling) unfortunately cannot be performed within the DCA-NCA approach for this parameter set, for the following reasons: As discussed in Sec. 3.2.1 the transition temperatures to the antiferromagnetic phase are found to be highest at half-filling. The calculations show further that as U increases from $U = 4t$, the Neél temperature decreases. Furthermore, when the DOS is gapped at the Fermi level the NCA fails at low temperatures necessary to observe the transition. This is not related to an intrinsic feature of the perturbational expansion performed in the NCA. The NCA treats the hybridization to the effective medium as a perturbation. The latter is represented by the hybridization function $\Gamma(\mathbf{K})$. Since the vanishing spectral weight in the insulator is also reflected in $\Gamma(\mathbf{K})$, the NCA should even become better. It rather originates in the fact that the vanishing spectral weight in $\Gamma(\mathbf{K})$ at the Fermi surface results in an infinite life time of a few cluster eigenstates since Renormalization effects due to the coupling to $\Gamma(\mathbf{K})$ vanish. Thus the corresponding propagators are singular at the corresponding eigenenergies of these states. The poles in the spectrum of these resolvents can in principle be treated analytically within the NCA. However it turns out that convergence of the method in the course of the DCA iterations cannot be accomplished numerically as soon as poles are present in the spectrum of some NCA propagators. This shortcoming of the combined DCA-NCA approach at low temperatures also extends to finite small doping levels $\delta \lesssim 0.5$. As discussed in Sec. 3.3.2 for $U = 12t$ a pseudogap opens in the DOS for $\delta \lesssim 0.20$. This pseudogap is most pronounced in the highly underdoped system for $\delta \lesssim 0.05$ and hence inhibits low temperature calculations in this regime for the above given reasons. And since the Neél temperatures for $N_c = 4$ fall off very quickly with doping the actual transition cannot be observed within the NCA approach to the DCA equations for $U = 12t$.

However the QMC approach to the DCA cluster problem can be employed in this regime and yields a narrow antiferromagnetic phase around half-filling and a critical doping $\delta_c(T_N = 0) \approx 0.05$, beyond which antiferromagnetism vanishes [Jar00].

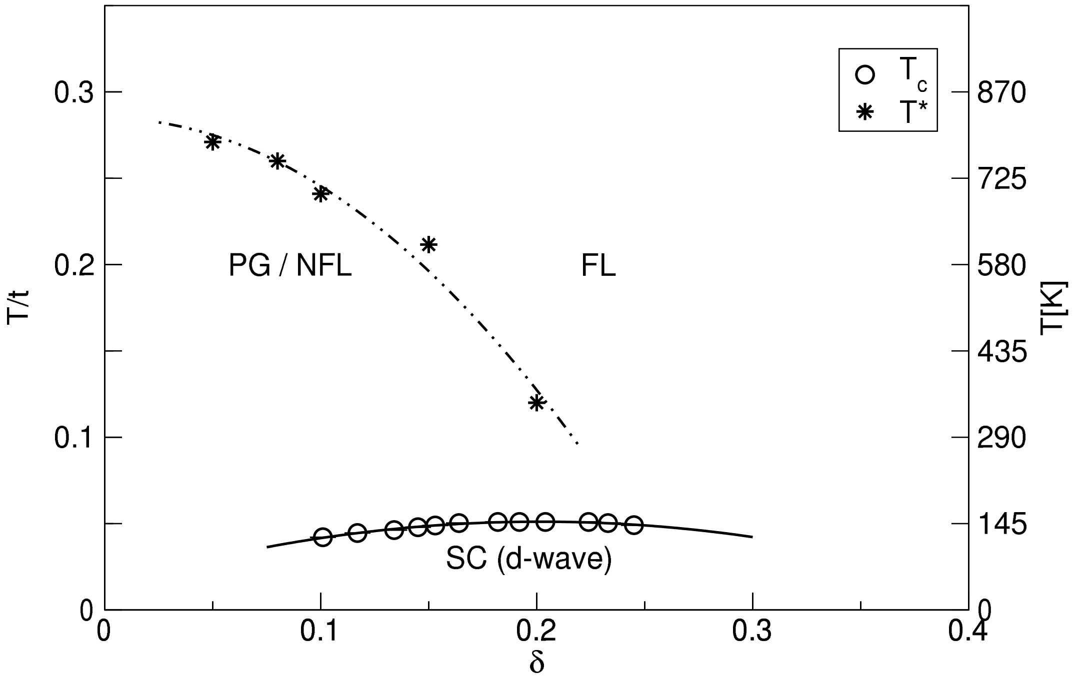

FIGURE 3.31: *The phase-diagram of the 2D Hubbard model calculated with NCA and DCA for $N_c = 4$ and $U = 12t$. The crossover temperature $T^\star$, obtained from the maximum of the uniform spin susceptibility, separates the regions with Fermi liquid (FL) and non-Fermi liquid (NFL) behavior in form of a pseudogap (PG) in the DOS. The superconducting transition temperature T_c is determined by the vanishing order parameter $\bar{\Delta}_{\mathbf{K}}(T_c) = 0\ \forall \mathbf{K}$. The solid and dash-dotted lines are guides to the eye. To compare with experiments, a Kelvin scale has been added on the right.*

The DCA-NCA phase-diagram for $U = 12t$ and $t' = 0$ presented in Fig. 3.31 is restricted to doping levels $\delta \geq 0.05$ for the above given reasons. The NCA also fails at low temperatures due to the neglect of crossing diagrams (see discussion in Sec. 2.5). Thus the phase-diagram terminates at temperatures $T < 0.040t$. The distinct treatment of antiferromagnetic and superconducting phases is now a posteriori justified by the phase diagram, since no sign of antiferromagnetism is found where the instability to the superconducting phase occurs. Furthermore it seems reasonable to assume that even within a generalization that allows for the coexistence of superconductivity and antiferromagnetism at the same time, superconductivity will not stabilize antiferromagnetism.

In addition to the critical temperature T_c, which delineates the transition to the superconducting phase with $d_{x^2-y^2}$-wave order parameter, the pseudogap temperature $T^\star$ is included, which is fixed by the maximum of the uniform magnetic susceptibility (see Sec. 3.3.3). As shown in Sec. 3.3.4, it delineates the crossover temperature between Fermi liquid and non-Fermi liquid regions. For temperatures below $T^\star$, a pseudogap emerges in the DOS at the Fermi level. Consistent with ARPES experiments on cuprates, the study of the $\mathbf{k}$-dependent spectral density reveals that the spectrum becomes gapped near $(\pi, 0)$, whereas well defined quasiparticles along the diagonal, i.e. near $(\pi/2, \pi/2)$ are found. The fact that $T^\star \sim J = 4t^2/U$ in the highly underdoped system strongly suggest that the pseudogaps originates in the coupling to antiferromagnetic spin-fluctuations. Concomitant to the pseudogap in the DOS for $\delta \lesssim 0.20$ and $T < T^\star$, the self-energy shows non-Fermi liquid character for the parts of the Fermi surface near $\mathbf{k} = (\pi, 0)$. In the overdoped regime ($\delta > 0.2$) Fermi liquid behavior is recovered. In agreement with the generic high-T_c phase-diagram (see Fig. 1.2 in Sec. 1.1), the line representing the crossover temperature $T^\star$ merges into the superconducting phase boundary in the slightly overdoped regime. As a function of doping, the maximum $T_c \approx 0.05t \approx 150$K at $\delta \approx 0.20$, and decreases with increasing (overdoped system) or decreasing (underdoped system) doping, consistent with the experimental phase-diagram.

The results presented in Sec. 3.4.5 show evidence that the existence of superconductivity in the 2D Hubbard model originates in magnetically mediated pairing. This explains the downturn of T_c with doping in overdoped systems $\delta > 0.20$, since the antiferromagnetic correlations are substantially weakened upon doping. In the underdoped system $\delta < 0.20$ the opening of the pseudogap in the DOS seems to be responsible for suppressing T_c.

To summarize, the results discussed in the preceding sections and summarized in the phase-diagram shown in Fig. 3.31 demonstrate that the DCA approximation for the 2D Hubbard model at $U \gtrsim W$ captures qualitatively as well as quantitatively the relevant physics to describe the observed low energy electronic behavior observed in high-T_c cuprate superconductors. In particular, the short-ranged spin-fluctuations appear to dominate the low temperature behavior of the 2D Hubbard model.

Chapter 4

Summary and Outlook

4.1 Summary

In this thesis a cluster approach for the thermodynamic limit to study intersite correlations in strongly interacting Fermionic systems was developed and used to investigate the single-particle properties of the two-dimensional (2D) Hubbard model and some related aspects of the 2D tJ-model.

Method

The method is based on a novel technique, the Dynamical Cluster Approximation (DCA), a systematic extension of the Dynamical Mean Field Approximation (DMFA) (Chapter 2). The DMFA assumes that local correlations are dominant and neglects nonlocal dynamical fluctuations. As a consequence of the purely local self-energy, the lattice system may be mapped onto a single impurity embedded in a self-consistently determined time-dependent Weiss field (Sec. 2.2). The DCA systematically incorporates nonlocal corrections to the DMFA by partially restoring the momentum dependence of the self-energy. To reduce the complexity of the problem, the reciprocal space is coarse grained, and the self-energy is calculated on a reduced set of N_c momentum points, the cluster **K**-points. In close analogy to the DMFA, the lattice system may then be mapped onto an effective periodic cluster of size N_c embedded in a self-consistently determined host (Sec. 2.3.1). Therefore short-ranged correlations (of the order of the cluster size) are included accurately, whereas longer-ranged fluctuations are treated on a mean field level (Sec. 2.3.2). For $N_c = 1$ the DCA is equivalent to the DMFA and by increasing N_c the length scale of incorporated dynamical correlations can be gradually increased while the calculation remains in the thermodynamic limit. In two dimensions the DCA is exact with corrections $\mathcal{O}(1/N_c)$. By construction the DCA is a fully causal approach. It does not violate the analyticity of the self-energy and spectral function in the upper half of the complex plane, a major advantage of the DCA over other cluster approaches. Furthermore the DCA preserves the translational and point-group symmetries of the lattice.

To solve the effective cluster problem an extended resolvent technique for clusters was developed by extending the Non Crossing Approximation (NCA) originally set up in [Kei71] for the single impurity Anderson model (Sec. 2.5). The "cluster-NCA" approach starts with the eigenstates of the cluster and performs a particular resummation of the diagrammatic expansion in terms of the coupling to the host. Based on the observation that the host is of the order $\mathcal{O}(1/N_c)$, the cluster-NCA approach can be shown to become exact as $N_c \to \infty$. Furthermore, this cluster-NCA approach allows calculations on the real frequency axis and most importantly in the strong coupling regime, two main advantages of the NCA over other existing methods.

For the first time, within the work presented here, the DCA scheme was generalized to allow for calculations in symmetry broken phases, including the superconducting (Sec. 2.6.2) and the antiferromagnetic state (Sec. 2.6.3). The modified equations made it possible to explore fundamental issues, like the low temperature properties and instabilities of the Hubbard model and closely related models. To allow for the symmetry breaking, it is indispensable to introduce anomalous propagators into the theory. The reduced translational symmetry in the magnetically ordered state is described by the antiferromagnetic wave-vector $\mathbf{Q} = (\pi, \pi)$ and hence is signalled by a finite propagator $\langle\langle c_{\mathbf{k}+\mathbf{Q}\sigma}; c^\dagger_{\mathbf{k}\sigma}\rangle\rangle_z$. A finite anomalous propagator $\langle\langle c_{\mathbf{k}\uparrow}; c_{-\mathbf{k}\downarrow}\rangle\rangle_z$ indicates the existence of Cooper pairs in the superconducting phase. The self-consistent calculation of these propagators is implicitly accounted for by modifying the DCA equations to a Nambu-Gorkov matrix representation.

The existence of these finite anomalous propagators calls for an extension of the paramagnetic cluster-NCA approach to the symmetry broken phases (Sec. 2.6). It is vital for the stability of the ordered phases to consider additional diagrams for the resolvent of the cluster eigenstates, which involve the anomalous parts of the host. The symmetry breaking nature of these diagrams results in additional off-diagonal matrix elements of the cluster resolvent, between states with different particle numbers (in the superconducting state) or different momenta (in the antiferromagnetic state). The exact derivation of these additional diagrams for the different phases and their analytical implementation was discussed in detail.

Results

Within this work, fundamental results for the 2D Hubbard and tJ-model of broad interest were obtained (Chapter 3). In particular it was shown that the DCA formalism is able to resolve questions that cannot be answered or addressed by other existing methods. By using the smallest cluster size ($N_c = 4$) that preserves the full translational and point-group symmetries of the lattice, the initial corrections to the DMFA phase diagram were studied. The fact that longer-ranged correlations are treated on a mean field level renders the Mermin-Wagner theorem irrelevant in the context of the DCA calculations. Finite temperature instabilities of the 2D model to phases, where the broken symmetry is continuous are therefore not in contradiction with the Mermin-Wagner theorem. Regions of antiferromagnetism, d-wave superconducting, pseudogap non-Fermi liquid and Fermi liquid behaviors are found, in qualitative and quantitative agreement with the generic phase diagram of the high-T_c superconductors (Fig. 3.31). Furthermore the results were compared to DMFA calculations ($N_c = 1$) to study the effect of the initial nonlocal corrections.

Half filling - Antiferromagnetic correlations

The physics of the half-filled 2D Hubbard model is found to be dominated by antiferromagnetic correlations when $N_c = 1$ and 4. In the weak coupling regime, when the Coulomb repulsion U is half the bare bandwidth W, a finite temperature transition to the antiferromagnetically ordered state is found for both cluster sizes. However, as expected for a theory that adds fluctuations to a mean field approach, the nonlocal correlations present in the $N_c = 4$ result strongly suppress antiferromagnetism. The Neél temperature is reduced to about 60% of its value for $N_c = 1$ and the sub-lattice magnetization in the ordered state to about 25% (Sec. 3.2.1).

To investigate the long open question of possible precursor effects of the antiferromagnetic phase transition, results for the spectra in the paramagnetic state were presented. So far it was unclear if the 2D Hubbard model shows these effects, since studies employing numerically exact methods, like e.g. QMC, are restricted to small system sizes and statements for the thermodynamic limit are problematic. When $N_c = 1$ Kondo-like behavior leads to the formation of a Fermi liquid. Due to the lack of nonlocal fluctuations no signs of precursors were found. Spatial correlations incorporated when $N_c = 4$ change the low temperature character significantly by inducing pronounced non-Fermi liquid behavior accompanied by precursors of the antiferromagnetic phase transition at lower temperatures (Sec. 3.2.2):

- The onset of magnetic ordering is preceded by the opening of a pseudogap in the electronic spectrum at the Fermi energy when $U = W/2$ (Fig. 3.5).
- As a consequence of the short-range magnetic order on short time scales, a shadow band develops in the normal phase (Fig. 3.7).

Furthermore the pseudogap is found to diminish upon frustrating the lattice by adding a finite next-nearest neighbor hopping t' (Sec. 3.2.3). This result strongly suggests a magnetic origin for the evolution of the pseudogap and the related non-Fermi liquid behavior observed when $N_c = 4$.

Finite doping - From non-Fermi liquid to Fermi liquid-behavior

The parameter regime relevant for a description of the high-T_c cuprates is the strong coupling regime ($U \geq W$). Thus calculations for $U = 1.5W$ were carried through. Upon weak doping $\delta < 0.20$, the $N_c = 4$ result for the 2D Hubbard model continues to display non-Fermi liquid behavior (Sec. 3.3):

- With decreasing temperature the uniform spin susceptibility first increases, goes through a maximum at a temperature $T^\star$, and then decreases again, qualitatively in agreement with Knight-shift measurements on the underdoped cuprates. $T^\star$ falls with increasing doping δ (Sec. 3.3.3).
- For temperatures below $T^\star$ a pseudogap emerges in the electronic spectrum at the Fermi energy accompanying the anomaly in the susceptibility (Fig. 3.13). A further analysis of the momentum dependent spectrum reveals a $d_{x^2-y^2}$-wave anisotropy of the pseudogap. The spectrum is gapped near $(\pi, 0)$ and consists of well defined quasiparticles near $(\pi/2, \pi/2)$, in agreement with ARPES-experiments on underdoped cuprates (Fig. 3.16).
- Concomitant with this behavior the self-energy is found to display pronounced non-Fermi liquid behavior at momenta near $(\pi, 0)$ (Fig. 3.15).
- In the weakly doped system ($\delta = 0.05$) the Fermi surface changes its topology compared to the non-interacting one. While the latter is closed around the zone center for every finite doping, the interacting Fermi surface changes its shape to a hole-like Fermi surface, closed around (π, π) (Sec. 3.3.5). This behavior is induced by a strong energy reduction of the states near $(\pi, 0)$, consistent with observations on LSCO.

The observation that the temperature $T^\star$, where the pseudogap becomes apparent in the spectrum and where the susceptibility begins to fall, is set by the effective exchange interaction $J = 4t^2/U$ can be understood in terms of a magnetic scenario, where renormalizations due to antiferromagnetic spin fluctuations are responsible for the anomalous behavior. This also explains the pronounced doping dependence of the character of the low energy excitations. With increasing doping $\delta > 0.20$, where the antiferromagnetic spin fluctuations are weakened, Fermi liquid behavior is recovered, the pseudogap in the spectrum diminishes and the Fermi surface displays the expected shape.

To add evidence to the idea of a magnetically driven pseudogap, calculations for the weakly doped 2D tJ-model were performed (Sec. 3.3.7). As a striking feature, the width of the pseudogap also observed in the tJ-model is found to vary linearly with the antiferromagnetic spin interaction J, strongly supporting the magnetic scenario.

Optimal doping - Superconductivity

The DCA-NCA method was further used to study the interesting question of a possible instability of the 2D Hubbard model towards a superconducting phase (Sec. 3.4). While the weak coupling Hubbard model is known to show superconductivity, there are no conclusive results for the strong coupling regime, which is the relevant regime for a description of the cuprates. Within this manuscript it was demonstrated that even at strong coupling a transition to a superconducting state occurs when $N_c = 4$ at moderate doping. The characteristic features of this phase transition are qualitatively and quantitatively consistent with the experimental situation:

- The anisotropy of the corresponding order parameter is found to be consistent with a $d_{x^2-y^2}$-symmetry (Sec. 3.4.1).
- As a function of doping the maximal transition temperature $T_c \approx 150$K is found to occur at about $\delta \approx 20\%$, in excellent agreement with the experimental phase diagram. With decreasing (underdoped system) and increasing (overdoped system) doping T_c decreases (Sec. 3.4.3).
- The crossover temperature $T^\star$ separating the observed non-Fermi and Fermi liquid behaviors in the normal state is seen to merge into the superconducting phase boundary in the slightly overdoped regime (Fig. 3.31).

Further studies on the effect of a finite next-nearest neighbor hopping t' were performed (Sec. 3.4.4). For $t' < 0$ the strong coupling of quasiparticles to magnetic excitations is found to induce pronounced non-Fermi liquid behavior and thus suppresses pairing. Hence T_c decreases. Positive values of t' on the other hand are found to enhance pairing and thus increase T_c. This result is in striking contrast to the weak coupling point of view, where negative values of t' are expected to promote pairing.

To support the claim of a magnetically driven pairing mechanism, the dependence of T_c on the magnitude of U was studied at optimal doping (Sec. 3.4.5). As U decreases from $U = 1.5W$, T_c first increases, reaches a maximum at about $U = 3/4W$ and then decreases again, reflecting the known U-dependence of the strength of the antiferromagnetic correlations. This result is clearly supportive of the scenario, where pairing occurs through the exchange of antiferromagnetic spin fluctuations.

For the first time a microscopic theory was able to explain all the fundamental features observed in high-T_c superconductors, including the antiferromagnetic phase in proximity to the d-wave superconducting state and the normal state pseudogap dominating the physics in the underdoped system. To summarize, the results obtained within this thesis present striking evidence that the 2D Hubbard model at $U \gtrsim W$ comprises the needed ingredients to describe qualitatively as well as quantitatively the low energy electronic behavior observed in high-T_c cuprate superconductors. And, since short-ranged antiferromagnetic correlations are found to dominate the physics in the Hubbard model, it seems reasonable to hold them responsible for the anomalous normal state behavior and the high-temperature superconductivity found in the cuprates.

4.2 Outlook

The present work offers various perspectives for future studies on the Hubbard or closely related models. Motivated by the structure of the high-T_c compounds, a first step towards a more realistic description of these materials would be to extend the 2D model to the third dimension, i.e. consider a periodic array of weakly coupled two-dimensional Hubbard layers. As a first approximation, the effects of a finite interlayer coupling $t_\perp$ may then be studied by neglecting dynamical correlations between different layers. This can be achieved by treating the additional coupling at the DMFA level, i.e. neglecting the k_z-dependence of the self-energy, but retaining the in-plane $\mathbf{k} = (k_x, k_y)$-dependence partially within the DCA. First results on this level indicate that a finite coupling between the planes of the form $t_\perp(k_x, k_y) = t_\perp(\cos k_x - \cos k_y)^2$ [And94] acts to enhance the superconducting transition temperature T_c at optimal doping (see Fig. 4.1). Studies to clarify the underlying mechanism for this enhancement are in progress. Furthermore the effect of a finite $t_\perp$ on the antiferromagnetic phase transition remains to be studied. The next step would be to account also for dynamic interlayer correlations by extending the DCA spirit to the third dimension. This could help to gain more insight in the important issue of whether the reduced dimensionality of the CuO_2-layers is responsible for the observed anomalous behavior in the cuprates.

Moreover the presented generalizations of the DCA to symmetry broken phases establish the basis for further investigations on the character of these phases. As a first step, a comparison of the total energies in the superconducting and paramagnetic state, respectively, can help to draw further conclusions about the nature of the superconducting phase in the 2D Hubbard model. Beyond that, the presented scheme can easily be generalized to incorporate a finite external magnetic field in the superconducting phase. Interesting aspects, e.g. the effect of a magnetic field on the transition temperature T_c could then be investigated. Furthermore, it then seems feasible to study the formation of vortices (of the size of the DCA cluster) in the superconducting state and the vast variety of related phenomena. The additional generalization of the formalism to states with odd-parity (spin-triplet) pairing by introducing a three-component order parameter would open another interesting area of application of the DCA. Then the unconventional superconducting phase with a p-wave order parameter observed in the layered oxide-superconductor Sr_2RuO_4 can be studied on a microscopic level.

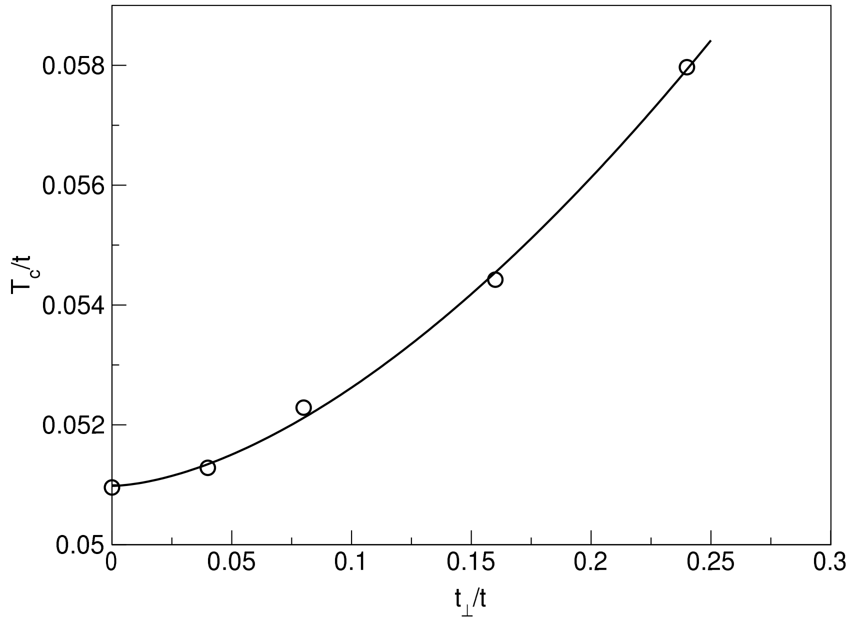

FIGURE 4.1: *The superconducting transition temperature T_c versus the inter-layer coupling $t_\perp$ between 2D Hubbard planes when the in-plane DCA cluster size $N_c = 4$, the Coulomb repulsion $U = 12t$ and next-nearest neighbor hopping $t' = 0$ at optimal doping $\delta = 0.20$. Dynamical correlations between layers are neglected.*

Formally possible is also the evaluation of two-particle correlation functions. This would open the possibility to study e.g. transport properties within the DCA. The DMFA (=DCA for $N_c = 1$) was already shown to capture some important aspects of the transport observed in the cuprates, including the linear behavior of the resistivity over a wide range of temperatures in the optimally doped cuprates (see Fig. 1.4). However the DMFA fails to describe the semiconducting behavior of the resistivity in underdoped samples. Based on the observation of the pseudogap within the DCA calculations for $N_c = 4$ it seems likely that the DCA is able to describe this semiconducting behavior. Studies along this line remain to be done to draw a complete picture of the physics of the planar Hubbard model of the cuprates.

Moreover the evaluation of two-particle correlation functions can be used to further elucidate the the nature of the low energy excitations in the observed non-Fermi liquid region of the 2D Hubbard model at low temperatures. Scenarios, based on spin-charge separation have been proposed to explain the non-Fermi liquid nature of the underdoped cuprates [And97]. By studying the behavior of spin- and charge susceptibilities at low temperatures, the DCA can help to promote or rule out microscopic theories based on that scenario.

Due to its universal nature, the DCA can also be applied to study various other models of strongly correlated electrons, including e.g. the periodic Anderson model for heavy Fermion materials. The rich phenomenology occurring in these systems including non-Fermi liquid states, long-range magnetic order, superconductivity and the coexistence of both magnetic order and superconductivity still lacks a microscopic description. In particular the DCA seems to be well suited to study the interplay of local dynamics related to the Kondo effect and nonlocal correlations resulting from RKKY interactions. Both effects are known to play an important role in heavy Fermion materials.

Appendix A

Properties of the hybridization function $\Gamma(\mathbf{K}, z)$

The following sections proof that the DCA coarse grained Green function (2.24) can be written in the form (Eq. (2.25)) with $\mathrm{Im}\,\Gamma(\mathbf{K}, z) < 0$ (Sec. A.1) and that $\Gamma(\mathbf{K}, z) \sim \mathcal{O}(1/N_c)$ (Sec. A.2). Sec. A.3 shows that $\Gamma(\mathbf{K}, z)$ can alternatively be obtained by a cavity construction and therefore can be interpreted as self-energy effect for the cluster states due to excursions to surrounding sites of the cluster. The following considerations apply also to the local hybridization function $\Gamma(z)$ of the DMFA, if the cluster size N_c is taken to be 1. Wherever it is feasible, the frequency argument of Green functions will be omitted for convenience.

A.1 On the analyticity of $\Gamma(\mathbf{K}, z)$

The following proof [Pru99] of the analyticity of $\Gamma(\mathbf{K}, z)$ is based on the derivation of an analytic expression for the cluster Green function

$$\bar{G}(\mathbf{K}, z) = \frac{N_c}{N} \sum_{\mathbf{k}'} \frac{1}{z - \epsilon_{\mathbf{K}+\mathbf{k}'} + \mu - \Sigma(\mathbf{K}, z)} \tag{A.1}$$

and employs standard methods of the projection technique [Gro85, Mag85]. The cluster self-energy $\Sigma(\mathbf{K}, z)$ is assumed to be analytic in the upper and lower half of the complex plane with $\mathrm{sign}(\mathrm{Im}\,\Sigma(\mathbf{K}, z)) = -\mathrm{sign}(\mathrm{Im}\, z)$.

Furthermore $\xi_{\mathbf{K}} := z + \mu - \Sigma(\mathbf{K}, z)$, $\mathrm{Im}\,(\xi_{\mathbf{K}}) > 0$ is used and a N/N_c dimensional set of linearly independent vectors $|\mathbf{k}'\rangle$ is introduced along with a linear hermitian operator $\mathcal{H}_{\mathbf{K}}$ satisfying $\mathcal{H}_{\mathbf{K}}|\mathbf{k}'\rangle = \epsilon_{\mathbf{K}+\mathbf{k}'}|\mathbf{k}'\rangle$ and $\sum_{\mathbf{k}'} |\mathbf{k}'\rangle\langle\mathbf{k}'| = 1$. Then there exists another vector $|f_0\rangle$ defined via $\langle\mathbf{k}'|f_0\rangle = \sqrt{N_c/N}$ for all $\mathbf{k}'$. With these conventions Eq. (A.1) may be written as

$$\bar{G}(\mathbf{K}, z) = \langle f_0|\frac{1}{\xi_{\mathbf{K}} - \mathcal{H}_{\mathbf{K}}}|f_0\rangle\,. \tag{A.2}$$

The resolvent operator may be trivially rewritten as

$$\frac{1}{\xi_{\mathbf{K}} - \mathcal{H}_{\mathbf{K}}} = \frac{1}{\xi_{\mathbf{K}}} + \frac{1}{\xi_{\mathbf{K}}} \mathcal{H}_{\mathbf{K}} \frac{1}{\xi_{\mathbf{K}} - \mathcal{H}_{\mathbf{K}}} \tag{A.3}$$

and thus

$$\langle f_0 | \frac{1}{\xi_{\mathbf{K}} - \mathcal{H}_{\mathbf{K}}} | f_0 \rangle = \frac{1}{\xi_{\mathbf{K}}} + \frac{1}{\xi_{\mathbf{K}}} \langle f_0 | \mathcal{H}_{\mathbf{K}} \frac{1}{\xi_{\mathbf{K}} - \mathcal{H}_{\mathbf{K}}} | f_0 \rangle \,, \tag{A.4}$$

where use of $\langle f_0 | f_0 \rangle = 1$ was made. Then two projection operators $P := |f_0\rangle\langle f_0|$ and $Q := 1 - P$ are defined and $1 = P + Q$ is inserted after $\mathcal{H}_{\mathbf{K}}$ in the second term, leading to

$$\begin{aligned} \langle f_0 | \frac{1}{\xi_{\mathbf{K}} - \mathcal{H}_{\mathbf{K}}} | f_0 \rangle = & \frac{1}{\xi_{\mathbf{K}}} + \frac{1}{\xi_{\mathbf{K}}} \langle f_0 | \mathcal{H}_{\mathbf{K}} | f_0 \rangle \langle f_0 | \frac{1}{\xi_{\mathbf{K}} - \mathcal{H}_{\mathbf{K}}} | f_0 \rangle \\ & + \frac{1}{\xi_{\mathbf{K}}} \langle f_0 | \mathcal{H}_{\mathbf{K}} Q \frac{1}{\xi_{\mathbf{K}} - \mathcal{H}_{\mathbf{K}}} | f_0 \rangle \,. \end{aligned} \tag{A.5}$$

Since furthermore

$$\begin{aligned} \frac{1}{\xi_{\mathbf{K}} - \mathcal{H}_{\mathbf{K}}} = & \frac{1}{\xi_{\mathbf{K}} - \mathcal{H}_{\mathbf{K}} Q - \mathcal{H}_{\mathbf{K}} P} = \\ & \frac{1}{\xi_{\mathbf{K}} - \mathcal{H}_{\mathbf{K}} Q} + \frac{1}{\xi_{\mathbf{K}} - \mathcal{H}_{\mathbf{K}} Q} \mathcal{H}_{\mathbf{K}} P \frac{1}{\xi_{\mathbf{K}} - \mathcal{H}_{\mathbf{K}}} \end{aligned} \tag{A.6}$$

and due to $Q|f_0\rangle = 0$

$$Q \frac{1}{\xi_{\mathbf{K}} - \mathcal{H}_{\mathbf{K}} Q} | f_0 \rangle = 0 \tag{A.7}$$

it is finally obtained

$$\begin{aligned} \langle f_0 | \frac{1}{\xi_{\mathbf{K}} - \mathcal{H}_{\mathbf{K}}} | f_0 \rangle = & \frac{1}{\xi_{\mathbf{K}}} + \frac{1}{\xi_{\mathbf{K}}} \langle f_0 | \mathcal{H}_{\mathbf{K}} | f_0 \rangle \langle f_0 | \frac{1}{\xi_{\mathbf{K}} - \mathcal{H}_{\mathbf{K}}} | f_0 \rangle \\ + \frac{1}{\xi_{\mathbf{K}}} \langle f_0 | \mathcal{H}_{\mathbf{K}} Q & \frac{1}{\xi_{\mathbf{K}} - \mathcal{H}_{\mathbf{K}} Q} \mathcal{H}_{\mathbf{K}} | f_0 \rangle \langle f_0 | \frac{1}{\xi_{\mathbf{K}} - \mathcal{H}_{\mathbf{K}}} | f_0 \rangle \,. \end{aligned} \tag{A.8}$$

Since $Q^2 = Q$,

$$\mathcal{H}_{\mathbf{K}} Q \frac{1}{\xi_{\mathbf{K}} - \mathcal{H}_{\mathbf{K}} Q} \mathcal{H}_{\mathbf{K}} = \mathcal{H}_{\mathbf{K}} Q \frac{1}{\xi_{\mathbf{K}} - Q \mathcal{H}_{\mathbf{K}} Q} Q \mathcal{H}_{\mathbf{K}} \,. \tag{A.9}$$

With the abbreviations

$$\Gamma(\mathbf{K}, z) = \langle f_0 | \mathcal{H}_{\mathbf{K}} Q \frac{1}{\xi_{\mathbf{K}} - Q \mathcal{H}_{\mathbf{K}} Q} Q \mathcal{H}_{\mathbf{K}} | f_0 \rangle \tag{A.10}$$

and

$$\bar{\epsilon}_{\mathbf{K}} = \langle f_0|\mathcal{H}_{\mathbf{K}}|f_0\rangle = \frac{N_c}{N}\sum_{\mathbf{k}'}\epsilon_{\mathbf{K}+\mathbf{k}'} \tag{A.11}$$

the final result is

$$\bar{G}(\mathbf{K},z) = \frac{1}{\xi_{\mathbf{K}} - \bar{\epsilon}_{\mathbf{K}} - \Gamma(\mathbf{K},z)}\,. \tag{A.12}$$

The averaging procedure replaces the kinetic energy of the lattice $\epsilon_{\mathbf{k}}$ by a quantity coarse grained onto the cluster $\bar{\epsilon}_{\mathbf{K}}$.

The second part of the argument is to show that $\mathrm{sign}(\mathrm{Im}\,\Gamma(\mathbf{K},z)) = -\mathrm{sign}(\mathrm{Im}\,z)$ is fulfilled. This however can easily be done by repeating the above step for the new vector $|f_1\rangle = Q\mathcal{H}_{\mathbf{K}}|f_0\rangle = \mathcal{H}_{\mathbf{K}}|f_0\rangle - \bar{\epsilon}_{\mathbf{K}}|f_0\rangle$, $\langle f_0|f_1\rangle = 0$, appearing in the definition of $\Gamma(\mathbf{K},z)$. This is simply the first step in a process to generate an orthogonal set of vectors. With $\tilde{\mathcal{H}}_{\mathbf{K}} = Q\mathcal{H}_{\mathbf{K}}Q$ it follows that

$$\Gamma(\mathbf{K},z) = \frac{b_0^2}{\xi_{\mathbf{K}} - a_1 - \bar{\Gamma}(\mathbf{K},z)}\,, \tag{A.13}$$

where

$$\begin{aligned}
b_0^2 &= \frac{\langle f_1|f_1\rangle}{\langle f_0|f_0\rangle} \geq 0 \\
a_1 &= \frac{\langle f_1|\mathcal{H}_{\mathbf{K}}|f_1\rangle}{\langle f_1|f_1\rangle} \\
\bar{\Gamma}(\mathbf{K},z) &= \frac{1}{\langle f_1|f_1\rangle}\langle f_1|\tilde{\mathcal{H}}_{\mathbf{K}}\tilde{Q}\frac{1}{\xi_{\mathbf{K}} - \tilde{Q}\tilde{\mathcal{H}}_{\mathbf{K}}\tilde{Q}}\tilde{Q}\tilde{\mathcal{H}}_{\mathbf{K}}|f_1\rangle \quad ,
\end{aligned} \tag{A.14}$$

where $\tilde{Q}$ now projects onto the subspace orthogonal to $|f_0\rangle$ and $|f_1\rangle$. It is clear from the above result that this procedure can be repeated, leading to a sequence of mutually orthogonal vectors $|f_n\rangle = \mathcal{H}_{\mathbf{K}}|f_{n-1}\rangle - a_{n-1}|f_{n-1}\rangle - b_{n-2}^2|f_{n-2}\rangle$ and a continued fraction representation of $\bar{G}(\mathbf{K},z)$ with coefficients

$$\begin{aligned}
b_{n-1}^2 &= \frac{\langle f_n|f_n\rangle}{\langle f_{n-1}|f_{n-1}\rangle} \geq 0 \\
a_n &= \frac{\langle f_n|\mathcal{H}_{\mathbf{K}}|f_n\rangle}{\langle f_n|f_n\rangle}
\end{aligned} \tag{A.15}$$

for $n \geq 1$. It is important to emphasize that the resulting coefficients b_{n-1}^2 are non-negative by construction. This however immediately leads to the relation $\mathrm{sign}(\mathrm{Im}\,\Gamma(\mathbf{K},z)) = -\mathrm{sign}(\mathrm{Im}\,z)$ and hence to the causality of $\Gamma(\mathbf{K},z)$.

A.2 Proof of $\Gamma(\mathbf{K}) \sim \mathcal{O}(1/N_c)$

The following proof is based on the expressions (2.24) and (2.25) for the coarse grained Green function $\bar{G}$. By defining

$$g(\mathbf{K}) = [z - \bar{\epsilon}_{\mathbf{K}} - \Sigma(\mathbf{K})]^{-1}\,, \tag{A.16}$$

$\bar{G}$ can be rewritten in the form

$$\begin{aligned}\bar{G}(\mathbf{K}) &= \frac{N_c}{N}\sum_{\mathbf{k}'} G(\mathbf{K}+\mathbf{k}') \\ &= \frac{1}{g^{-1}(\mathbf{K}) - \Gamma(\mathbf{K})}\,,\end{aligned} \tag{A.17}$$

where the frequency argument was dropped for convenience. By defining

$$t_{\mathbf{K}+\mathbf{k}'} = \epsilon_{\mathbf{K}+\mathbf{k}'} - \bar{\epsilon}_{\mathbf{K}}\,, \tag{A.18}$$

such that $N_c/N \sum_{\mathbf{k}'} t_{\mathbf{K}+\mathbf{k}'} = 0$, use of the exact relation

$$G(\mathbf{K}+\mathbf{k}') = g(\mathbf{K}) + g(\mathbf{K}) t_{\mathbf{K}+\mathbf{k}'} G(\mathbf{K}+\mathbf{k}') \tag{A.19}$$

can be made. By inserting Eq. (A.19) in Eq. (A.17) it is straightforward to show that $\Gamma(\mathbf{K})$ is given by

$$\Gamma(\mathbf{K}) = \frac{\dfrac{N_c}{N}\displaystyle\sum_{\mathbf{k}'} t^2_{\mathbf{K}+\mathbf{k}'} G(\mathbf{K}+\mathbf{k}')}{1 + \dfrac{N_c}{N}\displaystyle\sum_{\mathbf{k}'} t_{\mathbf{K}+\mathbf{k}'} G(\mathbf{K}+\mathbf{k}')}\,. \tag{A.20}$$

The momenta $\mathbf{k}'$ are restricted to a coarse graining cell so that $\mathbf{K}+\mathbf{k}'$ lies within the cell containing $\mathbf{K}$. Therefore the momenta $\mathbf{k}'$ are maximal of the order of Δk, where $\Delta k = 2\pi/N_c^{1/D}$ is the linear size of the DCA coarse graining cells. Since furthermore $\epsilon_{\mathbf{K}} - \bar{\epsilon}_{\mathbf{K}} \sim \mathcal{O}(\Delta k)$ it can be seen by performing a Taylor series expansion of $t_{\mathbf{K}+\mathbf{k}'}$ around the cluster momenta $\mathbf{K}$ that $t_{\mathbf{K}+\mathbf{k}'}$ is of order $\mathcal{O}(\Delta k)$. Therefore it follows from Eq. (A.20) that $\Gamma(\mathbf{K})$ is of order $\mathcal{O}((\Delta k)^2)$ and for two dimensions

$$\Gamma(\mathbf{K}) \sim \mathcal{O}(1/N_c)\,. \tag{A.21}$$

A.3 $\Gamma(\mathbf{K}, z)$ from cavity construction

In this section it will be shown that the hybridization function $\Gamma(\mathbf{K}, z)$ and hence the Weiss field (Eq. (2.27)) can also be obtained from the cavity construction method, i.e. $\Gamma(\mathbf{K}, z)$ describes hybridization with sites outside the cluster [Kel98].

To this end the lattice is divided into L^D-sized clusters and a discrete set of real space lattice vectors $\{\mathbf{x}_n\}$ is introduced. Now it is necessary to focus on one particular cluster located around the origin $\mathbf{x}_o$, which shall be called the "impurity cluster" in the following. Then, by going over to the discrete Fourier representation[1]

$$\Gamma(\mathbf{K}) = \sum_n \mathrm{e}^{-i\mathbf{K}\cdot(\mathbf{x}_n - \mathbf{x}_o)} \Gamma_{no} \,, \tag{A.22}$$

for sites on the impurity cluster $\mathbf{x}_n$ and $\mathbf{x}_o$, it has to be shown that in the spirit of a cavity construction, Γ_{no} can be written as

$$\Gamma_{no} = \sum_{l,m} \delta^c_{on} T_{nl} \tilde{G}_{lm} T_{mo} \,. \tag{A.23}$$

$\delta^c_{on} = N_c/N \sum_{\mathbf{k}'} \mathrm{e}^{i\mathbf{k}\cdot(\mathbf{x}_o - \mathbf{x}_n)}$ is the cluster δ-like function defined in Eq. (2.28) for the distance $\mathbf{R} + \mathbf{r} = \mathbf{x}_o - \mathbf{x}_n$ between the lattice vectors $\mathbf{x}_n$ and $\mathbf{x}_o$. δ^c_{on} is essentially 1 for sites n on the impurity cluster and falls off quickly for sites outside the cluster. The "cluster hopping integral" T_{nl} is given by

$$T_{nl} = 1/N \sum_{\mathbf{k}} \mathrm{e}^{i\mathbf{k}\cdot(\mathbf{x}_n - \mathbf{x}_l)} t_{\mathbf{k}} \,, \tag{A.24}$$

where $t_{\mathbf{k}}$ was defined in Eq. (A.18) for $\mathbf{k} = \mathbf{K} + \mathbf{k}'$. $\widetilde{G}_{lm}$ is defined as the full lattice Green function of the Hubbard model with the impurity cluster removed. Therefore it describes propagation of Fermions over lattice sites outside the impurity cluster.

The strategy now is to show that the definition (A.22) of $\Gamma(\mathbf{K})$ using the cavity construction (A.23) equals the expression (A.20) for $\Gamma(\mathbf{K})$, which was obtained by extracting $\Gamma(\mathbf{K})$ from the expression (A.17) for the coarse grained Green function. To this end one has to find an expression for $\widetilde{G}_{lm}$ in real space. The full lattice Green function G_{lm} in real space is obtained from the Fourier transform of the full lattice propagator $G(\mathbf{k})$ (Eq. (A.19)) and can be written as

$$\tilde{G}_{lm} = g_{lm} \delta^c_{lm} + \sum_{l',m'} g_{ll'} \delta^c_{ll'} T_{l'm'} \tilde{G}_{m'm} \,, \tag{A.25}$$

where $g_{lm} = 1/N_c \sum_{\mathbf{K}} \mathrm{e}^{i\mathbf{K}\cdot(\mathbf{x}_l - \mathbf{x}_n)} g(\mathbf{K})$ is the discrete Fourier transform of the cluster Green function $g(\mathbf{K})$ defined in Eq. (A.16). Thus

$$\widetilde{G}_{lm} = g_{lm} \delta^c_{lm} + {\sum_{l',m'}}' g_{ll'} \delta^c_{ll'} T_{l'm'} \widetilde{G}_{m'm} \tag{A.26}$$

is obtained by restricting the sum to sites outside the cluster (indicated by the prime). To evaluate Eq. (A.23), the auxiliary quantity

$$Q_{lo} = \sum_m \widetilde{G}_{lm} T_{mo} \tag{A.27}$$

[1] The frequency argument is omitted for convenience.

is defined. Inserting Eq. (A.26) leads to

$$Q_{lo} = \sum_m g_{lm}\delta^c_{lm}T_{mo} + \sum_{l',m'} g_{ll'}\delta^c_{ll'}T_{l'm'}Q_{m'o} + f_{lo}\,, \tag{A.28}$$

where instead of restricting the second sum to sites m' outside the cluster, an additional term f_{lo} has been added to account for the site exclusion. Therefore f_{lo} is determined by the requirement that

$$\sum_l \delta^c_{ol}Q_{lo}\mathrm{e}^{-i\mathbf{K}\cdot(\mathbf{x}_l-\mathbf{x}_o)} = 0 \tag{A.29}$$

for each value of $\mathbf{K}$. Going over to a Fourier representation, this requirement is expressed by the condition

$$\frac{N_c}{N}\sum_{\mathbf{k}'} Q(\mathbf{K}+\mathbf{k}') = 0 \tag{A.30}$$

for all $\mathbf{K}$. Then $Q(\mathbf{K}+\mathbf{k}')$ is determined by the following equation in Fourier space:

$$Q(\mathbf{K}+\mathbf{k}') = g(\mathbf{K})t_{\mathbf{K}+\mathbf{k}'} + g(\mathbf{K})t_{\mathbf{K}+\mathbf{k}'}Q(\mathbf{K}+\mathbf{k}') - g(\mathbf{K})\frac{N_c}{N}\sum_{\mathbf{k}_1} t_{\mathbf{K}+\mathbf{k}_1}Q(\mathbf{K}+\mathbf{k}_1) \tag{A.31}$$

With Eqs. (A.22), (A.23) and (A.27) $\Gamma(\mathbf{K})$ can be expressed as

$$\Gamma(\mathbf{K}) = \sum_{nl} \mathrm{e}^{-i\mathbf{K}\cdot(\mathbf{x}_n-\mathbf{x}_o)}\delta^c_{on}T_{nl}Q_{lo} = \frac{N_c}{N}\sum_{\mathbf{k}_1} t_{\mathbf{K}+\mathbf{k}_1}Q(\mathbf{K}+\mathbf{k}_1)\,, \tag{A.32}$$

and, after solving for $Q(\mathbf{K}+\mathbf{k}')$, Eq. (A.31) reads

$$Q(\mathbf{K}+\mathbf{k}') = G(\mathbf{K}+\mathbf{k}')(t_{\mathbf{K}+\mathbf{k}'} - \Gamma(\mathbf{K}))\,. \tag{A.33}$$

By multiplying with $t_{\mathbf{K}+\mathbf{k}'}$, summing over $\mathbf{k}'$ and solving for $\Gamma(\mathbf{K})$ it is straightforward to show that

$$\Gamma(\mathbf{K}) = \frac{\dfrac{N_c}{N}\displaystyle\sum_{\mathbf{k}'} t^2_{\mathbf{K}+\mathbf{k}'}G(\mathbf{K}+\mathbf{k}')}{1 + \dfrac{N_c}{N}\displaystyle\sum_{\mathbf{k}'} t_{\mathbf{K}+\mathbf{k}'}G(\mathbf{K}+\mathbf{k}')}\,, \tag{A.34}$$

which is exactly the desired relation (A.20).

$N_c = 1$:

For the cluster size $N_c = 1$ (DMFA) the above calculation still holds. Then the quantities Γ and g are purely local, the cluster delta-like function is replaced by the regular Kronecker function $\delta^c_{lm} \to \delta_{lm} = 1/N \sum_{\mathbf{k}} \mathrm{e}^{i\mathbf{k}\cdot(\mathbf{x}_l - \mathbf{x}_m)}$ and sums over cells extend to sums over the full BZ. The DMFA hybridization function Γ can then be written as

$$\Gamma = \frac{\dfrac{1}{N}\sum\limits_{\mathbf{k}} t^2_{\mathbf{k}} G(\mathbf{k})}{1 + \dfrac{1}{N}\sum\limits_{\mathbf{k}} t_{\mathbf{k}} G(\mathbf{k})}, \tag{A.35}$$

which is identical to the expression (A.20) for $N_c = 1$.

Appendix B

Non Crossing Approximation

A brief summary of the concepts and details of the resolvent technique [Kei71, Bec86] along with its application, the NCA, is presented. The method will be derived by means of the single impurity Anderson model (SIAM) (Eq. (2.13)). However, by using a general notation (close to the notation used in [Bec86]), the derived equations are also applicable to more general situations, where a discrete level system couples to a non-interacting Fermionic or Bosonic continuous system.

The resolvent technique is a perturbational expansion around the atomic limit with respect to the coupling to the conduction electrons. Therefore the Hamiltonian is split into two parts

$$H_f = H_o + H_1 \tag{B.1}$$

with the unperturbed term

$$H_o = H_{\text{loc}} + H_c\,. \tag{B.2}$$

The local term

$$H_{\text{loc}} = \sum_{\sigma} \epsilon_f f_\sigma^\dagger f_\sigma + U n_{f\uparrow} n_{f\downarrow} \tag{B.3}$$

describes particles on the impurity and

$$H_c = \sum_{\mathbf{k}\sigma} \varepsilon_{\mathbf{k}} a_{\mathbf{k}\sigma}^\dagger a_{\mathbf{k}\sigma} \tag{B.4}$$

stands for the non-interacting conduction electrons. The hybridization between the localized electrons and conduction electron states is given by the perturbation term

$$H_1 = \sum_{\mathbf{k}\sigma} (V_{\mathbf{k}} f_\sigma^\dagger a_{\mathbf{k}\sigma} + \text{h.c.})\,. \tag{B.5}$$

The Fermionic operators f_σ ($f_\sigma^\dagger$) are expanded in terms of the Hubbard-operators $X_{mn} = |m\rangle\langle n|$,

$$f_\sigma = \sum_{m,n} F_{mn}^\sigma X_{mn} \quad , \quad f_\sigma^\dagger = \sum_{m,n} (F_{mn}^\sigma)^\star X_{nm}\,, \tag{B.6}$$

where $\{|m\rangle\}$ are the eigenstates of the local Hamiltonian

$$H_{\mathrm{loc}} = \sum_m E_m X_{mm} \tag{B.7}$$

with eigenenergies E_m and $F^{\sigma}_{mn} = \langle m|f_\sigma|n\rangle$. The hybridization term H_1 (Eq. (B.5)) then becomes

$$H_1 = \sum_{\mathbf{k},\sigma,m,n} \left[V_{\mathbf{k}} (F^{\sigma}_{mn})^\star X_{nm} a_{\mathbf{k}\sigma} + V^\star_{\mathbf{k}} F^{\sigma}_{mn} a^\dagger_{\mathbf{k}\sigma} X_{mn} \right] . \tag{B.8}$$

Before its diagonalization, the local part of the Hamiltonian H_{loc} contained an interaction bilinear in the Fermionic operators. For this reason the Hubbard-operators X_{mn} do not obey standard Fermionic or Bosonic commutation relations, and therefore the conventional Feynman diagram technique cannot be used for a perturbation expansion. Instead the concept of resolvents must be introduced [Kei71].

Partition function

The partition function is defined as

$$Z = \mathrm{Tr}_f \mathrm{Tr}_c \, \mathrm{e}^{-\beta H} \tag{B.9}$$

with the total degrees of freedom separated into an impurity part (f) and a conduction electron part (c). The resolvent technique is based on the idea to factorize

$$\mathrm{e}^{-\beta H} = \mathrm{e}^{-\beta(H_{\mathrm{loc}} + \mathcal{L}_c + H_1)} \mathrm{e}^{-\beta H_c} \tag{B.10}$$

into two parts, since Wicks theorem can be applied to the part $\mathrm{e}^{-\beta H_c}$. The Liouville operator is defined by $\mathcal{L}_c A = [H_c, A]_-$. Then by using the definition $\langle A \rangle_c = \frac{1}{Z_c} \mathrm{Tr}_c \, (\mathrm{e}^{-\beta H_c} A)$, the partition function factorizes according to

$$Z = Z_c \cdot Z_f \, , \tag{B.11}$$

with $Z_c = \mathrm{Tr}_c \, \mathrm{e}^{-\beta H_c}$ and the renormalized f-partition function

$$Z_f = \mathrm{Tr}_f \, \left\langle \mathrm{e}^{-\beta(H_{\mathrm{loc}} + \mathcal{L}_c + H_1)} \right\rangle_c \, . \tag{B.12}$$

By introducing the resolvent

$$R(z) = \frac{1}{z - H_{\mathrm{loc}} - \mathcal{L}_c - H_1} \, , \tag{B.13}$$

Eq. (B.12) can be rewritten as a contour integral

$$Z_f = \int_{\mathcal{C}} \frac{\mathrm{d}z}{2\pi i} \, \mathrm{e}^{-\beta z} \mathrm{Tr}_f \, \langle R(z) \rangle_c \, , \tag{B.14}$$

where the integration path $\mathcal{C}$ encloses all the poles of the resolvent operator $R(z)$ counterclockwise. By introducing the reduced resolvent

$$\bar{R}(z) = \langle R(z) \rangle_c \,, \tag{B.15}$$

and making use of the spectral representation

$$\bar{R}_m(z) = -\frac{1}{\pi} \int\limits_{-\infty}^{+\infty} \mathrm{d}\omega \, \frac{\mathrm{Im}\, \bar{R}_m(\omega)}{z - \omega} \tag{B.16}$$

for the matrix elements $\bar{R}_m(\omega) = \langle m|\bar{R}(\omega)|m\rangle$ of the reduced resolvent, Z_f can finally be written as

$$Z_f = -\frac{1}{\pi} \int\limits_{-\infty}^{+\infty} \mathrm{d}\omega \, \mathrm{e}^{-\beta\omega} \sum_m \mathrm{Im}\, \bar{R}_m(\omega) \,. \tag{B.17}$$

$\bar{R}_m(\omega)$ are often called ionic propagators.

Green function

It can be shown that the thermodynamic Green function $G_{AB}(i\omega_n) = \langle\langle A; B\rangle\rangle(i\omega_n)$ for arbitrary operators A and B, as a function of the Matsubara frequencies $\omega_n = (2n+1)\pi/\beta$, where n is an integer and $\beta = 1/T$ is the inverse temperature, can be expressed in terms of the resolvent [Bec86]

$$G_{AB}(i\omega_n) = \frac{1}{Z_f} \int\limits_{\mathcal{C}} \frac{\mathrm{d}z}{2\pi i} \, \mathrm{e}^{-\beta z} \mathrm{Tr}_f \, \langle R(z) A R(z + i\omega_n) B \rangle_c \,. \tag{B.18}$$

The integration path $\mathcal{C}$ encloses all poles of the integrand counterclockwise. Using the expansion (B.6) for the operators of the f-electron Green function $G_f(i\omega_n) = \langle\langle f_\sigma; f_\sigma^\dagger\rangle\rangle(i\omega_n)$, one obtains

$$G_f(z) = \sum_{\substack{m,m' \\ n,n'}} F^\sigma_{mm'} (F^\sigma_{nn'})^\star \langle\langle X_{mm'}; X_{n'n}\rangle\rangle_z \,, \tag{B.19}$$

with the correlation function

$$\langle\langle X_{mm'}; X_{n'n}\rangle\rangle_z = \frac{1}{Z_f} \int\limits_{\mathcal{C}} \frac{\mathrm{d}z}{2\pi i} \, \mathrm{e}^{-\beta z} \mathrm{Tr}_f \, \langle R(z) X_{mm'} R(z + i\omega_n) X_{n'n} \rangle_c \,. \tag{B.20}$$

Perturbation theory and diagram expansion

The perturbation theory for the partition function Z_f and Green function G_f is based on the expansion of the resolvent

$$R(z) = R^o(z) \sum_{n=0}^{\infty} [H_1 R^o(z)]^n \tag{B.21}$$

with the bare resolvent $R^o(z) = (z - H_{\text{loc}} - \mathcal{L}_c)^{-1}$. $\mathcal{L}_c$ acts on the conduction electron states only and can be replaced by the energy levels $\varepsilon_{\mathbf{k}}$ of the continuous spectrum. The result of such an expansion is conveniently expressed by a set of diagrams. The types of vertices in these diagrams depends on the expression for the interaction Hamiltonian H_1. The form (B.8) corresponds to the two vertices

The diagram on the left corresponds to the first term in H_1, where a conduction electron (represented by the solid line) hops onto the impurity, which consequently changes its state from m to n with one more particle. The amplitude for this process is given by the product $V_{\mathbf{k}}(F^{\sigma}_{mn})^{\star}$. The diagram on the right corresponds to the second term in H_1, describing the reverse process. The dotted (wavy) line stands for the zero order ionic propagator $\bar{R}^o_m = \langle m|\langle R_o\rangle_c|m\rangle$ ($\bar{R}^o_n$). They are diagonal in the local states $\{|m\rangle\}$ and given by

$$\bar{R}^o_m(z) = \frac{1}{z - E_m}\,. \tag{B.22}$$

Higher order terms contain thermal averages over conduction electron operators, which separate into sums of products of the thermal averages $\langle c^{\dagger}_{\mathbf{k}\sigma} c_{\mathbf{k}\sigma}\rangle_c = f(\varepsilon_{\mathbf{k}})$ and $\langle c_{\mathbf{k}\sigma} c^{\dagger}_{\mathbf{k}\sigma}\rangle_c = 1 - f(\varepsilon_{\mathbf{k}})$ after applying Wicks theorem. Since the diagrammatic expansion for the reduced resolvent factorizes, $\bar{R}(z)$ can be written in form of a Dyson equation

$$\bar{R}(z) = \bar{R}^o(z) + \bar{R}^o(z)\Sigma^R(z)\bar{R}(z)\,. \tag{B.23}$$

Its matrix elements in the space of the local eigenstates $\{|n\rangle\}$ then read

$$[\bar{R}^{-1}]_{mn}(z) = (z - E_m)\delta_{mn} - \Sigma^R_{mn}(z)\,. \tag{B.24}$$

This defines the irreducible resolvent self-energy Σ^R. The NCA-approximation for Σ^R collects diagrams to all orders in V with non-crossing conduction electron

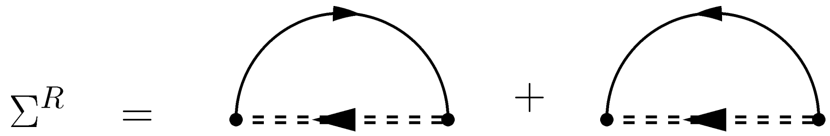

FIGURE B.1: *The NCA-approximation for the resolvent self energy Σ^R. The solid curved lines from left to right and right to left denote the Fermi functions $f(\varepsilon_{\mathbf{k}})$ and $1 - f(\varepsilon_{\mathbf{k}}) = f(-\varepsilon_{\mathbf{k}})$, respectively. The double-dashed line corresponds to the reduced resolvent $\bar{R}$.*

lines. Fig. B.1 illustrates the NCA diagrams for the resolvent self-energy Σ^R. The solid curved lines from left to right and right to left respectively stand for the Fermi function $f(\varepsilon_{\mathbf{k}})$ and $1 - f(\varepsilon_{\mathbf{k}}) = f(-\varepsilon_{\mathbf{k}})$. The double-dashed line represents the reduced resolvent $\bar{R}$. After adding products $V_{\mathbf{k}} F^{\sigma}_{mn}$ to the vertices, summing over the degrees of freedom of the internal lines and observing energy conservation on the vertices, the analytical expression for the matrix elements mn of Σ^R reads

$$\begin{aligned}\Sigma^R_{mn}(z) \;&=\; \frac{1}{N}\sum_{\mathbf{k},\sigma} |V_{\mathbf{k}}|^2 \sum_{l,l'} \left[f(\varepsilon_{\mathbf{k}}) F^{\sigma}_{ml} \bar{R}_{ll'}(z+\varepsilon_{\mathbf{k}})(F^{\sigma}_{nl'})^{\star} \right. \\ &\quad \left. + f(-\varepsilon_{\mathbf{k}})(F^{\sigma}_{lm})^{\star} \bar{R}_{ll'}(z-\varepsilon_{\mathbf{k}}) F^{\sigma}_{l'n} \right] . \end{aligned} \tag{B.25}$$

In general non-diagonal elements $m \neq n$ may exist. If the interaction term H_1 does not break the symmetry of the local Hamiltonian H_{loc}, they vanish and the matrix equation (B.23) reduces to a set of scalar equations for each local eigenstate m. Eqs. (B.24)) and (B.25) define a closed set of equations to self-consistently determine the ionic propagators $\bar{R}_{mn}(z) = \langle m|\bar{R}(z)|n\rangle$.

The correlation function (Eq. (B.20)) is further simplified in NCA-approximation [Bec86], i.e. by neglecting diagrams with crossing conduction electron lines. Then the integrand

$$\mathrm{Tr}_f \, \langle R(z) X_{mm'} R(z+i\omega_n) X_{n'n} \rangle_c \to \bar{R}_{nm}(z) \bar{R}_{m'n'}(z+i\omega_n) \tag{B.26}$$

is replaced by a product of reduced resolvents and after analytically continuing the result to real frequencies the correlation function can be written as

$$\langle\langle X_{mm'}; X_{n'n}\rangle\rangle_z = \frac{1}{Z_f} \int\limits_{-\infty}^{+\infty} \mathrm{d}\varepsilon \, \mathrm{e}^{-\beta\varepsilon} [\rho_{nm}(\varepsilon) \bar{R}_{m'n'}(\varepsilon+\omega+i\delta) - \rho_{m'n'}(\varepsilon) \bar{R}^{\star}_{nm}(\varepsilon-\omega+i\delta)] \, , \tag{B.27}$$

with the spectral density of the resolvents, $\rho_{nm}(\omega) = -\frac{1}{\pi}\mathrm{Im}\, R_{nm}(z)$.

Appendix C

Generalizations for symmetry broken states

This chapter presents a detailed derivation and description of the generalizations for the cluster-NCA algorithm to solve the cluster model in symmetry broken phases. General concepts of the resolvent technique can be found in App. B.

C.1 Cluster-NCA in the superconducting state

Effective cluster model in the superconducting phase

The mapping onto a corresponding cluster model in the superconducting phase is fixed by the condition that the bare Green function of the cluster-Fermions is identical to the effective medium $\mathcal{G}$. Thus the expression (2.74) for the effective medium determines the type of uncorrelated Hamiltonian for the effective cluster problem. It differs from the corresponding effective medium for the paramagnetic state (right hand side of Eq. 2.48) by the off-diagonal elements of the hybridization function $\mathbf{\Gamma}$. Therefore the cluster Hamiltonian H_{cluster} (Eq. (2.41)) has to be extended by adding further terms that are off-diagonal in the quantum numbers $(\mathbf{k}, \uparrow)$ and $(-\mathbf{k}, \downarrow)$ to the term describing the effective medium H_{med} (Eq. (2.44)). Then the superconducting modification of the medium term reads

$$H^{\text{sc}}_{\text{med}} = H_{\text{med}} + H^{\text{sc}} = \sum_{\mathbf{k}\sigma} (\varepsilon_{\mathbf{k}} - \mu) a^{\dagger}_{\mathbf{k}\sigma} a_{\mathbf{k}\sigma} + \sum_{\mathbf{k}} \left[\Delta(\mathbf{k}) a^{\dagger}_{-\mathbf{k}\downarrow} a^{\dagger}_{\mathbf{k}\uparrow} + \Delta^{\star}(\mathbf{k}) a_{\mathbf{k}\uparrow} a_{-\mathbf{k}\downarrow} \right] , \tag{C.1}$$

where a BCS-like term H^{sc} with a fictive pairing amplitude $\Delta(\mathbf{k}) = \Delta_1(\mathbf{k}) + i\Delta_2(\mathbf{k})$, with $\Delta_{1/2}$ real, was added to the paramagnetic term H_{med}. The chemical potential μ was added to account for the fact that the BCS term does not conserve the particle number. The modified cluster Hamiltonian for the superconducting phase is then given by

$$H^{\mathrm{sc}}_{\mathrm{cluster}} = H_f + H_U + H_{\mathrm{hyb}} + H^{\mathrm{sc}}_{\mathrm{med}}\,, \tag{C.2}$$

with H_f, H_U, and H_{hyb} defined in Eqs. (2.42) and (2.45). It describes Fermions on a periodic cluster, coupled to a superconducting host, which is described in BCS-like fashion by Eq. (C.1). At this point it is important to stress that the BCS-form for the effective medium does not mean any limitation of this algorithm to the treatment of BCS-like superconductivity only. The Hamiltonian representing the effective medium $H^{\mathrm{sc}}_{\mathrm{med}}$ (Eq. (C.1)) is an auxiliary construction and serves to imitate the effective medium $\mathbf{\Gamma}(\mathbf{K})$ (Eq. (2.75)). The NCA algorithm replaces the auxiliary quantities by the hybridization function $\mathbf{\Gamma}(\mathbf{K})$. Their only use is to setup the generalized cluster-NCA formalism. After the replacement of the auxiliary medium term, the algorithm is fully general in the sense, that it includes retardation as well as damping effects. The presence of paired states has also feedback effects on the low energy excitations and no assumption about the origin of superconductivity is being made.

It has to be shown that the bare Green function for the f-electrons of the cluster Hamiltonian $H^{\mathrm{sc}}_{\mathrm{cluster}}$ (Eq. (C.2)) has the same form as the effective medium $\mathcal{G}(\mathbf{K})$ (Eq. (2.74)) calculated from lattice quantities. To this end the Hamiltonian is rewritten in terms of the Nambu spinors

$$\begin{aligned}\Psi^\dagger_{f\mathbf{K}} &:= \left(f^\dagger_{\mathbf{K}\uparrow}\,,\, f_{-\mathbf{K}\downarrow}\right) \quad , \quad \Psi_{f\mathbf{K}} := (\Psi^\dagger_{f\mathbf{K}})^\dagger \\ \Psi^\dagger_{a\mathbf{k}} &:= \left(a^\dagger_{\mathbf{k}\uparrow}\,,\, a_{-\mathbf{k}\downarrow}\right) \quad , \quad \Psi_{a\mathbf{k}} := (\Psi^\dagger_{a\mathbf{k}})^\dagger\end{aligned} \tag{C.3}$$

for the cluster electrons (f) and auxiliary fermions (a). With the Pauli-spin matrices

$$\sigma_o = \begin{pmatrix} 1 & 0 \\ 0 & 1 \end{pmatrix}\,,\ \sigma_1 = \begin{pmatrix} 0 & 1 \\ 1 & 0 \end{pmatrix}\,,\ \sigma_2 = \begin{pmatrix} 0 & -i \\ i & 0 \end{pmatrix}\,,\ \sigma_3 = \begin{pmatrix} 1 & 0 \\ 0 & -1 \end{pmatrix} \tag{C.4}$$

the uncorrelated parts H_f, $H^{\mathrm{sc}}_{\mathrm{med}}$ and H_{hyb} of the cluster Hamiltonian (2.41) can be rewritten as

$$H_f = \sum_{\mathbf{K}} (\bar{\epsilon}_{\mathbf{K}} - \mu)\Psi^\dagger_{f\mathbf{K}}\sigma_3\Psi_{f\mathbf{K}} \tag{C.5}$$

$$H^{\mathrm{sc}}_{\mathrm{med}} = \sum_{\mathbf{k}} \Psi^\dagger_{a\mathbf{k}}[\varepsilon_{\mathbf{k}}\sigma_3 - \Delta_1(\mathbf{k})\sigma_1 + \Delta_2(\mathbf{k})\sigma_2]\Psi_{a\mathbf{k}} \tag{C.6}$$

$$H_{\mathrm{hyb}} = \frac{1}{\sqrt{N}}\sum_{\mathbf{K},\mathbf{k}'} (V_{\mathbf{K},\mathbf{k}'}\Psi^\dagger_{f\mathbf{K}}\sigma_3\Psi_{a\mathbf{K}+\mathbf{k}'} + \mathrm{h.c.})\,. \tag{C.7}$$

It is straightforward to solve the equation of motion for the uncorrelated part $H_f + H^{\mathrm{sc}}_{\mathrm{med}} + H_{\mathrm{hyb}}$ of the generalized cluster Hamiltonian $H^{\mathrm{sc}}_{\mathrm{cluster}}$ to obtain for the bare f-Green function

$$\mathbf{G}_f^o(\mathbf{K},z) = \langle\langle \Psi_{f\mathbf{K}\sigma}\,;\,\Psi_{f\mathbf{K}\sigma}^\dagger\rangle\rangle_z^o = \left[z\sigma_o - (\bar{\epsilon}_{\mathbf{K}} - \mu)\sigma_3 - \mathbf{\Gamma}_c(\mathbf{K},z)\right]^{-1} \tag{C.8}$$

the same form as for $\mathcal{G}(\mathbf{K})$ (Eq. (2.74)) with the cluster hybridization function

$$\begin{aligned} \mathbf{\Gamma}_c(\mathbf{K},z) &= \frac{1}{N}\sum_{\mathbf{k}'} |V_{\mathbf{K},\mathbf{k}'}|^2 \langle\langle \Psi_{a\mathbf{K}+\mathbf{k}'}\,;\,\Psi_{a\mathbf{K}+\mathbf{k}'}^\dagger\rangle\rangle_z^o = \\ &= \frac{1}{N}\sum_{\mathbf{k}'} |V_{\mathbf{K},\mathbf{k}'}|^2 \left[z\sigma_o - (\varepsilon_{\mathbf{K}+\mathbf{k}'} - \mu)\sigma_3 + \Delta_1(\mathbf{K}+\mathbf{k}')\sigma_1 - \Delta_2(\mathbf{K}+\mathbf{k}')\sigma_2\right]^{-1} . \end{aligned} \tag{C.9}$$

$\langle\langle \Psi_{a\mathbf{k}}\,;\,\Psi_{a\mathbf{k}}^\dagger\rangle\rangle_z^o$ denotes the bare Green function of the effective medium part $H_{\mathrm{med}}^{\mathrm{sc}}$. For $\Delta = 0$, Eq. (C.9) is diagonal in Nambu space and reduces to the paramagnetic form (2.46). For $\Delta \neq 0$, $\mathbf{\Gamma}_c$ describes the hybridization to a superconducting host, represented by $H_{\mathrm{med}}^{\mathrm{sc}}$ (Eq. (C.1)).

Generalized cluster-NCA for the superconducting phase

To apply the resolvent technique to the modified cluster model described by $H_{\mathrm{cluster}}^{\mathrm{sc}}$ (Eq. (C.2)) it is convenient to diagonalize the term describing the superconducting effective medium $H_{\mathrm{med}}^{\mathrm{sc}}$ (Eq. (C.1)) by the Bogliubov-transformation (see e.g. [Sch61]) to the quasiparticle operators

$$\gamma_{\mathbf{k}\sigma}^\dagger := u_{\mathbf{k}} a_{\mathbf{k}\sigma}^\dagger - \sigma v_{\mathbf{k}} a_{-\mathbf{k}\bar{\sigma}}\ ;\ \gamma_{\mathbf{k}\sigma} := u_{\mathbf{k}} a_{\mathbf{k}\sigma} - \sigma v_{\mathbf{k}} a_{-\mathbf{k}\bar{\sigma}}^\dagger\ ;\ \sigma \in \{-1,1\}\ ;\ \bar{\sigma} := -\sigma\,, \tag{C.10}$$

with the coherence factors [Sch61]

$$u_{\mathbf{k}} := \sqrt{\frac{1}{2}\left(1 + \frac{\varepsilon_{\mathbf{k}} - \mu}{E_{\mathbf{k}}}\right)}\ ;\ v_{\mathbf{k}} := \sqrt{\frac{1}{2}\left(1 - \frac{\varepsilon_{\mathbf{k}} - \mu}{E_{\mathbf{k}}}\right)}\,, \tag{C.11}$$

with $u_{\mathbf{k}}^2 + v_{\mathbf{k}}^2 = 1$ and the quasiparticle energies

$$E_{\mathbf{k}} = \sqrt{(\varepsilon_{\mathbf{k}} - \mu)^2 - |\Delta(\mathbf{k})|^2} \tag{C.12}$$

to give

$$H_{\mathrm{med}}^{\mathrm{sc}} = \sum_{\mathbf{k}\sigma} E_{\mathbf{k}} \gamma_{\mathbf{k}\sigma}^\dagger \gamma_{\mathbf{k}\sigma}\,. \tag{C.13}$$

It is convenient to retain the Nambu representation by introducing Nambu spinors for the γ-operators

$$\Psi_{\gamma\mathbf{k}}^\dagger := \left(\gamma_{\mathbf{k}\uparrow}^\dagger\,,\,\gamma_{-\mathbf{k}\downarrow}\right) \quad , \quad \Psi_{\gamma\mathbf{k}} := (\Psi_{\gamma\mathbf{k}}^\dagger)^\dagger\,. \tag{C.14}$$

With this definition it holds that

$$\Psi_{a\mathbf{k}} = \mathbf{U}\Psi_{\gamma\mathbf{k}} \quad , \quad \Psi_{a\mathbf{k}}^\dagger = \Psi_{\gamma\mathbf{k}}^\dagger \mathbf{U}^{-1} \tag{C.15}$$

with the unitary matrix

$$\mathbf{U} = \begin{pmatrix} u_{\mathbf{k}} & v_{\mathbf{k}} \\ -v_{\mathbf{k}} & u_{\mathbf{k}} \end{pmatrix} . \tag{C.16}$$

In terms of these Nambu spinors the effective medium term reads

$$H^{\mathrm{sc}}_{\mathrm{med}} = \sum_{\mathbf{k}} E_{\mathbf{k}} \Psi^{\dagger}_{\gamma\mathbf{k}} \sigma_3 \Psi_{\gamma\mathbf{k}} . \tag{C.17}$$

This diagonalization step was necessary to simplify the following perturbational expansion. It involves products of thermal averages over conduction electron operators (compare App. B), which then reduce to simple Fermi functions

$$\langle (\Psi^{\dagger}_{\gamma\mathbf{k}})^T (\Psi_{\gamma\mathbf{k}})^T \rangle = \begin{pmatrix} f(E_{\mathbf{k}}) & 0 \\ 0 & f(-E_{\mathbf{k}}) \end{pmatrix} \quad ; \quad \langle \Psi_{\gamma\mathbf{k}} \Psi^{\dagger}_{\gamma\mathbf{k}} \rangle = \begin{pmatrix} f(-E_{\mathbf{k}}) & 0 \\ 0 & f(E_{\mathbf{k}}) \end{pmatrix} . \tag{C.18}$$

$(\ldots)^T$ denotes the corresponding transposed vector of the vector in brackets. After diagonalizing the local part $H_{\mathrm{loc}} = H_f + H_U$, the cluster Nambu spinors $\Psi_{f\mathbf{k}}$ $(\Psi^{\dagger}_{f\mathbf{K}})$ can be expanded in terms of the Hubbard operators $X_{mn} = |m\rangle\langle n|$

$$\Psi_{f\mathbf{K}} = \sum_{m,n} \mathbf{F}^{\mathbf{K}}_{mn} X_{mn} \quad , \quad \Psi^{\dagger}_{f\mathbf{K}} = \sum_{m,n} (\mathbf{F}^{\mathbf{K}}_{mn})^{\dagger} X_{nm} , \tag{C.19}$$

with the eigenstates $\{|n\rangle\}$ of the local part H_{loc}. The relation between the vectors $\mathbf{F}^{\mathbf{K}}_{mn} = \langle m|\Psi_{f\mathbf{K}}|n\rangle$, $(\mathbf{F}^{\mathbf{K}}_{mn})^{\dagger} = \langle n|\Psi^{\dagger}_{f\mathbf{K}}|m\rangle$ and the matrix elements $F^{\mathbf{K}\sigma}_{mn}$ defined in Eq. (2.51) is given by

$$\mathbf{F}^{\mathbf{K}}_{mn} = \begin{pmatrix} F^{\mathbf{K}\uparrow}_{mn} \\ (F^{-\mathbf{K}\downarrow}_{nm})^{\star} \end{pmatrix} \quad , \quad (\mathbf{F}^{\mathbf{K}}_{mn})^{\dagger} = \left((F^{\mathbf{K}\uparrow}_{mn})^{\star} \, ; \, F^{-\mathbf{K}\downarrow}_{nm} \right) . \tag{C.20}$$

With these definitions the hybridization term can be written as

$$\begin{aligned} H_{\mathrm{hyb}} \;=\; & \frac{1}{\sqrt{N}} \sum_{\mathbf{K},\mathbf{k}'} \sum_{m,n} \Big[\\ & V_{\mathbf{K},\mathbf{k}'} (\mathbf{F}^{\mathbf{K}}_{mn})^{\dagger} X_{nm} \sigma_3 \mathbf{U} \Psi_{\gamma\mathbf{K}+\mathbf{k}'} + V^{\star}_{\mathbf{K},\mathbf{k}'} \Psi^{\dagger}_{\gamma\mathbf{K}+\mathbf{k}'} \mathbf{U}^{-1} \sigma_3 \mathbf{F}^{\mathbf{K}}_{mn} X_{mn} \Big] . \end{aligned} \tag{C.21}$$

H_{hyb} describes the coupling of the cluster states to the excited states of the superconducting system. If $\Delta(\mathbf{k}) = 0 \; \forall \, \mathbf{k}$ the coherence factors $u_{\mathbf{k}} = 1$ and $v_{\mathbf{k}} = 0$, $\mathbf{U}$ is the unity matrix so that $\Psi_{\gamma\mathbf{k}} = \Psi_{a\mathbf{k}}$ and the hybridization term reduces to the paramagnetic form (Eq. (2.45)).

H_{hyb} defines the type of vertices in the perturbational expansion (B.21) for the resolvent. Fig. C.1 illustrates the two vertices. In contrast to the paramagnetic case, the Fermion line (double solid line) now represents the Nambu spinors $\Psi_{a\mathbf{k}}$ $(\Psi^{\dagger}_{a\mathbf{k}})$ and the vertices are vectors in Nambu space. Thus, in addition to the

FIGURE C.1: *The vertices occurring in a diagrammatic expansion of the reduced resolvent $\bar{R}$ for cluster states coupled to a superconducting conduction electron system.*

normal parts which are also present in the paramagnetic state, the vertices here have anomalous contributions, describing the simultaneous creation (destruction) of a cluster Fermion and a Bogliubov quasiparticle with opposite momentum and spin. The application of the bare resolvent $R^o(z) = (z - H_{\text{loc}} - \mathcal{L}_c)^{-1}$ in the perturbative expansion (B.21) to the Nambu spinors (C.14) describing the diagonalized effective medium, e.g $\Psi^{\dagger}_{\gamma\mathbf{k}}$ now yields

$$R^o(z)\Psi^{\dagger}_{\gamma\mathbf{k}} = \Psi^{\dagger}_{\gamma\mathbf{k}}\mathbf{R}^{\mathbf{o}}(z - E_{\mathbf{k}})\,, \tag{C.22}$$

with the (diagonal) matrix $\mathbf{R}^o(z - E_{\mathbf{k}}) = [(z - H_{\text{loc}})\sigma_o - E_{\mathbf{k}}\sigma_3]^{-1}$. The perturbational expansion for the reduced resolvent $\bar{R}$ (Eq. (B.21) can again be written in form of the Dyson equation (B.24),

$$[\bar{R}^{-1}]_{mn}(z) = (z - E_m)\delta_{mn} - \Sigma^R_{mn}(z) \tag{C.23}$$

and the self-energy Σ^R in NCA approximation sums all the diagrams with non-crossing conduction electron lines. The diagrams for the self-energy are illustrated in Fig. C.2 They are formally identical to the ones in the paramagnetic state

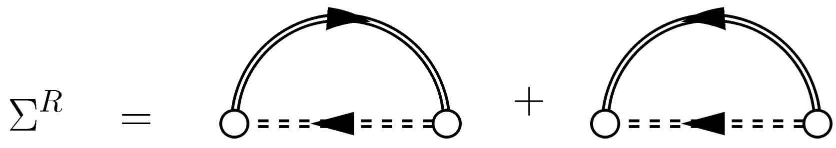

FIGURE C.2: *The NCA self-energy Σ^R in the superconducting state. The double solid curved lines from left to right and right to left stand for the expectation values $\langle(\Psi^{\dagger}_{a\mathbf{k}})^T(\Psi_{a\mathbf{k}})^T\rangle$ and $\langle\Psi_{a\mathbf{k}}\Psi^{\dagger}_{a\mathbf{k}}\rangle$, respectively. The double-dashed arrow represents the Nambu matrix for the dressed reduced resolvent $\bar{\mathbf{R}}$ with matrix elements given by Eq. (C.24).*

(see Fig. 2.7). However the solid curved lines from left to right and right to left now represent the expectation values $\langle(\Psi^\dagger_{a\mathbf{k}})^T(\Psi_{a\mathbf{k}})^T\rangle$ and $\langle\Psi_{a\mathbf{k}}\Psi^\dagger_{a\mathbf{k}}\rangle$, respectively. According to Eq. (C.18) they are diagonal in Nambu space with matrix elements given by the Fermi function $f(\pm E_{\mathbf{k}})$. The double-dashed arrow now represents the Nambu matrix for the dressed reduced resolvent $\bar{\mathbf{R}}$ with matrix elements ll' given by

$$\bar{\mathbf{R}}_{ll'}(z \pm E_{\mathbf{k}}) = \begin{pmatrix} \bar{R}_{ll'}(z \pm E_{\mathbf{k}}) & 0 \\ 0 & \bar{R}_{ll'}(z \mp E_{\mathbf{k}}) \end{pmatrix} . \tag{C.24}$$

After applying the appropriate vectors to the vertices, observing energy and momentum conservation and summing over internal degrees of freedom one obtains for the analytical expression of the resolvent self-energy

$$\begin{aligned} \Sigma^R_{mn}(z) &= \frac{1}{N}\sum_{\mathbf{K},\mathbf{k}'}\sum_{ll'}|V_{\mathbf{K},\mathbf{k}'}|^2 \times \qquad\qquad (C.25) \\ &\Big\{[\mathbf{F}^{\mathbf{K}}_{ml}]^T\sigma_3\mathbf{U}\langle(\Psi^\dagger_{\gamma\mathbf{K}+\mathbf{k}'})^T(\Psi_{\gamma\mathbf{K}+\mathbf{k}'})^T\rangle\bar{\mathbf{R}}_{ll'}(z+E_{\mathbf{K}+\mathbf{k}'})\mathbf{U}^{-1}\sigma_3[(F^{\mathbf{K}}_{nl'})^\dagger]^T \\ &+(\mathbf{F}^{\mathbf{K}}_{lm})^\dagger\sigma_3\mathbf{U}\langle\Psi_{\gamma\mathbf{K}+\mathbf{k}'}\Psi^\dagger_{\gamma\mathbf{K}+\mathbf{k}'}\rangle\bar{\mathbf{R}}_{ll'}(z-E_{\mathbf{K}+\mathbf{k}'})\mathbf{U}^{-1}\sigma_3\mathbf{F}^{\mathbf{K}}_{l'n}\Big\} . \end{aligned}$$

This expression for the NCA-self-energy still contains the auxiliary quantities, which are determined by the lattice quantities encoded in the effective medium Green function (Eq. (2.74)). By using the unitary transformation (C.15) $\mathbf{\Gamma}_c(\mathbf{K})$ in Eq. (C.9) can be written as

$$\mathbf{\Gamma}_c(\mathbf{K}, z) = \frac{1}{N}\sum_{\mathbf{k}'}|V_{\mathbf{K},\mathbf{k}'}|^2\mathbf{U}\langle\langle\Psi_{\gamma\mathbf{K}+\mathbf{k}'}\,;\,\Psi^\dagger_{\gamma\mathbf{K}+\mathbf{k}'}\rangle\rangle^o_z\mathbf{U}^{-1} . \tag{C.26}$$

By applying the identity $\frac{1}{\omega+i\delta} = P\frac{1}{\omega} - i\pi\delta(\omega)$ to $\langle\langle\Psi_{\gamma\mathbf{k}}\,;\,\Psi^\dagger_{\gamma\mathbf{k}}\rangle\rangle^o_z = [z\sigma_o - E_{\mathbf{k}}\sigma_3]^{-1}$ it is straightforward to show with Eqs. (C.18) and (C.24) that

$$\begin{aligned} &\frac{1}{N}\sum_{\mathbf{k}'}|V_{\mathbf{K},\mathbf{k}'}|^2[\mathbf{F}^{\mathbf{K}}_{ml}]^T\sigma_3\mathbf{U}\langle(\Psi^\dagger_{\gamma\mathbf{K}+\mathbf{k}'})^T(\Psi_{\gamma\mathbf{K}+\mathbf{k}'})^T\rangle\bar{\mathbf{R}}_{ll'}(z+E_{\mathbf{K}+\mathbf{k}'})\mathbf{U}^{-1}\sigma_3[(F^{\mathbf{K}}_{nl'})^\dagger]^T = \\ &\qquad = -\frac{1}{\pi}\int_{-\infty}^{+\infty} d\varepsilon\,[\mathbf{F}^{\mathbf{K}}_{ml}]^T\sigma_3 f(\varepsilon)\sigma_o\mathrm{Im}\,\mathbf{\Gamma}_c(\mathbf{K},\varepsilon)\sigma_o\bar{R}_{ll\prime}(z+\varepsilon)\sigma_3[(F^{\mathbf{K}}_{nl'})^\dagger]^T . \qquad (C.27) \end{aligned}$$

The second line of Eq. (C.25) can be expressed via $\mathbf{\Gamma}_c(\mathbf{K})$ accordingly. Now the cluster hybridization function $\mathbf{\Gamma}_c(\mathbf{K})$ can be replaced by the lattice quantity $\mathbf{\Gamma}(\mathbf{K})$ defined in Eq. (2.74) to finally obtain for the resolvent self-energy in the superconducting state

$$\Sigma^R_{mn}(z) = -\frac{1}{\pi}\sum_{\mathbf{K}}\sum_{ll'}\Big\{ \tag{C.28}$$

$$\int_{-\infty}^{+\infty} \mathrm{d}\varepsilon\, [\mathbf{F}^{\mathbf{K}}_{ml}]^T \sigma_3 f(\varepsilon)\sigma_o \mathrm{Im}\, \mathbf{\Gamma}(\mathbf{K},\varepsilon)\sigma_o \bar{R}_{ll'}(z+\varepsilon)\sigma_3[(\mathbf{F}^{\mathbf{K}}_{nl'})^\dagger]^T$$
$$\left. + \int_{-\infty}^{+\infty} \mathrm{d}\varepsilon\, (\mathbf{F}^{\mathbf{K}}_{lm})^\dagger \sigma_3 f(-\varepsilon)\sigma_o \mathrm{Im}\, \mathbf{\Gamma}(\mathbf{K},\varepsilon)\sigma_o \bar{R}_{ll'}(z-\varepsilon)\sigma_3 \mathbf{F}^{\mathbf{K}}_{l'n} \right\} .$$

Together with the Dyson equation (C.23) for the reduced resolvent the expression (C.28) for the NCA self-energy is used to compute the matrix-elements of the reduced resolvent $\bar{R}$ self-consistently. The latter may then be used to calculate the partition function (Eq. (B.17)) and in particular the cluster Green function

$$\mathbf{G}_{\mathrm{c}}(\mathbf{K},z) = \langle\langle \Psi_{f\mathbf{K}}; \Psi^\dagger_{f\mathbf{K}} \rangle\rangle_z \,. \tag{C.29}$$

By using the expansion (C.19) for the Nambu spinors $\Psi_{f\mathbf{K}}$ ($\Psi^\dagger_{f\mathbf{K}}$) in terms of the Hubbard operators X_{mn}, $\mathbf{G}_{\mathrm{c}}$ can be written as

$$\mathbf{G}_{\mathrm{c}}(\mathbf{K},z) = \sum_{\substack{m,m' \\ n,n'}} \mathbf{F}^{\mathbf{K}}_{mm'} (\mathbf{F}^{\mathbf{K}}_{nn'})^\dagger \langle\langle X_{mm'}; X_{n'n} \rangle\rangle_z \tag{C.30}$$

with the correlation function $\langle\langle X_{mm'}; X_{n'n} \rangle\rangle_z$ given by Eq. (2.58).

C.2 Cluster-NCA in the antiferromagnetic state

Effective cluster model for the antiferromagnetic phase

The presence of antiferromagnetic ordering in the effective medium can be simulated by applying a finite staggered magnetic field in z-direction

$$h(\mathbf{x}_i) = h\cos(\mathbf{Q}\mathbf{x}_i) \tag{C.31}$$

with the antiferromagnetic wave-vector $\mathbf{Q} = (\pi,\pi)$ to the auxiliary particles describing the effective medium. Then the term

$$-\sum_{i\sigma} \sigma h(\mathbf{x}_i) a^\dagger_{i\sigma} a_{i\sigma} \tag{C.32}$$

is added to the medium term H_{med} (Eq. (2.44)), where the operators $a_{i\sigma}$ ($a^\dagger_{i\sigma}$) are the Fourier transforms of the auxiliary Fermions $a_{\mathbf{k}\sigma}$ ($a^\dagger_{\mathbf{k}\sigma}$). After transforming Eq. (C.32) to $\mathbf{k}$-space, the modified medium Hamiltonian

$$H^{\mathrm{AF}}_{\mathrm{med}} = H_{\mathrm{med}} + H^{\mathrm{AF}} = \sum_{\mathbf{k}\sigma} \varepsilon_{\mathbf{k}} a^\dagger_{\mathbf{k}\sigma} a_{\mathbf{k}\sigma} - h \sum_{\mathbf{k}\sigma} \sigma a^\dagger_{\mathbf{k}+\mathbf{Q}\sigma} a_{\mathbf{k}\sigma} \tag{C.33}$$

contains a term off-diagonal in $\mathbf{k}$ by coupling particles with momenta $\mathbf{k}$ to particles with momenta $\mathbf{k}+\mathbf{Q}$. The modified cluster Hamiltonian for the antiferromagnetically ordered system is then given by

$$H_{\text{cluster}}^{\text{AF}} = H_f + H_U + H_{\text{hyb}} + H_{\text{med}}^{\text{AF}}\,, \tag{C.34}$$

with H_f, H_U, and H_{hyb} defined in Eqs. (2.42) and (2.45). It describes Fermions on a periodic cluster, coupled to a host with broken translational symmetry due to the presence of a staggered magnetic field h.

It remains to be shown that the bare Green function for the f-electrons of this Hamiltonian has the same form as the effective medium $\mathcal{G}(\mathbf{K})$ (Eq. (2.94)). To enhance the readability of the following equations this is done for the case $t'=0$ in the dispersion $\epsilon_{\mathbf{k}}$ (Eq. (1.4)). The inclusion of a finite t' is straightforward. For $t'=0$ the dispersion fulfills $\epsilon_{\mathbf{k}+\mathbf{Q}} = -\epsilon_{\mathbf{k}}$, thus the inverse of the effective medium Green function $\mathcal{G}$ (Eq. (2.94)) can conveniently be written as

$$\mathcal{G}^{-1}(\mathbf{K},z) = z\sigma_o - (\bar{\epsilon}_{\mathbf{K}} - \mu)\sigma_3 - \mathbf{\Gamma}_\sigma(\mathbf{K},z)\,, \tag{C.35}$$

with the Pauli-spin matrices σ_i defined in Eq. (C.4) and the host-function matrix $\mathbf{\Gamma}_\sigma(\mathbf{K})$. In close analogy to the treatment of superconductivity (see Sec. C.1) the Hamiltonian is then rewritten in terms of the spinors

$$\begin{aligned} \Psi^\dagger_{f\mathbf{K}\sigma} &:= \left(f^\dagger_{\mathbf{K}\sigma}\,,\, f^\dagger_{\mathbf{K}+\mathbf{Q}\sigma}\right) \quad , \quad \Psi_{f\mathbf{K}\sigma} := (\Psi^\dagger_{f\mathbf{K}\sigma})^\dagger \\ \Psi^\dagger_{a\mathbf{K}\sigma} &:= \left(a^\dagger_{\mathbf{K}\sigma}\,,\, a^\dagger_{\mathbf{K}+\mathbf{Q}\sigma}\right) \quad , \quad \Psi_{a\mathbf{K}\sigma} := (\Psi^\dagger_{a\mathbf{K}\sigma})^\dagger \end{aligned} \tag{C.36}$$

for the cluster electrons (f) and auxiliary Fermions (a). Then the uncorrelated parts H_f, $H_{\text{med}}^{\text{AF}}$ and H_{hyb} of the cluster Hamiltonian $H_{\text{cluster}}^{\text{AF}}$ (Eq. (C.34)) can be rewritten to the form

$$H_f = \sum_{\mathbf{K}\sigma}{}' \,(\bar{\epsilon}_{\mathbf{K}} - \mu)\Psi^\dagger_{f\mathbf{K}\sigma}\sigma_3\Psi_{f\mathbf{K}\sigma} \tag{C.37}$$

$$H_{\text{med}}^{\text{AF}} = \sum_{\mathbf{k}\sigma}{}' \,\Psi^\dagger_{a\mathbf{k}\sigma}[\varepsilon_{\mathbf{k}}\sigma_3 - \sigma h\sigma_1]\Psi_{a\mathbf{k}\sigma} \tag{C.38}$$

$$H_{\text{hyb}} = \frac{1}{\sqrt{N}}\sum_{\mathbf{K},\mathbf{k}'\sigma}{}' \,(V_{\mathbf{K},\mathbf{k}'}\Psi^\dagger_{f\mathbf{K}\sigma}\sigma_o\Psi_{a\mathbf{K}+\mathbf{k}'\sigma} + \text{h.c.})\,, \tag{C.39}$$

where the prime on the sums indicates the restriction to momenta within the reduced BZ (see Fig. 2.10 in Sec. 2.6.3). Solving the equation of motion for the bare f-Green function of the uncorrelated part $H_f + H_{\text{med}}^{AF} + H_{\text{hyb}}$ of the generalized cluster Hamiltonian $H_{\text{cluster}}^{\text{AF}}$ (Eq. (C.34)) yields

$$\mathbf{G}^o_f(\mathbf{K},z) = \langle\langle \Psi_{f\mathbf{K}}\,;\,\Psi^\dagger_{f\mathbf{K}}\rangle\rangle^o_z = [z\sigma_o - (\bar{\epsilon}_{\mathbf{K}} - \mu)\sigma_3 - \mathbf{\Gamma}_c(\mathbf{K},z)]^{-1} \tag{C.40}$$

the same form as Eq. (C.35) for the corresponding lattice quantity $\mathcal{G}$. The cluster hybridization function is given by

$$\begin{aligned}\mathbf{\Gamma}_c(\mathbf{K}, z) &= \frac{1}{N}\sum_{\mathbf{k}'} |V_{\mathbf{K},\mathbf{k}'}|^2 \langle\langle \Psi_{\mathbf{K}+\mathbf{k}'\sigma}\,;\,\Psi^\dagger_{\mathbf{K}+\mathbf{k}'\sigma}\rangle\rangle^o_z = \\ &= \frac{1}{N}\sum_{\mathbf{k}'} |V_{\mathbf{K},\mathbf{k}'}|^2 [z\sigma_o - (\bar{\epsilon}_{\mathbf{K}} - \mu)\sigma_3 + \sigma h \sigma_1]^{-1}\,, \qquad \text{(C.41)}\end{aligned}$$

where $\langle\langle \Psi_{\mathbf{k}\sigma}\,;\,\Psi^\dagger_{\mathbf{k}\sigma}\rangle\rangle^o_z$ denotes the bare Green function of the effective medium part $H^{\mathrm{AF}}_{\mathrm{med}}$.

Generalized cluster-NCA for the antiferromagnetic phase

To setup the NCA-algorithm for the extended cluster model (C.34) in the antiferromagnetic phase the steps used for the treatment of superconductivity in the preceding section can be followed. When written in terms of the spinors $\Psi_{f\mathbf{K}\sigma}$ ($\Psi^\dagger_{f\mathbf{K}\sigma}$) the Hamiltonian describing the effective medium $H^{\mathrm{AF}}_{\mathrm{med}}$ is formally similar to the corresponding term in the superconducting state (C.6). Thus the operators that diagonalize the auxiliary medium part are easily obtained by following the steps known for the superconducting state. They are given by

$$\gamma^\dagger_{1\mathbf{k}\sigma} := u_{\mathbf{k}} c^\dagger_{\mathbf{k}\sigma} - \sigma v_{\mathbf{k}} c^\dagger_{\mathbf{k}+\mathbf{Q}\sigma} \quad ; \quad \gamma_{1\mathbf{k}\sigma} = (\gamma^\dagger_{1\mathbf{k}\sigma})^\dagger \qquad \text{(C.42)}$$

$$\gamma^\dagger_{2\mathbf{k}\sigma} := v_{\mathbf{k}} c^\dagger_{\mathbf{k}\sigma} + \sigma u_{\mathbf{k}} c^\dagger_{\mathbf{k}+\mathbf{Q}\sigma} \quad ; \quad \gamma_{2\mathbf{k}\sigma} = (\gamma^\dagger_{2\mathbf{k}\sigma})^\dagger \qquad \text{(C.43)}$$

with the prefactors

$$u_{\mathbf{k}} := \sqrt{\frac{1}{2}\left(1 + \frac{\varepsilon_{\mathbf{k}}}{E_{\mathbf{k}}}\right)}\,;\; v_{\mathbf{k}} := \sqrt{\frac{1}{2}\left(1 - \frac{\varepsilon_{\mathbf{k}}}{E_{\mathbf{k}}}\right)} \qquad \text{(C.44)}$$

and quasiparticle energies

$$E_{\mathbf{k}} = \sqrt{\varepsilon^2_{\mathbf{k}} + h^2}\,. \qquad \text{(C.45)}$$

The medium part can then be written as

$$H^{\mathrm{AF}}_{\mathrm{med}} = {\sum_{\mathbf{k}\sigma}}' E_{\mathbf{k}} (\gamma^\dagger_{1\mathbf{k}\sigma}\gamma_{1\mathbf{k}\sigma} - \gamma^\dagger_{2\mathbf{k}\sigma}\gamma_{2\mathbf{k}\sigma})\,. \qquad \text{(C.46)}$$

Due to the similarity to the corresponding expressions for the superconducting state (see Sec. C.1) it is straightforward to carry through the remaining steps. The spinors $\Psi_{f\mathbf{K}\sigma}$ ($\Psi^\dagger_{f\mathbf{K}\sigma}$) defined in Eq. (C.36) are expanded in terms of the Hubbard operators X_{mn}

$$\Psi_{f\mathbf{K}\sigma} = \sum_{m,n} \mathbf{F}^{\mathbf{K}\sigma}_{mn} X_{mn} \quad , \quad \Psi^\dagger_{f\mathbf{K}\sigma} = \sum_{m,n} (\mathbf{F}^{\mathbf{K}\sigma}_{mn})^\dagger X_{nm}\,, \qquad \text{(C.47)}$$

with expansion coefficients

$$\mathbf{F}_{mn}^{\mathbf{K}\sigma} = \begin{pmatrix} F_{mn}^{\mathbf{K}\sigma} \\ F_{mn}^{\mathbf{K}+\mathbf{Q}\sigma} \end{pmatrix} \quad , \quad (\mathbf{F}_{mn}^{\mathbf{K}\sigma})^\dagger = \big((F_{mn}^{\mathbf{K}\sigma})^\star \, ; \, (F_{mn}^{\mathbf{K}+\mathbf{Q}\sigma})^\star\big) \ . \tag{C.48}$$

Then the hybridization term H_{hyb} (Eq. (C.39)) is formally identical to the corresponding term (C.21) in the superconducting state, with the Pauli matrix σ_3 replaced by σ_o. The remaining calculation is entirely analogous to the corresponding calculation for the superconducting state. It is therefore straightforward to obtain for the resolvent self-energy

$$\begin{aligned}\Sigma_{mn}^R(z) \quad = \quad & -\frac{1}{\pi}\sum_{\mathbf{K}\sigma}\sum_{l,l'}\Bigg\{ \qquad\qquad (C.49)\\ & \int\limits_{-\infty}^{+\infty} \mathrm{d}\varepsilon \, [\mathbf{F}_{ml}^{\mathbf{K}\sigma}]^T \sigma_o f(\varepsilon)\sigma_o \mathrm{Im}\, \mathbf{\Gamma}_\sigma(\mathbf{K},\varepsilon)\sigma_o \bar{R}_{ll'}(z+\varepsilon)\sigma_o[(\mathbf{F}_{nl'}^{\mathbf{K}\sigma})^\dagger]^T \\ & + \int\limits_{-\infty}^{+\infty} \mathrm{d}\varepsilon \, (\mathbf{F}_{lm}^{\mathbf{K}\sigma})^\dagger \sigma_o f(-\varepsilon)\sigma_o \mathrm{Im}\, \mathbf{\Gamma}_\sigma(\mathbf{K},\varepsilon)\sigma_o \bar{R}_{ll'}(z-\varepsilon)\sigma_o \mathbf{F}_{l'n}^{\mathbf{K}\sigma} \Bigg\} \ ,\end{aligned}$$

where the lattice hybridization function $\mathbf{\Gamma}_\sigma(\mathbf{K})$ defined in Eq. (C.35) was already worked in. Since the off-diagonal elements of $\mathbf{\Gamma}_\sigma(\mathbf{K})$ are finite in the antiferromagnetic state, Σ^R now contains diagrams connecting states m and n with momenta $\mathbf{K}$ and $\mathbf{K}+\mathbf{Q}$ and the reduced resolvent

$$[\bar{R}^{-1}]_{mn}(z) = (z - E_m)\delta_{mn} - \Sigma_{mn}^R(z) \tag{C.50}$$

contains off-diagonal elements between these states. The set of equations (C.50) and (C.49) has to be solved self-consistently to evaluate the matrix elements of the reduced resolvent $\bar{R}$. These may then be used to calculate the cluster Green function $\mathbf{G}_\mathrm{c}(\mathbf{K},z) = \langle\langle \Psi_{f\mathbf{K}\sigma} \, ; \, \Psi_{f\mathbf{K}\sigma}^\dagger \rangle\rangle_z$ which can again be written as

$$\mathbf{G}_\mathrm{c}(\mathbf{K},z) = \sum_{\substack{m,m'\\ n,n'}} \mathbf{F}_{mm'}^{\mathbf{K}\sigma}(\mathbf{F}_{nn'}^{\mathbf{K}\sigma})^\dagger \langle\langle X_{mm'} ; X_{n'n}\rangle\rangle_z \ , \tag{C.51}$$

with the correlation function $\langle\langle X_{mm'} ; X_{n'n}\rangle\rangle_z$ given by Eq. (2.58).

C.3 DMFA in the antiferromagnetic state

The formalism presented in Sec. 2.6.3 cannot be utilized for the cluster size $N_c = 1$ (=DMFA), since it involves the calculation of Green functions and self-energies at the cluster momenta $\mathbf{K}+\mathbf{Q}$ in addition to momenta $\mathbf{K}$, whereas the DMFA self-energy $\Sigma(z)$ is purely local and therefore $\mathbf{k}$-independent. Hence a real space approach must be formulated for this special case.

In the antiferromagnetic phase the DMFA equations have to be extended to account for two inequivalent sub-lattices A and B (see Sec. 2.6.3) and corresponding self-energies $\Sigma^A \neq \Sigma^B$ [Bra90]. To this end the uncorrelated part of the Hubbard Hamiltonian, $H_o = \sum_{\mathbf{k}\sigma} \epsilon_{\mathbf{k}} c^\dagger_{\mathbf{k}\sigma} c_{\mathbf{k}\sigma}$ is written in terms of the sub-lattice operators (2.97) acting in the reduced BZ

$$H_o = \sum_{\mathbf{k}\sigma}{}' \epsilon_o (c^\dagger_{A\mathbf{k}\sigma} c_{A\mathbf{k}\sigma} + c^\dagger_{B\mathbf{k}\sigma} c_{B\mathbf{k}\sigma}) + \sum_{\mathbf{k}\sigma}{}' t_{\mathbf{k}} (c^\dagger_{A\mathbf{k}\sigma} c_{B\mathbf{k}\sigma} + c^\dagger_{B\mathbf{k}\sigma} c_{A\mathbf{k}\sigma})\,, \tag{C.52}$$

where $\epsilon_{\mathbf{k}} = \epsilon_o + t_{\mathbf{k}}$. The prime on the sum indicates summation over the reduced BZ only. The Green function is then written as a matrix in the two sub-lattices

$$G^{-1}_\sigma(\mathbf{k}, z) = \begin{pmatrix} \zeta^A_\sigma & -t_{\mathbf{k}} \\ -t_{\mathbf{k}} & \zeta^B_\sigma \end{pmatrix}\,, \tag{C.53}$$

with $\zeta^{A/B}_\sigma = z - (\epsilon_o + \mu) - \Sigma^{A/B}_\sigma$. Due to the symmetry of the sub-lattices $\zeta^A_\sigma = \zeta^B_{\bar\sigma}$ the sub-lattice index A/B can be dropped and the local Green function on a given sub-lattice, e.g. A, is obtained by summing $G_\sigma(\mathbf{k}, z)$ over $\mathbf{k}$

$$G_{ii,\sigma}(z) = \frac{1}{N} \sum_{\mathbf{k}} \frac{\zeta_{\bar\sigma}}{\zeta_\uparrow \zeta_\downarrow - t^2_{\mathbf{k}}}\,. \tag{C.54}$$

This is again written in the form (2.12)

$$G_{ii,\sigma}(z) = \frac{1}{z - \epsilon_o + \mu - \Sigma_\sigma(z) - \Gamma_\sigma(z)}\,, \tag{C.55}$$

where the spin index was kept to account for a finite magnetization $m = |n^A_\uparrow - n^A_\downarrow|$ on the A-sub-lattice. The corresponding impurity model is still given by (2.13), with the effective medium fixed by

$$\mathcal{G}^{-1}_\sigma(z) = G^{-1}_{ii,\sigma}(z) + \Sigma_\sigma(z)\,, \tag{C.56}$$

which now depends on the spin σ. For a vanishing sub-lattice magnetization $\zeta_\uparrow = \zeta_\downarrow$, Eq. (C.54) is equivalent to the corresponding equation (2.11) in the paramagnetic phase and the algorithm reduces to the one presented in Sec. 2.2.

Literature

[Aeb94] P. Aebi, J. Osterwalder, P. Schwaller, L. Schlapbach, M. Shimoda, T. Mochiku, K. Kadowaki, *Complete Fermi surface mapping of $Bi_2Sr_2CaCu_2O_{8+x}$(001): Coexistence of short range antiferromagnetic correlations and metallicity in the same phase*, Phys. Rev. Lett. **72**, 2757 (1994).

[All93] H. Alloul, A. Mahajan, H. Casalta, O. Klein, *^{89}Y NMR study of the anisotropy of the static and dynamic susceptibilities in $YBa_2Cu_3O_{6+x}$*, Phys. Rev. Lett. **70**, 1171 (1993).

[And91] P. W. Anderson, J. R. Schrieffer, *A Dialogue on the Theory of High T_c*, Phys. Today **44**, 55 (1991).

[And94] O. K. Andersen, O. Jepsen, A. I. Liechtenstein, I. I. Mazin, *Plane dimpling and saddle-point bifurcation in the band structures of optimally doped high-temperature superconductors: A tight-binding model*, Phys. Rev. B **49**, 4145 (1994).

[And97] P. W. Anderson, *The Theory of Superconductivity in the High-T_c Cuprates*, Princeton Univ. Press (1997).

[Bac91] S. B. Bacci, E. R. Gagliano, R. M. Martin, J F. Annett, *Derivation of a one-band Hubbard model for CuO planar materials*, Phys. Rev B **44**, 7504 (1991).

[Bay62] G. Baym, *Self-Consistent Approximations in Many-Body Systems*, Phys. Rev. **127**, 1391 (1962).

[Bec86] K. W. Becker, J. Keller, *Self-Trapping of a Dipole Coupled to a Lattice: Application of a New Theoretical Method to an Old Problem*, Z. Phys. B **62**, 477 (1986).

[Bic87] N. E. Bickers, D. L. Cox, J. W. Wilkins, *Self-consistent large-N expansion for normal-state properties of dilute magnetic alloys*, Phys. Rev. B **36**, 2036 (1987).

[Bic89] N. E. Bickers, D. J. Scalapino, S. R. White, *Conserving approximations for strongly correlated electron systems: Bethe-Salpeter equation and dynamics for the two-dimensional Hubbard model*, Phys. Rev. Lett. **62**, 961 (1989).

[Bir99] R. J. Birgeneau, M. Greven, M. A. Kastner, Y. S. Lee, B. O. Wells, Y. Endoh and K. Yamada, *Instantaneous spin correlations in La_2CuO_4*, Phys. Rev B **59**, 13788 (1991).

[Bro55] H. A. Brown, J. M. Luttinger, *Ferromagnetic and Antiferromagnetic Curie Temperatures*, Phys. Rev **100**, 685 (1955).

[Bul94] N. Bulut, D. J. Scalapino, S. R. White, *Effective electron-electron interaction in the two-dimensional Hubbard model*, Phys. Rev. B **50**, 9623 (1994).

[Bul97] R. Bulla, Th. Pruschke, A. C. Hewson, *Anderson impurity in pseudo-gap Fermi systems*, J. Phys.: Cond. Matter **9**, 10463 (1997).

[Bul00] R. Bulla, *The Numerical Renormalization Group Method for correlated electrons*, preprint, cond-mat/0003377 (2000).

[Buc93] B. Bucher, P. Steiner, J. Karpinski, E. Kaldis, P. Wachter, *Influence of the spin gap on the normal state transport in $YBa_2Cu_4O_8$*, Phys. Rev. Lett. **70**, 2012 (1993).

[Bra89] U. Brandt, C. Mielsch, *Thermodynamic and correlation functions of the Falicov-Kimball model in large dimensions*, Z. Phys. B **75**, 365 (1989).

[Bra90] U. Brandt, C. Mielsch, *Thermodynamics of the Falicov-Kimball model II*, Z. Phys. B **79**, 295 (1990).

[Caf94] M. Caffarel, W. Krauth, *Exact diagonalization approach to correlated fermions in infinite dimensions: Mott transition and superconductivity*, Phys. Rev. Lett. **72**, 1545 (1994).

[Cre95] C. E. Creffield, E. G. Klepfish, E. R. Pike, S. Sarkar, *Spectral weight function for the half-filled Hubbard model: A singular value decomposition approach* , Phys. Rev. Lett. **75**, 517 (1995).

[Dag92] E. Dagotto, F. Ortolani, D. Scalapino, *Single-particle spectral weight of a two-dimensional Hubbard model*, Phys. Rev. B **46**, 3183 (1992).

[Dag94a] E. Dagotto, *Correlated Electrons in high-temperature superconductors*, Rev. Mod. Phys. **66**, 763 (1994).

[Dag94b] E. Dagotto, A. Nazarenko M. Boninsegni, *Flat quasiparticle dispersion in the 2D t-J model*, Phys. Rev. Lett. **73**, 728 (1994).

[Dei96] J. J. Deisz, D. W. Hess, J. W. Serene, *Incipient antiferromagnetism and low-energy excitations in the half-filled two-dimensional Hubbard model*, Phys. Rev. Lett. **76**, 1312 (1996).

[Des93] D. S. Dessau, Z.-X. Shen, D. M. King, D. S. Marshall, L. W. Lombardo, P. H. Dickinson, A. G. Loeser, J. DiCarlo, C.-H Park, A. Kapitulnik, W. E. Spicer, *Key features in the measured band structure of $Bi_2Sr_2CaCu_2O_{8+\delta}$: Flat bands at E_F and Fermi surface nesting*, Phys. Rev. Lett. **71**, 2781 (1993).

[Din96] H. Ding, T. Yokoya, J. C. Campuzano, T. Takahashi, M. Randeria, M. R. Norman, T. Mochiku, K. Kadowaki, J. Giapintzakis, *Spectroscopic evidence for a pseudogap in the normal state of underdoped high-T_c superconductors*, Nature (London) **382**, 51 (1996).

[Don91] P. G. J. van Dongen, *Thermodynamics of the extended Hubbard model in high dimensions*, Phys. Rev. Lett. **67**, 757 (1991).

[Don94] P. G. J. van Dongen, *Extended Hubbard model at weak coupling*, Phys. Rev. B **50**, 14016 (1994).

[Ell82] D. F. Elliot, K. R. Rao, *Fast Transform Algorithms, Analyses, Applications*, Academic Press, New York (1982).

[Eme87] V. J. Emery, *Theory of high-T_c superconductivity in oxides*, Phys. Rev. Lett. **58**, 2794 (1987).

[Eme88] V. J. Emery, G. Reiter, *Mechanism for high-temperature superconductivity*, Phys. Rev. B **38**, 4547 (1988).

[Fet99] W. Fettes, I. Morgenstern, *Evidence for d-wave superconductivity in the repulsive Hubbard model*, Eur. Phys. J. B **9**, 635 (1999).

[Ful91] P. Fulde, *Electron Correlations in Molecules and Solids*, Springer Series in Solid-State Sciences, Vol. **89**, Springer-Verlag, Berlin/Heidelberg/New-York (1991).

[Geo92] A. Georges and G. Kotliar, *Hubbard model in infinite dimensions*, Phys. Rev. B **45**, 6479 (1992).

[Geo96] A. Georges, G. Kotliar, W. Krauth, M. Rozenberg, *The Local Impurity Self Consistent Approximation (LISA) to Strongly Correlated Fermion Systems and the Limit of Infinite Dimensions*, Rev. Mod. Phys. **68**, 13 (1996).

[Gro85] G. Grosso, G. Parravicini, *Memory Function Approaches to Stochastic Problems in Condensed Matter*, Advances in Chemical Physics, Vol. **62**, Wiley, New York (1985), p. 133.

[Hal00] C. J. Halboth, W. Metzner, *Renormalization-group analysis of the two-dimensional Hubbard model*, Phys. Rev. B, **61** 7364 (2000).

[Hei99] W. Heindl, T. Pruschke, J. Keller, *c-axis transport in the bilayer t-J model*, Physica B **259**, 745 (1999).

[Hei00a] W. Heindl, T. Pruschke, J. Keller, *Incoherence in bilayer systems with strong electronic correlations*, J. Phys., Condens. Matter **12**, 2245 (2000).

[Hei00b] W. Heindl, *Stark korrelierte Mehrbandsysteme*, Dissertation, Universität Regensburg (2000).

[Het98] M.H. Hettler, A. N. Tahvildar-Zadeh, M. Jarrell, T. Pruschke, H. R. Krishnamurthy, *Nonlocal dynamical correlations of strongly interacting electron systems*, Phys. Rev. B **58**, 7475 (1998).

[Het00] M.H. Hettler, M. Mukherjee, M. Jarrell, H. R. Krishnamurthy, *The Dynamical Cluster Approximation: Non-Local Dynamics of Correlated Electron Systems*, Phys. Rev. B **61**, 12739 (2000).

[Hir85] J. E. Hirsch, *Two-dimensional Hubbard Model: Numerical Simulation Study*, Phys. Rev. B **31**, 4403 (1985).

[Hir86] J. E. Hirsch, R. M. Fye, *Monte Carlo method for magnetic impurities in metals*, Phys. Rev. Lett **56**, 2521 (1986).

[Hoh67] P. C. Hohenberg, *Existence of Long-Range Order in One and Two Dimensions*, Phys. Rev. **158**, 383 (1967).

[Hus96] T. Husslein, I. Morgenstern, D. M. Newns, P. C. Pattnaik, J. M. Singer, H. G. Matuttis, *Quantum Monte Carlo evidence for d-wave pairing in the two dimensionl Hubbard model at a van Hove singularity*, Phys. Rev. B **54**, 16179 (1996).

[Hus99] C. Huscroft, M. Jarrell, Th. Maier, S. Moukouri, A. N. Tahvildarzadeh, *Pseudogaps in the 2D half-filled Hubbard model*, preprint, cond-mat/9910226, to appear in Phys. Rev. Lett. (1999).

[Hwa94] H. Y. Hwang, B. Batlogg, H. Takagi, H. L. Kao, J. Kwo, R. J. Cava, J. J. Krajewski, W. F. Peck, Jr., *Scaling of the temperature dependent Hall effect in $La_{2-x}Sr_xCuO_4$*, Phys. Rev. Lett. **72**, 2636 (1994).

[Hyb90] M. S. Hybertsen, E. B. Stechel, M. Schluter, D. R. Jennison , *Renormalization from density-functional theory to strong coupling models for electronic states in Cu-O materials*, Phys. Rev. B **41**, 11068 (1990).

[Ima98] M. Imada, A. Fujimori, Y. Tokura, *Metal-insulator transitions*, Rev. Mod. Phys. **70** 1039 (1998).

[Ino98] A. Ino, C. Kim, T. Mizokawa, Z.-X. Shen, A. Fujimori, M. Takaba, K. Tamasaku, H. Eisaki, S. Uchida, *Fermi Surface and Band Dispersion in $La_{2-x}Sr_xCuO_4$*, preprint, cond-mat/9809311 (1998).

[Itz89] C. Itzykson, J. M. Drouffe, *Statistical Field Theory Vol.I & II*, Cambridge University Press, Cambridge (1989).

[Jak99] J. Jaklic, P. Prelovsek, *Finite-temperature properties of doped antiferromagnets*, Adv. Phys. **49**, 1 (1999).

[Jan91] V. Janiš, *A new construction of thermodynamic mean-field theories of itinerant fermions: application to the Falicov-Kimball model*, Z. Phys. B **83**, 227 (1991).

[Jar92] M. Jarrell, *Hubbard model in infinite dimensions: A quantum Monte Carlo study*, Phys. Rev. Lett. **69**, 168 (1992).

[Jar93] M. Jarrell, Th. Pruschke, *Magnetic and Dynamic Properties of the Hubbard model in infinite dimensions*, Z. Phys. B **90**, 187 (1992).

[Jar99] M. Jarrell, *private communication* (1999).

[Jar00] M. Jarrell, Th. Maier, M. H. Hettler, A. N. Tahvildarzadeh, *Phase Diagram of the Hubbard Model: Beyond the Dynamical Mean Field*, preprint, cond-mat/0011282 (2000).

[Kam90] A. P. Kampf, J. R. Schrieffer, *Spectral function and photoemission spectra in antiferromagnetically correlated metals*, Phys. Rev. B **42**, 7967 (1990).

[Kei71] H. Keiter, J. C. Kimball, *Diagrammatic perturbation technique for the Anderson Hamiltonian, and relation to the s-d exchange Hamiltonian*, Int. J. Magn. **1**, 233 (1971).

[Kel98] J. Keller, private communication (1998).

[Kos73] J. M. Kosterlitz, D. J. Thouless, *Ordering, metastability and phase-transitions in two-dimensional systems*, J. Phys. C **6**, 1181 (1973).

[Lan95] M. Langer, J. Schmalian, S. Grabowski, K. H. Bennemann, *Theory for the excitation spectrum of high-T_c superconductors: quasi-particle dispersion and shadows of the Fermi surface*, Phys. Rev. Lett. **75**, 4508 (1995).

[Leu92] P. W. Leung, Z. Liu, E. Manousakis, M. A. Novotny, P. E. Oppenheimer, *Density of states of the two-dimensional Hubbard model on a 4 x 4 lattice*, Phys. Rev. B **46**, 11779 (1992).

[Lie99] A. I. Lichtenstein, M. I. Katsnelson, *Antiferromagnetism and d-wave superconductivity in cuprates: a cluster DMFT study*, preprint cond-mat/9911320 (1999).

[Lut60] J. M. Luttinger, *Fermi Surface and Some Simple Equilibrium Properties of a System of Interacting Fermions*, Phys. Rev. **119**, 1153 (1960).

[Mag85] A. Magnus, *The Recursion Method and its Applications*, Springer Series in Solid State Sciences Vol. **58**, Springer Berlin (1985).

[Mah90] G. Mahan, *Many Particle Physics*, Plenum Press, New York (1969).

[Mai97] Th. Maier, *Untersuchung magnetischer Eigenschaften von 3-Band-Hubbard-Systemen*, Diplomarbeit, Universität Regensburg (1997).

[Mai99] Th. Maier, M. B. Zölfl, Th. Pruschke, J. Keller, *Magnetic properties of the 3-band Hubbard model*, Eur. Phys. J. B **7**, 377 (1999).

[Mai00a] Th. Maier, M. Jarrell, Th. Pruschke, J. Keller, *A Non-Crossing Approximation for the Study of Intersite Correlations*, Eur. Phys. J. B **13**, 613 (2000).

[Mai00b] Th. Maier, M. Jarrell, Th. Pruschke, J. Keller, *d-Wave Superconductivity in the Hubbard Model*, Phys. Rev. Lett. **85**, 1524 (2000).

[Map98] M. B. Maple, *High Temperature Superconductivity*, Proceedings of "International Conference on Magnetism 1997",Cairns, Australia (1997), J. of Mag. and Mag. Mat. **177**, 18 (1998).

[Mer66] N. D. Mermin, H. Wagner, *Absence of Ferromagnetism in One or Two Dimensional Isotropic Heisenberg Models*, Phys. Rev. Lett. **17**, 1133 (1966).

[Met89] W. Metzner and D. Vollhardt, *Correlated lattice fermions in $d = \infty$ dimensions*, Phys. Rev. Lett. **62**, 324 (1989).

[Mil90] A. Millis, H. Monien, D. Pines, *Weak-coupling theory of high-temperature superconductivity in the antiferromagnetically correlated copper oxides*, Phys. Rev. B **46**, 14803 (1990).

[Mon91] P. Monthoux, A.V. Balatsky, D. Pines, *Toward a theory of high-temperature superconductivity in the antiferromagnetically correlated cuprate oxides*, Phys. Rev. Lett. **67**, 3448, (1991).

[Mon92] P. Monthoux, D. Pines, *Spin-fluctuation-induced superconductivity in the copper oxides: A strong coupling calculation*, Phys. Rev. Lett. **69**, 961, (1992).

[Mon94] P. Monthoux, D. J. Scalapino, *Self-Consistent $d_{x^2-y^2}$ Pairing in a Two Dimensional Hubbard Model*, Phys. Rev. Lett. **72**, 1874, (1994).

[Mor90] T. Moriya, Y. Takahashi, K. Ueda, *Antiferromagnetic Spin Fluctuations and Superconductivity in Two-Dimensional Metals: A Possible Model for High T_c Oxides*, J. Phys. Soc. Japan **59**, 2905 (1990).

[Mor92] A. Moreo, *Pairing correlations in the two-dimensional Hubbard model*, Phys. Rev. B **45**, 5059, (1992).

[Mou99] S. Moukouri, S. Allen, F. Lemay, B. Kyung, D. Poulin, Y. M. Vilk, A.-M. S. Tremblay, *Many-body Theory vs Simulations for the pseudogap in the Hubbard model*, preprint, cond-mat/9908053 (1999).

[Mou00] S. Moukouri, C. Huscroft, M. Jarrell, *The Dynamical Cluster Approximation: A New Technique for Simulations of Strongly Correlated Electron Systems*, preprint, cond-mat/0004279 (2000), to appear in *Computer Simulations in Condensed Matter Physics VII*, edited by D. P. Landau, K. K. Mon and H. B. Schütler, Springer Verlag, Heidelberg, Berlin (2000).

[Mül84] E. Müller-Hartmann, *Self-Consistent Perturbation Theory of the Anderson Model: Ground State Properties*, Z. Phys. B **57**, 281 (1984).

[Mül89] E. Müller-Hartmann, *Correlated fermions on a lattice in high dimensions*, Z. Phys. B **74**, 507 (1989).

[Nor97] M. R. Norman, H. Ding, M. Randeria, J. C. Campuzano, T. Yokoya, T. Takeuchi, T. Takahashi, T. Mochiku, K. Kadowaki, P. Guptasarma, D. G. Hinks , *Destruction of the Fermi Surface in Underdoped High T_c Superconductors*, Nature **392**, 157 (1998).

[Nüc87] N. Nücker, J. Fink, B. Renker, D. Ewert, C. Politis, P. J. W. Weijs, J. C. Fuggle , *Experimental Electronic Structure Studies of $La_{2-x}Sr_xCuO_4$*, Z. Phys. B **67**, 9 (1987).

[Obe97] Th. Obermeier, Th. Pruschke, J. Keller, *Effects of spin fluctuations in the t-J model*, Physica B **230-232**, 892 (1997).

[Pin97] D. Pines, *Nearly antiferromagnet Fermi liquids: a progress report*, Z. Phys. B **103**, 129 (1997).

[Poi93] D. Poilblanc, T. Ziman, H. J. Schulz, E. Dagotto, *Dynamical properties of a single hole in an antiferromagnet*, Phys. Rev. B **47**, 14267 (1993).

[Pre95] R. Preuss, W. Hanke, W. von der Linden, *Quasiparticle Dispersion of the 2D Hubbard Model: From an Insulator to a Metal*, Phys. Rev. Lett. **75**, 1344 (1995).

[Pru89] Th. Pruschke, N. Grewe, *The Anderson model with finite Coulomb repulsion*, Z. Phys. B **74**, 439 (1989).

[Pru95a] Th. Pruschke, M. Jarrell, J. K. Freericks, *Anomalous Normal-State Properties of High-Tc Superconductors - Intrinsic Properties of Strongly Correlated Electron Systems?*, Adv. in Phys. **42**, 187 (1995).

[Pru95b] Th. Pruschke *Dynamische Molekularfeldtheorie für stark korrelierte Fermionensysteme*, Habilitationsschrift, Universität Regensburg (1995).

[Pru99] Th. Pruschke, private notes (1999).

[Ran97] R. Randeria and J. C. Campuzano, *High Tc Superconductors: New Insights from Angle-Resolved Photoemission*, preprint cond-mat/9709107 (1997).

[Sak94] O. Sakai, Y. Kuramoto, *Application of the Numerical Renormalization Group Method to the Hubbard Model in infinite dimensions*, Sol. Stat. Comm. **89**, 307 (1994).

[Sch61] J. R. Schrieffer, *Theory of Superconductivity*, Reading, Massachusetts (1961).

[Sch89] J. R. Schrieffer, X. G. Wen, S. C. Zhang, *Dynamic spin fluctuations and the bag mechanism of high-T_c superconductivity*, Phys. Rev. B **39**, 11663 (1989).

[Sch99] J. Schmalian, D. Pines, B. Stojkovic, *Microscopic theory of weak pseudogap behavior in the underdoped cuprate superconductors: General theory and quasiparticle properties*, Phys. Rev. B **60**, 667, (1999).

[Sch95] A. Schiller, K. Ingersent, *Systematic 1/d corrections to the infinite-dimensional limit of correlated lattice electron models*, Phys. Rev. Lett. **75**, 113, (1995).

[Sca99] D. J. Scalapino, *Superconductivity and Spin Fluctuations* , preprint cond-mat/9908287 (1999).

[Ste98] B. Steininger, *Starke Korrelationen in Supraleitern*, Dissertation, Universität Regensburg (1998).

[Tak92] H. Takagi, B. Batlogg, H. L. Kao, J. Kwo, R. J. Cava, J. J. Krajewski, W. F. Peck, Jr., *Systematic evolution of temperature-dependent resistivity in* $La_{2-x}Sr_xCuO_4$, Phys. Rev. Lett. **69**, 2975 (1992).

[Tim99] T. Timusk, B. Statt, *The pseudogap in high temperature superconductors: an experimental survey*, preprint, cond-mat/9905219 (1999).

[Vek93] M. Vekic, S. R. White, *Pseudogap formation in the half-filled Hubbard model*, Phys. Rev. B **47**, 1160 (1993).

[Wei48] P. R. Weiss, *The Application of the Bethe-Peierls Method to Ferromagnetism*, Phys. Rev. **74**, 1493 (1948).

[Whi89a] S. R. White, D. J. Scalapino, R. L. Sugar, N. E. Bickers, R. T. Scalletar, *Attractive and repulsive pairing interaction vertices for the two-dimensional Hubbard model*, Phys. Rev. B **39**, 839 (1989).

[Whi89b] S. R. White, D. J. Scalapino, R. L. Sugar, E. Y. Loh, J. E. Gubernatis, R. T. Scalettar, *Numerical study of the two-dimensional Hubbard model*, Phys. Rev. B **40**, 506 (1989).

[Wil75] K. G. Wilson, *The renormalization group: critical phenomena and the Kondo problem*, Rev. Mod. Phys. **47** 773 (1975).

[Zan85] J. Zaanen, G. A. Sawatzky, J. W. Allen, *Band Gaps and Electronic Structure of Transition Metal Compounds*, Phys. Rev. Lett. **55**, 418 (1985).

[Zha96] Y. Zha, V. Barzykin, D. Pines, *NMR and neutron-scattering experiments on the cuprate superconductors: A critical re-examination*, Phys. Rev. B **54**, 7561 (1996).

[Zha97] S. Zhang, J. Carlson, J. E. Gubernatis, *Pairing Correlations in the Two-Dimensional Hubbard Model*, Phys. Rev. Lett. **78**, 4486 (1997).

[Zöl97] M. Zölfl, *Elektronische Eigenschaften der CuO_2-Ebenen in Hoch-Temperatur-Supraleitern*, Diplomarbeit, Universität Regensburg (1997).

[Zöl00] M. Zölfl, Th. Maier, Th. Pruschke, J. Keller, *Electronic properties of* $\mathrm{CuO_2}$*-planes: A DMFT study* , Eur. Phys. J. B **13**, 47 (2000).

Acknowledgements

First of all I thank my advisor **Dr. habil. Thomas Pruschke** and the head of our working group **Prof. Dr. Joachim Keller** for their invaluable competent assistance during the years of research and for many stimulating discussions. I am especially grateful to the first-mentioned for giving me the chance to spend a wonderful year at the University of Cincinnati, USA, where major parts of this research were done.

I am greatly indebted to **Prof. Dr. Mark Jarrell** for giving me the opportunity to work on a new technique, providing me with his stimulating advice, criticism and instructions, for his never-ending patience with all my questions and for his hospitality throughout my stay in Cincinnati.

I am most thankful to **Werner Heindl**, **Markus Zölfl**, **Dr. Christian Preis** and **Dr. Christian Helm** for their meticulous proof-reading of my thesis and tons of constructive comments. I also want to thank them for many interesting discussions and for the fun time off work. Especially the last-mentioned deserves special credit for making my life much more difficult by his unrelenting insistence to be more intelligible.

Further I feel pleasure to thank all former and not already mentioned members of our group for the wonderful working atmosphere. Inparticular I want to mention **Dr. Thomas Obermeier**, **Dr. Bärbel Steininger**, **Markus Dittrich**, **Bernhard Rieder**, **Robert Zitzler** and **Karin Schmalzl**.

Of all the colleagues at the University of Cincinnati I would like to mention **Dr. Alireza Niki Tahvildarzadeh** and **Dr. Carey Huscroft**. It was great fun to work with them! I also want to thank Niki for being a very good friend throughout my stay in Cincinnati.

Furthermore I like to thank **Angela Reißer** for her great organizing talent and for the years of keeping the coffee machine running.

I am greatly indebted to my girl friend **Barbara Lillard**. She made my life so much easier with her understanding and patient nature. My **parents** deserve special credit for their unconditional support throughout the years. Last but not least I thank all my **friends** in Regensburg and everybody I forgot to mention.

This research was supported by the **Deutsche Forschungsgemeinschaft**, Graduiertenkolleg *Komplexität in Festkörpern.*